Lanthanide-doped upconversion nanoparticles (UCNPs) for biomedical applications

By

Afshin Karami, MPhil, MIChemE

Supervisors:

Dr Stephen Kidd

Professor Christopher Sumby

Associate Professor Jingxiu Bi

Thesis submitted in fulfilment of the requirements for the degree of

Doctor of Philosophy

School of Chemical Engineering

Faculty of Science, Engineering and Technology

The University of Adelaide

September 2023

List of Abbreviations

AMR	Antimicrobial resistance
ANOVA	Analysis of variance
APF	3′-p-(aminophenyl) fluorescein
CB	Conduction band
CFU	Colony-forming units
Ce6	Chlorin e6
CNT	Carbon nanotubes
CS	Cationic polysaccharide chitosan
CT	Computed tomography
CTAB	Cetyltrimethylammonium bromide
CW	Continuous wave
DLS	Dynamic light scattering
DNA	Deoxyribonucleic acid
DSB	Double-stranded breaks
EDS	Energy dispersive spectroscopy
EDX	Energy-dispersive X-ray analysis
ETC	Electron transport chain
ETU	Energy transfer upconversion
FDA	Food and drug administration
GFP	Green fluorescent protein
GO	Graphene oxide
GRAS	Generally recognised as safe
GW	Gigawatt
HCl	Hydrochloric acid
HR	High resolution
HRSEM	High-resolution TEM
ICP-MS	Inductively-coupled plasma mass spectrometry
IDE	Idebenone
JCPDS	Joint Committee on Powder Diffraction Standards
LB	Luria-Bertani
LED	Light-emitting diode
LNP	Lipid nanoparticles
LPHN	Lipid-polymer hybrid nanoparticles
LSPR	Localised surface plasmon resonance
MDR	Multidrug-resistance
MIC	Minimum inhibitory concentration
MOF	Metal-organic framework

MRI	Magnetic resonance imaging
MRSA	Methicillin-resistant *Staphylococcus aureus*
MW	Microwave
NADH	Nicotinamide adenine dinucleotide (NAD) + hydrogen (H)
NIR	Near-infrared
NLC	Nanostructured lipid carriers
NP	Nanoparticle
OA	Oleic acid
ODE	1-octadecene
OPO	Optical parametric oscillator
ORE	Optimising resource extraction
PAMAM	Polyamidoamine
PBS	Phosphate-buffered saline
PDF	Powder diffraction file
PDT	Photodynamic therapy
PL	Photoluminescence
PLGA	Lactic-co-glycolic acid
PNIPAm	Poly(N-isopropylacrylamide
PS	Photosensitisers
PTT	Photothermal therapy
PVP	Polyvinylpyrrolidone
PXRD	Powder X-ray diffraction
QD	Polyvinylpyrrolidone
RB	Rose bengal
RE	Rare earth
RNA	Ribonucleic acid
ROS	Reactive oxygen species
RSD	Relative standard deviation
SAED	Selected area electron diffraction
S. aureus	*Staphylococcus aureus*
SCV	Small colony variants
SEM	Scanning electron microscopy
SIM	Structured illumination microscopy
SLN	Solid lipid nanoparticles
SPION	Superparamagnetic iron oxide nanoparticles
SRM	Super-resolution microscopy
STED	Stimulated emission depletion microscopy
TDM	Therapeutic drug monitoring
TEM	Transmission electron microscopy
TGA	Thermal gravimetric analysis

TPP-4CB7	Cucurbit[7]uril-anchored porphyrin assembly
TSB	Tryptic soy broth
UCNP	Lanthanide-doped upconversion nanoparticle
UV	Ultraviolet
VB	Valence band
VLP	Virus-like particles
VRE	Vancomycin-resistant
VRSA	Vancomycin-resistant *Staphylococcus aureus*
WHO	World health organization
XPS	X-ray photoelectron spectroscopy
ZIF-8	Zeolite imidazolate framework 8

Abstract

This thesis examines the need for new antibacterial materials to treat small colony variants (SCVs) of *Staphylococcus (S.) aureus* bacteria and their parental strains. While ZnO-based nanoparticles (NPs) activated by ultraviolet (UV) and short wavelength visible light have been researched for their antibacterial properties, the potential benefits of incorporating UCNPs to allow activation by near-infrared (NIR) light have been overlooked. This study aims to fill this research gap by comprehensively investigating the synthesis and performance of ZnO-coated lanthanide-doped upconversion nanoparticle (UCNP) composites activated by NIR light against *S. aureus* SCVs and parental strains.

Furthermore, this research addresses the limited understanding of the potential risks associated with UV emission from UCNPs used as fluorescent probes in super-resolution microscopy (SRM). Despite extensive research on the usage of UCNPs as fluorescent probes for SRMs, the potential cytotoxic effects of UV emission from UCNPs have not been thoroughly studied. To advance cellular imaging techniques and ensure cellular viability, a comprehensive investigation of UV emission from UCNPs is necessary. This thesis aims to identify and quantify UV emission by UCNPs used in SRM and develop strategies to minimise UV emission and mitigate potential cytotoxic effects.

These two main aims are addressed in three results chapters. The first aim, the focus of chapters 2 and 3, focuses on the synthesis UCNP@ZnO composites that can be activated by NIR light for antimicrobial photodynamic therapy (aPDT) applications against *S. aureus* SCVs and parental strains. Chapter 2 reports the synthesis and performance of these composites, showing these materials to be effective antibacterial therapies against *S. aureus* SCVs, while chapter 3 improves upon the performance of these composites by careful tuning of the UCNP core and provides enhancements to the ZnO shell composition to improve reactive oxygen species generation and add a second mode of action in the form of silver nanoparticles. The second aim of this research is covered in chapter 4, which reports an investigation into the UV emission from UCNPs used as fluorescent probes in SRM. The work posits the need to understand the UV emission properties of these UCNPs as knowledge of these and the potential for cytotoxic effects are crucial for optimizing cellular imaging experiments and ensuring accurate and reliable results. Chapter 4 identifies design features and compositions that can limit UV emission, thereby minimizing the risk of phototoxicity and advancing the field of cellular imaging.

Overall, the findings from this research have the potential to contribute to the development of safer and more effective targeted antibacterial therapies and enhance the understanding of UV emissions in cellular imaging techniques.

Declaration

I certify that this work contains no material which has been accepted for the award of any other degree or diploma in my name, in any university or other tertiary institution and, to the best of my knowledge and belief, contains no material previously published or written by another person, except where due reference has been made in the text. In addition, I certify that no part of this work will, in the future, be used in a submission in my name, for any other degree or diploma in any university or other tertiary institution without the prior approval of the University of Adelaide and where applicable, any partner institution responsible for the joint-award of this degree.

I acknowledge that copyright of published works contained within this thesis resides with the copyright holder(s) of those works.

I also give permission for the digital version of my thesis to be made available on the web, via the University's digital research repository, the Library Search and also through web search engines, unless permission has been granted by the University to restrict access for a period of time.

I acknowledge the support I have received for my research through the provision of an Australian Government Research Training Program Scholarship.

Afshin Karami

September 2023

Acknowledgement

I would like to express my heartfelt gratitude to my supervisors, Dr Stephen Kidd, Prof Christopher Sumby and Associate Prof Jingxiu Bi, for their unwavering support, patience, encouragement, and invaluable knowledge throughout my journey. Their guidance and expertise have been instrumental in shaping the direction of my research and enriching my academic experience.

I am deeply thankful to the staff of Adelaide University, particularly the School of Chemical Engineering and Adelaide Microscopy, for their continuous support and assistance. Their resources, facilities, and expertise have played a crucial role in the successful completion of my research work.

I would like to acknowledge the financial support received from the Australian Government Research Training Program Scholarship and Alice Chu postgraduate scholarship in Chemical Engineering.

I am indebted to my wife, siblings and parents for their unconditional love, encouragement, and understanding throughout this challenging academic journey. Their unwavering support has been a constant source of motivation and inspiration.

Lastly, I would like to express my gratitude to all my friends who have been by my side during my studies. Their friendship, companionship, and shared experiences have brought joy, laughter, and balance to my life, making this academic journey even more memorable.

Without the support and contributions of all these individuals and institutions, the completion of this PhD thesis would not have been possible.

Table of contents

Chapter 1: Introduction and literature review

1.1 A brief overview of nanomedicines

This chapter is divided into three sections that outline the field of nanomedicine. The first section provides a brief overview of nanomedicines and illustrates their diverse applications. As relevant to this thesis, it focuses on their role as therapeutic agents in anticancer and antibacterial treatment applications. A more specific overview of inorganic antibacterial nanomedicines, a subgroup of therapeutic nanomedicines that are a focus of this thesis, as well as their mechanisms of action is provided, emphasizing their importance in the detection and monitoring of disease. In the second section, the design and synthesis of lanthanide-doped upconversion nanoparticles (UCNPs) will be discussed. In this section, the synthetic procedures used to prepare UCNPs will be reviewed. Furthermore, the procedures used to form ZnO-coated UCNP composites will be discussed, providing insight into current synthesis methods. Lastly, the document will address the knowledge gap and present the objectives of this study. The purpose of this section is to identify gaps in the current understanding of nanomedicines, as well as highlight areas that need more research. Moreover, it will outline the specific objectives of the project, and provide a roadmap for the remainder of the thesis.

As nanotechnology develops, it is finding applications in diverse fields, including electronics, the energy sector, cosmetics, agriculture, and medicine.[1-5] In general, nanomedicine is the application of knowledge and techniques from nanoscience to medical biology, disease prevention and treatment.[6] A nanomedicine encompasses any material that is intended for therapeutic or diagnostic purposes with at least one of its dimensions falling within the nanoscale (1-100 nm).[7] Despite this broad definition, nanomedicines are typically nanoparticles (NPs), which can be classified by their composition[8] and include lipid nanoparticles (LNPs), polymer-based nanomedicines, protein-based NPs, drug nanocrystals and inorganic/metallic NPs.[8,9] Several

examples of each of these groups are provided in Table 1. The properties of nanoparticles make them a diverse class of materials both in terms of their structures and physicochemical properties, and they have a wide range of applications.[6] In recent years, NPs have been extensively studied for the treatment of cancer and bacterial infections (as therapeutic agents), and in bioimaging applications (diagnostic and imaging agents).

Table 1. Examples of nanomedicines and diverse applications.

Nanomedicines	**Examples**	**Application**	**Ref.**
Lipid NPs	liposomes: doxorubicin liposome (Doxil) and doxorubicin citrate liposome (Myocet)	drug delivery	10,11
	solid lipid nanoparticles (SLNs): cyclosporine-loaded SLNs		12
	nanostructured lipid carriers (NLCs): coenzyme Q10 (CoQ10)-loaded NLC and idebenone (IDE) loaded NLC		13,14
	lipid-polymer hybrid nanoparticles (LPHNs): paclitaxel encapsulated LPHN and norfloxacin encapsulated LPHN		15
	solid lipid nanocarriers (SLNCs): fenofibrate-loaded SLNC (Lipanthylnano)		16,17
Polymer-based	polymeric NPs and polymer-drug conjugates: microgels (e.g. poly(N-isopropylacrylamide) (PNIPAm)), dendrimers (e.g. polyamidoamine (PAMAM)), nanospheres (e.g. poly(lactic-co-glycolic acid) (PLGA)), and	drug delivery and tissue engineering, gene therapy, medical imaging and diagnostic agent	18-21

Nanomedicines	Examples	Application	Ref.
	nanocapsules (e.g. polymeric lipid hybrid nanocapsules)		
	polymeric drug: glatiramer acetate (Copaxone) and colesevelam hydrochloride (Welchol)	drug	22,23
Protein-based NPs	protein NPs: virus-like particles (VLPs) and albumin-based nanocarriers	drug delivery	24,25
Drug nanocrystals	sirolimus (Rapamune) and aprepitant (Emend)	drug delivery	26,27
Inorganic/metallic NPs	semiconductor polyvinylpyrrolidone (QDs) as a fluorescent label	imaging	28
	iron oxide (Fe_3O_4) NPs in magnetic resonance imaging (MRI)	medical imaging and diagnostic agent	29
	plasmonic NPs: gold (Au) and silver (Ag) NPs	drug, drug delivery, imaging and diagnostic agent	30

1.1.1 Applications of nanomedicines as therapeutic agents

1.1.1.1 Cancer treatment

One of the most important applications of nanomedicines is the treatment of cancer, which is a major public health problem worldwide. According to the World Health Organization,[31] 18.1 million people worldwide suffered from cancer in 2018, and 9.6 million died from it. By 2040, these figures are predicted to nearly double, with the greatest increase occurring in low- and middle-income countries, where more than two-thirds of all cancers will occur. Lung cancer is the most frequently diagnosed type of cancer (11.6%), followed by breast cancer (11.6%) and

colorectal cancer (10.2%). The most common cause of cancer death is lung cancer (18.4% of all cancer deaths), followed by colorectal cancer (9.2%) and stomach cancer (8.2%).[31] Surgery,[32] radiation therapy,[33] chemotherapy,[34] phototherapies (photodynamic therapy (PDT) and photothermal therapy (PTT)),[35] vaccinations,[36] immunotherapy,[37] stem cell transplantation,[38] or combinations of these therapies are the conventional treatment options for cancer.[39] The treatment procedure may involve a combination of techniques in which the primary tumour is typically removed through surgery, often followed by further treatment.[40] While these techniques have achieved success, they are associated with severe side effects as well. The side effects of these treatment options range from mild discomfort to secondary tumour development and severe toxicity to multiple systems, including the immune system.[41] Furthermore, an increasing number of relapses, drug resistance, and metastatic tumours are being reported.[40]

It is difficult to treat the major types of cancer, mainly due to the heterogeneous and idiosyncratic nature of each cancer and the difficulty in targeting therapeutics to cancerous cells without damaging the normal tissues.[42,43] The unique properties of nanomedicines have revolutionised theranostics (the pairing of diagnostic and therapeutic agents that share a specific target in diseased cells or tissues)[44] for cancer because they feature small particle size, high drug loading, and highly active targeting features.[39] The development of anticancer nanomedicines has primarily focused on improving therapeutic activity and selectivity for the above-mentioned cancer treatment methods. Liposomes and micelles were the first generation of NP-based drug-delivery nanomedicines that were approved by the Food and Drug Administration (FDA).[6] A number of cancer treatments use liposome-based encapsulation systems (for example, Myocet, Daunoxome, and Doxil).

1.1.1.2 Antimicrobial agents

Another important application of nanomedicines is to treat bacterial infections, which is also a global major public health problem. Antimicrobial resistance (AMR) may be attributed to several factors,[45] but the emergence and spread of new mechanisms may have been significantly accelerated by the overuse and misuse of antimicrobials.[46] The emergence of AMR results in decreased drug effectiveness and persistent infections, which increases the risk of serious disease and disease transmission.[47] The occurrence of AMR has become an endemic and widespread problem affecting both high-income and low-income countries.[48] *Acinetobacter baumannii*, *Staphylococcus (S.) aureus*, *Klebsiella pneumoniae*, *Streptococcus (P.) pneumoniae*, *Escherichia (E.) coli*, and *Pseudomonas (P.) aeruginosa* represent the six pathogens associated with the majority of deaths worldwide. During 2019, this group of pathogens was responsible for an average of 929,000 deaths, with methicillin-resistant *S. aureus* (MRSA) alone causing more than 100,000 deaths.[49] Among the above AMR pathogens, *S. aureus*, is a particularly important bacteria as it can cause chronic, persistent infections that do not respond well to antibiotic treatment.

1.1.1.3 Persistent *S. aureus* diseases

The *S. aureus* bacterium is a Gram-positive, coagulase-positive bacterium,[50] with a spherical shape, that is non-motile and forms clusters of approximately 1 μm in diameter that are similar to grape clusters.[51] There are 52 species and 28 subspecies of *S. aureus*, and it is estimated that between 20 and 40% of the general population harbour commensal *S. aureus* in the nasal mucosa and on the skin.[50] *S. aureus* was initially identified by Ogston in 1880 and was isolated by Rosenbach soon after.[52] *S. aureus* quickly became identified as one of the most common causes of healthcare-associated infections. Despite the discovery of penicillin and its clinical use only

commencing in the 1940s, resistance to penicillin emerged shortly afterwards (as early as 1952) as a result of the β-lactamase gene *blaZ*. This is a plasmid-encoded penicillinase produced by *S. aureus* that hydrolyzes the β-lactam ring of penicillin, the primary antimicrobial component of penicillin. Around 1960, the first semi-synthetic anti-Staphylococcal penicillin (methicillin) was developed, and within one year, methicillin-resistant *S. aureus* emerged in clinical settings. Evidence suggests that methicillin resistance occurred even before the first anti-Staphylococcal penicillins were clinically used.[53]

The human infections caused by *S. aureus* are generally acute; however, *S. aureus* can cause a wide range of chronic and persistent infections including bacteriemia, osteomyelitis and endocarditis, and it is a significant cause of hospital-associated infections.[54] Staphylococcal infections are primarily fought by neutrophils. Several virulence factors and immune evasion factors are produced by *S. aureus*, hindering the human immune response.[55] *S. aureus* infections are typically treated with antibiotics but, there is a continuing problem with methicillin-resistant *S. aureus* (MRSA) and vancomycin-resistant *S. aureus* (VRSA) preventing effective clinical treatments.[56,57]

Another major aspect of *S. aureus* infections is their ability to establish chronic and persistent infections despite appropriate antibiotic treatment.[58] A genetically identical population of *S. aureus* cells can harbour a sub-population of different cell types as a result of developing alternative lifestyles during their growth.[59] These sub-populations of *S. aureus* have changes in cell biology, providing additional survival strategies in stressful conditions. One example is the switch to a Small Colony Variant (SCV).[60] *S. aureus* SCVs grow very slowly and produce very small, non-pigmented colonies (Figure 1) and lack or exhibit a reduction of β-hemolysis, low coagulase activity, less sensitivity to aminoglycosides, and they often require exogenous hemin,

menadione, thiamine, or CO_2 for their growth.[61-63] In general, SCVs take more than 24 hours to become visible on solid media (typically 48 to 72 hours) due to their slower growth rate compared with metabolically normal *S. aureus* (Figure 1b). As a result, SCVs may be overgrown or missed during the routine processing of clinical specimens.[58] In acute infection by *S. aureus*, multiple antimicrobial agents are effective; however, during chronic infection, when SCVs are dominant in the bacterial population, these agents are ineffective.[60] Additionally, antibiotics such as gentamicin, moxifloxacin, and clindamycin, when used at low concentrations, enhance the formation of SCV in infected cells.[58,60] These SCV cells can therefore avoid clearance by the antibiotic identified as able to be effective against the infecting strain. Furthermore, these cells do not generate the usual immune mediators and can hide from immune responses.

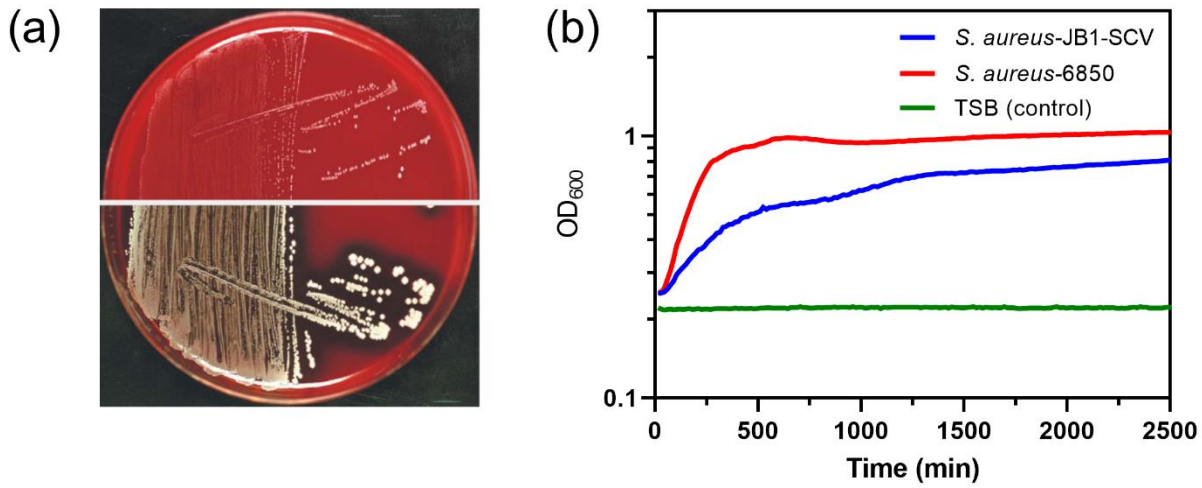

Figure 1. Incubation of *S. aureus* colonies on Columbia blood agar for 48 hours, showing the small colony variant (SCV) on the upper section, and the normal phenotype on the lower section, adopted from von Eiff et al.[62] (a), growth curves for *S. aureus* JB1-SCV and parental 6850 on tryptone soy broth (TSB) (b).

In general, a clear preventative treatment strategy is not available to prevent the formation of SCVs and the resulting chronic infections. Since bacterial persistence mechanisms – such as SCV formation – develop early in the infection period, the most effective strategy is to eliminate

infection as soon as possible, before bacteria adapt to the development of SCVs. This could be accomplished by utilizing antibiotics for MRSA and specifically their SCVs. Fluoroquinolones (a family of broad-spectrum and systemic antibacterial agents) are generally used to treat SCVs.[58] However, as fluoroquinolone resistance is also frequent, vancomycin was the "gold standard" MRSA therapy for many years. Vancomycin has, however, several significant downsides, including the fact that it is not absorbed in the gastrointestinal tract, its side effect profile, and the need to conduct therapeutic drug monitoring (TDM).[64] As a result, a number of nanomedicine strategies have been developed to combat MRSA bacteria, including metal ions (Ag and Au), antibacterial peptides, peptidomimetics, oligonucleotides (RNAi, TFD, CRISPR, Aptamers) and nanoparticles (chitosan and liposomes) for antibiotic delivery. In addition to being cytotoxic to bacteria, NPs can also protect molecular antibiotics from detection and degradation, enhance the efficacy of current antibiotics, and provide a method of delivering agents locally to microorganisms to maximise their local concentrations and bactericidal effect. However, despite the wealth of research studies that have been conducted,[65] and the potential benefits of nanomedicine in treating *S. aureus* SCVs, several limitations have prevented clinical trials and widespread use. Nanomedicines are subject to various limitations, such as the development of antibacterial resistance, toxicity and side effects, and uncertainty in their performance. The development of metal or metal oxide nanoparticles that possess inherent antibacterial properties has made great progress, but their toxicity is a significant drawback. For example, as Ag NPs are not selective for bacterial cells, they may cause local toxicity to normal cells.[66] In the following section, the inorganic antibacterial nanomedicines, and their mechanism of action will be explored.

1.1.2 Inorganic antibacterial agents: materials and mechanisms of action

Inorganic antibacterial nanomedicines can be categorised into two major groups based on the mechanisms underlying their antibacterial effects: endogenous and exogenous antibacterial agents.[67] The primary antibacterial mechanism of action for endogenous inorganic nanomedicine is ion toxicity. The noble metals such as Ag and Au NPs are the most common materials in this category. Fast and effective antibacterial action are the advantages of this strategy, but they do not guarantee safety and their antibacterial action is uncontrolled. Alternatively, exogenous inorganic nanomedicines possess antibacterial properties due to the release of reactive oxygen species (ROS) or the generation of heat as a result of light activation. Metal oxides such as titanium dioxide (TiO_2) and zinc oxide (ZnO) and more recently semiconductor-coated UCNPs are examples of these materials. Besides light, other external stimuli (e.g. electricity, magnetism, microwave, and ultrasound) have also been reported to stimulate materials, among which light-responsive materials have long been a subject of considerable research.[67-70]

The effectiveness of Ag NPs has been demonstrated against a wide range of both Gram-positive (e.g. *S. aureus*, *S. pneumoniae*) and Gram-negative (e.g. *E. coli*, *P. aeruginosa*) bacteria, making them a promising alternative to conventional antibacterials.[71,72] Nanotechnology has enabled the synthesis of Ag NPs, which have remarkable antibacterial properties due to their large surface area-to-volume ratio compared to larger particles and bulk metals.[73] Several reports demonstrate the effectiveness of Ag NPs against bacterial cells in slow-growing or resting states (e.g. SCVs).[74] The antibacterial action is attributed to both Ag NPs and Ag ions (Ag^+) formed during their dissolution.[73,75,76] Although extensive studies have been conducted on both Ag^+ ions and Ag NPs, the exact antibacterial mechanism of action is still debated.[77] It has been shown that both Ag NPs and Ag^+ ions are capable of interacting with multiple components of bacteria. As a result of these

interactions, they may interfere with bacterial metabolism and harm outer cellular functioning.[78,79] Generally, Ag NPs possess antibacterial properties due to the destruction of cell walls, destabilisation of structural proteins, inactivation of membrane proteins, inactivation of enzymes, inhibition of the electron transport chain (ETC), damage to nucleic acids, and oxidative stress induced by the generation of ROS.[80]

Currently, experimental studies are combining the use of Ag NPs with certain molecular antibiotics as antibacterial agents.[81,82] There is, however, a limitation to this synergistic effect as not all molecular antibiotics combined with Ag NPs display a beneficial effect.[83] Ag NPs combined with well-known antibiotics such as enoxacin, kanamycin, neomycin, and tetracycline inhibited the growth of multiple drug-resistant *Salmonella* Typhimurium, whereas ampicillin and penicillin did not have a similar effect.[82] As an example of the beneficial activity of combined antibiotics, it was observed that tetracycline may enhance the binding of Ag NPs to the bacterial cell surface. Combined with streptomycin, vancomycin, tetracycline, amoxicillin, gentamicin, erythromycin, and ciprofloxacin, Ag NPs have also been shown to have a synergistic effect against *S. aureus* and *E. coli*,[84] while Ag NPs in combination with ampicillin, chloramphenicol, and kanamycin have also been demonstrated to be effective against *Enterococcus (E.) faecium*, *S. aureus*, *Streptococcus mutans*, and *E. coli*.[81,85]

As noted, antimicrobials face the challenge of decreased efficacy over time due to the development of resistance. Contrary to conventional antibacterials, the study of Ag NP resistance in bacteria and the mechanisms by which it occurs has been limited and has not led to any conclusive results.[86] Despite the existence of well-established resistance to Ag^+ ions, the evolution of Ag NP resistance in bacteria has only recently been recognised.[87-89] It has been shown that Gram-positive bacteria are more resistant to Ag NP treatment due to their comparatively thicker cell walls and higher

levels of peptidoglycan than Gram-negative bacteria.[90] While Ag NPs may have significant potential for nanomedicine, their primary drawback is that they release silver ions uncontrollably causing cytotoxicity.[91-93] Since the therapeutic window concentration range (determined by the difference between therapeutic and toxic concentrations) for Ag NPs is very narrow, Ag NPs are severely limited in their application as antimicrobials.[94]

Although Au NPs are less commonly studied than Ag NPs, they also possess antibacterial properties. The antibacterial activity of Au NPs appears to be dependent on surface functionalisation, which may add to their complexity.[95] Gold atoms exhibit a low level of reactivity, particularly concerning oxidation by dissolved oxygen. As a result, fewer free Au^{+} ions are released from Au NPs, and fewer ROS are generated. As a consequence, ROS generation and ion release are thought to contribute much less to the antibacterial activity of Au NPs compared to Ag NPs, while direct interaction with the cell envelope, and binding to the intracellular components of the bacteria are the key mechanisms.[77] A special feature of Au NPs is their localised surface plasmon resonance (LSPR), which is useful in many nanotechnological applications. LSPR occurs as the electrons on the surface of noble metal nanoparticles interact with electromagnetic radiation, producing LSPR.[96] As a result, metal nanoparticles exhibit strong extinction and scattering spectra, which are very useful in a variety of applications.

There are two main approaches to increasing the antibacterial activity of Au NPs that employ light activation: antibacterial photothermal therapy (aPTT) and antibacterial photodynamic therapy (aPDT).[97] It has been demonstrated that vancomycin-immobilized Au NPs (Au@Van NPs) have antibacterial and photothermal properties against vancomycin-resistant *E. faecalis* (VRE1 and VRE4). After 5 minutes of irradiation with an 808 nm near-infrared (NIR) laser, the sample solution temperature increased by approximately 15 °C. For VRE growth inhibition, the amount

of vancomycin required on the vancomycin-coated Au NPs combined with NIR irradiation is approximately 16-fold less than the amount required when the same cells were treated with free vancomycin.[98] However, despite these positive results, there are several limitations and challenges associated with the use of Au NPs as antibacterial nanomedicines. In comparison to other antibacterial agents, Au NPs have limited antibacterial activity. Additionally, Au NPs may not be toxic at low doses; however, higher doses have been reported to disrupt the functioning of all tested organs, including the brain, liver, spleen, kidney, heart and lung in animal experiments. Furthermore, long-term effects on human health are not fully understood.[30,97,99-101]

Exogenous antibacterial inorganic nanomedicines activated by light can also be used for aPDT. In aPDT, nontoxic photosensitizing NPs absorb light at a specific wavelength and produce ROS molecules that provide antibacterial action. There are two ways in which aPDT produces ROS. Type I reactions produce hydroxyl radicals ($HO^{\bullet}$), superoxide anion ($O_2^{\bullet-}$), and hydrogen peroxide (H_2O_2) from the direct reaction between the activated photosensitiser and the cell membrane. Type II reactions involve the activated photosensitiser transferring energy to molecular oxygen to produce excited singlet oxygen ($^1O_2$). Even though both reactions occur simultaneously, the Type II pathway is generally more dominant for antibacterial activity because excited singlet oxygen causes the majority of cellular damage due to its high quantum yields.[102] There have been several recent studies that demonstrate the antibacterial properties of semiconductor TiO_2 NPs.[103,104] With a band gap of 3.2 eV, TiO_2 NPs can generate electron-hole (e^-/H^+) pairs with high energy when exposed to UV light with a wavelength of 385 nm or lower.[105,106] The irradiation of UV light results in the production of ROS with high oxidative potential when oxygen is present.[107] This can result in the alteration of cellular DNA synthesis processes, damage to DNA and proteins, and inactivation of metabolic enzymes caused by ROS.[105,107,108] TiO_2 NPs may also cause cell death

through attachment to the microbial cell wall and subsequent internalisation, thus damaging the integrity of the membrane. Furthermore, TiO_2 NP accumulation causes the development of "pits" on the surface and the accumulation of free radicals. It has been reported that TiO_2 NPs have antibacterial properties against a range of bacteria including *E. coli* and *S. aureus*.[99,109,110]

Another example of a material used for aPDT is ZnO NPs. ZnO NPs are compatible with human cells, and their properties make them useful for a wide range of biomedical applications, including tissue engineering, drug delivery systems, and bioimaging. Furthermore, ZnO NPs have also been demonstrated to possess antibacterial properties due to their large surface area, reduced volume, high surface reactivity, and ability to produce ROS when exposed to UV radiation.[99,110-112] The antibacterial mechanisms of ZnO materials have been reported previously, but are still under debate.[113] Among its antibacterial mechanisms that have been suggested are the release of Zn^{2+} metal ions from ZnO NPs, the production of ROS produced by photo-induced reactions and the direct interaction between ZnO NPs and the bacteria. As a result of the release of Zn^{2+} ions, they could interact with the membrane of the bacterial cell, enter the cell, and form chemical bonds with the sulfhydryl, amino, and hydroxyl functional groups of the bacteria in order to disrupt the metabolism of the cell.[114] However, the antibacterial activity of ZnO NPs in dark (non-illuminated) conditions against both *E. coli* and *S. aureus* has been found to be a minor component of their mode of action in previous research,[91] suggesting that Zn^{2+} ions and mechanical damage to bacterial cells may have had limited contributions to the death of bacteria. Other studies have also demonstrated similar results regarding the role played by Zn^{2+} ions in ZnO NPs antibacterial activity.[115] As with TiO_2 NPs, photo-induced ROS generation is considered to be the main mechanism of action of ZnO NPs in antibacterial applications.

One of the main drawbacks of both TiO_2 and ZnO NPs is their wide band gap that can only be activated by UV light, with the usage of UV in biological systems being constrained due to the potential for irradiation-induced cellular damage. As a result of this drawback, several metals, and non-metals have been incorporated into ZnO NPs to extend their photo-response into the visible spectrum.[116,117] Despite these efforts to narrow the band gap for TiO_2 and ZnO NPs, they must still be activated by visible light, which does not penetrate the tissues well. Consequently, the development of advanced NP composites based on ZnO or TiO_2 NPs with light activation in the longer wavelength near-infrared (NIR) region, which has limited absorption by biological tissues, is highly desirable.

A potential alternative to semiconductor NPs could be core-shell NPs composed of upconverting nanoparticles (UCNPs), such as $NaYF_4$:Yb/Tm, as the core and a ZnO semiconductor in the shell.[118] To induce cell death, 980 nm NIR light can be used to activate the core UCNP to produce UV emission, which in turn is then absorbed by the ZnO shell, resulting in cytotoxic ROS that induce cell death. In contrast to commonly used photosensitisers, core/shell UCNP@ZnO NP composites may have several advantages. The main advantage of these composites is the ability to be activated by NIR light and biocompatibility. The NIR light that excites the UCNP core is within the optical window (700-1100 nm) of biological systems, which means that it is generally safe since biological tissue exhibits relatively low attenuation at these wavelengths.[119] A further advantage of NIR light is its ability to penetrate deeper into biological tissues.[120] Finally, the ZnO shell also has attracted attention for biological applications due to its abundance and biocompatibility (non-toxicity), and acceptance as a generally recognised as safe (GRAS) substance by the FDA.[121] This approach is the focus of two chapters in this thesis, focussing specifically on "Facile multistep synthesis of ZnO-coated β-$NaYF_4$:Yb/Tm upconversion

nanoparticles as an antimicrobial photodynamic therapy for persistent *Staphylococcus aureus* small colony variants" (Chapter 2) and "Reactive oxygen species (ROS) and ROS-stimulated Ag release by UCNP@ZnO:Co/Ag composites for antibacterial photodynamic therapy" (Chapter 3).

1.1.3 Applications of nanomedicines as diagnostic and imaging agents

In addition to being used for the treatment of diseases such as cancer and bacterial infections, nanomedicine can also assist in the differentiation of normal cells from diseased cells or detect pathogens themselves. Medical diagnosis has been improved due to the development of nanomaterials in the form of sensors or imaging agents that are sensitive, and highly specific.[122-129] Biosensors are chemical sensors that contain a biological recognition element that recognises analytes and a transducer that transmits the signals.[130,131] It is possible to generate optical, electrochemical, thermal, or piezoelectric signals based on different biological interactions, for example, antigen-antibody or antigen-aptamer interactions, which can be used to detect diseases caused by bacteria or viruses.[130] As noted previously, NPs possess high surface area per unit volume, high electrical conductivity, colourimetric properties, and high mechanical strength, all of which make them suitable for conjugation with antibodies and aptamers in biosensor applications.[122,132-139]

Anatomical and functional imaging with nanomaterials is also a key focus in nanomedicine. Bioimaging techniques are crucial for detecting and locating cancerous tumours, characterising them, monitoring the treatment, and detecting cancer recurrence.[140] The use of nanomaterials as contrast agents can help visualise structures inside the human body and to enable clinicians to differentiate healthy from diseased tissues. A variety of imaging configurations are available, including computed tomography (CT),[141-146] magnetic resonance imaging (MRI),[147,148] photoacoustic imaging,[149] and fluorescence imaging.[150,151] In all these techniques, NPs serve as

contrast agents and can be engineered to localise in specific tissues and produce high contrast.[9] The examples of nanomedicines as diagnostic and imaging agents are presented in Table 2.

Table 2. Examples of nanomedicines used as diagnostic and imaging agents.

Nanomedicines as diagnostic and imaging agents		**Examples of NPs**	**Ref.**
Biosensors		Au NPs and their derivatives	132,152,153
		Ag NPs and their derivatives	124,126,136,154
Diagnostic and imaging agents	computed tomography (CT)	Au coated with folic acid and silica,	143-145,155
		lanthanide-doped upconversion nanoparticles (UCNPs) based on NaGdF4 NPs	146
	magnetic resonance imaging (MRI)	paramagnetic agents (e.g. gadolinium-based agents)	156,157
		superparamagnetic agents (e.g., iron oxide-based agents such as SPIONs)	158,159
		$NaGdF_4$:Yb:Er-Ag nanowire hybrid nanocomposites	160
		Gd_2O_3:SiO_2@Au NPs	161
		carbonized paramagnetic complexes of manganese (II) (Mn@CCs)	162
	photoacoustic imaging	Au-based NPs, UCNPs, gallium@rGO and Fe@γ-Fe_2O_3@H-TiO_2	163-166
	fluorescence imaging	SiO_2-based NPs, F- and Cl-doped carbon quantum dots (confocal microscopy), $NaYF_4$:Yb/Tm UCNPs (SRMs)	167-169

In recent years, optical microscopy, which can examine morphological details as well as physiological details in real-time with high sensitivity, has become a crucial part of diagnosing diseases.[170] Optical imaging technology has developed significantly in both preclinical and clinical translational research. Optical imaging, especially fluorescence imaging, has become increasingly popular in the study of tissues and has potential applications intraoperatively.[151] Imaging techniques based on fluorescence involve the excitation of fluorescent probes (fluorophores) by light at a specific wavelength, followed by the visualization of their emission by using an appropriate detector, such as optical microscopy. Depending on the application, fluorescence imaging can be divided into two categories: in vivo and in vitro imaging. While there is an overlap between in vivo and in vitro fluorescence imaging techniques,[171] confocal microscopy and super-resolution microscopy (SRM) are the most widely used techniques for in vitro imaging. One of the major disadvantages of fluorescence microscopy for imaging is the limitation to a spatial resolution of 200 nm, which is due to the light diffraction limit rationalised by Abbe's rule.[172] With the development of SRM techniques, the resolution limitations of fluorescence microscopy have been overcome.[173]

Fluorescent probes are crucial components of SRM since they can identify target molecules and structures with high precision by labelling and thereby revealing insights into cellular structure and activity.[174] Fluorescent probes are being developed and evaluated continuously for SRM, including fluorescent dyes, fluorescent proteins, quantum dots (QDs), and UCNPs.[151,171,174-179] It is critical that a fluorescent probe exhibits adequate brightness, excellent photostability, and superior biocompatibility.[180] Recent developments in UCNPs have established them as novel fluorescent probes for SRM techniques.[175] UCNPs have unique optical properties compared to organic fluorophores or QDs. Among the advantages of UCNP probes are sharp and controllable

light emission, tunable and long lifetime, low background autofluorescence, and limited photobleaching.[119,173] UCNPs have been tested in a wide variety of SRM techniques, including ion beam excitation, stimulated emission depletion microscopy (STED), fluorescence emission difference microscopy (FED), and structured illumination microscopy (SIM).[175] It was successfully shown in 2017 that $NaYF_4$:Yb/Tm UCNPs can be used as a fluorescent probe for STED microscopy.[169,181] As another example, it has been reported that $NaYF_4$:Nd/Yb/Er@$NaYF_4$:Nd UCNP can be used as a fluorescent probe in FED.[182] However, there are a number of disadvantages to using UCNPs as fluorescent probes in SRMs, including their poor water solubility, low fluorescent quantum yields, and the difficulty of tuning the luminescence, in comparison with organic dyes and QDs. Furthermore, high excitation powers should be avoided in the wavelength range relevant for UCNPs, since sample heating is an issue.[170,175]

Ongoing research efforts in this field are focused on developing brighter emissions in UCNPs for use as fluorescent probes in SRMs. Despite this, there are concerns regarding the emergence of UV emission for cellular photodamage from UCNP probes in SRMs. Thesis Chapter 4 reports an investigation of commonly reported UCNPs and their potential for UV emission as a tradeoff against the visible emissions targeted for SRM applications.

1.2 Design and synthesis of UCNP materials and their composites

The purpose of this section is to provide an overview of the design and the synthetic methods used to form UCNPs and their ZnO-coated composites. UCNPs consist of an inorganic host matrix and lanthanide ions distributed uniformly within a host matrix that insulates the ions from one another.[183] The ion emitting the radiation is referred to as an activator, whereas the energy donor is referred to as a sensitiser. The ideal host matrix should possess the following characteristics: a

high tolerance for luminescent centres, low phonon energy that minimises deleterious nonradiative relaxations, high transparency so that NIR photons may migrate freely throughout the lattice, and excellent chemical and thermal stability for preserving crystal structure.[183] The lanthanoid elements comprise fifteen elements from lanthanum (La) to lutetium (Lu), which share similar ground-state electronic properties (Figure 2). The fifteen lanthanides together with scandium and yttrium are called rare earth (RE) elements. Upconversion luminescence in these materials is typically induced by electronic transitions between 4f orbitals with associated wave functions within a single lanthanide.[184] A weak shielding of the 4f electrons occurs as a result of $5s^2$ and $5p^6$ orbitals lying outside the 4f orbitals, resulting in sharp and narrow emissions from the 4f to 4f transition.[183,185]

H																	He
Li	Be											B	C	N	O	F	Ne
Na	Mg											Al	Si	P	S	Cl	Ar
K	Ca	Sc	Ti	V	Cr	Mn	Fe	Co	Ni	Cu	Zn	Ga	Ge	As	Se	Br	Kr
Rb	Sr	Y	Zr	Nb	Mo	Tc	ru	Rh	Pd	Ag	Cd	In	Sn	Sb	Te	I	Xe
Cs	Ba	*	Hf	Ta	W	Re	Os	Ir	Pt	Au	Hg	Tl	Pb	Bi	Po	At	Rn
Fr	Ra	**	Rf	Db	Sg	Bh	Hs	Mt	Ds	Rg	Cn	Nh	Fl	Mc	Lv	Ts	Og

*	La	Ce	Pr	Nd	Pm	Sm	Eu	Gd	Tb	Dy	Ho	Er	Tm	Yb	Lu
**	Ac	Th	Pa	U	Np	Pu	Am	Cm	Bk	Cf	Es	Fm	Md	No	Lr

* Lanthanoides ** Actinoides

Figure 2. Periodic table of elements. The lanthanoid elements are highlighted with a red dashed line.

Efficient upconversion occurs only with carefully selected host and activator-sensitiser combinations. The hexagonal β-$NaYF_4$ crystal is one of the most efficient host matrixes for UCNPs.[186] Other host matrixes such as hexagonal β-$NaYbF_4$ and β-$NaGdF_4$ are also important host UCNP crystals for biological applications. UCNPs are optically tuned by manipulating the dopant concentration and changing the lanthanide dopant.[183,187] In general, Er^{3+}, Tm^{3+}, and Ho^{3+} are the most commonly used lanthanide activators. UCNPs utilizing Er^{3+} and Tm^{3+} as activators

are among the most efficient UCNPs due to their relatively large energy gaps and low probability of non-radiative transitions between excited state energy levels.[188] Using a sensitiser with a sufficient absorption cross-section in the NIR region can also greatly enhance the efficiency of upconversion luminescence. Co-doping a host with a sensitiser allows for efficient energy transfer upconversion (ETU) between the sensitiser and the activator. Several sensitisers can be used for Er^{3+} and Tm^{3+}, but the most widely used is Yb^{3+}.[183]

In general, good quality UCNPs with small, uniform and highly crystalline structures are synthesised by the thermolysis method because it allows precise control of composition, phase, and size for core-only and core/shell UCNP structures.[184] First used by Yan et al.[189] for the synthesis of LaF_3, the thermolysis method is now standard for the synthesis of UCNPs. Although thermolysis produces high-quality crystals with a narrow size distribution, it is not without its limitations. A few examples of the issues of the thermolysis approach are requiring high temperatures of approximately 300 °C or greater for synthesis, being difficult and laborious to use, and giving crystal defects arising from fast nucleation or growth that may result in lower upconversion quantum yields.[190,191] The thermolysis synthesis method uses lanthanide salts as precursors, which decompose at elevated temperatures in a high boiling point organic solvent with the assistance of surfactants. Salts of chloride or trifluoroacetate are the most common sources. The thermolysis method utilises the non-coordinating 1-octadecene (ODE) as a solvent with a boiling point of 320 °C, along with oleic acid (OA) as both a solvent and surfactant. As a surfactant, OA stabilises metallic elements (preventing their aggregation) and regulates the growth and shape of nanoparticles.[192] Alternatively, UCNPs are also synthesised using solvo(hydro)thermal synthesis methods.[193,194] During the solvothermal process, the precursors are dissolved in ethylene glycol and then transferred to a Teflon-lined stainless steel autoclave where they are heated at

200 °C for approximately 12 hours. Following centrifugation, a series of washing steps are performed in order to collect the product. The hydrothermal synthesis method is similar, except that water serves as the solvent.[195] Despite solvo(hydro)thermal synthesis capabilities, UCNPs are more commonly synthesised by thermolysis, which provides uniform, high-quality NP crystals.[184,190,191,196]

Hexagonal β-$NaREF_4$ UCNPs (RE = rare earth; for example hexagonal β-$NaYF_4$ and β-$NaYbF_4$) are generally regarded to have higher upconversion efficiency than their cubic counterparts, with this attributable to features of their crystal structures.[183,197,198] In both of these host crystal UCNPs, emission from the cubic phase is extremely weak, as a result of several structural differences. In particular, the hexagonal β-$NaYF_4$ crystal structure has two types of low-symmetry lanthanide sites where distorted electron clouds are strongly coupled to the lattice. In comparison, the cubic phase is characterised by random substitutions between Na^+ and lanthanide cations in the lattice, which complicates their bonding. This results in more non-harmonic phonon modes providing detrimental energy loss channels, in comparison with the highly ordered cation distribution in the hexagonal lattice.[199] Additionally, there is a smaller distance between adjacent lanthanide ions in the hexagonal structure, 3.548 Å compared to 3.868 Å in the cubic phase.[197] For these reasons, the upconversion efficiency of cubic lanthanide-doped $NaYF_4$ materials is typically much lower than that of the hexagonal $NaYF_4$ phase.[199] The cubic phase is usually formed at the beginning of the synthesis process, and then the cubic UCNP phase is converted into the hexagonal phase.[200]

The photoluminescence efficiency of UCNPs has been enhanced by a variety of strategies, including size or phase control, incorporation of impurities, modification of the host matrix, core/shell structures and increasing activator concentrations.[185,190,196,201,202] The primary strategy to enhance the UV emission from the UCNPs is the manipulation of the sensitiser and activator

concentration within the host matrix. The use of NaYb(99%)F_4:Tm(1%) UCNP compositions has been shown to produce intense emissions in the UV region compared with the commonly used $NaYF_4$:Yb(18%)/Tm(1%) composition.[200] The high sensitiser (Yb^{3+}) to activator (Tm^{3+}) ion ratio leads to saturation of the Tm energy levels resulting in much higher UV emission than a non-saturated system. However, surface quenching, which is detrimental to the emission intensity from UCNPs, is more pronounced in highly Yb^{3+} doped materials like NaYb(99%)F_4:Tm(1%) UCNPs. Surface quenching involves energy migration from lanthanide ions in the centre of the nanocrystal to those on the surface and relaxation non-radiatively leading to a decrease in the luminescence intensity. To reduce the quenching effects, an inert UCNP shell can be coated on an active UCNP core. The inert UCNP shell crystal is typically synthesised using the same composition of the core but without the active lanthanide dopants. This is an important factor allowing the synthesis of a homogenous and uniform shell. For example, for $NaYF_4$:Yb/Tm and $NaYbF_4$:Tm UCNPs, an inert $NaYF_4$ shell would be a suitable structure. An additional advantage of core-shell structural engineering is the possibility of incorporating organic dyes into energy transfer pathways for more flexible optical tuning.[202] It is worth noting that, the inert shell does not contribute to generating a new emission peak and also the majority of core/shell UCNPs have been reported to enhance the emissions in the visible rather than UV range. The next section will provide an overview of the current methods of synthesising ZnO-coated UCNPs.

Despite the comprehensive development of the UCNP core/shell materials, a reproducible synthesis protocol for the UCNP core/ZnO shell with a uniform ZnO shell and precisely controlled thickness remains to be developed. The epitaxial growth in heterostructure NPs creates a homogenous interface between the core and the outer shell, resulting in a high degree of atomic order at the interface, which provides an ideal channel for efficient energy transfer between the

core and outer shell (e.g. energy transfer from core UCNP to ZnO shell). As a result, epitaxial core-shell NPs often exhibit improved photocatalytic activity compared to non-epitaxial NPs.[203,204] The oleate ligands on the surface of the UCNPs render them hydrophobic (and able to be dispersed in nonpolar solvents), while ZnO shell formation typically preferences NPs with hydrophilic surfaces.[205-207] Removing the oleate ligand by washing it with acids like hydrochloric acid (HCl) or exchanging it with other ligands such as polyvinylpyrrolidone (PVP) to make the hydrophobic UCNPs more hydrophilic have been reported as effective strategies.[208,209] A simple method of removing the oleate ligands in UCNP samples that are sensitive to stronger acids has also been reported using formic acid as a stripping agent.[210] However, this is not the only difficulty in coating uniform ZnO NPs onto the surface of UCNPs. It is generally accepted that in a core/shell nanoparticle structure, the host and shell materials should have a low lattice mismatch in order to form a homogeneous interface between them, which results in epitaxial growth. However, the synthesis of homogenous epitaxial ZnO-coated UCNPs (UCNPs@ZnO) is a challenging task due to significant lattice mismatching between the UCNP core and ZnO shell. The application of an inert thin SiO_2 shell between UCNP and ZnO shell appears to be a viable method of not only facilitating the deposition of a ZnO shell but also preventing surface quenching on the UCNP core. The following section summarises the synthesis methods that have been reported in the literature for the synthesis of core/shell ZnO-coated UCNPs.

ZnO-coated $NaYF_4$:Yb/Tm UCNPs have been synthesised from existing UCNPs without modification of the surface chemistry, e.g. the removal of the oleate ligand.[118] This method used zinc acetate ($Zn(acac)_2$), oleic acid (OA) and oleylamine as surfactants and a relatively high temperature of 220 °C in the synthesis. The study claimed the formation of continuous ZnO shells on UCNP based on the high-resolution transmission electron microscopy (TEM) and elemental

mapping of scanning electron microscopy (SEM) images. An alternative study used a similar protocol with some variations to coat ZnO onto β-$NaYF_4$:Yb/Tm at the slightly higher temperature of 250 °C; however, the ZnO shell was not uniformly coated around the UCNP core.[211]

Another study formed a zeolitic imidazolate framework 8 (ZIF-8) coating on the UCNPs, which was then converted into ZnO.[212] In this case, HCl was used to remove the oleate ligand from the surface of the UCNP and the UCNPs were coated with PVP to increase their hydrophilicity. This allowed ZIF-8 coated UCNPs to be formed followed by the calcination at 400 °C to give ZnO-coated $NaYF_4$:Yb/Tm UCNPs. A potential advantage of this method is the ability to incorporate other elements into the ZIF-8 shell to modify the final ZnO shell (e.g. doping ZnO with impurities). However, this method also fails to produce a uniform ZnO shell around the UCNP core. Additionally, ZnO-coated UCNPs have been prepared using a chemically inert SiO_2 layer between the UCNP core and ZnO shell. Microemulsions were used to coat UCNP with SiO_2, and then ZnO shells were deposited on top of the SiO_2.[206] Then PVP was coated on the surface of the sample before coating the ZnO. This method has presented a continuous ZnO shell around the UCNP@SiO_2 which is considered desirable.

1.3 Thesis knowledge gap and objectives

For targeted antibacterial therapies against MRSA, ZnO-coated UCNP composites which can be activated by NIR light represent a promising approach. However, the current literature lacks comprehensive studies focused on the development of these composites, particularly materials with enhanced antibacterial efficacy against methicillin-resistant *S. aureus* SCVs and their parental strains. There has been a significant amount of research into ZnO-based NPs activated by UV and near visible light and their antibacterial properties, without considering the potential benefits of incorporating UCNPs to allow activation by NIR light, which can result in deeper tissue

penetration as well as less photodamage than UV and/or near visible light irradiation. Additionally, the synthesis of ZnO-coated UCNPs has not been widely studied and preliminary results indicated these methods have limitations or issues with reproducibility. This study aims to address this research gap in understanding the synthesis and performance of ZnO-coated UCNP composites activated by NIR light against *S. aureus* SCVs and their parental strains.

Additionally, UV emissions from UCNPs used as fluorescent probes in SRM may cause cellular damage during these imaging experiments that may complicate or interfere with the results. In particular, there is limited knowledge about the potential risks associated with UV emissions from UCNPs, despite their popularity as versatile fluorescent probes for SRM imaging. Research on UCNPs has primarily focused on their visible fluorescence properties and imaging capabilities, neglecting their UV emission and potential cytotoxic effects. As it is essential to maintain cellular viability and minimise phototoxicity in certain SRM studies, an extensive investigation of the UV emissions from UCNPs is necessary. In order to advance the field of cellular imaging, this study aims to identify and understand the UV emission by UCNPs being used as fluorescent probes in SRM, as well as develop strategies to minimise UV emission and thereby mitigate potential cytotoxic effects.

This research work had two aims. First, it aimed to synthesise UCNPs@ZnO composites that will be activated by NIR light for aPDT applications against methicillin-resistant *S. aureus* SCVs and the parental strains. The second aim of this overall study was to investigate the UV emissions from UCNPs when used as fluorescent probes within SRM and to understand the design features and compositions that could be used to limit UV emission. In order to achieve the research aims, the following research objectives were determined.

1. Synthesise UCNP@ZnO materials activated by NIR light for aPDT application against methicillin-resistant *S. aureus* and their SCVs.
    a. synthesise UCNP@ZnO materials.
    b. enhance the antibacterial activity of the UCNP@ZnO composite by:
        i. improving the efficiency of UV generation by the UCNP core and
        ii. improving the absorption and photocatalytic efficiency of the ZnO shell.
2. Examine UV emissions from UCNPs when used under SRM conditions.
    a. synthesise UCNPs commonly used as fluorescent probes in SRM.
    b. investigate the UV emission from as-synthesised UCNPs.
    c. analyse the emission results and determine the potential for cell damage from UV emissions by UCNPs.

To address the first aim of this research, a reproducible synthesis of ZnO-coated UCNP materials was developed using a step-by-step approach. Several synthesis techniques were adopted and modified, including the surface modification of the UCNP cores and the intermediacy of the metal-organic framework (MOF, ZIF-8) templating approach to synthesise UCNP@ZnO. The synthetic parameters for ZIF-8 formation were evaluated to determine the optimal conditions for forming ZIF-8 around the UCNPs, and further the best conditions to convert the ZIF-8 into the ZnO NP shell without converting the UCNPs into the less desirable cubic phase. The as-synthesised UCNP@ZnO materials were tested against *S. aureus* WCH-SK2-SCV and parental *S. aureus* WCH-SK2 strains. LEDs with a wavelength of 980 nm were used as the source of NIR light to activate the materials (since the required NIR laser setup was under construction during the first stage of the project). LEDs are also more portable and safer sources of light, and they can activate

a larger area. The results of this work are presented in Chapter 2 and published as a research paper in the peer-reviewed journal *ACS Applied Bio Materials*.

Based on the outcomes of this work, the ZnO-coated UCNP composite was optimised to enhance its antibacterial activity. Both the UCNP core and the ZnO shell were evaluated independently using different strategies to enhance the overall photocatalytic activity. To enhance UV light generation from the UCNP core for activation of the ZnO shell, UCNPs of various compositions were examined. Additionally, the ZnO shell was formed with different dopants to determine whether it would be more capable of utilizing near-visible light and UV emitted from the UCNP core. The combination of an improved UCNP core with an optimised ZnO shell resulted in materials with better antibacterial activity. The antibacterial activity of the improved UCNP@ZnO composites was evaluated using a continuous wave (CW) NIR laser against antibacterial-resistant *S. aureus* JB1-SCV and the parental *S. aureus* 6850. Additionally, different protocols were used to examine the antibacterial mechanism of action for the as-synthesised compound. This work is currently being prepared for publication and is presented in Chapter 3.

The second objective of this PhD project was to investigate the potential UV emissions from UCNPs when used as fluorescent probes in SRMs. A total of eight UCNPs based on $NaYF_4$:Yb/Tm, $NaYbF_4$:Tm, and $NaYbF_4$:Tm/Gd structures were synthesised, characterised, and assessed for their UV emissions. A UV-sensitive detector system was used to detect the presence and extent of UV emissions from these UCNPs under continuous and pulsed excitation regimes. The potentially negative impact of high-energy UV emissions on the surrounding biological sample was discussed. A key rationale for this research was to shed light upon the importance of accurate measurement of UV emission characteristics of UCNPs, in addition to the targeted visible emission measurements, when developing UCNPs as fluorescent probes for SRM applications.

The findings concerning UV emission from UCNPs were published in the journal *ACS Applied Nano Materials* and are presented in Chapter 4.

In the course of this PhD project, an additional research paper was published as collaborative work that is presented in the appendices section. This paper leveraged the synthetic methodologies and understanding of UCNP materials that was garnered in this research, and thus, while not central to the aims of the overall work, provides a useful contribution to the area and supporting knowledge for the thesis. This research paper has been referenced in another thesis with the title of "A Dual Tuneable-Laser Excitation System for the Discovery of Naturally Occurring Fluorescence Signals".

1.4 Thesis outline

Chapter title	Chapter	Type
Introduction and project overview	1	literature review/research output
Facile multistep synthesis of ZnO-coated β-$NaYF_4$:Yb/Tm upconversion nanoparticles as an antimicrobial photodynamic therapy for persistent *Staphylococcus aureus* small colony variants	2	research output (published)
Reactive oxygen species (ROS) and ROS-stimulated Ag release by UCNP@ZnO:Co/Ag composites for antibacterial photodynamic therapy	3	research output (to be submitted to a peer-reviewed journal)
UV emission from lanthanide-doped upconversion nanoparticles in super-resolution microscopy: potential for cellular damage	4	research output (published)
Conclusion and outlook	5	conclusion

1.5 References

(1) Ramos, A. P.; Cruz, M. A. E.; Tovani, C. B.; Ciancaglini, P. Biomedical applications of nanotechnology. *Biophys. Rev.* **2017**, *9* (2), 79-89. DOI: 10.1007/s12551-016-0246-2.

(2) Hussein, A. K. Applications of nanotechnology in renewable energies—A comprehensive overview and understanding. *Renewable and Sustainable Energy Reviews* **2015**, *42*, 460-476.

(3) Peng, B.; Tang, J.; Luo, J.; Wang, P.; Ding, B.; Tam, K. C. Applications of nanotechnology in oil and gas industry: Progress and perspective. *The Canadian Journal of Chemical Engineering* **2018**, *96* (1), 91-100. DOI: 10.1002/cjce.23042.

(4) Mauter, M. S.; Zucker, I.; Perreault, F.; Werber, J. R.; Kim, J.-H.; Elimelech, M. The role of nanotechnology in tackling global water challenges. *Nature Sustainability* **2018**, *1* (4), 166-175. DOI: 10.1038/s41893-018-0046-8.

(5) Lee, S.; Sasaki, D.; Kim, D.; Mori, M.; et al. Ultrasoft electronics to monitor dynamically pulsing cardiomyocytes. *Nature Nanotechnology* **2019**, *14* (2), 156-160. DOI: 10.1038/s41565-018-0331-8.

(6) Patra, J. K.; Das, G.; Fraceto, L. F.; Campos, E. V. R.; et al. Nano based drug delivery systems: recent developments and future prospects. *Journal of Nanobiotechnology* **2018**, *16* (1), 71. DOI: 10.1186/s12951-018-0392-8.

(7) Soares, S.; Sousa, J.; Pais, A.; Vitorino, C. Nanomedicine: Principles, Properties, and Regulatory Issues. *Frontiers in Chemistry* **2018**, *6*. DOI: 10.3389/fchem.2018.00360.

(8) Younis, M. A.; Tawfeek, H. M.; Abdellatif, A. A. H.; Abdel-Aleem, J. A.; Harashima, H. Clinical translation of nanomedicines: Challenges, opportunities, and keys. *Adv. Drug Del. Rev.* **2022**, *181*, 114083. DOI: 10.1016/j.addr.2021.114083.

(9) Pelaz, B.; Alexiou, C.; Alvarez-Puebla, R. A.; Alves, F.; et al. Diverse Applications of Nanomedicine. *ACS Nano* **2017**, *11* (3), 2313-2381. DOI: 10.1021/acsnano.6b06040.

(10) Wagner, V.; Dullaart, A.; Bock, A.-K.; Zweck, A. The emerging nanomedicine landscape. *Nat. Biotechnol.* **2006**, *24* (10), 1211-1217. DOI: 10.1038/nbt1006-1211.

(11) Mross, K.; Niemann, B.; Massing, U.; Drevs, J.; Unger, C.; Bhamra, R.; Swenson, C. E. Pharmacokinetics of liposomal doxorubicin (TLC-D99; Myocet) in patients with solid tumors: an open-label, single-dose study. *Cancer Chemother. Pharmacol.* **2004**, *54* (6), 514-524. DOI: 10.1007/s00280-004-0825-y.

(12) Müller, R. H.; Runge, S. A.; Ravelli, V.; Thünemann, A. F.; Mehnert, W.; Souto, E. B. Cyclosporine-loaded solid lipid nanoparticles (SLN®): Drug–lipid physicochemical interactions and characterization of drug incorporation. *Eur. J. Pharm. Biopharm.* **2008**, *68* (3), 535-544. DOI: 10.1016/j.ejpb.2007.07.006.

(13) Martinelli, C.; Battaglini, M.; Pucci, C.; Gioi, S.; et al. Development of Nanostructured Lipid Carriers for the Delivery of Idebenone in Autosomal Recessive Spastic Ataxia of Charlevoix-Saguenay. *ACS Omega* **2020**, *5* (21), 12451-12466. DOI: 10.1021/acsomega.0c01282.

(14) Chauhan, I.; Yasir, M.; Verma, M.; Singh, A. P. Nanostructured Lipid Carriers: A Groundbreaking Approach for Transdermal Drug Delivery. *Adv Pharm Bull* **2020**, *10* (2), 150-165. DOI: 10.34172/apb.2020.021 From NLM.

(15) Dave, V.; Tak, K.; Sohgaura, A.; Gupta, A.; Sadhu, V.; Reddy, K. R. Lipid-polymer hybrid nanoparticles: Synthesis strategies and biomedical applications. *J. Microbiol. Methods* **2019**, *160*, 130-142. DOI: 10.1016/j.mimet.2019.03.017.

(16) Berben, P.; Brouwers, J.; Augustijns, P. The artificial membrane insert system as predictive tool for formulation performance evaluation. *Int. J. Pharm.* **2018**, *537* (1), 22-29. DOI: 10.1016/j.ijpharm.2017.12.025.

(17) Wei, W.; Lu, X.; Wang, Z.; Pérez, B.; et al. Single-component solid lipid nanocarriers prepared with ultra-long chain amphiphilic lipids. *Journal of Colloid and Interface Science* **2017**, *505*, 392-401. DOI: 10.1016/j.jcis.2017.06.022.

(18) Sanzari, I.; Buratti, E.; Huang, R.; Tusan, C. G.; et al. Poly(N-isopropylacrylamide) based thin microgel films for use in cell culture applications. *Sci. Rep.* **2020**, *10* (1), 6126. DOI: 10.1038/s41598-020-63228-9.

(19) Li, J.; Liang, H.; Liu, J.; Wang, Z. Poly (amidoamine) (PAMAM) dendrimer mediated delivery of drug and pDNA/siRNA for cancer therapy. *Int. J. Pharm.* **2018**, *546* (1), 215-225. DOI: 10.1016/j.ijpharm.2018.05.045.

(20) Yang, H.; Li, J.; Patel, S. K.; Palmer, K. E.; Devlin, B.; Rohan, L. C. Design of Poly(lactic-co-glycolic Acid) (PLGA) Nanoparticles for Vaginal Co-Delivery of Griffithsin and Dapivirine and Their Synergistic Effect for HIV Prophylaxis. *Pharmaceutics* **2019**, *11* (4), 184. DOI: 10.3390/pharmaceutics11040184.

(21) Frank, L. A.; Contri, R. V.; Beck, R. C. R.; Pohlmann, A. R.; Guterres, S. S. Improving drug biological effects by encapsulation into polymeric nanocapsules. *WIREs Nanomedicine and Nanobiotechnology* **2015**, *7* (5), 623-639. DOI: 10.1002/wnan.1334.

(22) Lebrun-Frenay, C.; Moulignier, A.; Pierrot-Deseilligny, C.; Benrabah, R.; et al. Five-year outcome in the copaxone observatory: a nationwide cohort of patients with multiple sclerosis starting treatment with glatiramer acetate in France. *J. Neurol.* **2019**, *266* (4), 888-901. DOI: 10.1007/s00415-019-09211-5.

(23) Park, K.; Vishnevetskaya, K.; Vaidyanathan, J.; Burckart, G. J.; Green, D. J. Pediatric Drug Development Studies for Familial Hypercholesterolemia Submitted to the US Food and Drug Administration Between 2007 and 2020. *The Journal of Clinical Pharmacology* **2022**, *62* (3), 397-408. DOI: 10.1002/jcph.1973.

(24) Ikwuagwu, B.; Tullman-Ercek, D. Virus-like particles for drug delivery: a review of methods and applications. *Curr. Opin. Biotechnol.* **2022**, *78*, 102785. DOI: 10.1016/j.copbio.2022.102785.

(25) Hassanin, I.; Elzoghby, A. Albumin-based nanoparticles: a promising strategy to overcome cancer drug resistance. *Cancer Drug Resist* **2020**, *3* (4), 930-946. DOI: 10.20517/cdr.2020.68.

(26) Haeri, A.; Osouli, M.; Bayat, F.; Alavi, S.; Dadashzadeh, S. Nanomedicine approaches for sirolimus delivery: a review of pharmaceutical properties and preclinical studies. *Artificial Cells, Nanomedicine, and Biotechnology* **2018**, *46*, 1-14. DOI: 10.1080/21691401.2017.1408123.

(27) Kanaparthi, A.; Kukura, S.; Slenkovich, N.; AlGhamdi, F.; Shafy, S. Z.; Hakim, M.; Tobias, J. D. Perioperative Administration of Emend® (Aprepitant) at a Tertiary Care Children's Hospital: A 12-Month Survey. *Clin. Pharmacol.* **2019**, *11*, 155-160. DOI: 10.2147/CPAA.S221736.

(28) Cotta, M. A. Quantum Dots and Their Applications: What Lies Ahead? *ACS Applied Nano Materials* **2020**, *3* (6), 4920-4924. DOI: 10.1021/acsanm.0c01386.

(29) Li, Y.; Zhang, H. Fe3O4-based nanotheranostics for magnetic resonance imaging-synergized multifunctional cancer management. *Nanomedicine* **2019**, *14* (11), 1493-1512. DOI: 10.2217/nnm-2018-0346.

(30) Pasparakis, G. Recent developments in the use of gold and silver nanoparticles in biomedicine. *WIREs Nanomedicine and Nanobiotechnology* **2022**, *14* (5), e1817. DOI: 10.1002/wnan.1817.

(31) IARC-WHO. *WHO report on cancer: setting priorities, investing wisely and providing care for all*; Geneva: World Health Organization;, 2020.

(32) Wyld, L.; Audisio, R. A.; Poston, G. J. The evolution of cancer surgery and future perspectives. *Nature Reviews Clinical Oncology* **2015**, *12* (2), 115-124. DOI: 10.1038/nrclinonc.2014.191.

(33) Wang, K.; Tepper, J. E. Radiation therapy-associated toxicity: Etiology, management, and prevention. *CA Cancer J. Clin.* **2021**, *71* (5), 437-454. DOI: 10.3322/caac.21689.

(34) Galluzzi, L.; Buqué, A.; Kepp, O.; Zitvogel, L.; Kroemer, G. Immunological Effects of Conventional Chemotherapy and Targeted Anticancer Agents. *Cancer Cell* **2015**, *28* (6), 690-714. DOI: 10.1016/j.ccell.2015.10.012.

(35) Li, X.; Lovell, J. F.; Yoon, J.; Chen, X. Clinical development and potential of photothermal and photodynamic therapies for cancer. *Nature Reviews Clinical Oncology* **2020**, *17* (11), 657-674. DOI: 10.1038/s41571-020-0410-2.

(36) Saxena, M.; van der Burg, S. H.; Melief, C. J. M.; Bhardwaj, N. Therapeutic cancer vaccines. *Nature Reviews Cancer* **2021**, *21* (6), 360-378. DOI: 10.1038/s41568-021-00346-0.

(37) Fukumura, D.; Kloepper, J.; Amoozgar, Z.; Duda, D. G.; Jain, R. K. Enhancing cancer immunotherapy using antiangiogenics: opportunities and challenges. *Nature Reviews Clinical Oncology* **2018**, *15* (5), 325-340. DOI: 10.1038/nrclinonc.2018.29.

(38) Batlle, E.; Clevers, H. Cancer stem cells revisited. *Nat. Med.* **2017**, *23* (10), 1124-1134. DOI: 10.1038/nm.4409.

(39) Mukherjee, S. Recent progress toward antiangiogenesis application of nanomedicine in cancer therapy. *Future Science OA* **2018**, *4* (7), FSO318. DOI: 10.4155/fsoa-2018-0051.

(40) Karges, J. Clinical Development of Metal Complexes as Photosensitizers for Photodynamic Therapy of Cancer. *Angew. Chem. Int. Ed.* **2022**, *61* (5), e202112236. DOI: 10.1002/anie.202112236.

(41) Lettieri-Barbato, D.; Aquilano, K. Pushing the Limits of Cancer Therapy: The Nutrient Game. *Front. Oncol.* **2018**, *8*. DOI: 10.3389/fonc.2018.00148.

(42) Hanahan, D. Hallmarks of Cancer: New Dimensions. *Cancer Discov.* **2022**, *12* (1), 31-46. DOI: 10.1158/2159-8290.Cd-21-1059.

(43) Sanna, V.; Pala, N.; Sechi, M. Targeted therapy using nanotechnology: focus on cancer. *Int J Nanomedicine* **2014**, *9*, 467-483. DOI: 10.2147/ijn.S36654.

(44) Marin, J. F. G.; Nunes, R. F.; Coutinho, A. M.; Zaniboni, E. C.; et al. Theranostics in Nuclear Medicine: Emerging and Re-emerging Integrated Imaging and Therapies in the Era of Precision Oncology. *Radiographics* **2020**, *40* (6), 1715-1740. DOI: 10.1148/rg.2020200021.

(45) Kapoor, G.; Saigal, S.; Elongavan, A. Action and resistance mechanisms of antibiotics: A guide for clinicians. *J. Anaesthesiol. Clin. Pharmacol.* **2017**, *33* (3), 300-305. DOI: 10.4103/joacp.JOACP_349_15.

(46) Mladenovic-Antic, S.; Kocic, B.; Velickovic-Radovanovic, R.; Dinic, M.; Petrovic, J.; Randjelovic, G.; Mitic, R. Correlation between antimicrobial consumption and antimicrobial resistance of Pseudomonas aeruginosa in a hospital setting: a 10-year study. *J. Clin. Pharm. Ther.* **2016**, *41* (5), 532-537. DOI: 10.1111/jcpt.12432.

(47) Micoli, F.; Bagnoli, F.; Rappuoli, R.; Serruto, D. The role of vaccines in combatting antimicrobial resistance. *Nature Reviews Microbiology* **2021**. DOI: 10.1038/s41579-020-00506-3.

(48) Hay, S. I.; Rao, P. C.; Dolecek, C.; Day, N. P. J.; Stergachis, A.; Lopez, A. D.; Murray, C. J. L. Measuring and mapping the global burden of antimicrobial resistance. *BMC Med.* **2018**, *16* (1), 78. DOI: 10.1186/s12916-018-1073-z.

(49) Murray, C. J.; Ikuta, K. S.; Sharara, F.; Swetschinski, L.; et al. Global burden of bacterial antimicrobial resistance in 2019: a systematic analysis. *The Lancet* **2022**, *399* (10325), 629-655.

(50) Lee, A. S.; de Lencastre, H.; Garau, J.; Kluytmans, J.; Malhotra-Kumar, S.; Peschel, A.; Harbarth, S. Methicillin-resistant Staphylococcus aureus. *Nature Reviews Disease Primers* **2018**, *4* (1), 18033. DOI: 10.1038/nrdp.2018.33.

(51) Lakhundi, S.; Zhang, K. Methicillin-Resistant Staphylococcus aureus: Molecular Characterization, Evolution, and Epidemiology. *Clin. Microbiol. Rev.* **2018**, *31* (4). DOI: 10.1128/cmr.00020-18.

(52) Missiakas, D. M.; Schneewind, O. Growth and Laboratory Maintenance of Staphylococcus aureus. *Curr. Protoc. Microbiol.* **2013**, *28* (1), 9C.1.1-9C.1.9. DOI: 10.1002/9780471729259.mc09c01s28.

(53) Turner, N. A.; Sharma-Kuinkel, B. K.; Maskarinec, S. A.; Eichenberger, E. M.; et al. Methicillin-resistant Staphylococcus aureus: an overview of basic and clinical research. *Nature Reviews Microbiology* **2019**, *17* (4), 203-218. DOI: 10.1038/s41579-018-0147-4.

(54) Salgado-Pabón, W.; Schlievert, P. M. Models matter: the search for an effective Staphylococcus aureus vaccine. *Nature Reviews Microbiology* **2014**, *12* (8), 585-591. DOI: 10.1038/nrmicro3308.

(55) Howden, B. P.; Giulieri, S. G.; Wong Fok Lung, T.; Baines, S. L.; et al. Staphylococcus aureus host interactions and adaptation. *Nature Reviews Microbiology* **2023**. DOI: 10.1038/s41579-023-00852-y.

(56) Miller, L. S.; Cho, J. S. Immunity against Staphylococcus aureus cutaneous infections. *Nature Reviews Immunology* **2011**, *11* (8), 505-518. DOI: 10.1038/nri3010.

(57) McGuinness, W. A.; Malachowa, N.; DeLeo, F. R. Vancomycin Resistance in Staphylococcus aureus. *Yale J. Biol. Med.* **2017**, *90* (2), 269-281.

(58) Kahl, B. C.; Becker, K.; Loffler, B. Clinical Significance and Pathogenesis of Staphylococcal Small Colony Variants in Persistent Infections. *Clin. Microbiol. Rev.* **2016**, *29* (2), 401-427. DOI: 10.1128/cmr.00069-15.

(59) Bui, L. M.; Conlon, B. P.; Kidd, S. P. Antibiotic tolerance and the alternative lifestyles of Staphylococcus aureus. *Essays Biochem.* **2017**, *61* (1), 71-79. DOI: 10.1042/ebc20160061 From NLM.

(60) Tuchscherr, L.; Löffler, B.; Proctor, R. A. Persistence of Staphylococcus aureus: Multiple Metabolic Pathways Impact the Expression of Virulence Factors in Small-Colony Variants (SCVs). *Front. Microbiol.* **2020**, *11*. DOI: 10.3389/fmicb.2020.01028.

(61) Melter, O.; Radojevič, B. Small colony variants of Staphylococcus aureus-review. *Folia Microbiol. (Praha)* **2010**, *55* (6), 548-558. DOI: 10.1007/s12223-010-0089-3.

(62) von Eiff, C.; Peters, G.; Becker, K. The small colony variant (SCV) concept - the role of staphylococcal SCVs in persistent infections. *Injury* **2006**, *37* (2), S26-S33. DOI: 10.1016/j.injury.2006.04.006.

(63) Proctor, R. A.; Vanlangevelde, P.; Kristjansson, M.; Maslow, J. N.; Arbeit, R. D. Persistent and relapsing infections associated with Small-Colony variants of *staphylococcus aureus*. *Clin. Infect. Dis.* **1995**, *20* (1), 95-102. DOI: 10.1093/clinids/20.1.95.

(64) Gajdács, M. The Continuing Threat of Methicillin-Resistant Staphylococcus aureus. *Antibiotics (Basel)* **2019**, *8* (2). DOI: 10.3390/antibiotics8020052.

(65) Hibbitts, A.; O'Leary, C. Emerging Nanomedicine Therapies to Counter the Rise of Methicillin-Resistant Staphylococcus aureus. *Materials* **2018**, *11* (2), 321.

(66) Zhou, K.; Li, C.; Chen, D.; Pan, Y.; et al. A review on nanosystems as an effective approach against infections of Staphylococcus aureus. *Int J Nanomedicine* **2018**, *13*, 7333-7347. DOI: 10.2147/ijn.S169935 From NLM.

(67) Zhou, Z.; Li, B.; Liu, X.; Li, Z.; et al. Recent Progress in Photocatalytic Antibacterial. *ACS Applied Bio Materials* **2021**, *4* (5), 3909-3936. DOI: 10.1021/acsabm.0c01335.

(68) Su, K.; Tan, L.; Liu, X.; Cui, Z.; et al. Rapid Photo-Sonotherapy for Clinical Treatment of Bacterial Infected Bone Implants by Creating Oxygen Deficiency Using Sulfur Doping. *ACS Nano* **2020**, *14* (2), 2077-2089. DOI: 10.1021/acsnano.9b08686.

(69) Qiao, Y.; Liu, X.; Li, B.; Han, Y.; et al. Treatment of MRSA-infected osteomyelitis using bacterial capturing, magnetically targeted composites with microwave-assisted bacterial killing. *Nature Communications* **2020**, *11* (1), 4446. DOI: 10.1038/s41467-020-18268-0.

(70) Aydin, M.; Köksal, F.; Günay, İ.; Serin, M.; Polat, S. The effect of antibacterial silver electrodes and the nature of ion emission in the outer side of inhibition zone. *Annals of Medical Sciences* **1996**, *5*, 52-57.

(71) Durán, N.; Durán, M.; de Jesus, M. B.; Seabra, A. B.; Fávaro, W. J.; Nakazato, G. Silver nanoparticles: A new view on mechanistic aspects on antimicrobial activity. *Nanomed. Nanotechnol. Biol. Med.* **2016**, *12* (3), 789-799. DOI: 10.1016/j.nano.2015.11.016.

(72) Franci, G.; Falanga, A.; Galdiero, S.; Palomba, L.; Rai, M.; Morelli, G.; Galdiero, M. Silver Nanoparticles as Potential Antibacterial Agents. *Molecules* **2015**, *20* (5), 8856-8874.

(73) Singh, P.; Pandit, S.; Jers, C.; Joshi, A. S.; Garnæs, J.; Mijakovic, I. Silver nanoparticles produced from Cedecea sp. exhibit antibiofilm activity and remarkable stability. *Sci. Rep.* **2021**, *11* (1), 12619. DOI: 10.1038/s41598-021-92006-4.

(74) Dos Santos Ramos, M. A.; Da Silva, P. B.; Spósito, L.; De Toledo, L. G.; et al. Nanotechnology-based drug delivery systems for control of microbial biofilms: a review. *International journal of nanomedicine* **2018**, 1179-1213.

(75) Mathur, P.; Jha, S.; Ramteke, S.; Jain, N. K. Pharmaceutical aspects of silver nanoparticles. *Artificial Cells, Nanomedicine, and Biotechnology* **2018**, *46* (sup1), 115-126. DOI: 10.1080/21691401.2017.1414825.

(76) Grün, A. Y.; App, C. B.; Breidenbach, A.; Meier, J.; Metreveli, G.; Schaumann, G. E.; Manz, W. Effects of low dose silver nanoparticle treatment on the structure and community composition of bacterial freshwater biofilms. *PLoS One* **2018**, *13* (6), e0199132. DOI: 10.1371/journal.pone.0199132.

(77) Godoy-Gallardo, M.; Eckhard, U.; Delgado, L. M.; de Roo Puente, Y. J. D.; Hoyos-Nogués, M.; Gil, F. J.; Perez, R. A. Antibacterial approaches in tissue engineering using metal ions and nanoparticles: From mechanisms to applications. *Bioactive Materials* **2021**, *6* (12), 4470-4490. DOI: 10.1016/j.bioactmat.2021.04.033.

(78) Yin, I. X.; Zhang, J.; Zhao, I. S.; Mei, M. L.; Li, Q.; Chu, C. H. The antibacterial mechanism of silver nanoparticles and its application in dentistry. *International journal of nanomedicine* **2020**, 2555-2562.

(79) Reidy, B.; Haase, A.; Luch, A.; Dawson, K. A.; Lynch, I. Mechanisms of Silver Nanoparticle Release, Transformation and Toxicity: A Critical Review of Current Knowledge and Recommendations for Future Studies and Applications. *Materials* **2013**, *6* (6), 2295-2350. DOI: 10.3390/ma6062295.

(80) Singh, P.; Pandit, S.; Beshay, M.; Mokkapati, V. R. S. S.; et al. Anti-biofilm effects of gold and silver nanoparticles synthesized by the Rhodiola rosea rhizome extracts. *Artificial Cells, Nanomedicine, and Biotechnology* **2018**, *46* (sup3), 886-899. DOI: 10.1080/21691401.2018.1518909.

(81) Mikhailova, E. O. Silver Nanoparticles: Mechanism of Action and Probable Bio-Application. *Journal of Functional Biomaterials* **2020**, *11* (4), 84. DOI: 10.3390/jfb11040084.

(82) Deng, H.; McShan, D.; Zhang, Y.; Sinha, S. S.; Arslan, Z.; Ray, P. C.; Yu, H. Mechanistic Study of the Synergistic Antibacterial Activity of Combined Silver Nanoparticles and Common Antibiotics. *Environ. Sci. Technol.* **2016**, *50* (16), 8840-8848. DOI: 10.1021/acs.est.6b00998.

(83) Tăbăran, A.-F.; Matea, C. T.; Mocan, T.; Tăbăran, A.; Mihaiu, M.; Iancu, C.; Mocan, L. Silver nanoparticles for the therapy of tuberculosis. *International journal of nanomedicine* **2020**, 2231-2258. DOI: 10.2147/IJN.S241183.

(84) Saratale, G. D.; Saratale, R. G.; Benelli, G.; Kumar, G.; Pugazhendhi, A.; Kim, D.-S.; Shin, H.-S. Anti-diabetic Potential of Silver Nanoparticles Synthesized with Argyreia nervosa Leaf Extract High Synergistic Antibacterial Activity with Standard Antibiotics Against Foodborne Bacteria. *J. Cluster Sci.* **2017**, *28* (3), 1709-1727. DOI: 10.1007/s10876-017-1179-z.

(85) Hwang, I.-s.; Hwang, J. H.; Choi, H.; Kim, K.-J.; Lee, D. G. Synergistic effects between silver nanoparticles and antibiotics and the mechanisms involved. *J. Med. Microbiol.* **2012**, *61* (12), 1719-1726. DOI: 10.1099/jmm.0.047100-0.

(86) Stabryla, L. M.; Johnston, K. A.; Diemler, N. A.; Cooper, V. S.; Millstone, J. E.; Haig, S.-J.; Gilbertson, L. M. Role of bacterial motility in differential resistance mechanisms of silver nanoparticles and silver ions. *Nature Nanotechnology* **2021**, *16* (9), 996-1003. DOI: 10.1038/s41565-021-00929-w.

(87) Valentin, E.; Bottomley, A. L.; Chilambi, G. S.; Harry, E. J.; et al. Heritable nanosilver resistance in priority pathogen: a unique genetic adaptation and comparison with ionic silver and antibiotics. *Nanoscale* **2020**, *12* (4), 2384-2392. DOI: 10.1039/C9NR08424J.

(88) Gunawan, C.; Marquis, C. P.; Amal, R.; Sotiriou, G. A.; Rice, S. A.; Harry, E. J. Widespread and Indiscriminate Nanosilver Use: Genuine Potential for Microbial Resistance. *ACS Nano* **2017**, *11* (4), 3438-3445. DOI: 10.1021/acsnano.7b01166.

(89) Lara, H. H.; Ayala-Núñez, N. V.; Ixtepan Turrent, L. d. C.; Rodríguez Padilla, C. Bactericidal effect of silver nanoparticles against multidrug-resistant bacteria. *World J. Microbiol. Biotechnol.* **2010**, *26* (4), 615-621. DOI: 10.1007/s11274-009-0211-3.

(90) Tang, S.; Zheng, J. Antibacterial Activity of Silver Nanoparticles: Structural Effects. *Advanced Healthcare Materials* **2018**, *7* (13), 1701503. DOI: 10.1002/adhm.201701503.

(91) Karami, A.; Xie, Z.; Zhang, J.; Kabir, M. S.; Munroe, P.; Kidd, S.; Zhang, H. Insights into the antimicrobial mechanism of Ag and I incorporated ZnO nanoparticle derivatives under visible light. *Materials Science and Engineering: C* **2020**, *107*, 110220. DOI: 10.1016/j.msec.2019.110220.

(92) Haidari, H.; Vasilev, K.; Cowin, A. J.; Kopecki, Z. Bacteria-Activated Dual pH- and Temperature-Responsive Hydrogel for Targeted Elimination of Infection and Improved Wound Healing. *ACS Applied Materials & Interfaces* **2022**, *14* (46), 51744-51762. DOI: 10.1021/acsami.2c15659.

(93) Tripathi, N.; Goshisht, M. K. Recent Advances and Mechanistic Insights into Antibacterial Activity, Antibiofilm Activity, and Cytotoxicity of Silver Nanoparticles. *ACS Applied Bio Materials* **2022**, *5* (4), 1391-1463. DOI: 10.1021/acsabm.2c00014.

(94) Wang, Y.; Wan, J.; Miron, R. J.; Zhao, Y.; Zhang, Y. Antibacterial properties and mechanisms of gold–silver nanocages. *Nanoscale* **2016**, *8* (21), 11143-11152. DOI: 10.1039/C6NR01114D.

(95) Frei, A.; Verderosa, A. D.; Elliott, A. G.; Zuegg, J.; Blaskovich, M. A. T. Metals to combat antimicrobial resistance. *Nature Reviews Chemistry* **2023**, *7* (3), 202-224. DOI: 10.1038/s41570-023-00463-4.

(96) Yang, X.; Yang, M.; Pang, B.; Vara, M.; Xia, Y. Gold Nanomaterials at Work in Biomedicine. *Chem. Rev.* **2015**, *115* (19), 10410-10488. DOI: 10.1021/acs.chemrev.5b00193.

(97) Okkeh, M.; Bloise, N.; Restivo, E.; De Vita, L.; Pallavicini, P.; Visai, L. Gold Nanoparticles: Can They Be the Next Magic Bullet for Multidrug-Resistant Bacteria? *Nanomaterials* **2021**, *11* (2), 312. DOI: 10.3390/nano11020312.

(98) Wang, S.-G.; Chen, Y.-C.; Chen, Y.-C. Antibacterial gold nanoparticle-based photothermal killing of vancomycin-resistant bacteria. *Nanomedicine* **2018**, *13* (12), 1405-1416. DOI: 10.2217/nnm-2017-0380.

(99) Spirescu, V. A.; Chircov, C.; Grumezescu, A. M.; Vasile, B. Ș.; Andronescu, E. Inorganic Nanoparticles and Composite Films for Antimicrobial Therapies. *Int. J. Mol. Sci.* **2021**, *22* (9), 4595. DOI: 10.3390/ijms22094595.

(100) Mikhailova, E. O. Gold Nanoparticles: Biosynthesis and Potential of Biomedical Application. *Journal of Functional Biomaterials* **2021**, *12* (4), 70. DOI: 10.3390/jfb12040070.

(101) Tao, C. Antimicrobial activity and toxicity of gold nanoparticles: research progress, challenges and prospects. *Lett. Appl. Microbiol.* **2018**, *67* (6), 537-543. DOI: 10.1111/lam.13082.

(102) Bekmukhametova, A.; Ruprai, H.; Hook, J. M.; Mawad, D.; Houang, J.; Lauto, A. Photodynamic therapy with nanoparticles to combat microbial infection and resistance. *Nanoscale* **2020**, *12* (41), 21034-21059. DOI: 10.1039/D0NR04540C.

(103) Nazarzadeh Zare, E.; Makvandi, P.; Borzacchiello, A.; Tay, F. R.; Ashtari, B.; V, V. T. P. Antimicrobial gum bio-based nanocomposites and their industrial and biomedical applications. *Chem. Commun. (Camb.)* **2019**, *55* (99), 14871-14885. DOI: 10.1039/c9cc08207g.

(104) Makvandi, P.; Gu, J. T.; Zare, E. N.; Ashtari, B.; Moeini, A.; Tay, F. R.; Niu, L.-n. Polymeric and inorganic nanoscopical antimicrobial fillers in dentistry. *Acta Biomater.* **2020**, *101*, 69-101. DOI: 10.1016/j.actbio.2019.09.025.

(105) Azizi-Lalabadi, M.; Ehsani, A.; Divband, B.; Alizadeh-Sani, M. Antimicrobial activity of Titanium dioxide and Zinc oxide nanoparticles supported in 4A zeolite and evaluation the morphological characteristic. *Sci. Rep.* **2019**, *9* (1), 17439. DOI: 10.1038/s41598-019-54025-0.

(106) Carol López de, D.; Matias Guerrero, C.; Fernanda, B. M.; Camilo, S.; Maria José, G. Antimicrobial Effect of Titanium Dioxide Nanoparticles. In *Antimicrobial Resistance*, Mihai, M., Swee Hua Erin, L., Kok-Song, L., Romeo-Teodor, C. Eds.; IntechOpen, 2020; p Ch. 5.

(107) Nguyen, V. T.; Vu, V. T.; Nguyen, T. H.; Nguyen, T. A.; Tran, V. K.; Nguyen-Tri, P. Antibacterial Activity of TiO2- and ZnO-Decorated with Silver Nanoparticles. *Journal of Composites Science* **2019**, *3* (2), 61. DOI: 10.3390/jcs3020061.

(108) Akhtar, S.; Shahzad, K.; Mushtaq, S.; Ali, I.; Rafe, M. H.; Fazal-ul-Karim, S. M. Antibacterial and antiviral potential of colloidal Titanium dioxide (TiO2) nanoparticles suitable for biological applications. *Materials Research Express* **2019**, *6* (10), 105409. DOI: 10.1088/2053-1591/ab3b27.

(109) Luthfiah, A.; Permana, M. D.; Deawati, Y.; Firdaus, M. L.; Rahayu, I.; Eddy, D. R. Photocatalysis of nanocomposite titania–natural silica as antibacterial against Staphylococcus aureus and Pseudomonas aeruginosa. *RSC Advances* **2021**, *11* (61), 38528-38536. DOI: 10.1039/D1RA07043F.

(110) Makvandi, P.; Wang, C.-y.; Zare, E. N.; Borzacchiello, A.; Niu, L.-n.; Tay, F. R. Metal-Based Nanomaterials in Biomedical Applications: Antimicrobial Activity and Cytotoxicity Aspects. *Adv. Funct. Mater.* **2020**, *30* (22), 1910021. DOI: 10.1002/adfm.201910021.

(111) Mohd Yusof, H.; Mohamad, R.; Zaidan, U. H.; Abdul Rahman, N. A. Microbial synthesis of zinc oxide nanoparticles and their potential application as an antimicrobial agent and a feed supplement in animal industry: a review. *Journal of Animal Science and Biotechnology* **2019**, *10* (1), 57. DOI: 10.1186/s40104-019-0368-z.

(112) Singh, A.; Singh, N. B.; Afzal, S.; Singh, T.; Hussain, I. Zinc oxide nanoparticles: a review of their biological synthesis, antimicrobial activity, uptake, translocation and biotransformation in plants. *Journal of Materials Science* **2018**, *53* (1), 185-201. DOI: 10.1007/s10853-017-1544-1.

(113) Sirelkhatim, A.; Mahmud, S.; Seeni, A.; Kaus, N. H. M.; et al. Review on Zinc Oxide nanoparticles: antibacterial activity and toxicity mechanism. *Nanomicro Lett* **2015**, *7* (3), 219-242. DOI: 10.1007/s40820-015-0040-x.

(114) Qi, K.; Cheng, B.; Yu, J.; Ho, W. Review on the improvement of the photocatalytic and antibacterial activities of ZnO. *J. Alloys Compd.* **2017**, *727*, 792-820, Review article. DOI: 10.1016/j.jallcom.2017.08.142.

(115) Elbourne, A.; Cheeseman, S.; Wainer, P.; Kim, J.; et al. Significant Enhancement of Antimicrobial Activity in Oxygen-Deficient Zinc Oxide Nanowires. *ACS Applied Bio Materials* **2020**, *3* (5), 2997-3004. DOI: 10.1021/acsabm.0c00065.

(116) Mano, G.; Harinee, S.; Sridhar, S.; Ashok, M.; Viswanathan, A. Microwave assisted synthesis of ZnO-PbS heterojuction for degradation of organic pollutants under visible light. *Sci. Rep.* **2020**, *10* (1), 2224. DOI: 10.1038/s41598-020-59066-4.

(117) Khan, M. M.; Ansari, S. A.; Pradhan, D.; Ansari, M. O.; Han, D. H.; Lee, J.; Cho, M. H. Band gap engineered TiO2 nanoparticles for visible light induced photoelectrochemical and photocatalytic studies. *Journal of Materials Chemistry A* **2014**, *2* (3), 637-644. DOI: 10.1039/C3TA14052K.

(118) Dou, Q. Q.; Rengaramchandran, A.; Selvan, S. T.; Paulmurugan, R.; Zhang, Y. Core-shell upconversion nanoparticle semiconductor heterostructures for photodynamic therapy. *Sci. Rep.* **2015**, *5* (1), 1-8. DOI: 10.1038/srep08252.

(119) Mettenbrink, E. M.; Yang, W.; Wilhelm, S. Bioimaging with Upconversion Nanoparticles. *Advanced Photonics Research* **2022**, *3* (12), 2200098. DOI: 10.1002/adpr.202200098.

(120) Chen, Y.; Xiang, H.; Zhuang, S.; Shen, Y.; Chen, Y.; Zhang, J. Oxygen-Independent Photocleavage of Radical Nanogenerator for Near-IR-Gated and H2O-Mediated Free-Radical Nanotherapy. *Adv. Mater.* **2021**, *n/a* (n/a), 2100129. DOI: 10.1002/adma.202100129.

(121) El-Shafey, H. M.; Saif, M.; Aly, M. H.; Hafez, H. S. Enhancing the Photo and Biomedical Activity of ZnO by Incorporation with Zinc Silicate Nanocomposites. *Appl. Organomet. Chem.* **2020**, *34* (11), e5902. DOI: 10.1002/aoc.5902.

(122) Bansal, M.; Kumar, A.; Malinee, M.; Sharma, T. K. Nanomedicine: Diagnosis, Treatment, and Potential Prospects. In *Nanoscience in Medicine Vol. 1*, Daima, H. K., Pn, N., Ranjan, S., Dasgupta, N., Lichtfouse, E. Eds.; Springer International Publishing, 2020; pp 297-331.

(123) Shobana, M. K. Nanoferrites in biosensors – A review. *Materials Science and Engineering: B* **2021**, *272*, 115344. DOI: 10.1016/j.mseb.2021.115344.

(124) Pashchenko, O.; Shelby, T.; Banerjee, T.; Santra, S. A Comparison of Optical, Electrochemical, Magnetic, and Colorimetric Point-of-Care Biosensors for Infectious Disease Diagnosis. *ACS Infectious Diseases* **2018**, *4* (8), 1162-1178. DOI: 10.1021/acsinfecdis.8b00023.

(125) Liu, F.; Wong, M. M.-K.; Chiu, S.-K.; Lin, H.; Ho, J. C.; Pang, S. W. Effects of nanoparticle size and cell type on high sensitivity cell detection using a localized surface plasmon resonance biosensor. *Biosensors and Bioelectronics* **2014**, *55*, 141-148. DOI: 10.1016/j.bios.2013.11.075.

(126) Malekzad, H.; Zangabad, P. S.; Mirshekari, H.; Karimi, M.; Hamblin, M. R. Noble metal nanoparticles in biosensors: recent studies and applications. *Nanotechnology Reviews* **2017**, *6* (3), 301-329. DOI: 10.1515/ntrev-2016-0014.

(127) Solanki, P. R.; Kaushik, A.; Agrawal, V. V.; Malhotra, B. D. Nanostructured metal oxide-based biosensors. *NPG Asia Materials* **2011**, *3* (1), 17-24. DOI: 10.1038/asiamat.2010.137.

(128) Juan-Colás, J.; Parkin, A.; Dunn, K. E.; Scullion, M. G.; Krauss, T. F.; Johnson, S. D. The electrophotonic silicon biosensor. *Nature Communications* **2016**, *7* (1), 12769. DOI: 10.1038/ncomms12769.

(129) Hussein, H. A.; Hanora, A.; Solyman, S. M.; Hassan, R. Y. A. Designing and fabrication of electrochemical nano-biosensor for the fast detection of SARS-CoV-2-RNA. *Sci. Rep.* **2023**, *13* (1), 5139. DOI: 10.1038/s41598-023-32168-5.

(130) Purohit, B.; Vernekar, P. R.; Shetti, N. P.; Chandra, P. Biosensor nanoengineering: Design, operation, and implementation for biomolecular analysis. *Sensors International* **2020**, *1*, 100040. DOI: 10.1016/j.sintl.2020.100040.

(131) Fracchiolla, N. S.; Artuso, S.; Cortelezzi, A. Biosensors in Clinical Practice: Focus on Oncohematology. *Sensors* **2013**, *13* (5), 6423-6447. DOI: 10.3390/s130506423.

(132) Harish, V.; Tewari, D.; Gaur, M.; Yadav, A. B.; Swaroop, S.; Bechelany, M.; Barhoum, A. Review on Nanoparticles and Nanostructured Materials: Bioimaging, Biosensing, Drug Delivery, Tissue Engineering, Antimicrobial, and Agro-Food Applications. *Nanomaterials* **2022**, *12* (3), 457. DOI: 10.3390/nano12030457.

(133) Samson, R.; Navale, G. R.; Dharne, M. S. Biosensors: frontiers in rapid detection of COVID-19. *3 Biotech* **2020**, *10* (9), 385. DOI: 10.1007/s13205-020-02369-0.

(134) George Kerry, R.; Ukhurebor, K. E.; Kumari, S.; Maurya, G. K.; et al. A comprehensive review on the applications of nano-biosensor-based approaches for non-communicable and communicable disease detection. *Biomaterials Science* **2021**, *9* (10), 3576-3602. DOI: 10.1039/D0BM02164D.

(135) Macdonald, A.; Hawkes, L. A.; Corrigan, D. K. Recent advances in biomedical, biosensor and clinical measurement devices for use in humans and the potential application of these technologies for the study of

physiology and disease in wild animals. *Philosophical Transactions of the Royal Society B: Biological Sciences* **2021**, *376* (1831), 20200228. DOI: 10.1098/rstb.2020.0228.

(136) Tessaro, L.; Aquino, A.; de Almeida Rodrigues, P.; Joshi, N.; Ferrari, R. G.; Conte-Junior, C. A. Nucleic Acid-Based Nanobiosensor (NAB) Used for Salmonella Detection in Foods: A Systematic Review. *Nanomaterials* **2022**, *12* (5), 821. DOI: 10.3390/nano12050821.

(137) Wang, Y.; Zhou, J.; Li, J. Construction of Plasmonic Nano-Biosensor-Based Devices for Point-of-Care Testing. *Small Methods* **2017**, *1* (11), 1700197. DOI: 10.1002/smtd.201700197.

(138) Thangamani J., G.; Deshmukh, K.; Kumar Sadasivuni, K.; Chidambaram, K.; et al. Recent advances in electrochemical biosensor and gas sensors based on graphene and carbon nanotubes (CNT) - A review *Advanced Materials Letters* **2017**, *8* (3), 196-205. DOI: 10.5185/amlett.2017.7042.

(139) Demeke Teklemariam, A.; Samaddar, M.; Alharbi, M. G.; Al-Hindi, R. R.; Bhunia, A. K. Biosensor and molecular-based methods for the detection of human coronaviruses: A review. *Molecular and Cellular Probes* **2020**, *54*, 101662. DOI: 10.1016/j.mcp.2020.101662.

(140) Cui, S.; Zhang, S.; Yue, S. Raman Spectroscopy and Imaging for Cancer Diagnosis. *J. Healthc. Eng.* **2018**, *2018*, 8619342. DOI: 10.1155/2018/8619342.

(141) Zhang, Y.; Wen, S.; Zhao, L.; Li, D.; et al. Ultrastable polyethyleneimine-stabilized gold nanoparticles modified with polyethylene glycol for blood pool, lymph node and tumor CT imaging. *Nanoscale* **2016**, *8* (10), 5567-5577. DOI: 10.1039/C5NR07955A.

(142) Luo, D.; Wang, X.; Burda, C.; Basilion, J. P. Recent Development of Gold Nanoparticles as Contrast Agents for Cancer Diagnosis. *Cancers (Basel)* **2021**, *13* (8), 1825. DOI: 10.3390/cancers13081825.

(143) Prasad, R.; Agawane, S. B.; Chauhan, D. S.; Srivastava, R.; Selvaraj, K. In Vivo Examination of Folic Acid-Conjugated Gold-Silica Nanohybrids as Contrast Agents for Localized Tumor Diagnosis and Biodistribution. *Bioconjugate Chemistry* **2018**, *29* (12), 4012-4019. DOI: 10.1021/acs.bioconjchem.8b00522.

(144) Zhou, Z.; Zhang, C.; Qian, Q.; Ma, J.; et al. Folic acid-conjugated silica capped gold nanoclusters for targeted fluorescence/X-ray computed tomography imaging. *Journal of Nanobiotechnology* **2013**, *11* (1), 17. DOI: 10.1186/1477-3155-11-17.

(145) Zhang, C.; Li, C.; Liu, Y.; Zhang, J.; et al. Gold Nanoclusters-Based Nanoprobes for Simultaneous Fluorescence Imaging and Targeted Photodynamic Therapy with Superior Penetration and Retention Behavior in Tumors. *Adv. Funct. Mater.* **2015**, *25* (8), 1314-1325. DOI: 10.1002/adfm.201403095.

(146) Liu, M.; Shi, Z.; Wang, X.; Zhang, Y.; et al. Simultaneous enhancement of red upconversion luminescence and CT contrast of NaGdF4:Yb,Er nanoparticles via Lu3+ doping. *Nanoscale* **2018**, *10* (43), 20279-20288. DOI: 10.1039/C8NR06968A.

(147) Caspani, S.; Magalhães, R.; Araújo, J. P.; Sousa, C. T. Magnetic Nanomaterials as Contrast Agents for MRI. *Materials* **2020**, *13* (11), 2586. DOI: 10.3390/ma13112586.

(148) Comanescu, C. Magnetic Nanoparticles: Current Advances in Nanomedicine, Drug Delivery and MRI. *Chemistry (Easton)* **2022**, *4* (3), 872-930. DOI: 10.3390/chemistry4030063.

(149) Lin, L.; Wang, L. V. The emerging role of photoacoustic imaging in clinical oncology. *Nature Reviews Clinical Oncology* **2022**, *19* (6), 365-384. DOI: 10.1038/s41571-022-00615-3.

(150) Refaat, A.; Yap, M. L.; Pietersz, G.; Walsh, A. P. G.; et al. In vivo fluorescence imaging: success in preclinical imaging paves the way for clinical applications. *Journal of Nanobiotechnology* **2022**, *20* (1), 450. DOI: 10.1186/s12951-022-01648-7.

(151) Zhao, J.; Chen, J.; Ma, S.; Liu, Q.; et al. Recent developments in multimodality fluorescence imaging probes. *Acta Pharmaceutica Sinica B* **2018**, *8* (3), 320-338. DOI: 10.1016/j.apsb.2018.03.010.

(152) Lee, J.-H.; Cho, H.-Y.; Choi, H. K.; Lee, J.-Y.; Choi, J.-W. Application of Gold Nanoparticle to Plasmonic Biosensors. *Int. J. Mol. Sci.* **2018**, *19* (7), 2021. DOI: 10.3390/ijms19072021.

(153) Lei, X.; Xu, X.; Liu, L.; Xu, L.; Wang, L.; Kuang, H.; Xu, C. Gold-nanoparticle-based multiplex immuno-strip biosensor for simultaneous determination of 83 antibiotics. *Nano Research* **2023**, *16* (1), 1259-1268. DOI: 10.1007/s12274-022-4762-z.

(154) Akbari Nakhjavani, S.; Khalilzadeh, B.; Afsharan, H.; Hosseini, N.; et al. Electrochemiluminescent immunosensor for detection of carcinoembryonic antigen using luminol-coated silver nanoparticles. *Microchimica Acta* **2023**, *190* (2), 77. DOI: 10.1007/s00604-023-05656-8.

(155) Huang, P.; Bao, L.; Zhang, C.; Lin, J.; et al. Folic acid-conjugated Silica-modified gold nanorods for X-ray/CT imaging-guided dual-mode radiation and photo-thermal therapy. *Biomaterials* **2011**, *32* (36), 9796-9809. DOI: 10.1016/j.biomaterials.2011.08.086.

(156) Gai, Y.; Li, Y.; Wu, S.; Xu, L.; et al. Preparation and In Vitro Evaluation of a Gadolinium-Containing Vitamin E TPGS Micelle as a Potential Contrast Agent for MR Imaging. *Pharmaceutics* **2023**, *15* (2), 401. DOI: 10.3390/pharmaceutics15020401.

(157) Liu, S.; Jiang, Y.; Liu, P.; Yi, Y.; et al. Single-Atom Gadolinium Nano-Contrast Agents with High Stability for Tumor T1 Magnetic Resonance Imaging. *ACS Nano* **2023**, *17* (9), 8053-8063. DOI: 10.1021/acsnano.2c09664.

(158) Champagne, P.-O.; Sanon, N. T.; Carmant, L.; Nguyen, D. K.; et al. Superparamagnetic iron oxide nanoparticles-based detection of neuronal activity. *Nanomed. Nanotechnol. Biol. Med.* **2022**, *40*, 102478. DOI: 10.1016/j.nano.2021.102478.

(159) Yang, Q.; Li, Y.; Zhao, X.; Zhang, J.; Cheng, X.; Zhu, N. Recent advances of superparamagnetic iron oxide nanoparticles and its applications in neuroscience under external magnetic field. *Applied Nanoscience* **2023**. DOI: 10.1007/s13204-023-02803-8.

(160) Yamini, S.; Gunaseelan, M.; Kumar, G. A.; Singh, S.; et al. NaGdF4:Yb,Er-Ag nanowire hybrid nanocomposite for multifunctional upconversion emission, optical imaging, MRI and CT imaging applications. *Microchimica Acta* **2020**, *187* (6), 317. DOI: 10.1007/s00604-020-04285-9.

(161) Xiao, L.; Tian, X.; Harihar, S.; Li, Q.; Li, L.; Welch, D. R.; Zhou, A. Gd2O3-doped silica @ Au nanoparticles for in vitro imaging cancer biomarkers using surface-enhanced Raman scattering. *Spectrochimica Acta Part A: Molecular and Biomolecular Spectroscopy* **2017**, *181*, 218-225. DOI: 10.1016/j.saa.2017.03.033.

(162) Qin, R.; Li, S.; Qiu, Y.; Feng, Y.; et al. Carbonized paramagnetic complexes of Mn (II) as contrast agents for precise magnetic resonance imaging of sub-millimeter-sized orthotopic tumors. *Nature Communications* **2022**, *13* (1), 1938. DOI: 10.1038/s41467-022-29586-w.

(163) Sun, I.-C.; Jo, S.; Dumani, D.; Yun, W. S.; et al. Theragnostic Glycol Chitosan-Conjugated Gold Nanoparticles for Photoacoustic Imaging of Regional Lymph Nodes and Delivering Tumor Antigen to Lymph Nodes. *Nanomaterials* **2021**, *11* (7), 1700. DOI: 10.3390/nano11071700.

(164) Liu, C.; Zheng, X.; Dai, T.; Wang, H.; et al. Reversibly Photoswitching Upconversion Nanoparticles for Super-Sensitive Photoacoustic Molecular Imaging. *Angew. Chem. Int. Ed.* **2022**, *61* (19), e202116802. DOI: 10.1002/anie.202116802.

(165) Zhang, Y.; Guo, Z.; Zhu, H.; Xing, W.; et al. Synthesis of Liquid Gallium@Reduced Graphene Oxide Core–Shell Nanoparticles with Enhanced Photoacoustic and Photothermal Performance. *Journal of the American Chemical Society* **2022**, *144* (15), 6779-6790. DOI: 10.1021/jacs.2c00162.

(166) Wang, M.; Deng, K.; Lü, W.; Deng, X.; et al. Rational Design of Multifunctional Fe@γ-Fe2O3@H-TiO2 Nanocomposites with Enhanced Magnetic and Photoconversion Effects for Wide Applications: From Photocatalysis to Imaging-Guided Photothermal Cancer Therapy. *Adv. Mater.* **2018**, *30* (13), 1706747. DOI: 10.1002/adma.201706747.

(167) Fedorenko, S.; Stepanov, A.; Sibgatullina, G.; Samigullin, D.; et al. Fluorescent magnetic nanoparticles for modulating the level of intracellular Ca2+ in motoneurons. *Nanoscale* **2019**, *11* (34), 16103-16113. DOI: 10.1039/C9NR05071J.

(168) Marković, Z. M.; Labudová, M.; Danko, M.; Matijašević, D.; et al. Highly Efficient Antioxidant F- and Cl-Doped Carbon Quantum Dots for Bioimaging. *ACS Sustainable Chemistry & Engineering* **2020**, *8* (43), 16327-16338. DOI: 10.1021/acssuschemeng.0c06260.

(169) Liu, Y.; Lu, Y.; Yang, X.; Zheng, X.; et al. Amplified stimulated emission in upconversion nanoparticles for super-resolution nanoscopy. *Nature* **2017**, *543* (7644), 229-233. DOI: 10.1038/nature21366.

(170) Dong, H.; Sun, L.-D.; Yan, C.-H. Lanthanide-Doped Upconversion Nanoparticles for Super-Resolution Microscopy. *Frontiers in Chemistry* **2021**, *8*. DOI: 10.3389/fchem.2020.619377.

(171) Fernández-Suárez, M.; Ting, A. Y. Fluorescent probes for super-resolution imaging in living cells. *Nat. Rev. Mol. Cell Biol.* **2008**, *9* (12), 929-943. DOI: 10.1038/nrm2531.

(172) Valli, J.; Garcia-Burgos, A.; Rooney, L. M.; Vale de Melo e Oliveira, B.; Duncan, R. R.; Rickman, C. Seeing beyond the limit: A guide to choosing the right super-resolution microscopy technique. *J. Biol. Chem.* **2021**, *297* (1), 100791. DOI: 10.1016/j.jbc.2021.100791.

(173) Jing, Y.; Zhang, C.; Yu, B.; Lin, D.; Qu, J. Super-Resolution Microscopy: Shedding New Light on In Vivo Imaging. *Frontiers in chemistry* **2021**, *9*, 746900-746900. DOI: 10.3389/fchem.2021.746900.

(174) Liu, Z.; Liu, J.; Wang, X.; Mi, F.; Wang, D.; Wu, C. Fluorescent Bioconjugates for Super-Resolution Optical Nanoscopy. *Bioconjug. Chem.* **2020**, *31* (8), 1857-1872. DOI: 10.1021/acs.bioconjchem.0c00320.

(175) Li, W.; Kaminski Schierle, G. S.; Lei, B.; Liu, Y.; Kaminski, C. F. Fluorescent Nanoparticles for Super-Resolution Imaging. *Chem. Rev.* **2022**, *122* (15), 12495-12543. DOI: 10.1021/acs.chemrev.2c00050.

(176) Yadav, A.; Rao, C.; Nandi, C. K. Fluorescent Probes for Super-Resolution Microscopy of Lysosomes. *ACS Omega* **2020**, *5* (42), 26967-26977. DOI: 10.1021/acsomega.0c04018.

(177) Wang, L.; Frei, M. S.; Salim, A.; Johnsson, K. Small-Molecule Fluorescent Probes for Live-Cell Super-Resolution Microscopy. *J. Am. Chem. Soc.* **2019**, *141* (7), 2770-2781. DOI: 10.1021/jacs.8b11134.

(178) Kim, D.; Jeong, K.; Kwon, J. E.; Park, H.; Lee, S.; Kim, S.; Park, S. Y. Dual-color fluorescent nanoparticles showing perfect color-specific photoswitching for bioimaging and super-resolution microscopy. *Nature Communications* **2019**, *10* (1), 3089. DOI: 10.1038/s41467-019-10986-4.

(179) Hong, G.; Antaris, A. L.; Dai, H. Near-infrared fluorophores for biomedical imaging. *Nature Biomedical Engineering* **2017**, *1* (1), 0010. DOI: 10.1038/s41551-016-0010.

(180) Jeong, S.; Widengren, J.; Lee, J.-C. Fluorescent Probes for STED Optical Nanoscopy. *Nanomaterials* **2022**, *12* (1), 21. DOI: 10.3390/nano12010021.

(181) Zhan, Q.; Liu, H.; Wang, B.; Wu, Q.; et al. Achieving high-efficiency emission depletion nanoscopy by employing cross relaxation in upconversion nanoparticles. *Nature Communications* **2017**, *8* (1), 1058. DOI: 10.1038/s41467-017-01141-y.

(182) Wu, Q.; Huang, B.; Peng, X.; He, S.; Zhan, Q. Non-bleaching fluorescence emission difference microscopy using single 808-nm laser excited red upconversion emission. *Opt. Express* **2017**, *25* (25), 30885-30894. DOI: 10.1364/OE.25.030885.

(183) Dong, H.; Sun, L.-D.; Yan, C.-H. Energy transfer in lanthanide upconversion studies for extended optical applications. *Chem. Soc. Rev.* **2015**, *44* (6), 1608-1634, Review article. DOI: 10.1039/C4CS00188E.

(184) Chen, G. Y.; Qiu, H. Q.; Prasad, P. N.; Chen, X. Y. Upconversion Nanoparticles: Design, Nanochemistry, and Applications in Theranostics. *Chem. Rev.* **2014**, *114*, 5161.

(185) Zheng, B.; Fan, J.; Chen, B.; Qin, X.; et al. Rare-Earth Doping in Nanostructured Inorganic Materials. *Chem. Rev.* **2022**, *122* (6), 5519-5603. DOI: 10.1021/acs.chemrev.1c00644.

(186) Qiu, Z.; Shu, J.; Tang, D. Near-Infrared-to-Ultraviolet Light-Mediated Photoelectrochemical Aptasensing Platform for Cancer Biomarker Based on Core–Shell NaYF4:Yb,Tm@TiO2 Upconversion Microrods. *Anal. Chem.* **2018**, *90* (1), 1021-1028. DOI: 10.1021/acs.analchem.7b04479.

(187) Wang, F.; Wang, J.; Liu, X. Direct Evidence of a Surface Quenching Effect on Size-Dependent Luminescence of Upconversion Nanoparticles. *Angew. Chem. Int. Ed.* **2010**, *49* (41), 7456-7460. DOI: 10.1002/anie.201003959.

(188) Zhang, F. *Photon Upconversion Nanomaterials*; Springer Berlin Heidelberg, 2014.

(189) Zhang, Y.-W.; Sun, X.; Si, R.; You, L.-P.; Yan, C.-H. Single-Crystalline and Monodisperse LaF3 Triangular Nanoplates from a Single-Source Precursor. *Journal of the American Chemical Society* **2005**, *127* (10), 3260-3261. DOI: 10.1021/ja042801y.

(190) Chen, X.; Peng, D.; Ju, Q.; Wang, F. Photon upconversion in core-shell nanoparticles. *Chem. Soc. Rev.* **2015**, *44* (6), 1318-1330. DOI: 10.1039/c4cs00151f.

(191) Chen, G.; Qiu, H.; Prasad, P. N.; Chen, X. Upconversion Nanoparticles: Design, Nanochemistry, and Applications in Theranostics. *Chem. Rev.* **2014**, *114* (10), 5161-5214, Review article. DOI: 10.1021/cr400425h PMC.

(192) May, P. B.; Suter, J. D., II; May, P. S.; Berry, M. T. The Dynamics of Nanoparticle Growth and Phase Change During Synthesis of β-NaYF4. *The Journal of Physical Chemistry C* **2016**, *120* (17), 9482-9489. DOI: 10.1021/acs.jpcc.6b01365.

(193) Mi, C.; Tian, Z.; Cao, C.; Wang, Z.; Mao, C.; Xu, S. Novel Microwave-Assisted Solvothermal Synthesis of NaYF4:Yb,Er Upconversion Nanoparticles and Their Application in Cancer Cell Imaging. *Langmuir* **2011**, *27* (23), 14632-14637. DOI: 10.1021/la204015m.

(194) Xu, X. K.; Li, W.; Zhou, W.; Tan, G. P.; et al. Preparation and properties of dual-mode luminescent $NaYF_4$:Yb,Tm@SiO_2/carbon dot nanocomposites. *Journal of Materials Chemistry C* **2018**, *6* (38), 10360-10366. DOI: 10.1039/c8tc03508c.

(195) Yang, J.; Shen, D.; Li, X.; Li, W.; et al. One-Step Hydrothermal Synthesis of Carboxyl-Functionalized Upconversion Phosphors for Bioapplications. *Chemistry – A European Journal* **2012**, *18* (43), 13642-13650. DOI: 10.1002/chem.201202336.

(196) Li, X.; Zhang, F.; Zhao, D. Lab on upconversion nanoparticles: optical properties and applications engineering via designed nanostructure. *Chem. Soc. Rev.* **2015**, *44* (6), 1346-1378. DOI: 10.1039/C4CS00163J.

(197) Damasco, J. A.; Chen, G.; Shao, W.; Ågren, H.; et al. Size-Tunable and Monodisperse Tm^{3+}/Gd^{3+}-Doped Hexagonal $NaYbF_4$ Nanoparticles with Engineered Efficient Near Infrared-to-Near Infrared Upconversion for In Vivo Imaging. *ACS Applied Materials & Interfaces* **2014**, *6* (16), 13884-13893. DOI: 10.1021/am503288d.

(198) Wang, F.; Liu, X. G. Multicolor Tuning of Lanthanide-Doped Nanoparticles by Single Wavelength Excitation. *Acc. Chem. Res.* **2014**, *47*, 1378.

(199) Wang, L.; Li, X.; Li, Z.; Chu, W.; et al. A new cubic phase for a $NaYF_4$ host matrix offering high upconversion luminescence efficiency. *Adv. Mater.* **2015**, *27* (37), 5528-5533. DOI: 10.1002/adma.201502748.

(200) Shi, R.; Ling, X.; Li, X.; Zhang, L.; et al. Tuning hexagonal $NaYbF_4$ nanocrystals down to sub-10 nm for enhanced photon upconversion. *Nanoscale* **2017**, *9* (36), 13739-13746. DOI: 10.1039/C7NR04877G.

(201) Chen, G.; Ågren, H.; Ohulchanskyy, T. Y.; Prasad, P. N. Light upconverting core-shell nanostructures: nanophotonic control for emerging applications. *Chem. Soc. Rev.* **2015**, *44* (6), 1680-1713. DOI: 10.1039/C4CS00170B.

(202) Sun, T.; Ai, F.; Zhu, G.; Wang, F. Upconversion in Nanostructured Materials: From Optical Tuning to Biomedical Applications. *Chemistry – An Asian Journal* **2018**, *13* (4), 373-385. DOI: 10.1002/asia.201701660.

(203) Zhang, J.; Zhao, S.; Xu, Z.; Zhang, L.; Zuo, P.; Wu, Q. Near-infrared light-driven photocatalytic NaYF4:Yb,Tm@ZnO core/shell nanomaterials and their performance. *RSC Advances* **2019**, *9* (7), 3688-3692. DOI: 10.1039/C8RA07861K.

(204) Wang, L.; Ren, L.; Mitchell, D.; Casillas-Garcia, G.; et al. Enhanced energy transfer in heterogeneous nanocrystals for near infrared upconversion photocurrent generation. *Nanoscale* **2017**, *9* (47), 18661-18667. DOI: 10.1039/C7NR07010A.

(205) Chen, C.; Li, C.; Shi, Z. Current advances in lanthanide-doped upconversion nanostructures for detection and bioapplication. *Advanced Science* **2016**, *3* (10), 1600029. DOI: 10.1002/advs.201600029.

(206) Tou, M.; Luo, Z.; Bai, S.; Liu, F.; Chai, Q.; Li, S.; Li, Z. Sequential coating upconversion $NaYF_4$:Yb,Tm nanocrystals with SiO_2 and ZnO layers for NIR-driven photocatalytic and antibacterial applications. *Materials Science and Engineering: C* **2017**, *70*, 1141-1148. DOI: 10.1016/j.msec.2016.03.038.

(207) Sun, C.; Gradzielski, M. Advances in fluorescence sensing enabled by lanthanide-doped upconversion nanophosphors. *Advances in Colloid and Interface Science* **2022**, *300*, 102579. DOI: 10.1016/j.cis.2021.102579.

(208) Sedlmeier, A.; Gorris, H. H. Surface modification and characterization of photon-upconverting nanoparticles for bioanalytical applications. *Chem. Soc. Rev.* **2015**, *44* (6), 1526-1560. DOI: 10.1039/C4CS00186A.

(209) Wang, F.; Liu, X. Recent advances in the chemistry of lanthanide-doped upconversion nanocrystals. *Chem. Soc. Rev.* **2009**, *38* (4), 976-989. DOI: 10.1039/B809132N.

(210) Sun, C.; Simke, J. R. J.; Gradzielski, M. An efficient synthetic strategy for ligand-free upconversion nanoparticles. *Materials Advances* **2020**, *1* (6), 1602-1607. DOI: 10.1039/D0MA00411A.

(211) Guo, X.; Song, W.; Chen, C.; Di, W.; Qin, W. Near-infrared photocatalysis of b-$NaYF_4$:Yb^{3+},Tm^{3+}@ZnO composites. *Physical Chemistry Chemical Physics* **2013**, *15* (35), 14681-14688. DOI: 10.1039/c3cp52248b.

(212) Lv, S.; Zhang, K.; Zhu, L.; Tang, D. ZIF-8-Assisted NaYF4:Yb,Tm@ZnO Converter with Exonuclease III-Powered DNA Walker for Near-Infrared Light Responsive Biosensor. *Anal. Chem.* **2020**, *92* (1), 1470-1476. DOI: 10.1021/acs.analchem.9b04710.

Chapter 2: Publication 1

Publication title: Facile Multi-step Synthesis of ZnO Coated β-$NaYF_4$:Yb/Tm Upconversion Nanoparticles as Antimicrobial Photodynamic Therapy for Persistent *Staphylococcus aureus* Small Colony Variants

The manuscript was published in the journal *ACS Applied Bio Materials.*

Statement of Authorship

Title of Paper	Facile Multistep Synthesis of ZnO-Coated β-$NaYF_4$:Yb/Tm Upconversion Nanoparticles as an Antimicrobial Photodynamic Therapy for Persistent *Staphylococcus aureus* Small Colony Variants
Publication Status	☑ Published ☐ Accepted for Publication ☐ Submitted for Publication ☐ Unpublished and Unsubmitted work written in manuscript style
Publication Details	Karami, A., Farivar, F., de Prinse, T. J., Rabiee, H., Kidd, S., Sumby, C. J., & Bi, J. (2021). Facile Multistep Synthesis of ZnO-Coated β-$NaYF_4$:Yb/Tm Upconversion Nanoparticles as an Antimicrobial Photodynamic Therapy for Persistent *Staphylococcus aureus* Small Colony Variants. ACS Applied Bio Materials, 4(8), 6125-6136. doi:10.1021/acsabm.1c00473

Principal Author

Name of Principal Author (Candidate)	Afshin Karami		
Contribution to the Paper	Concept development, material characterization, manuscript writing		
Overall percentage (%)	85%		
Certification:	This paper reports on original research I conducted during the period of my Higher Degree by Research candidature and is not subject to any obligations or contractual agreements with a third party that would constrain its inclusion in this thesis. I am the primary author of this paper.		
Signature		Date	08/12/2022

Co-Author Contributions

By signing the Statement of Authorship, each author certifies that:

i. the candidate's stated contribution to the publication is accurate (as detailed above);

ii. permission is granted for the candidate in include the publication in the thesis; and

iii. the sum of all co-author contributions is equal to 100% less the candidate's stated contribution.

Name of Co-Author	A/Prof. Jingxiu Bi		
Contribution to the Paper	Concept development, manuscript writing and review, supervision of work		
Signature		Date	15/06/2023

Name of Co-Author	Prof. Christopher Sumby		
Contribution to the Paper	Concept development, manuscript writing and review, supervision of work.		
Signature		Date	08/06/2023

Name of Co-Author	Dr. Stephen Kidd		
Contribution to the Paper	Concept development, manuscript writing and review, supervision of work.		
Signature		Date	09/06/2023

Name of Co-Author	Dr. Farzaneh Farivar		
Contribution to the Paper	Material characterization and manuscript writing.		
Signature		Date	08/12/2022

Name of Co-Author	Thomas de Prinse		
Contribution to the Paper	Material characterization and manuscript writing.		
Signature		Date	19/06/2023

Name of Co-Author	Dr. Hesamoddin Rabiee		
Contribution to the Paper	Material characterization and manuscript writing.		
Signature		Date	09/11/2022

2.1 Abstract

Antibacterial treatment strategies using functional nanomaterials, such as photodynamic therapy, are urgently required to combat persistent *Staphylococcus aureus* small colony variant (SCV) bacteria. Using a stepwise approach involving thermolysis to form β-$NaYF_4$:Yb/Tm upconversion nanoparticles (UCNPs), surface ligand exchange with cetyltrimethylammonium bromide (CTAB), followed by zeolitic imidazolate-8 (ZIF-8) coating and conversion to zinc oxide (ZnO), β-$NaYF_4$:Yb/Tm@ZnO nanoparticles were synthesised. Direct synthesis of β-$NaYF_4$:Yb/Tm@ZIF-8 UCNPs proved problematic due to the hydrophobic nature of the as-synthesised material, which was shown by zeta potential measurements using dynamic light scattering (DLS). To facilitate deposition of a ZnO coating, the zeta potentials of (i) as-synthesised UCNPs, (ii) calcined UCNPs, (iii) polyvinylpyrrolidone (PVP), and (iv) CTAB-coated UCNPs were measured, which revealed the CTAB-coated UCNPs to be the most hydrophilic, and better-dispersed form in water. β-$NaYF_4$:Yb/Tm@ZIF-8 composites formed using the CTAB-coated UCNPs were then converted into β-$NaYF_4$:Yb/Tm@ZnO nanoparticles by calcination under carefully controlled conditions. Photoluminescence analysis confirmed the upconversion process for the UCNP core, which allows the β-$NaYF_4$:Yb/Tm@ZnO nanoparticles to photogenerate reactive oxygen species (ROS) when activated by near-infrared (NIR) radiation. The NIR-activated UCNPs@ZnO nanoparticles demonstrated potent efficacy against both *Staphylococcus aureus* (SK2) and associated SCV bacteria (0.67 and 0.76 in log CFU reduction, respectively), which was attributed to ROS generated from the NIR activated β-$NaYF_4$:Yb/Tm@ZnO nanoparticles.

2.2 Introduction

The *Staphylococcus (S.) aureus* is a significant bacterium associated with chronic infections.[1] *S. aureus* small colony variants (SCVs), as a subpopulation of *S. aureus*, are a slow-growing bacterial cell-type that is now known to be responsible for persistent, relapsing infections (such as osteomyelitis), which respond poorly to conventional antibiotics.[2] The persistent infections as a response to remaining SCVs are attributed to their tolerance of antimicrobials, intercellular survival and the limited production of toxins necessary to elicit immune clearance.[3,4] Despite significant efforts,[2,5-9] there remains an urgent need for developing effective antibiotics or preventative therapeutic strategies to eradicate both *S. aureus* and their SCVs.

Antimicrobial peptides,[5] nanoparticles,[6,7] bacteriophage therapy,[8,9] and antimicrobial photodynamic therapy (aPDT)[10-13] have all been considered as alternative strategies to antibiotics for combatting antimicrobial-resistant bacteria.[14] PDT has been used for decades as a cancer treatment due to its low toxicity and high selectivity; however, it has not seen significant use in antimicrobial applications.[12,15,16] In PDT, non-toxic photosensitisers (PS) are activated by light with an appropriate wavelength to generate reactive oxygen species (ROS) that are fatal to proximal cells. PS with absorption peaks between 600 and 800 nm are required as at this wavelength light will have adequate energy to penetrate tissue and excite the molecule for the therapy.[15,17] Porphyrin, chlorin, pheophorbide, chlorin-e6 (Ce6), and their derivatives are common PS for PDT.[12,18]

Lanthanide-doped upconversion nanoparticles (UCNPs) have been recently used as a novel class of PS nanomaterials for PDT against cancer cells.[19-23] Core/shell nanoparticles consisting of an UCNP as the core and a semiconductor coating (e.g. ZnO or TiO_2) can be used as a PS. These materials generate ROS upon activation by near-infrared (NIR) light, which is absorbed by the

UCNP core and which in turn emits visible and UV light that is used to excite the semiconductor and produce the reactive oxygen species (Scheme 1). The use of NIR light is advantageous as human tissues are transparent to wavelengths between 750 and 1100 nm, allowing for deep tissue penetration.[24] NIR light is also relatively safe for bio-applications due to the long wavelength (low energy), with recent studies having confirmed the effectiveness of UCNPs for *in vitro* cancer therapy.[19,25] In terms of a coating, ZnO has attracted attention for bio-applications due to low manufacturing cost, abundance, and acceptance as a generally recognised as safe (GRAS) substance by the Food and Drug Administration (FDA) in the USA.[26] ZnO-based nanoparticles can also inactivate microorganisms under UV light irradiation,[27] and a ZnO NP shell can be synthesised by various methods such as solvothermal, precipitation, and sol-gel syntheses.[27]

Despite examples of $NaYF_4$:Yb/Tm@semiconductor NPs being known, the reproducible synthesis of a semiconductor coated β-$NaYF_4$ core/shell NP structure remains challenging.[28] This is because β-$NaYF_4$ NPs, synthesised by a thermolysis method, have a hydrophobic surface, whereas water-dispersed or soluble NPs are required for the synthesis of the core/shell structure. The hydrophobic behaviour of the β-$NaYF_4$ NPs synthesised by thermolysis arises from the oleic acid capping agent used in the reaction.[28] Oleate ligand-oxidation, ligand-acidification, ligand-exchange, and ligand-interaction are several strategies that have been used to increase the hydrophilicity of the β-$NaYF_4$ NPs.[28]

This study evaluates the use of aPDT to treat both *S. aureus* and their SCVs using NIR-activated core/shell UCNPs. Scheme 1 illustrates the proposed mode of action, with the formation of ROS originating from ZnO-coated UCNPs, when activated by NIR light (typically 980 nm). As UCNPs without a semiconductor coating are inactive, in this work, a stepwise approach was developed to synthesise β-$NaYF_4$:Yb/Tm@ZnO nanoparticles. As-synthesised, hydrophobic β-$NaYF_4$:Yb/Tm

NPs were modified by a ligand interaction approach using cationic cetyltrimethylammonium bromide (CTAB). The hydrophilic UCNPs could then be dispersed in water to allow the growth of a zeolite imidazolate framework-8 (ZIF-8) coating, which in turn could be calcined to give a ZnO NP shell around the UCNP core. The effect of calcination temperature was also investigated, examining three different temperatures (400, 450, and 500 °C) to mitigate conversion of the NP core and enhance ZnO formation. The antibacterial efficacy of the resulting core/shell β-$NaYF_4$:Yb/Tm@ZnO NPs was assessed against *S. aureus* WCH-SK2-SCV and the parental WCH-SK2 in NIR light-illuminated and dark modes (control experiment). Our results showed that a stepwise synthesis approach could be used to overcome the synthesis challenges of core/shell UCNPs@semiconductor NPs. The aPDT using hybrid UCNPs/semiconductor could be a potent therapeutic strategy to eradicate both *S. aureus* and their SCVs.

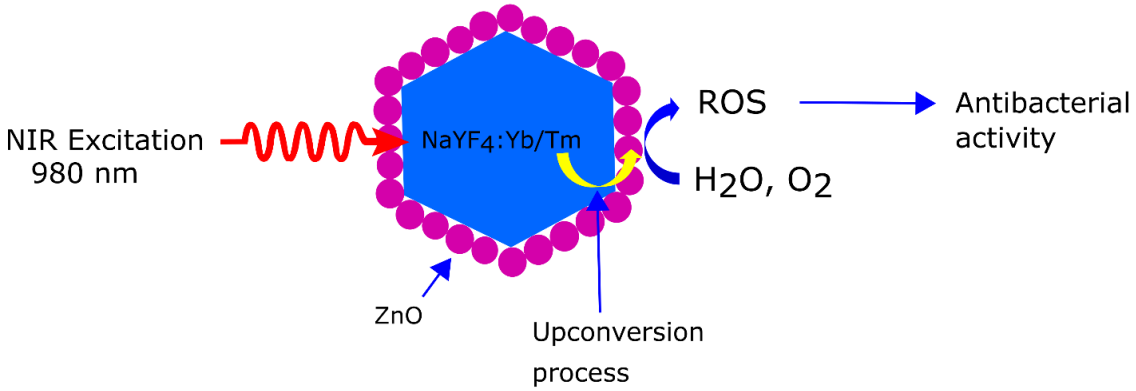

Scheme 1. An illustration of the mechanism of photocatalytic ROS generation by upconversion nanoparticles when irradiated by NIR light.

2.3 Results and discussion

2.3.1 Synthesis, composition, and morphology

UCNPs consist of a host material, such as $NaYF_4$, doped by lanthanide ions as sensitisers and activators. The selection of lanthanide ion dopants determines the excitation and emission profile of the UCNPs. The trivalent lanthanide ion Yb^{3+} is the most common sensitiser, while the trivalent ions Er^{3+} and Tm^{+3} are common activators; Tm^{+3} is particularly favourable in bio-applications due to very low heat generation and luminescence peaks in both the UV and visible ranges (350, 450, and 479 nm).[28] In terms of the host, hexagonal β-$NaYF_4$ NPs have been reported to be a more efficient host than cubic α-$NaYF_4$ for lanthanide-doped upconversion luminescence,[29,30] as the low lattice phonon energy of the hexagonal form minimises the nonradiative energy loss and increases the radiative emissions.[31]

$NaYF_4$:Yb/Tm@ZnO NPs were synthesised in a multistep process involving (a) core upconversion $NaYF_4$:Yb/Tm NP synthesis and elimination of organic impurities; (b) deposition of CTAB coating; (c) ZIF-8 formation; and, (d) conversion of ZIF-8 to ZnO by calcination (Scheme 2). Upconversion $NaYF_4$:Yb/Tm NPs with 18% Yb and 5% Tm doping were prepared by a thermal decomposition method.[32] In this method, non-coordinating ODE was used as a solvent due to its high boiling point (315 °C), while OA was used as both a solvent and surfactant to control nanoparticle growth and prevent aggregation of nanoparticles; [33] OA is often used for the synthesis of UCNPs and magnetic ferrite NPs.[28,34,35] Studies show/propose the carboxylate group of OA attaches to the surface of the NPs, with the nonpolar tail directed toward the solvent to facilitate the formation of highly uniform, monodisperse NPs, typically with highly hydrophobic surface characteristics.[36,37] While there is some debate, it has been proposed that the hydrophobic tail of additional OA can also interact with the nonpolar tail of the coated OA molecules to form a double

layer coating around the NPs.[35] Nevertheless, it is common to initially synthesise OA coated NPs before the exchange with other coatings to change the hydrophobicity of the NPs.

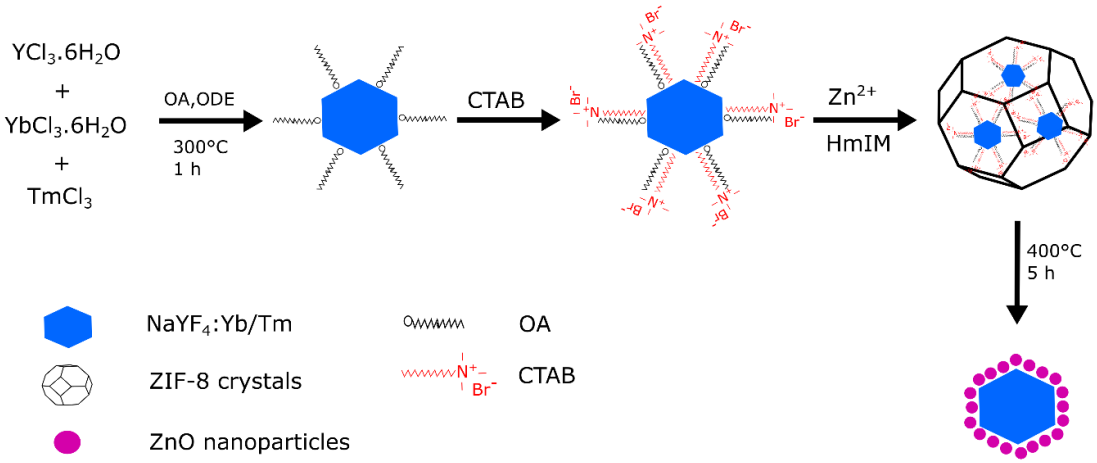

Scheme 2. Schematic illustration of the synthetic route used for the preparation of core/shell $NaYF_4$:Yb/Tm@ZnO NPs.

The structure of the synthesised NPs was confirmed by PXRD and data presented in Figure 1. The PXRD patterns for the synthesised $NaYF_4$:Yb/Tm NPs (Figure 1a) confirm samples are crystalline, with the diffraction peaks indexed to β-$NaYF_4$ (JCPDS # 16-034). The diffraction peaks located at 17.2°, 30.1°, 30.8°, 43.5°, and 53.7° (strong diffraction peaks) correspond to the $NaYF_4$ hexagonal structure indexed with (100), (110), (101), (201), and (211), respectively (JCPDS # 16-034).

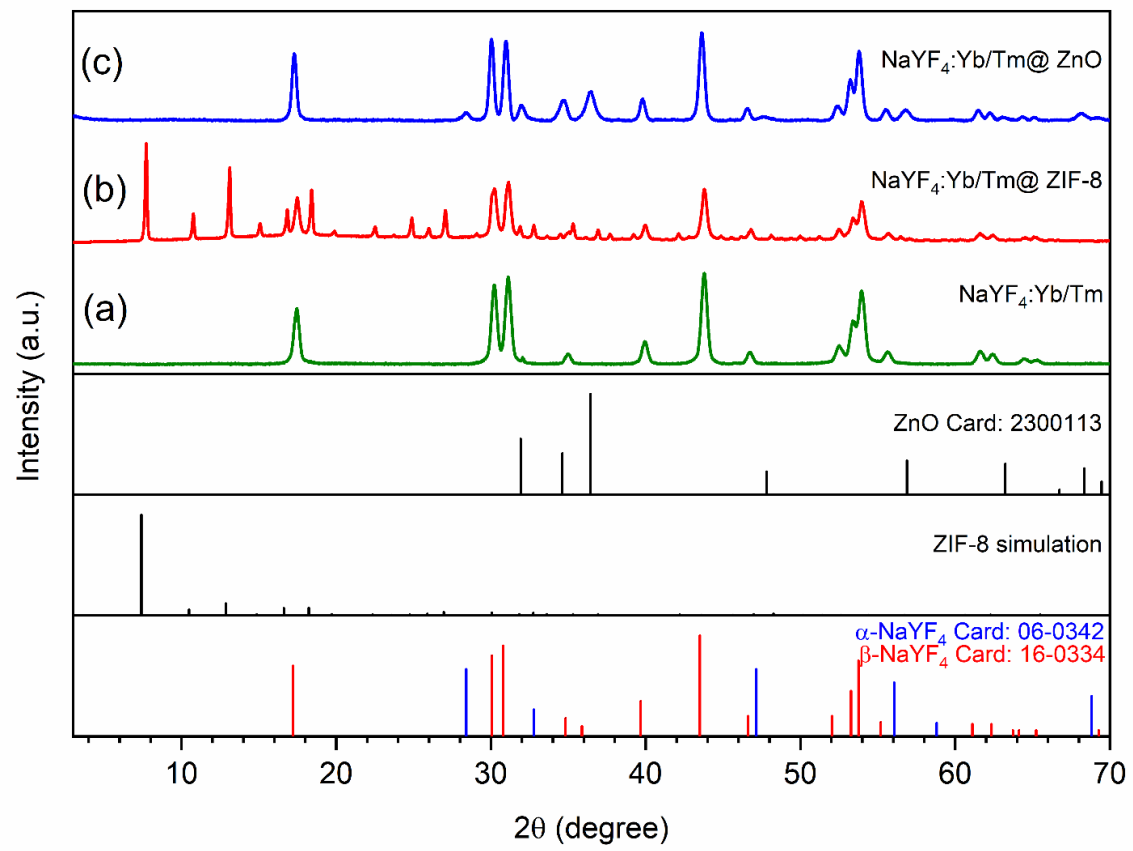

Figure 1. PXRD data for samples of (a) $NaYF_4$:Yb/Tm (b) $NaYF_4$:Yb/Tm@ZIF-8 and (c) $NaYF_4$:Yb/Tm@ZnO. The JCPDS cards for ZnO, ZIF-8 simulation, α-$NaYF_4$, and β-$NaYF_4$ are presented in the lower section.

The morphology of the as-synthesised NP samples was studied by TEM and SEM analysis, with the images, particle size measurement, and elemental analysis (EDS) results presented in Figure 2 (Energy-dispersive X-ray analysis (EDX) data is presented in Figure S7 – 9). High-resolution TEM imaging confirmed that particles with a hexagonal morphology are formed, consistent with the hexagonal β-$NaYF_4$ crystal structure (Figure 2a). The interplanar distance of the $NaYF_4$:Yb/Tm NPs was measured to be approximately 0.52 nm (Figure 2a), which can be indexed to the (100) lattice plane for the hexagonal β-$NaYF_4$ crystal structure (0.515 nm, JCPDS # 16-0334). The selected area electron diffraction (SAED) of synthesised $NaYF_4$:Yb/Tm NPs (Figure 2h) confirms a hexagonal structure for the NPs that is in good agreement with PXRD data. The HRTEM images

also revealed that synthesised $NaYF_4$:Yb/Tm NPs are uniformly sized with mean particle sizes of 30 $\pm$ 5 nm (based on 130 NPs, Figure 2i). The SEM image for the as-synthesised $NaYF_4$:Yb/Tm NP samples presented in Figure 2d is in good agreement with the TEM image, showing monodisperse NPs across the sample.

To confirm the composition and provide some insights into the distribution of Yb and Tm dopants within the $NaYF_4$:Yb/Tm NPs, elemental mapping was conducted. The elemental mapping of the as-synthesised $NaYF_4$:Yb/Tm NP samples (Figure 2g), confirms that Yb and Tm are distributed across the $NaYF_4$:Yb/Tm NP samples. EDX analysis showed that the atomic molar ratios for Yb/Tm elements in $NaYF_4$:Yb/Tm were 3.33, which is in good agreement with the feed Yb/Tm ratio of 3.6 that was used in the synthesis of $NaYF_4$:Yb (18%)/Tm (5%). While the dopant level used in the synthesis of the UCNPs is slightly lower, the EDX data confirmed the distribution of the dopants within the crystal nanoparticles.

XPS analysis was used to additionally confirm the elemental composition and chemical bonding on the surface of the as-synthesised $NaYF_4$:Yb/Tm NPs. The XPS spectra are included in the Supporting Information Figure S2. The XPS spectra (Figure S2a) confirm the presence of Na, Y, F, Yb, and Tm elements in the $NaYF_4$:Yb/Tm NP sample. The binding energy peak for Na_{1s} was found at 1,071.6 eV (Figure S2b). The two peaks at 159.2 and 161.3 eV are assigned to $Y_{3d5/2}$ and $Y_{3d3/2}$, respectively, while the peaks at 174.8, 178.7, and 198.7 eV are associated with Tm_{4d}, $Yb_{4d5/2,}$ and $Yb_{4d3/2}$, respectively (Figure S2c). The binding energy at 685 eV, ascribed to F_{1s} (Figure S2d). All the reported XPS binding energies are consistent with the typical values reported for $NaYF_4$:Yb/Tm NP.[38,39]

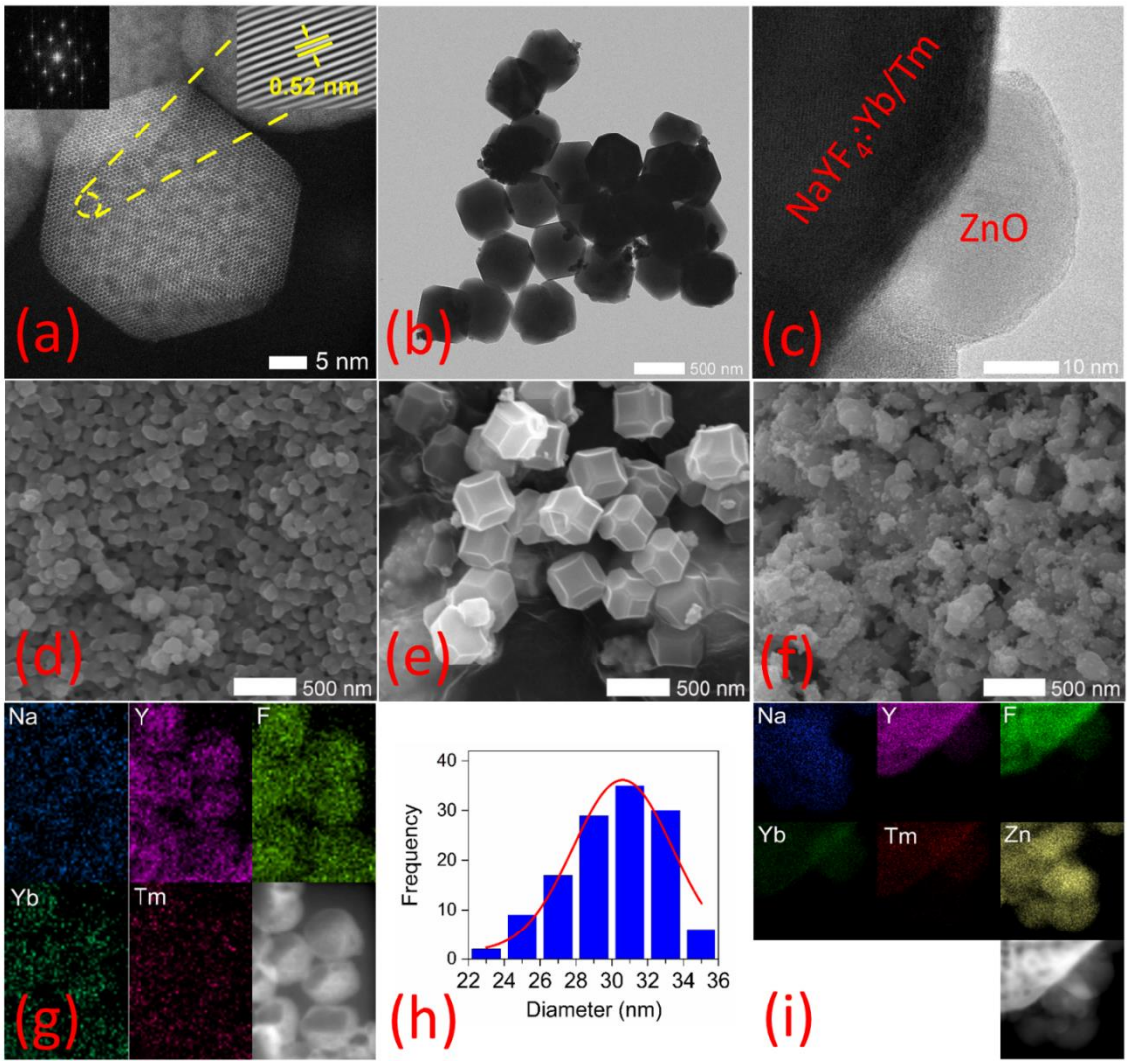

Figure 2. HR-TEM image of $NaYF_4$:Yb/Tm, selected area diffraction (inset) (a), TEM images of $NaYF_4$:Yb/Tm@ZIF-8, $NaYF_4$:Yb/Tm@ZnO (b-c), SEM images for $NaYF_4$:Yb/Tm, $NaYF_4$:Yb/Tm@ZIF-8, $NaYF_4$:Yb/Tm@ZnO (d-f), EDS element mapping, particle size distribution plot for $NaYF_4$:Yb/Tm (g-h), EDS element mapping for $NaYF_4$:Yb/Tm@ZnO (i).

The as-synthesised UCNPs appeared to contain a considerable amount of organic impurities, likely originating from ODE and OA. These impurities caused issues when isolating the nanoparticles, leading to the loss of material. TGA data (Figure S4a) showed an approximately 12% mass reduction, attributed to OA and ODE impurities in the as-synthesised UCNPs. To remove these, the NP samples were calcined at 450 °C for 30 min (the boiling points for OA and ODE are 360

and 320 °C, respectively), followed by a washing step, using Milli-Q water to remove the NaCl impurities (synthesis by-product) observed by close analysis of the PXRD data. The $NaYF_4$:Yb/Tm UCNPs were analysed with PXRD before and after the calcination to confirm the temperature was suitable for the elimination of organic impurities without modifying the UCNP structure. The PXRD results (Figure S3) showed a negligible change to the UCNP crystal structure after calcination. The TGA curve for the calcined UCNPs (Figure S4b) also showed a negligible mass change in the temperature range 100 - 600 °C, demonstrating that all the organic impurities have been eliminated from the sample in the calcination step.

Due to issues with the literature procedures used to apply the ZnO coating to the $NaYF_4$:Yb/Tm UCNPs,[38,40] zeta potential and associated pH values were measured to determine the hydrophobicity and colloidal stability of the as-synthesised UCNPs, calcined UCNPs, and additional PVP and CTAB coated UCNPs samples (Table S1). The latter two samples were prepared to improve the hydrophilicity and colloidal stability of the UCNP samples. The zeta potential results for the impure, calcined, PVP coated and CTAB coated $NaYF_4$:Yb/Tm NP samples were 14.9, 15.6, 21.9, and 54.5 (mV), respectively. The measured zeta potentials for the impure, calcined, and PVP coated UCNP samples all fall in the $\pm$30 mV range, which is considered to be the unstable range for colloids and indicates the possibility of agglomeration.[27,41] The positive zeta potential for the uncoated UCNP samples may also indicate a positive surface charge due to the lanthanide ions. Furthermore, calcination only seemed to have a very slight effect on the zeta potential despite being able to eliminate the organic impurities. Thus, these samples lacked the colloidal stability and surface chemistry for dispersal in water and issues encountered in the semiconductor coating steps could be attributed to lack of colloidal stability. In contrast, the CTAB-coated UCNPs were observed to have a much higher zeta potential value. The zeta potential

for the surface modification of UCNPs with cationic CTAB falls in a ±40 to ±60 mV range, consistent with colloidal stability.[42,43] Moreover, the CTAB coating could be inferred to be the most effective at changing the UCNPs surface chemistry to be more hydrophilic, which is ideal for the dispersion and growth of ZIF-8 in the following step.

Given that ZIF-8, and related Zn-based metal-organic frameworks, can be induced to readily grow around functionalised nanoparticles,[44] and moreover, that ZIF-8 can be converted into ZnO by calcination,[45,46] we adopted a new two-stage approach to introduce the semiconductor ZnO shell to the UCNP core. This was conducted by adding $Zn(OAc)_2$ to a suspension of the UCNPs in water and then adding an ethanol solution of HmIM. In the absence of the nanoparticles under these conditions, ZIF-8 only forms in trace amounts but with the UCNPs present to catalyze ZIF growth, ZIF-8 forms around the UCNPs.[47] The PXRD pattern for $NaYF_4$:Yb/Tm@ZIF-8 (Figure 1b) is similar to $NaYF_4$:Yb/Tm NPs with additional peaks at 7.4°, 10.5, 12.8, 14.8 and 16.6 corresponding with (110), (200), (211), (220), and (310) planes of ZIF-8. The TEM image for $NaYF_4$:Yb/Tm@ZIF-8 showed uniformly-sized ZIF-8 crystals around $NaYF_4$:Yb/Tm NPs with a mean particle size of ca. 500 nm (Figure 2b). The SEM image for the as-synthesised $NaYF_4$:Yb/Tm@ZIF-8 sample presented in Figure 2e is in good agreement with the TEM image.

The synthesised $NaYF_4$:Yb/Tm@ZIF-8 composite was calcined at 400 °C in the air for 5 h to convert the ZIF-8 to ZnO. The diffraction peaks for $NaYF_4$:Yb/Tm@ZnO (Figure 1c) show that the peaks for ZIF-8 have disappeared while new peaks for ZnO appear in the PXRD pattern. The diffraction peaks located at 34.7°, 36.5°, 47.8°, 56.8°, 63.1°, and 68.2° corresponding to the ZnO indexed with (002), (101), (102), (110), (103) and (112), respectively (JCPDS # 2300113). The three weak diffraction peaks at 28.8°, 47.6°, and 56.8° correspond with the cubic α-$NaYF_4$ (JCPDS # 06-342). This suggests a portion of UCNPs have converted from β-$NaYF_4$ to α-$NaYF_4$. The

TEM and SEM imaging of the $NaYF_4$:Yb/Tm@ZnO confirmed the non-epitaxial ZnO shell formation around $NaYF_4$:Yb/Tm NPs (Figure 2c and 2f). The TEM image for $NaYF_4$:Yb/Tm@ZnO (Figure 2c) confirmed the formation of small size ZnO particles with no changes in the size of the $NaYF_4$:Yb/Tm core material. The elemental mapping of the as-synthesised $NaYF_4$:Yb/Tm@ZnO NP samples (Figure 2j), confirms the distribution of elements across the $NaYF_4$:Yb/Tm@ZnO NP samples. As expected, the ZIF-8 conversion to ZnO NPs by calcination is concomitant with a reduction in particle size. This is due to ZIF-8 having a typical crystal density of between 1.05 to 1.19 g/cm[48] (influenced by synthesis methods), while the ZnO has a much higher density of 5.61 g/cm.[49] The SEM image for the $NaYF_4$:Yb/Tm@ZnO sample presented in Figure 2f is in good agreement with the TEM image however, slightly larger sized clusters were observed.

The calcination conditions, including the temperature and time, are important factors for the conversion of ZIF-8 to ZnO.[45,46] Additionally, a crystal phase change for the upconversion host material phase by calcination has also been reported,[30] which is a limitation. To study the effect of calcination temperature, three different calcination temperatures of 400, 450, and 500 °C with a calcination duration of 5 h in air were examined in this experiment and the samples were analysed by PXRD (Figure S5). The diffraction results for calcination at 450 and 500 °C showed the growth of new peaks at 28.4, 32.9, and 47.2°, corresponding with cubic α-$NaYF_4$ crystal form and indicating a portion of the $NaYF_4$ NP crystal underwent a phase change from the hexagonal to cubic form, which may affect the photoluminescence efficiency. Even using a calcination temperature of 400 °C, the diffraction peaks for the cubic α-$NaYF_4$ crystal form are observed; however, they show considerably lower intensity. The diffraction peaks for the ZnO NPs at 31.9, 34.7, and 36.4° were observed in all three samples with slightly reduced intensity of the peaks,

relative to β-$NaYF_4$, being observed for the 400 °C calcination temperature. Based on these results, a calcination temperature of 400 °C for 5 h in air was selected for all samples.

2.3.2 Photoluminescence analysis

Photoluminescence (PL) spectroscopy was performed to evaluate the upconversion emission spectra from UCNPs when excited with NIR light. The photoactivation efficiency of the ZnO shell in the $NaYF_4$:Yb/Tm@ZnO NPs was also examined by PL spectroscopy. The solid-state PL spectra of as-synthesised $NaYF_4$:Yb/Tm, $NaYF_4$:Yb/Tm@ZIF-8, and $NaYF_4$:Yb/Tm@ZnO NPs studied at room temperature are presented in Figure 3. The proposed mechanism of NIR-driven energy transfer is shown in Figure S6. As shown in Figure 3, four emission peaks were observed, all of which are assigned to the Tm^{3+} ion. The UV emission peaks centred at 345 and 361 nm correspond to the $^1I_6 \rightarrow {}^3F_4$ and $^1D_2 \rightarrow {}^3H_6$ transitions, while the blue emission peaks at 451 and 477 nm correspond to $^1D_2 \rightarrow {}^3F_4$, and $^1G_4 \rightarrow {}^3H_6$ transitions in the Tm^{3+} ion.[19] The large absorption cross-section at 980 nm for Yb^{3+} ions correspond with a $^2F_{7/2} \rightarrow {}^2F_{5/2}$ energy transition, and this matches well with a large number of f-f transitions in Tm^{3+} ions. The energy in the long-lived $^2F_{5/2}$ state in Yb^{3+} is transferred to the Tm^{3+} ions to generate emissions in the UV and visible ranges (Figure S6).[28,50] The mechanism of energy transfer is five photon energy transfer due to the high concentration of Tm^{3+} ions, and there is likely to be a strong contribution from cross-relaxation. The addition of the ZIF-8 coating in $NaYF_4$:Yb/Tm@ZIF-8 does not significantly change the UCNP emission, aside from some small reductions in the three shortest wavelength emission bands due to absorption. In comparison, the peak ratio of UV to blue emission is significantly reduced in the $NaYF_4$:Yb/Tm@ZnO NP sample, implying that the UV is being absorbed by ZnO as this absorption is not seen in the other samples (ZnO NPs cannot absorb the photon energy in the

visible region due to its wide bandgap of 3.3 eV). This result indicates that the ZnO shell utilises the emission from the UCNP core.

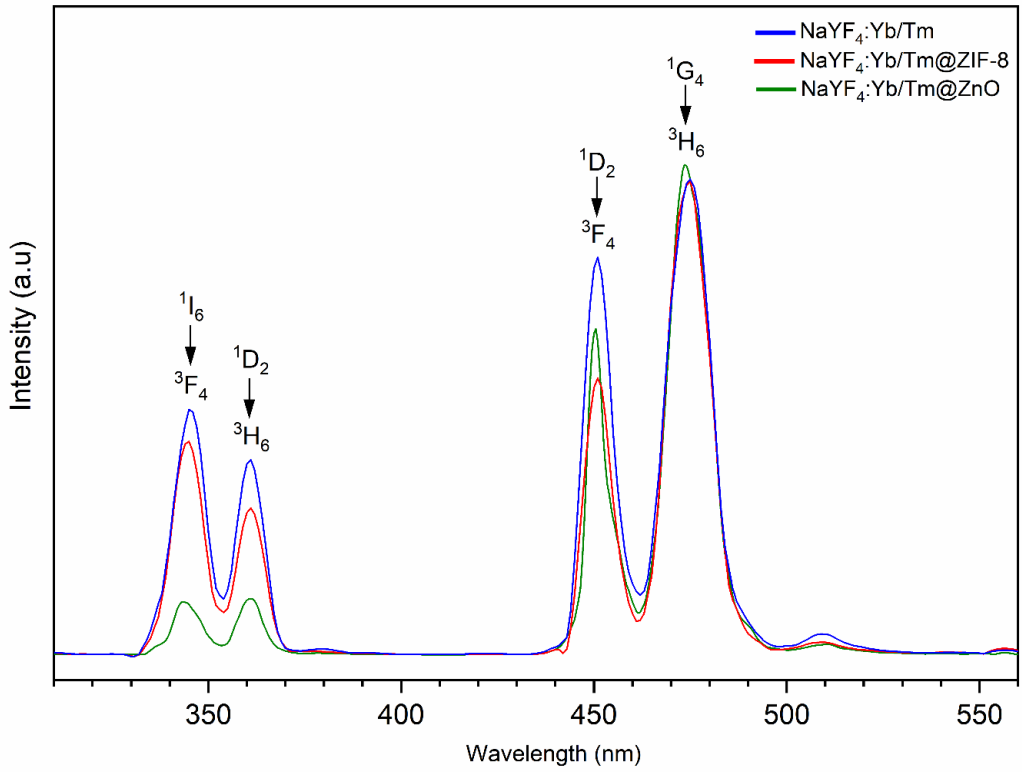

Figure 3. Photoluminescence spectra for $NaYF_4$:Yb/Tm, $NaYF_4$:Yb/Tm@ZIF-8, and $NaYF_4$:Yb/Tm@ZnO NPs.

2.3.3 Antibacterial properties

The antibacterial properties of $NaYF_4$:Yb/Tm@ZnO NPs were tested against *S. aureus* WCH-SK2-SCV and *S. aureus* WCH-SK2, with the results are presented in Figure 4. The experiments were conducted under both NIR light-illumination and dark conditions, with the summary of the antibacterial efficacy results presented in Table 1. Two LED lights with a total radiant intensity of 12 mW/cm^2 was used in this experiment. The efficacy results in NIR light-illuminated mode were found to be 0.76 and 0.67 log CFU reduction in cell viability for the *S. aureus* WCH-SK2-SCV and WCH-SK2, respectively. For the dark conditions mode, the log

CFU reduction in cell viability was found to only be 0.027 and 0.029 for the *S. aureus* WCH-SK2-SCV and *S. aureus* WCH-SK2, respectively. The results confirmed the effectiveness of the as-synthesised UCNPs@ZnO NPs against both *S. aureus* strains under NIR light-activated conditions. The non-illuminated experiment showed the as-synthesised $NaYF_4$:Yb/Tm@ZnO NPs were not toxic toward either bacteria when not illuminated by NIR light, with no significant antibacterial effects observed. The minor cell reduction observed for the dark conditions is related to the dilution and culturing of the bacteria upon completion of the efficacy test. In addition, bacteria without NPs as a control, showed no CFU reduction, demonstrating that the NIR light used in the experiment had minimal effects on eliminating the bacteria alone. All the antibacterial effects are therefore a result of the $NaYF_4$:Yb/Tm@ZnO NPs.

Ideally, antibacterial materials that eliminate all bacterial cells whilst providing no side effects, including toxicity to normal cells are typically desired. Among NP-based antibacterial materials, silver NPs have been shown to completely eradicate a bacterial population, even at very low nanoparticle concentrations.[6,51] Several studies have suggested silver ions (Ag^+) released from the dissolution of metallic silver nanoparticles to be the basis for these antimicrobial effects.[52] Such a mechanism, which lacks an activation mode, is also a drawback for silver NP which may cause a local toxicity for normal cells *in vivo*.[52-54] Furthermore, several studies have shown the antibacterial effectiveness of synthesised NPs to be lower than 100%.[13] For example, Fe-doped ZnO, Nb/N-doped ZnO, and Cu-doped TiO_2 have been reported to have antibacterial efficiencies of approximately 90%.[55-57] Other results have highlighted the value of having distinct performances for the activated and non-activated treatments. For example, cationic polysaccharide chitosan (CS) combined with chlorin e6 (Ce6) activated by NIR radiation has shown an 8.5 log reduction (>99.9999% CFU reduction) against methicillin-resistant *S. aureus* (MRSA) bacteria.

This composite material also shows a 1-2 log reduction (90-99% CFU reduction) in non-irradiated conditions.[11] In another study, Cucurbit[7]uril-anchored Porphyrin Assembly (TPP-4CB7) demonstrated 100% biocidal activity against *Bacillus subtilis* when activated by light; however, a 70% biocidal activity was observed in the dark condition.[58] In some cases, reduction of the bacterial cell population to a low level such that the immune system could take care of the remaining bacteria is an acceptable strategy for antibiotics.[59]

The combined results also allow discussion of the mechanism of action and comparison of the antibacterial efficacy of $NaYF_4$:Yb/Tm@ZnO to other photoactivated antibacterial materials. Given that UCNPs have been demonstrated to have low toxicity,[60] the observed antimicrobial activity can be attributed to the ZnO coating of the nanoparticles. The role of the core UCNPs is to excite the semiconductor ZnO coating by emitting light in the UV range (additional emission in the visible range is not absorbed by the ZnO coating).

The antimicrobial mechanisms for ZnO materials have been reported previously but remain debated.[61] The proposed antimicrobial mechanisms include Zn^{2+} metal ion release, photo-generated ROS formation (e.g. hydroxyl radicals, superoxide anions etc.), and mechanical damage of the bacterial cell due to direct interaction with NP forms. Released Zn^{2+} ions could interact with the bacterial cell membrane, enter into the bacterial cell and bind with the sulfhydryl, amino and hydroxyl functional groups of the bacteria to disrupt the cell metabolism.[62] In previous research,[27] studies of ZnO NP in dark (non-illuminated) conditions against both *Escherichia (E.) coli* and *S. aureus* were found to have negligible antibacterial activity, which suggests that Zn^{2+} ions and mechanical damage of bacterial cells may have limited contributions to the bacterial cell death. Similar results have also been shown in other studies about the role of the Zn^{2+} ion in the antibacterial activity of ZnO NPs.[63] These observations are in line with our current study that

shows under dark conditions a limited antibacterial activity of the $NaYF_4$:Yb/Tm@ZnO nanoparticles. On the other hand, formation of ROS has strong antimicrobial toxicity that is correlated with the extremely high oxidizing properties of these species. The experiments conducted here show ROS are produced under NIR illumination of $NaYF_4$:Yb/Tm@ZnO nanoparticles and only bacterial samples treated with $NaYF_4$:Yb/Tm@ZnO nanoparticles and illuminated have statistically significant log CFU reductions.

Given that ROS are the likely cause of the observed antibacterial activity, here we discuss their generation to highlight the importance of the core-shell composite used. ZnO is a wide bandgap (approximately 3.3 eV) semiconductor that only absorbs UV light (specifically photons with an energy equal to or greater than its band-gap, i.e. a $\lambda \leq 369$ nm).[64] The absorbed photons prompt an electron to be excited from the valence band (VB) to the conduction band (CB), which hence leads to the formation of free electrons (e^-) in the CB and holes (h^+) in VB. In the presence of water, the electron-hole pair simultaneously splits the water molecule into a hydroxyl radical ($^{\bullet}OH$) and a hydrogen ion (H^+). The electron-hole pair can also react with dissolved oxygen in water to form superoxide radicals ($^{\bullet}O_2^-$).[27,63,65,66] The Yb^{3+} dopant in the $NaYF_4$:Yb/Tm core of the ZnO coated UCNPs absorbs and transfers the NIR photon to the Tm^{3+} dopant within the core UCNPs. The Tm^{3+} dopant then converts the NIR radiation, via an upconversion mechanism (see Figure S6) to the shorter wavelength photons of visible and UV light. The generated UV is then absorbed by the ZnO shell to form the electron-hole pair which in turn generate ROS, as outlined above.

Porphyrin, chlorin, pheophorbide, chlorin-e6 (Ce6), and their derivatives are common PS for PDT. Cucurbit[7]uril-anchored Porphyrin Assembly (TPP-4CB7) was recently employed for phototherapy of cancer and bacterial cells.[58] In that work the authors demonstrated the antibacterial efficacy of TPP-4CB7 against *E. coli* bacteria when the PS was activated with broadband white

light (wavelengths between 400 to 700 nm). In another study, *trans*-AB-porphyrin was used as a PS in combination with gelatin; the composite was used in aPDT against Gram-positive and negative bacteria.[67] A green LED (520−560 nm) was used in this study, with a PS concentration between 4 to 8 μg/mL, which resulted in 99.999% growth inhibition. In another study, excellent antibacterial efficacy was demonstrated for the cationic polysaccharide chitosan (CS), combined with Chlorin e6 (Ce6) as a PS, for *E. coli* and *S. aureus* bacteria.[68] A 660 nm (200 mW/cm^2) light was used in this experiment to activate the PS. As can be seen from this set of studies, a significant advantage of the $NaYF_4$:Yb/Tm@ZnO nanoparticles used here over commonly used photosensitisers is that NIR light, which is not absorbed by cells and has excellent tissue penetration, can be used for activation.

Several studies have recently investigated UCNPs with organic and inorganic sensitisers for aPDT. For example, NIR activated $LiYF_4$:Yb/Er UCNPs coupled with CPZ (β-carboxyphthalocyanine zinc) as a photosensitiser and a polyvinylpyrrolidone (PVP) layer have shown excellent efficacy against Methicillin-Resistant *Staphylococcus aureus* (MRSA) and *Escherichia (E.) coli* multidrug-resistance (MDR) bacteria. The efficacy results have shown 4 to 4.5 $\log_{10}$ reduction in *E. coli* and 5 $\log_{10}$ reductions in *S. aureus*. The illumination time of 10 min using a 980 nm NIR laser (500 mW/cm^2) and NP samples with a concentration of 75 μg/ml were used in that experiment.[69] In a similar study, $LiYF_4$:Yb/Er UCNPs loaded with rose bengal (RB) as photosensitiser have shown almost 100% antibacterial efficacy against drug-resistant *Acinetobacter baumannii* (XDR-AB) using a 980 nm NIR laser (1,000 mW/cm^2) for a 10 min illumination of NP samples with a concentration of 50 μg/ml.[70] In another study, Tou et al.[38] tested $NaYF_4$:Yb,Tm@SiO_2@ZnO, $NaYF_4$:Yb,Tm@SiO_2 and ZnO NPs against *B. subtilis*. A 980 nm diode laser with a power density of 50 mW/cm^2 was used to activate NPs (5 mg of NPs in 8 ml of

bacteria, 625 μg/ml) with results demonstrating that after 45 min the majority of the bacteria population had been eradicated (although no bacteria colony counting had been performed). A minimum inhibitory concentration (MIC) of *E. coli* and *S. aureus* against these UCNPs were found to be 50 and 100 μg/ml.[38] It is worth highlighting that the LED light used in this work had a total radiant intensity of 12 mW/cm^2. This increased the treatment time to 3 h compared with other experiments listed above. However, the LED light is safer, more portable, cheaper and illuminates a bigger area compared with traditional laser systems. Despite the need to increase treatment time, an approximately 80% CFU reduction in cell viability was observed.

ROS quantification was conducted to evaluate the efficiency of the NPs in antibacterial applications and determine the antibacterial mechanism of the NP composites. Figure 4c presents data on the photogenerated ROS from $NaYF_4$:Yb/Tm@ZnO NPs. The assay was conducted in NIR light-illumination and dark conditions simultaneously for comparison. The results showed a notable amount of ROS is generated in the NIR light-illumination mode compared with the dark conditions. This result is consistent with the PL results for the $NaYF_4$:Yb/Tm@ZnO NPs shown in Figure 3.

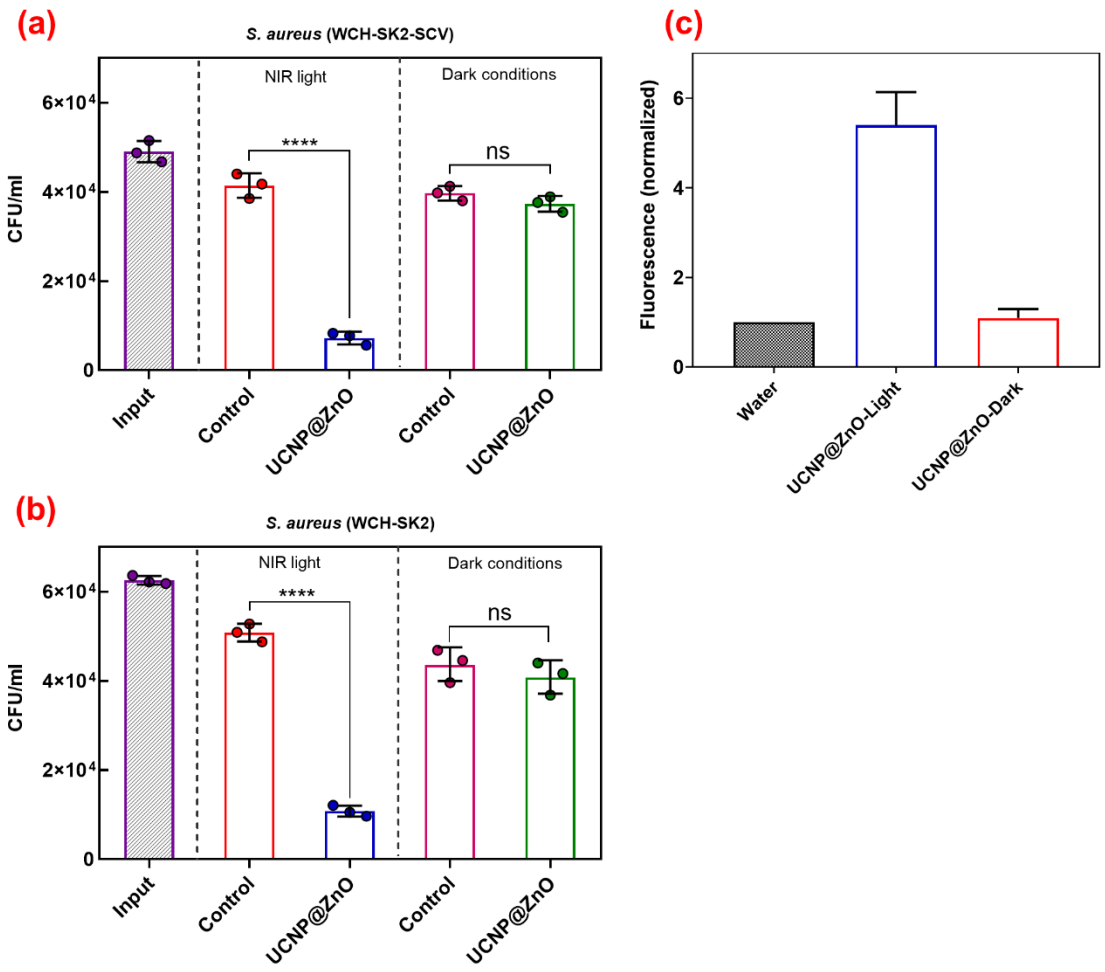

Figure 4. Antibacterial efficacy results for the $NaYF_4$:Yb/Tm@ZnO NPs against *S. aureus* WCH-SK2-SCV (a) and *S. aureus* WCH-SK2 (b) in the NIR light-activated and dark conditions modes (c) photo-generated ROS measurement for the $NaYF_4$:Yb/Tm@ZnO NPs evaluated by APF fluorescent agent.

Table 1. Summary of antibacterial efficacy results

Sample	CFU reduction ratio in NIR light-illuminated mode, %		CFU reduction ratio in dark conditions mode, %	
	SCV	*S. aureus*	SCV	*S. aureus*
NaYF4:Yb/Tm@ZnO	82.6	78.8	5.9	6.5

2.4 Conclusions

In summary, β-$NaYF_4$:Yb/Tm@ZnO nanoparticles were synthesised to target *Staphylococcus aureus* and associated small colony variant (SCV) bacteria using NIR light. Calcination at 450 °C in the air for 30 min was used to eliminate the organic impurities of OA and ODE from $NaYF_4$:Yb/Tm upconversion nanoparticles (UCNPs). A combination of PXRD and TGA was used to confirm that changes to the UCNPs structure by the calcination were negligible. Zeta potential data was used to evaluate the hydrophobicity and colloidal stability of the as-synthesised, calcined, PVP coated and CTAB coated UCNPs samples. The CTAB coating was determined to be the most suitable option, among the tested samples, to convert the hydrophobic UCNPs to the hydrophilic, water-soluble NPs required for the coating process. The water-soluble CTAB-coated UCNPs were then able to be readily coated with ZIF-8 by treatment with zinc acetate and 2-methylimidazolate, before the ZIF-8 was converted to a nanoparticle ZnO shell on the UCNPs by calcination at 400 °C for 5h. Given the potential trade-off between increased ZnO formation and UCNP structure modification, calcination conditions were also investigated across three different temperatures, showing the 400 °C calcination step was the most advantageous (limited UCNP phase change and good ZnO formation).

The desired upconversion luminescence properties were observed for each sample, with a reduction in the UV range seen in the β-$NaYF_4$:Yb/Tm@ZnO sample, showing its potential for photo-generating ROS when activated by NIR light. The NIR-activated UCNPs@ZnO nanoparticles demonstrated potent efficacy against *S. aureus* WCH-SK2-SCV and WCH-SK2 bacteria. Using a commercial APF fluorescent agent, the production of ROS from the NIR-activated NPs was confirmed and coupled with the data obtained under illuminated and dark conditions, photo-generated ROS were shown to be responsible for the observed reductions in bacterial CFUs. Given the ability to position and adhere MOF crystals on surfaces,[71] the new, ZIF-8 based synthetic methodologies used for the preparation of β-$NaYF_4$:Yb/Tm@ZnO composites could be adapted to form antibacterial surfaces activated by ambient light.

2.5 Experimental section

2.5.1 Raw materials

Oleic acid (Sigma-Aldrich, technical grade, 90%), 1-octadecene (Sigma–Aldrich, technical grade, 90%), chloroform (Chem–Supply, 99.8%), cyclohexane (Chem–Supply), methanol (Sigma-Aldrich, 100%), ethanol (Chem–Supply, 100%), yttrium (III) chloride hexahydrate (Sigma-Aldrich, 99.9%), ytterbium(III) chloride hexahydrate (Sigma–Aldrich, 99.9%), thulium (III) chloride (Sigma-Aldrich, 99.9%), sodium hydroxide (Sigma–Aldrich, 99.99%), zinc acetate dihydrate (Sigma-Aldrich, ≥98%), hexadecyltrimethylammonium bromide (Sigma-Aldrich, ≥98%), polyvinylpyrrolidone (Sigma-Aldrich), 2-methylimidazole (Sigma–Aldrich, 99%), 3′-p-(aminophenyl) fluorescein (APF) (Thermo Fisher (Invitrogen)), and ammonium fluoride (Chem–Supply, 98%) were obtained from commercial sources and used without further purification.

2.5.2 Synthesis of NaYF4:Yb/Tm@ZnO nanoparticles

The $NaYF_4$:Yb/Tm@ZnO NPs were synthesised in 4 steps, involving $NaYF_4$:Yb/Tm UCNP synthesis and purification; cationic ligand CTAB coated UCNPs synthesis; ZIF-8 coating of the UCNPs; and finally, conversion of ZIF-8 to ZnO by calcination.

Step (a) – NaYF4:Yb/Tm UCNPs: $NaYF_4$:Yb/Tm UCNPs were synthesised via a thermal decomposition method.[32] In a typical synthesis for $NaYF_4$:Yb/Tm NPs (18% Yb and 5% Tm), $YCl_3 \cdot 6H_2O$ (242.7 mg, 0.8 mmol), $YbCl_3 \cdot 6H_2O$ (69.8 mg, 0.18 mmol) and $TmCl_3$ (13.8 mg, 0.05 mmol) were mixed with oleic acid (OA, 6 mL) and 1-octadecene (ODE, 15 mL) in a 150 mL 3-neck round bottom flask. The suspension was heated to approximately 150 °C to form a homogeneous solution before being cooled to room temperature. A solution of NaOH (100 mg, 2.5 mmol) and NH_4F (148.1 mg, 4 mmol) in methanol (10 mL) was added to the reaction mixture and stirred at room temperature for 20 min. The solution was heated to approximately 70 °C to evaporate the methanol from the solution, increased gradually to 110 °C and maintained for approximately 10 min while argon gas flow was used to degas the solution, and finally heated to approximately 300 °C and maintained for 1 h under argon gas flow. The solution was then cooled to room temperature and the NPs were precipitated from the solution by the addition of ethanol (20 mL). The precipitated NPs were then collected by centrifugation (10,000 rpm for 5 min, Eppendorf 5920 R, Fa-6x50), washed with cyclohexane and ethanol several times, and finally dried at 70 °C overnight.

The UCNPs contain impurities of OA and ODE (organic impurities) and NaCl (reaction by-product) that need to be removed. Impure UCNPs were calcined in air at 450 °C for 30 min with a heating rate of 10 °C/min to eliminate the organic impurities, followed by washing several times with Milli-Q water to remove NaCl by-products, before being dried at 70 °C.

Step (b) – CTAB coating of the UCNPs: CTAB (300 mg, 0.82 mmol) was dissolved in Milli-Q water (10 mL) and then a suspension of UCNPs (45 mg), dispersed in chloroform (10 mL), was added and the combined biphasic solution stirred for 2 h. The mixture was then heated to 60 °C to evaporate the chloroform and produce a clear solution of CTAB coated UCNPs.

Step (c): Formation of NaYF4:Yb/Tm@ZIF-8: Zinc acetate dihydrate ($Zn(OAc)_2$, 219.5 mg, 1 mmol) was dissolved in the CTAB coated UCNP solution. 2-methylimidazole (HmIM, 266.8 mg, 3.25 mmol) was dissolved in ethanol (10 mL) and added to the previous solution, and stirred at 250 rpm overnight. The product was precipitated from the solution by addition of methanol (5 mL), collected by centrifugation (9,000 rpm for 10 min), washed with Milli-Q water and ethanol several times, and dried at 70 °C overnight.

Step (d) – Formation of NaYF4:Yb/Tm@ZnO: $NaYF_4$:Yb/Tm@ZnO NPs were synthesised by calcination in air at 400 °C for 5 h with a heating rate of 10 °C/ min.

Alternative PVP Coating of the UCNPs: The PVP coated UCNPs were also synthesised to compare against CTAB coated UCNPs. PVP (35 mg, MW = 24,000) was dissolved in ethanol (35 mL) then UCNPs (45 mg) were added and stirred overnight. The product was then obtained by centrifugation (9,000 rpm, 10 min) and washing with ethanol several times.

2.5.3 Characterisation of as-prepared NPs

Powder X-ray diffraction (PXRD) data collected on a MiniFlex 600 (Rigaku, Cu Kα, λ = 0.15418 nm) was used to confirm the structure of the synthesised NPs. Samples were mounted in a flat plate holder and the data was collected with the instrument operating at 40 kV and 15 mA by scanning 2θ from 10° to 70° with a step size of 0.02°. JCPDS cards # 16-0334 (hexagonal

β-$NaYF_4$), 06-0342 (cubic α-$NaYF_4$), 79-0208 (ZnO), and simulated PXRD pattern of ZIF-8 (from the cif) were used for comparison to the experimental data.

The particle size and morphology of the NPs were investigated by scanning electron microscopy (SEM) on a Quanta 450, and transmission electron microscopy (TEM) on an FEI Tecnai G2 Spirit TEM and high-resolution TEM (HRTEM) on an FEI Titan Themis 80-200 G TEM operated at an accelerating voltage of 120 and 200 kV, respectively. The NP samples were coated with platinum (3 nm) before SEM measurements. Samples for TEM were dispersed in absolute ethanol using a vortex shaker, a small droplet of each suspension was transferred to the TEM sample holder and the ethanol evaporated before placing into the TEM.

X-ray photoelectron spectroscopy (XPS) was employed to investigate the surface chemistry of the NPs using ESCALAB250Xi (Thermo Scientific, UK). Al Kα radiation (photon energy, hν = 1,486.68 eV) was used as the excitation source and high-resolution (HR) scans with a pass energy of 100 eV were measured. The spectrometer calibration was performed using binding energy levels of Cu $2p_3$ (932.62 eV), Ag $3d_5$ (368.21 eV), and Au $4f_7$ (83.96 eV).

Thermal gravimetric analysis (TGA) was conducted with a heating rate of 10 °C/min in a thermal analysis instrument (Mettler Toledo TGA/DSC2).

The zeta potentials of the synthesised NPs in aqueous suspensions (Milli-Q water) were evaluated by dynamic light scattering (DLS, Zetasizer Nano, Malvern Instruments Ltd., UK). A He-Ne laser with wavelength λ = 633 nm was used as the light source. The intensity of light was scattered at an angle of 173°.

Photoluminescence measurements were carried out under 980 nm excitation. The samples were excited by pulses with a 5 ns duration and 20 Hz repetition rate from an Optical Parametric

Oscillator (OPO) (Opotek LLC model "Opolette 355"). An 840 nm long-pass filter was placed before the sample to block visible wavelengths present in the OPO beam, and a silica lens was used to focus the spot size of the laser to approximately 2 mm. The emission was collected using a spectrofluorometer (Edinburgh Instruments F980) with an air-cooled photomultiplier (Hamamatsu R928) for detection. The sample emission was passed through a focusing lens into a monochromator (TMS302-M) and then the photomultiplier detector. An illustration of the experimental configuration of the Edinburgh instruments spectrofluorometer is presented in Figure S1.

2.5.4 Antibacterial assays

The *S. aureus* WCH-SK2-SCV along with parental *S. aureus* WCH-SK2 were used in the antibacterial efficacy studies.[72] The antibacterial efficacy of UCNPs@ZnO NPs was evaluated in both NIR light-illuminated and dark conditions. The NIR light source was used to activate the UCNPs, while the dark conditions were used as a control to compare the bacterial reduction due to the NIR light source. A bacterial assay without any NPs was also used as the control in both NIR light-illuminated and dark conditions.

The antibacterial properties of the NPs were assessed against *S. aureus* WCH-SK2 and the associated WCH-SK2-SCV in Luria-Bertani (LB) media. The cells were grown to the mid-logarithmic phase and then diluted by PBS solution to approximately 10^5 colony-forming units per mL (CFU/mL). Sterilised glass vials with a volume of 4 mL were used in the experiment due to their transparency to NIR light. Two LED NIR light sources (LED970-66-60) with a peak wavelength at 970 nm (960-980 nm) and a combined radiant intensity of 12 mW/cm^2 were used for the NIR activated mode. The LED NIR light sources were located at a distance of about 5 cm from the bacterial growth samples inside the shaker incubator. The experiment under dark

conditions was conducted by placing the glass vials inside a 50 mL black colour centrifuge tube. The NIR light-illuminated and dark mode experiments were performed simultaneously in two separate incubator shakers (to prevent NP sedimentation) at 37 °C for 3 h. A $NaYF_4$:Yb/Tm@ZnO NP sample with a concentration of 100 mg/mL was prepared using phosphate-buffered saline (PBS) for the antimicrobial assay. Each assay included 850 µL of normalised bacteria and 150 µL of NP sample. After completion of the experiment, the assay samples were spread on LB agar (1.5%) plates for bacterial counting and evaluation. The experiments were repeated at least three times. The one-way ANOVA was performed using GraphPad Prism V9.0.0, with a statistical significance indicated by ns for $P>0.05$; * for $P<0.05$; ** for $P<0.01$; *** for $P<0.001$; and **** for $P<0.0001$, respectively.

Aminophenyl fluorescein (APF, A36003) was used to determine the amount of ROS (hydroxyl radical (•OH)) generated by the NIR light-activated UCNPs. The APF agent exhibits green fluorescence upon chemical reactions with the hydroxyl radicals, peroxynitrite anion or the hypochlorite anion. Briefly, $NaYF_4$:Yb/Tm@ZnO NPs (100 mg) were dispersed in Milli-Q water (1 mL) inside a 4 mL glass vial. Then APF (5 µL, 5 µM) was added to the vial, vortexed, and placed into a shaker incubator to illuminate with the NIR light for 3 h. Upon completion of the experiment, the sample was centrifuged, then 100 µL of the supernatant was added to a black 96 well fluorescence microplate. Milli-Q water without any NPs was used as a control. The Fluorescence microplate reader (PHERAstar FS) was used to measure the fluorescence intensity of the APF agent at 520 nm (485 nm excitation). The experiment was repeated in dark conditions.

2.6 Supporting Information

Illustration of the experimental configuration for the Edinburgh instruments spectrofluorimeter; XPS spectra (survey and binding energies) for the $NaYF_4$:Yb/Tm core; PXRD data showing

removal of the organic impurities from $NaYF_4$:Yb/Tm: before and after calcination; TGA curves for $NaYF_4$:Yb/Tm UCNPs: before and after calcination; zeta potential and associated pH measurements for the impure, calcined, PVP coated and CTAB coated $NaYF_4$:Yb/Tm NP samples; PXRD data for the different calcination temperatures (400, 450 and 500 °C); proposed energy transfer mechanism from Yb^{3+} to Tm^{3+}; SEM elemental analysis for $NaYF_4$:Yb/Tm, $NaYF_4$:Yb/Tm@ZIF-8 NPs and $NaYF_4$:Yb/Tm@ZnO NPs.

2.7 Acknowledgements

The support from the Australian Government Research Training Program Scholarship, Alice Chu postgraduate scholarship in Chemical Engineering and The University of Adelaide is acknowledged. The authors acknowledge the instruments and scientific and technical assistance of Microscopy Australia at Adelaide Microscopy, The University of Adelaide, a facility that is funded by the university, and state and federal governments.

2.8 Supporting information

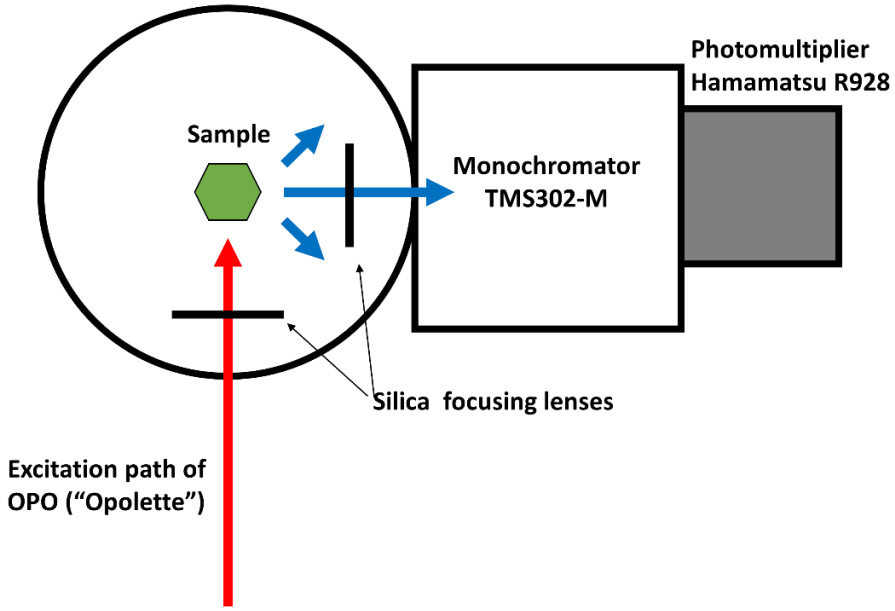

Figure S1. Illustration of the Edinburgh instruments spectrofluorimeter experimental configuration.

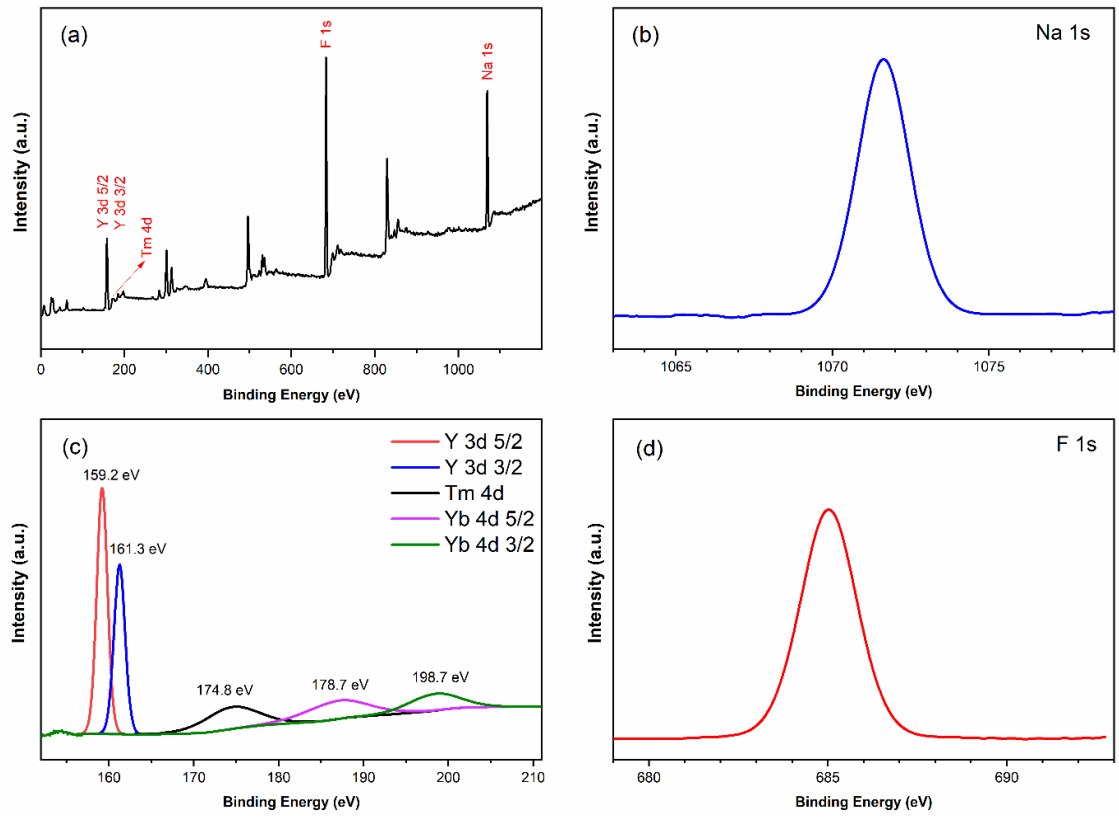

Figure S2. XPS spectra. $NaYF_4$:Yb/Tm survey (a), binding energy spectra for Na_{1s} (b), binding energy spectra for Y_{3d}, Yb_{4d} and Tm_{4d} (c), binding energy spectra for F_{1s} (d).

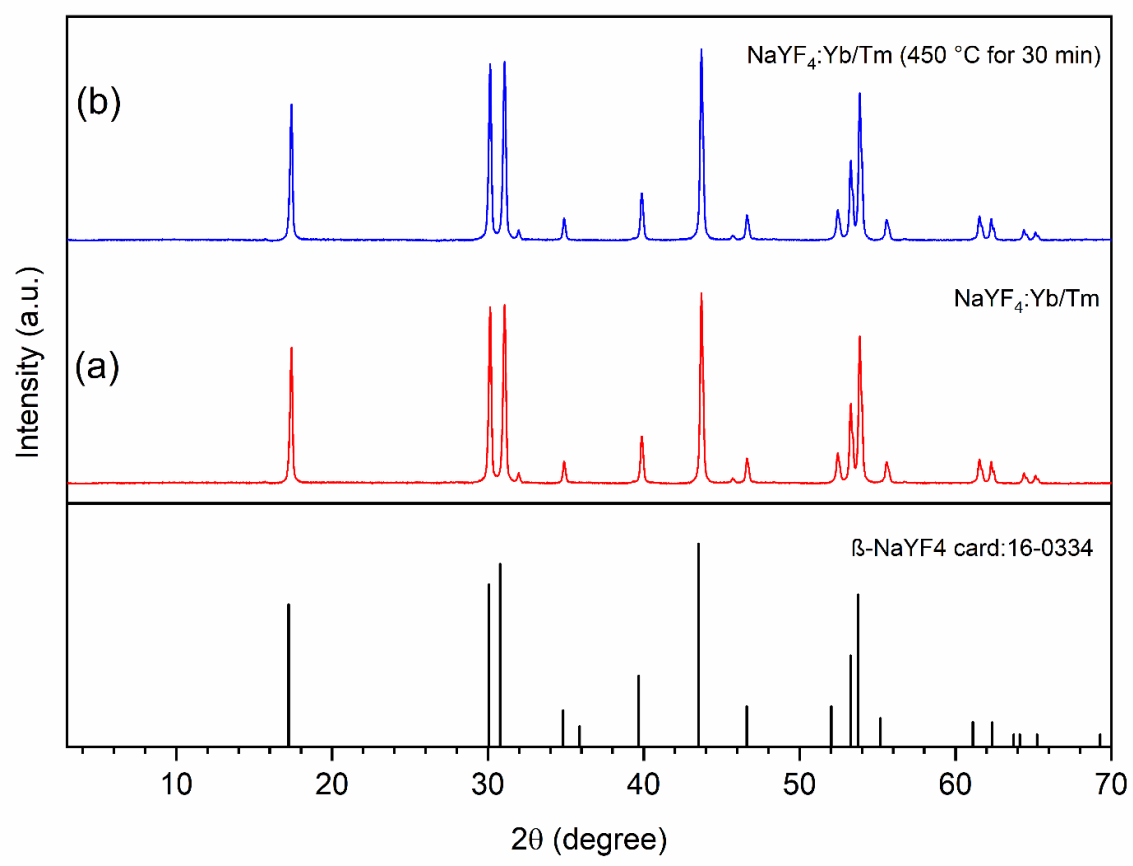

Figure S3. PXRD for removing organic impurities from $NaYF_4$:Yb/Tm (a) before calcination, (b) calcined 450 °C for 30 min.

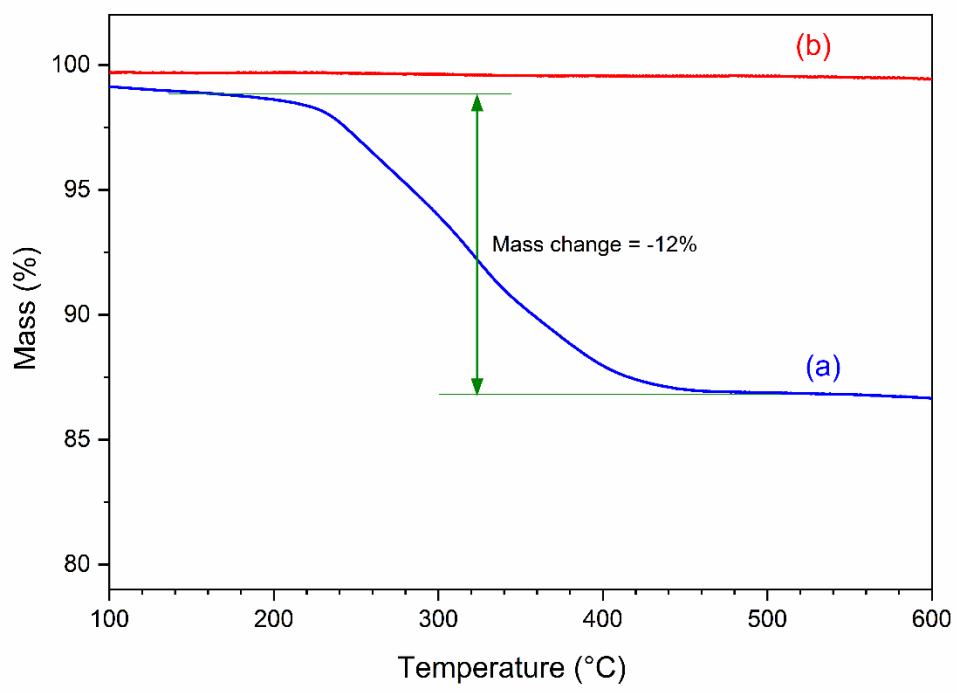

Figure S4. TGA curves for $NaYF_4$:Yb/Tm UCNPs (a) before calcination (b) after calcination at 450 °C for 30 min. Approximately, 12% mass reduction in the impure UCNPs is confirmed.

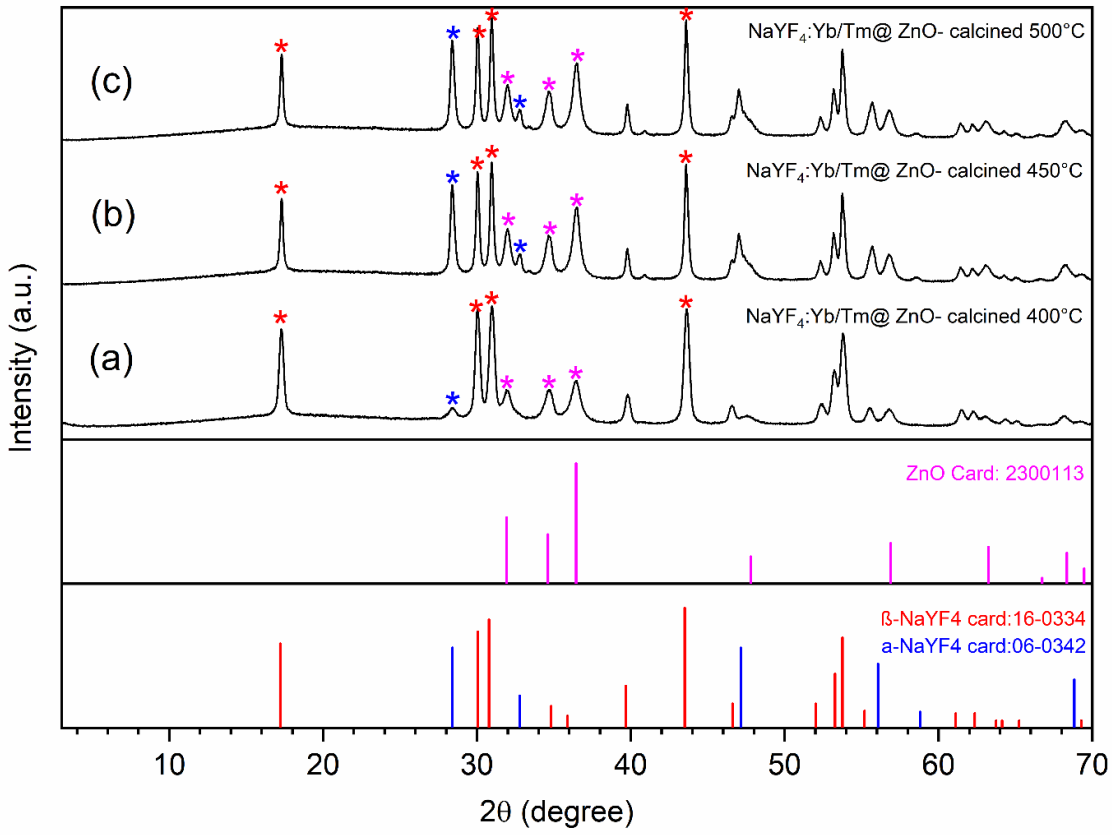

Figure S5. PXRD for different calcination temperature (a) 400 °C, (b) 450 °C and (c) 500 °C. The calcination time was 5 h in the air for all cases.

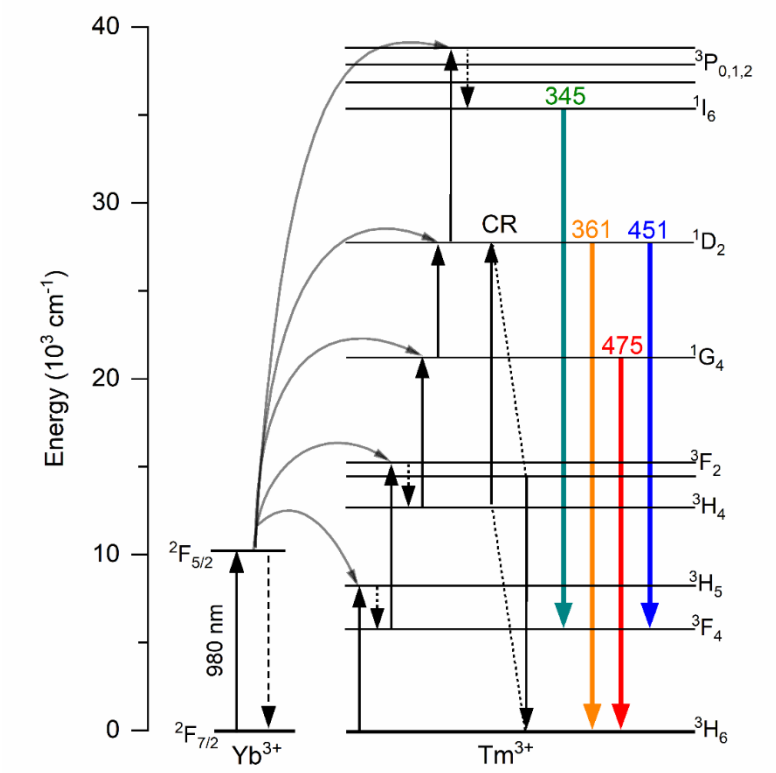

Figure S6. Proposed energy transfer mechanism from Yb^{3+} to Tm^{3+}.

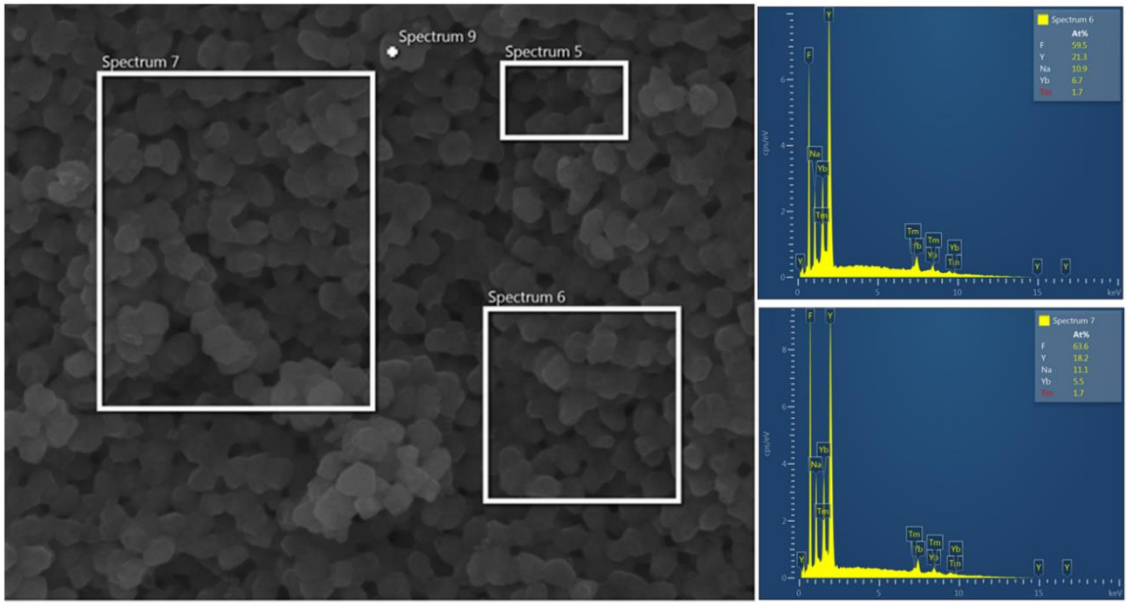

Figure S7. SEM elemental analysis for $NaYF_4$:Yb/Tm NPs.

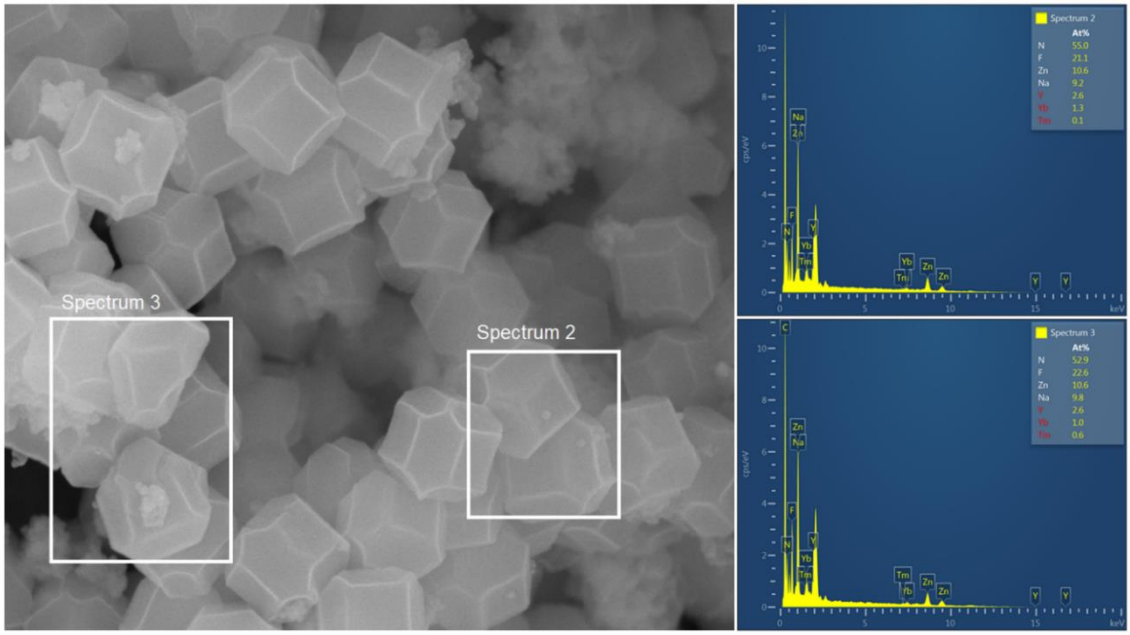

Figure S8. SEM elemental analysis for $NaYF_4$:Yb/Tm@ZIF-8 NPs.

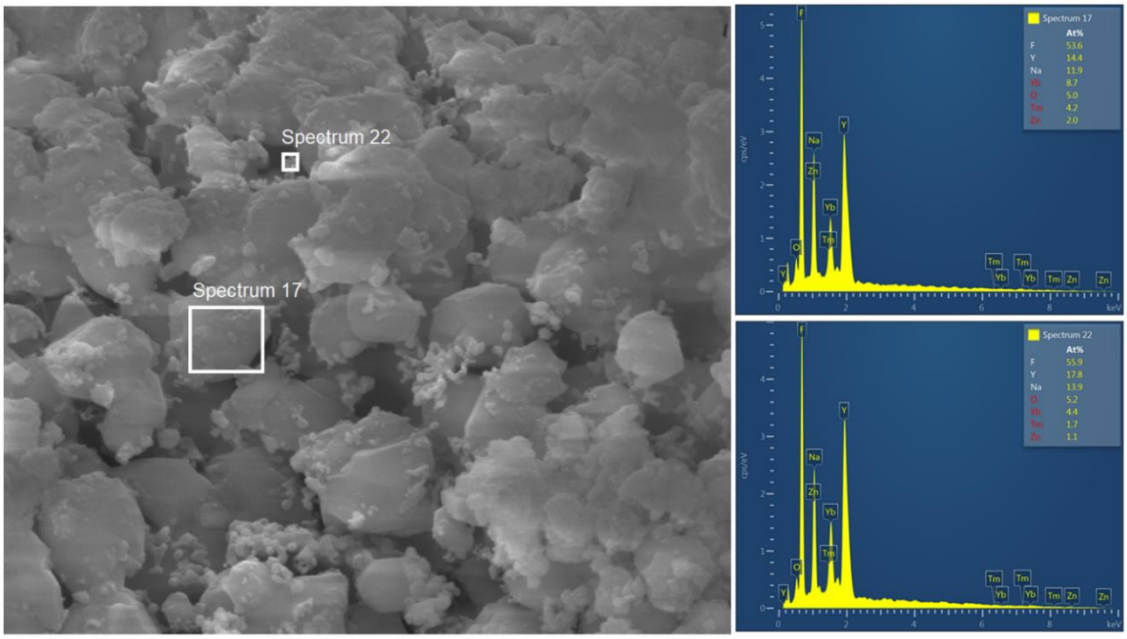

Figure S9. SEM elemental analysis for $NaYF_4$:Yb/Tm@ZnO NPs.

Table S1. The zeta potential and associated pH measurement for the impure, calcined, PVP coated and CTAB coated $NaYF_4$:Yb/Tm NP samples.

Sample	Zeta potential (mV)	pH
Impure $NaYF_4$:Yb/Tm	14.9	4.50
Calcined $NaYF_4$:Yb/Tm	15.6	6.25
PVP coated $NaYF_4$:Yb/Tm	21.9	4.39
CTAB coated $NaYF_4$:Yb/Tm	54.5	6.18

2.9 References

(1) von Eiff, C.; Peters, G.; Becker, K. The small colony variant (SCV) concept - the role of staphylococcal SCVs in persistent infections. *Injury* **2006**, *37* (2), S26-S33. DOI: 10.1016/j.injury.2006.04.006.

(2) Proctor, R. A.; Vanlangevelde, P.; Kristjansson, M.; Maslow, J. N.; Arbeit, R. D. Persistent and relapsing infections associated with Small-Colony variants of *staphylococcus aureus*. *Clin. Infect. Dis.* **1995**, *20* (1), 95-102. DOI: 10.1093/clinids/20.1.95.

(3) Lee, J.; Zilm, P. S.; Kidd, S. P. Novel Research Models for Staphylococcus aureus Small Colony Variants (SCV) Development: Co-pathogenesis and Growth Rate. *Front. Microbiol.* **2020**, *11*, 321-321. DOI: 10.3389/fmicb.2020.00321.

(4) Bui, L. M.; Conlon, B. P.; Kidd, S. P. Antibiotic tolerance and the alternative lifestyles of Staphylococcus aureus. *Essays Biochem.* **2017**, *61* (1), 71-79. DOI: 10.1042/ebc20160061 From NLM.

(5) Rajchakit, U.; Sarojini, V. Recent developments in antimicrobial-peptide-conjugated gold nanoparticles. *Bioconjugate Chemistry* **2017**, *28* (11), 2673-2686. DOI: 10.1021/acs.bioconjchem.7b00368.

(6) Wang, L.; Hu, C.; Shao, L. The antimicrobial activity of nanoparticles: present situation and prospects for the future. *International journal of nanomedicine* **2017**, *12*, 1227-1249. DOI: 10.2147/IJN.S121956.

(7) Huh, A. J.; Kwon, Y. J. "Nanoantibiotics": A new paradigm for treating infectious diseases using nanomaterials in the antibiotics resistant era. *Journal of Controlled Release* **2011**, *156* (2), 128-145. DOI: 10.1016/j.jconrel.2011.07.002.

(8) Luong, T.; Salabarria, A.-C.; Roach, D. R. Phage therapy in the resistance era: where do we stand and where are we going? *Clin. Ther.* **2020**, *42* (9), 1659-1680. DOI: 10.1016/j.clinthera.2020.07.014.

(9) Milho, C.; Andrade, M.; Vilas Boas, D.; Alves, D.; Sillankorva, S. Antimicrobial assessment of phage therapy using a porcine model of biofilm infection. *Int. J. Pharm.* **2019**, *557*, 112-123. DOI: 10.1016/j.ijpharm.2018.12.004.

(10) Rocca, D. M.; Silvero C, M. J.; Aiassa, V.; Cecilia Becerra, M. Rapid and effective photodynamic treatment of biofilm infections using low doses of amoxicillin-coated gold nanoparticles. *Photodiagnosis Photodyn. Ther.* **2020**, *31*, 101811. DOI: 10.1016/j.pdpdt.2020.101811.

(11) Zhang, R.; Li, Y.; Zhou, M.; Wang, C.; Feng, P.; Miao, W.; Huang, H. Photodynamic Chitosan Nano-Assembly as a Potent Alternative Candidate for Combating Antibiotic-Resistant Bacteria. *Acs Applied Materials & Interfaces* **2019**, *11* (30), 26711-26721. DOI: 10.1021/acsami.9b09020.

(12) Cieplik, F.; Deng, D.; Crielaard, W.; Buchalla, W.; Hellwig, E.; Al-Ahmad, A.; Maisch, T. Antimicrobial photodynamic therapy – what we know and what we don't. *Crit. Rev. Microbiol.* **2018**, *44* (5), 571-589. DOI: 10.1080/1040841X.2018.1467876.

(13) Zhou, Z.; Li, B.; Liu, X.; Li, Z.; et al. Recent Progress in Photocatalytic Antibacterial. *ACS Applied Bio Materials* **2021**. DOI: 10.1021/acsabm.0c01335.

(14) Garcez, A. S.; Kaplan, M.; Jensen, G. J.; Scheidt, F. R.; Oliveira, E. M.; Suzuki, S. S. Effects of antimicrobial photodynamic therapy on antibiotic-resistant Escherichia coli. *Photodiagnosis Photodyn. Ther*. **2020**, *32*, 102029. DOI: 10.1016/j.pdpdt.2020.102029.

(15) Agostinis, P.; Berg, K.; Cengel, K. A.; Foster, T. H.; et al. Photodynamic therapy of cancer: an update. *CA Cancer J. Clin.* **2011**, *61* (4), 250-281. DOI: 10.3322/caac.20114.

(16) Hamblin, M. R. Antimicrobial photodynamic inactivation: a bright new technique to kill resistant microbes. *Curr. Opin. Microbiol.* **2016**, *33*, 67-73. DOI: 10.1016/j.mib.2016.06.008.

(17) Han, Q.; Lau, J. W.; Do, T. C.; Zhang, Z.; Xing, B. Near-Infrared Light Brightens Bacterial Disinfection: Recent Progress and Perspectives. *ACS Applied Bio Materials* **2020**. DOI: 10.1021/acsabm.0c01341.

(18) Bekmukhametova, A.; Ruprai, H.; Hook, J. M.; Mawad, D.; Houang, J.; Lauto, A. Photodynamic therapy with nanoparticles to combat microbial infection and resistance. *Nanoscale* **2020**, *12* (41), 21034-21059. DOI: 10.1039/D0NR04540C.

(19) Qiu, Z.; Shu, J.; Tang, D. Near-Infrared-to-Ultraviolet Light-Mediated Photoelectrochemical Aptasensing Platform for Cancer Biomarker Based on Core–Shell NaYF4:Yb,Tm@TiO2 Upconversion Microrods. *Anal. Chem.* **2018**, *90* (1), 1021-1028. DOI: 10.1021/acs.analchem.7b04479.

(20) Dou, Q. Q.; Rengaramchandran, A.; Selvan, S. T.; Paulmurugan, R.; Zhang, Y. Core-shell upconversion nanoparticle semiconductor heterostructures for photodynamic therapy. *Sci. Rep.* **2015**, *5* (1), 1-8. DOI: 10.1038/srep08252.

(21) Wu, X.; Zhang, Y.; Wang, Z.; Wu, J.; Yan, R.; Guo, C.; Jin, Y. Near-Infrared Light-Initiated Upconversion Nanoplatform with Tumor Microenvironment Responsiveness for Improved Photodynamic Therapy. *ACS Applied Bio Materials* **2020**, *3* (9), 5813-5823. DOI: 10.1021/acsabm.0c00545.

(22) Zhao, K.; Sun, J.; Wang, F.; Song, A.; Liu, K.; Zhang, H. Lanthanide-Based Photothermal Materials: Fabrication and Biomedical Applications. *ACS Applied Bio Materials* **2020**, *3* (7), 3975-3986. DOI: 10.1021/acsabm.0c00618.

(23) Maji, S. K.; Kim, D. H. AgInS2-Coated Upconversion Nanoparticle as a Photocatalyst for Near-Infrared Light-Activated Photodynamic Therapy of Cancer Cells. *ACS Applied Bio Materials* **2018**, *1* (5), 1628-1638. DOI: 10.1021/acsabm.8b00467.

(24) Zhao, J.; Hu, Y.; Lin, S. w.; Resch-Genger, U.; et al. Enhanced luminescence intensity of near-infrared-sensitized upconversion nanoparticles via Ca^{2+} doping for a nitric oxide release platform. *Journal of Materials Chemistry B* **2020**, *8* (30), 6481-6489. DOI: 10.1039/D0TB00088D.

(25) Chen, G.; Ågren, H.; Ohulchanskyy, T. Y.; Prasad, P. N. Light upconverting core-shell nanostructures: nanophotonic control for emerging applications. *Chem. Soc. Rev.* **2015**, *44* (6), 1680-1713. DOI: 10.1039/C4CS00170B.

(26) Carofiglio, M.; Barui, S.; Cauda, V.; Laurenti, M. Doped zinc oxide nanoparticles: synthesis, characterization and potential use in nanomedicine. *Applied Sciences* **2020**, *10* (15), 5194, Review. DOI: 10.3390/app10155194.

(27) Karami, A.; Xie, Z.; Zhang, J.; Kabir, M. S.; Munroe, P.; Kidd, S.; Zhang, H. Insights into the antimicrobial mechanism of Ag and I incorporated ZnO nanoparticle derivatives under visible light. *Materials Science and Engineering: C* **2020**, *107*, 110220. DOI: 10.1016/j.msec.2019.110220.

(28) Chen, C.; Li, C.; Shi, Z. Current advances in lanthanide-doped upconversion nanostructures for detection and bioapplication. *Advanced Science* **2016**, *3* (10), 1600029. DOI: 10.1002/advs.201600029.

(29) Zheng, K.; Loh, K. Y.; Wang, Y.; Chen, Q.; et al. Recent advances in upconversion nanocrystals: Expanding the kaleidoscopic toolbox for emerging applications. *Nano Today* **2019**, *29*, 100797. DOI: 10.1016/j.nantod.2019.100797.

(30) Wang, L.; Li, X.; Li, Z.; Chu, W.; et al. A new cubic phase for a $NaYF_4$ host matrix offering high upconversion luminescence efficiency. *Adv. Mater.* **2015**, *27* (37), 5528-5533. DOI: 10.1002/adma.201502748.

(31) Zhu, X.; Su, Q.; Feng, W.; Li, F. Anti-Stokes shift luminescent materials for bio-applications. *Chem. Soc. Rev.* **2017**, *46* (4), 1025-1039. DOI: 10.1039/c6cs00415f.

(32) Guo, X.; Song, W.; Chen, C.; Di, W.; Qin, W. Near-infrared photocatalysis of b-$NaYF_4$:Yb^{3+},Tm^{3+}@ZnO composites. *Physical Chemistry Chemical Physics* **2013**, *15* (35), 14681-14688. DOI: 10.1039/c3cp52248b.

(33) Chen, X.; Peng, D.; Ju, Q.; Wang, F. Photon upconversion in core-shell nanoparticles. *Chem. Soc. Rev.* **2015**, *44* (6), 1318-1330. DOI: 10.1039/c4cs00151f.

(34) Roth, H.-C.; Schwaminger, S.; Fraga García, P.; Ritscher, J.; Berensmeier, S. Oleate coating of iron oxide nanoparticles in aqueous systems: the role of temperature and surfactant concentration. *J. Nanopart. Res.* **2016**, *18* (4), 99. DOI: 10.1007/s11051-016-3405-2.

(35) Kharisov, B. I.; Dias, H. V. R.; Kharissova, O. V.; Vázquez, A.; Peña, Y.; Gómez, I. Solubilization, dispersion and stabilization of magnetic nanoparticles in water and non-aqueous solvents: recent trends. *RSC Advances* **2014**, *4* (85), 45354-45381, 10.1039/C4RA06902A. DOI: 10.1039/C4RA06902A.

(36) Lai, C. W.; Low, F. W.; Tai, M. F.; Abdul Hamid, S. B. Iron oxide nanoparticles decorated oleic acid for high colloidal stability. *Adv. Polym. Tech.* **2018**, *37* (6), 1712-1721. DOI: doi.org/10.1002/adv.21829.

(37) Zhang, L.; He, R.; Gu, H.-C. Oleic acid coating on the monodisperse magnetite nanoparticles. *Appl. Surf. Sci.* **2006**, *253* (5), 2611-2617. DOI: 10.1016/j.apsusc.2006.05.023.

(38) Tou, M.; Luo, Z.; Bai, S.; Liu, F.; Chai, Q.; Li, S.; Li, Z. Sequential coating upconversion $NaYF_4$:Yb,Tm nanocrystals with SiO_2 and ZnO layers for NIR-driven photocatalytic and antibacterial applications. *Materials Science and Engineering: C* **2017**, *70*, 1141-1148. DOI: 10.1016/j.msec.2016.03.038.

(39) Wu, S.; Lv, J.; Wang, F.; Duan, N.; Li, Q.; Wang, Z. Photocatalytic degradation of microcystin-LR with a nanostructured photocatalyst based on upconversion nanoparticles@TiO_2 composite under simulated solar lights. *Sci. Rep.* **2017**, *7* (1), 14435-14435. DOI: 10.1038/s41598-017-14746-6.

(40) Wang, F.; Liu, X. Recent advances in the chemistry of lanthanide-doped upconversion nanocrystals. *Chem. Soc. Rev.* **2009**, *38* (4), 976-989. DOI: 10.1039/B809132N.

(41) Joseph, E.; Singhvi, G. Chapter 4 - Multifunctional nanocrystals for cancer therapy: a potential nanocarrier. In *Nanomaterials for Drug Delivery and Therapy*, Grumezescu, A. M. Ed.; William Andrew Publishing, 2019; pp 91-116.

(42) Kovacevic, A.; Savic, S.; Vuleta, G.; Müller, R. H.; Keck, C. M. Polyhydroxy surfactants for the formulation of lipid nanoparticles (SLN and NLC): Effects on size, physical stability and particle matrix structure. *Int. J. Pharm.* **2011**, *406* (1), 163-172. DOI: 10.1016/j.ijpharm.2010.12.036.

(43) Uskoković, V. Dynamic Light Scattering Based Microelectrophoresis: Main Prospects and Limitations. *J. Dispersion Sci. Technol.* **2012**, *33* (12), 1762-1786. DOI: 10.1080/01932691.2011.625523.

(44) Liang, W.; Ricco, R.; Maddigan, N. K.; Dickinson, R. P.; et al. Control of Structure Topology and Spatial Distribution of Biomacromolecules in Protein@ZIF-8 Biocomposites. *Chem. Mater.* **2018**, *30* (3), 1069-1077. DOI: 10.1021/acs.chemmater.7b04977.

(45) Pan, L.; Muhammad, T.; Ma, L.; Huang, Z.-F.; et al. MOF-derived C-doped ZnO prepared via a two-step calcination for efficient photocatalysis. *Applied Catalysis B: Environmental* **2016**, *189*, 181-191. DOI: 10.1016/j.apcatb.2016.02.066.

(46) Du, Y.; Chen, R. Z.; Yao, J. F.; Wang, H. T. Facile fabrication of porous ZnO by thermal treatment of zeolitic imidazolate framework-8 and its photocatalytic activity. *J. Alloys Compd.* **2013**, *551*, 125-130. DOI: 10.1016/j.jallcom.2012.10.045.

(47) Lv, S.; Zhang, K.; Zhu, L.; Tang, D. ZIF-8-Assisted NaYF4:Yb,Tm@ZnO Converter with Exonuclease III-Powered DNA Walker for Near-Infrared Light Responsive Biosensor. *Anal. Chem.* **2020**, *92* (1), 1470-1476. DOI: 10.1021/acs.analchem.9b04710.

(48) Wei, R.; Chi, H.-Y.; Li, X.; Lu, D.; Wan, Y.; Yang, C.-W.; Lai, Z. Aqueously Cathodic Deposition of ZIF-8 Membranes for Superior Propylene/Propane Separation. *Adv. Funct. Mater.* **2020**, *30* (7), 1907089. DOI: 10.1002/adfm.201907089.

(49) Saha, J. K.; Bukke, R. N.; Mude, N. N.; Jang, J. Significant improvement of spray pyrolyzed ZnO thin film by precursor optimization for high mobility thin film transistors. *Sci. Rep.* **2020**, *10* (1), 8999. DOI: 10.1038/s41598-020-65938-6.

(50) Xu, Z.; Quintanilla, M.; Vetrone, F.; Govorov, A. O.; Chaker, M.; Ma, D. Harvesting Lost Photons: Plasmon and Upconversion Enhanced Broadband Photocatalytic Activity in Core@Shell Microspheres Based on Lanthanide-Doped $NaYF_4$, TiO_2, and Au. *Adv. Funct. Mater.* **2015**, *25* (20), 2950-2960. DOI: 10.1002/adfm.201500810.

(51) Makvandi, P.; Wang, C.-y.; Zare, E. N.; Borzacchiello, A.; Niu, L.-n.; Tay, F. R. Metal-Based Nanomaterials in Biomedical Applications: Antimicrobial Activity and Cytotoxicity Aspects. *Adv. Funct. Mater.* **2020**, *30* (22), 1910021. DOI: 10.1002/adfm.201910021.

(52) Karami, A.; Zhang, H.; Pederick, V. G.; McDevitt, C. A.; et al. Cr–Ag coatings: synthesis, microstructure and antimicrobial properties. *Surf. Eng.* **2018**, *35* (7), 596-603. DOI: 10.1080/02670844.2018.1537082.

(53) Ferdous, Z.; Nemmar, A. Health Impact of Silver Nanoparticles: A Review of the Biodistribution and Toxicity Following Various Routes of Exposure. *Int. J. Mol. Sci.* **2020**, *21* (7), 2375. DOI: 10.3390/ijms21072375 PubMed.

(54) Campoccia, D.; Montanaro, L.; Arciola, C. R. A review of the biomaterials technologies for infection-resistant surfaces. *Biomaterials* **2013**, *34* (34), 8533-8554.

(55) Habeeb Rahman, A. P.; Misra, A. J.; Das, S.; Das, B.; et al. Mechanistic insight into the disinfection of Salmonella sp. by sun-light assisted sonophotocatalysis using doped ZnO nanoparticles. *Chem. Eng. J.* **2018**, *336*, 476-488. DOI: 10.1016/j.cej.2017.12.053.

(56) Gao, S.; Yang, W.; Xiao, J.; Li, B.; Li, Q. Creation of passivated Nb/N p-n co-doped ZnO nanoparticles and their enhanced photocatalytic performance under visible light illumination. *Journal of Materials Science & Technology* **2019**, *35* (4), 610-614. DOI: 10.1016/j.jmst.2018.09.056.

(57) Pham, T.-D.; Lee, B.-K. Cu doped TiO2/GF for photocatalytic disinfection of Escherichia coli in bioaerosols under visible light irradiation: Application and mechanism. *Appl. Surf. Sci.* **2014**, *296*, 15-23. DOI: 10.1016/j.apsusc.2014.01.006.

(58) Özkan, M.; Kumar, Y.; Keser, Y.; Hadi, S. E.; Tuncel, D. Cucurbit[7]uril-Anchored Porphyrin-Based Multifunctional Molecular Platform for Photodynamic Antimicrobial and Cancer Therapy. *ACS Applied Bio Materials* **2019**, *2* (11), 4693-4697. DOI: 10.1021/acsabm.9b00763.

(59) Wheatley, R.; Diaz Caballero, J.; Kapel, N.; de Winter, F. H. R.; et al. Rapid evolution and host immunity drive the rise and fall of carbapenem resistance during an acute Pseudomonas aeruginosa infection. *Nature Communications* **2021**, *12* (1), 2460. DOI: 10.1038/s41467-021-22814-9.

(60) Gnach, A.; Lipinski, T.; Bednarkiewicz, A.; Rybka, J.; Capobianco, J. A. Upconverting nanoparticles: assessing the toxicity. *Chem. Soc. Rev.* **2015**, *44* (6), 1561-1584, Review article. DOI: 10.1039/C4CS00177J.

(61) Sirelkhatim, A.; Mahmud, S.; Seeni, A.; Kaus, N. H. M.; et al. Review on Zinc Oxide nanoparticles: antibacterial activity and toxicity mechanism. *Nanomicro Lett* **2015**, *7* (3), 219-242. DOI: 10.1007/s40820-015-0040-x.

(62) Qi, K.; Cheng, B.; Yu, J.; Ho, W. Review on the improvement of the photocatalytic and antibacterial activities of ZnO. *J. Alloys Compd.* **2017**, *727*, 792-820, Review article. DOI: 10.1016/j.jallcom.2017.08.142.

(63) Elbourne, A.; Cheeseman, S.; Wainer, P.; Kim, J.; et al. Significant Enhancement of Antimicrobial Activity in Oxygen-Deficient Zinc Oxide Nanowires. *ACS Applied Bio Materials* **2020**, *3* (5), 2997-3004. DOI: 10.1021/acsabm.0c00065.

(64) Zhou, Z.; Li, B.; Liu, X.; Li, Z.; et al. Recent Progress in Photocatalytic Antibacterial. *ACS Applied Bio Materials* **2021**, *4* (5), 3909-3936. DOI: 10.1021/acsabm.0c01335.

(65) De Corrado, J. M.; Fernando, J. F. S.; Shortell, M. P.; Poad, B. L. J.; Blanksby, S. J.; Waclawik, E. R. ZnO Colloid Crystal Facet-Type Determines both Au Photodeposition and Photocatalytic Activity. *ACS Applied Nano Materials* **2019**, *2* (12), 7856-7869. DOI: 10.1021/acsanm.9b01864.

(66) Lakshmi Prasanna, V.; Vijayaraghavan, R. Insight into the Mechanism of Antibacterial Activity of ZnO: Surface Defects Mediated Reactive Oxygen Species Even in the Dark. *Langmuir* **2015**, *31* (33), 9155-9162. DOI: 10.1021/acs.langmuir.5b02266.

(67) Kirar, S.; Thakur, N. S.; Laha, J. K.; Banerjee, U. C. Porphyrin Functionalized Gelatin Nanoparticle-Based Biodegradable Phototheranostics: Potential Tools for Antimicrobial Photodynamic Therapy. *ACS Applied Bio Materials* **2019**, *2* (10), 4202-4212. DOI: 10.1021/acsabm.9b00493.

(68) Yue, L.; Zheng, M.; Khan, I. M.; Wang, Z. Chlorin e6 conjugated chitosan as an efficient photoantimicrobial agent. *Int. J. Biol. Macromol.* **2021**, *183*, 1309-1316. DOI: 10.1016/j.ijbiomac.2021.05.085.

(69) Zhang, Y.; Huang, P.; Wang, D.; Chen, J.; et al. Near-infrared-triggered antibacterial and antifungal photodynamic therapy based on lanthanide-doped upconversion nanoparticles. *Nanoscale* **2018**, *10* (33), 15485-15495. DOI: 10.1039/C8NR01967C.

(70) Liu, W.; Zhang, Y.; You, W.; Su, J.; et al. Near-infrared-excited upconversion photodynamic therapy of extensively drug-resistant Acinetobacter baumannii based on lanthanide nanoparticles. *Nanoscale* **2020**, *12* (26), 13948-13957. DOI: 10.1039/D0NR01073A.

(71) Falcaro, P.; Ricco, R.; Doherty, C. M.; Liang, K.; Hill, A. J.; Styles, M. J. MOF positioning technology and device fabrication. *Chem. Soc. Rev.* **2014**, *43* (16), 5513-5560. DOI: 10.1039/C4CS00089G.

(72) Bui, L. M. G.; Hoffmann, P.; Turnidge, J. D.; Zilm, P. S.; Kidd, S. P. Prolonged growth of a clinical Staphylococcus aureus strain selects for a stable small-colony-variant cell type. *Infection and immunity* **2014**, *83* (2), 470-481.

Chapter 3: Publication 2

Publication title: UCNP@ZnO:Co/Ag Composites: A Dual-Action Platform for Antibacterial Photodynamic Therapy via Reactive Oxygen Species Stimulation

The manuscript is to be submitted to a peer-reviewed journal.

Statement of Authorship

Title of Paper	UCNP@ZnO:Co/Ag Composites: A Dual-Action Platform for Antibacterial Photodynamic Therapy via Reactive Oxygen Species Stimulation
Publication Status	☐ Published ☐ Accepted for Publication ☐ Submitted for Publication ☑ Unpublished and Unsubmitted work written in manuscript style
Publication Details	

Principal Author

Name of Principal Author (Candidate)	Afshin Karami		
Contribution to the Paper	Concept development, samples synthesis and characterization, efficacy experiments, manuscript writing and review		
Overall percentage (%)	85%		
Certification:	This paper reports on original research I conducted during the period of my Higher Degree by Research candidature and is not subject to any obligations or contractual agreements with a third party that would constrain its inclusion in this thesis. I am the primary author of this paper.		
Signature		Date	01/06//23

Co-Author Contributions

By signing the Statement of Authorship, each author certifies that:

i. the candidate's stated contribution to the publication is accurate (as detailed above);

ii. permission is granted for the candidate in include the publication in the thesis; and

iii. the sum of all co-author contributions is equal to 100% less the candidate's stated contribution.

Name of Co-Author	Dr. Stephen Kidd		
Contribution to the Paper	Concept development, manuscript writing and review, supervision of work		
Signature		Date	09/06/23

Name of Co-Author	Prof. Christopher Sumby		
Contribution to the Paper	Concept development, manuscript writing and review, supervision of work.		
Signature		Date	08/06/2023

Name of Co-Author	A/Prof. Jingxiu Bi		
Contribution to the Paper	Concept development, manuscript writing and review, supervision of work.		
Signature		Date	15/06/2023

3.1 Abstract

Antibacterial photodynamic therapy (aPDT) based on ZnO-coated lanthanide-doped upconversion nanoparticles (UCNP@ZnO) is a promising alternative for treating infections caused by antibacterial-resistant bacteria. By doping the ZnO shell of UCNP@ZnO materials with cobalt and silver, the latter in the form of Ag nanoparticles on the UCNP@ZnO:Co surface, we narrow the band gap and prevent electron-hole pair recombination, enhancing reactive oxygen species (ROS) generation and stimulating Ag ion release. When these improved UCNP@ZnO:Co/Ag materials are activated by near-infrared (NIR) light (980 nm) they demonstrated strong antibacterial efficacy against *Staphylococcus (S.) aureus* small colony variant (*S. aureus* JB1-SCV) and parental (6850) bacteria. Control experiments with the two bacteria strains in dark conditions showed no antibacterial activity. Ag NPs loaded onto the UCNPs@ZnO:Co surface, act as a co-catalyst and in combination with a localized surface plasmon resonance (LSPR) enhance the photogeneration of ROS by ZnO:Co shells. The photogenerated ROS also causes oxidation of co-located Ag NPs, resulting in the release of Ag ions and a more pronounced antibacterial response. This novel dual mode of action promises efficient treatment of resistant or hard to treat bacterial strains in exposed wounds.

3.2 Introduction

Nosocomial infections caused by the bacterium *Staphylococcus (S.) aureus* are steadily increasing, with a common characteristic being its resistance to antibiotics.[1,2] Methicillin-resistant *S. aureus* (MRSA), which was historically associated with hospitals, has evolved into community-associated methicillin *S. aureus* (CA-MRSA).[3-5] A significant part of the *S. aureus* problem can be attributed to chronic infections caused by *S. aureus* small colony variants (SCVs), a subpopulation of

S. aureus.[6] It is possible for SCVs to cause bone (osteomyelitis), heart (endocarditis), implant-associated and skin infections.[7] Infections of the skin are also a major issue, especially for people with compromised immune systems, such as those suffering from diabetes or having chronic wounds.[8] As a result of their slow growth, SCVs have a high level of resistance, making treatment of chronic skin infections difficult.[6] Due to the lack of new antibiotics to combat antibacterial-resistant SCVs, and other resistant bacteria, alternative strategies have been pursued. One of these strategies, photodynamic therapy (PDT) using lanthanide-doped upconversion nanoparticles (UCNPs), may offer a new option for combating antibacterial-resistant *S. aureus* and their SCVs.[9]

Antibacterial PDT (aPDT) can be performed with a core/shell structure that consists of a zinc oxide (ZnO) semiconductor shell and a $NaYF_4$:Yb/Tm UCNP core,[10] leading to photogeneration of reactive oxygen species (ROS) that are lethal to proximal cells.[11] In the core, near-infrared (NIR) light, typically at 980 nm, is absorbed by the Yb^{3+} ion (sensitizer) and transferred sequentially to the Tm^{3+} ion (activator) to generate visible and UV light emission. The UV emission is then absorbed by the ZnO shell, resulting in electron-hole (e^-/h^+) pairs that react with oxygen and water to produce ROS (Scheme 1).

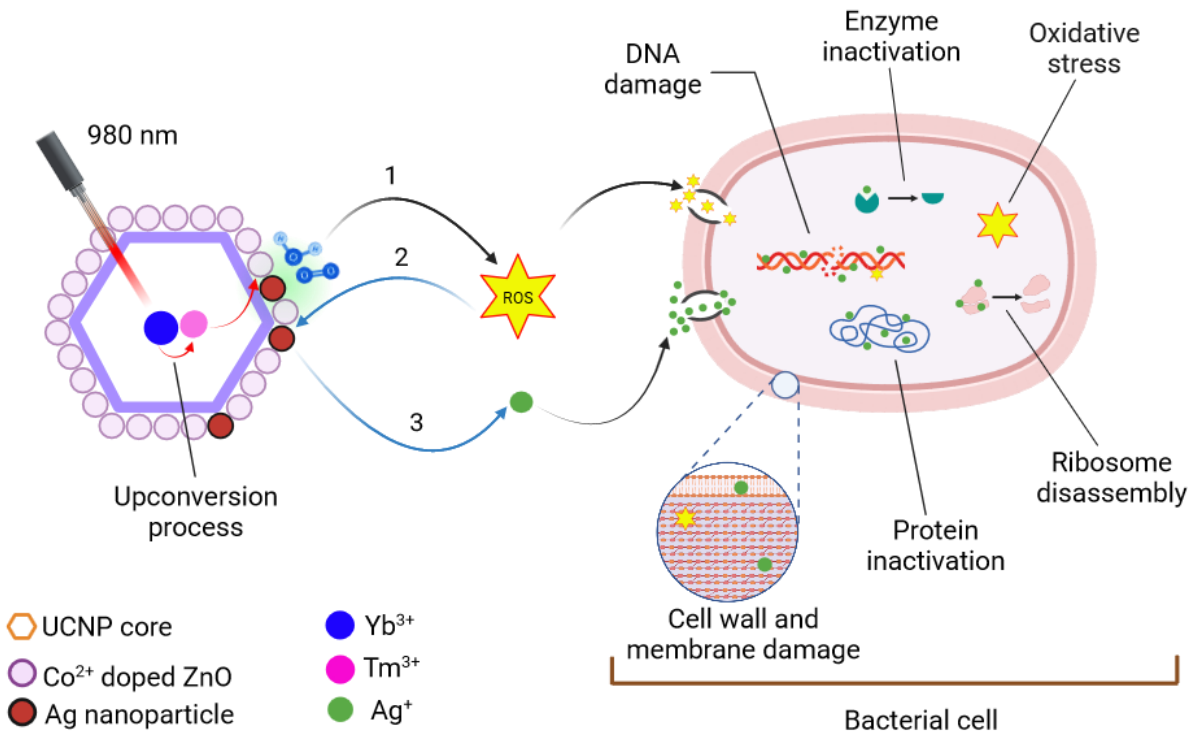

Scheme 1. Proposed mechanisms of antibacterial activity for doped ZnO-coated UCNPs. Photogeneration of reactive oxygen species (ROS) by doped ZnO-coated UCNP activated by NIR light could result in bacterial cell death. Cobalt ion dopants and Ag NPs could enhance the photocatalytic performance of the ZnO shell, improving ROS generation and facilitating Ag^+ ion release, which in turn could inactivate bacteria through multiple modes of activity. Created with BioRender.com.

ZnO-coated UCNPs have several advantages over alternative antibacterial agents, including their ability to be activated safely by NIR light (even within the body due to the transparency of human tissue to NIR radiation) and biocompatibility due to the ZnO shell.[12] Although examples of $NaYF_4$:Yb/Tm@ZnO NPs have been synthesised recently, their low photocatalytic ROS generation, stemming from limitations of both the core UCNP and the ZnO shell, have limited their efficacy for aPDT. This is because ZnO has a wide band gap (3.37 eV), meaning it mostly absorbs only the UV portion of the $NaYF_4$:Yb/Tm UCNP emission. Moreover, the UV emission from the $NaYF_4$:Yb/Tm UCNPs is of considerably lower intensity compared with the visible light

emission at 450 and 475 nm.[13] Finally, the recombination of electron-hole pairs on the surface of ZnO, reducing ROS generation, is another limitation of purely ZnO-coated aPDT systems.[14,15]

In this work, we proposed to improve the performance of ZnO-coated UCNPs for aPDT by doping the ZnO shell with cobalt ions (Co^{2+}) to improve core-to-shell energy transfer and decoration with silver NP to act as a co-catalyst and a secondary antibacterial agent. Doping the ZnO semiconductor, introduces a dopant-related energy level into the mid-gap region of the semiconductor, providing optical properties that are determined by the nature of these mid-gap states.[16] Additionally, by decorating the surface of ZnO with Ag, which acts as an electron sink, the separation of electron-hole pairs can be improved resulting in the retention of the holes on the ZnO surface.[17] Ag NPs also have strong absorption in the visible region due to their localized surface plasmon resonance (LSPR) effect,[18] allowing them to act as plasmonic sensitizers, which can enhance the absorption of light by ZnO and thereby lead to the generation of more electron-hole pairs, ROS and thereby improving performance for aPDT. Additionally, Ag ions released by Ag NPs are proven antibacterial agents[19] (Scheme 1) and could provide a synergistic antibacterial activity to the ROS. Finally, considering the UCNP component, the inherently low upconversion quantum yield can be improved by several strategies including size or phase control, incorporation of impurities, modification of the host matrix, core/shell structure, and increasing the activator concentration.[20] Herein, we use a high activator concentration to improve the overall photoluminescence of the ZnO-coated UCNPs.

Utilising these design principles, this study evaluates the performance of optimised ZnO-coated $NaYF_4$:Yb/Tm materials for aPDT of *S. aureus* and their SCVs. We assessed the photoluminescence of two different core UCNPs, NaY(81%)F_4:Yb(18%)/Tm(1%) and a higher Yb^{3+} composition of NaYb(99%)F_4:Tm(1%) to improve the emission. Additionally, we doped

cobalt ions (Co^{2+}) into the ZnO (formed from a Co-doped zeolitic imidazolate-8 coating) to reduce the band gap energy and added Ag NPs to the surface of the cobalt-doped ZnO (ZnO:Co) to prevent the recombination of electron-holes on the doped ZnO surface and further enhance the antibacterial activity of ZnO-coated UCNP. The antibacterial performance of the resulting core/shell doped ZnO-coated UCNPs was assessed against *S. aureus* JB1-SCV and the parental *S. aureus* 6850 in NIR light-illuminated and dark conditions to demonstrate these materials are viable aPDT agents for the treatment of resistant bacteria.

3.3 Results and discussion

3.3.1 $NaYF_4$:Yb/Tm@ZnO:Co/Ag Synthesis

To improve the photoluminescence efficiency of the UCNP core, we used a high sensitizer concentration and synthesised hexagonal β-NaYb(99%)F_4:Tm(1%) by a thermal decomposition method.[11,21] As a comparison, a hexagonal β-NaY(81%)F_4:Yb(18%)/Tm(1%) UCNP core was synthesised directly at 300 °C, while the hexagonal β-$NaYbF_4$:Tm sample with the higher sensitizer loading was synthesised in two steps by first preparing the cubic form at 160 °C then converting it into the hexagonal structure at an elevated temperature (320 °C). PXRD data for $NaYF_4$:Yb/Tm NP (Figure 1c) and $NaYbF_4$:Tm NP (Figure S1) confirmed the samples are crystalline, with the diffraction peaks indexed to hexagonal β-$NaYF_4$ (# 16-0334) and β-$NaYbF_4$ phase (# 27-1427), respectively. This was supported by high-resolution TEM imaging and the selected area electron diffraction (SAED) which confirmed that UCNPs with a hexagonal morphology are formed (Figures 1d and 1h). The interplanar distances of the $NaYF_4$:Yb/Tm and $NaYbF_4$:Tm NPs were measured to both be approximately 0.52 nm, which can be indexed to the (100) lattice plane for the hexagonal β-$NaYF_4$ (0.515 nm, # 16-0334) and β-$NaYbF_4$ (0.513 nm, # 27-1427) crystal structures. The TEM images also revealed that synthesised β-$NaYF_4$:Yb/Tm

and β-$NaYbF_4$:Tm NPs are uniformly sized with mean particle sizes of 24 ± 2 nm and 642 ± 99 nm, respectively (Figure S4 a to c). The β-$NaYbF_4$:Tm samples were notably larger, as increasing the Yb^{3+} concentration typically leads to an increase in particle size, especially where there is no change in synthetic conditions.[21] Here, the same synthetic conditions were used to prevent variation in the surface chemistry which has been shown to perturb ZnO shell formation.[11] The HRSEM images for β-$NaYF_4$:Yb/Tm and β-$NaYbF_4$:Tm NP confirm the TEM data, showing monodisperse NPs for both samples (Figure S5a and d). An even distribution of Yb and Tm was confirmed for both samples by HRTEM elemental mapping (Figure 1e and i), with EDS analysis confirming 16 mol% Yb and 2 mol% Tm for $NaYF_4$:Yb/Tm (slightly below the feed ratio for Yb) and 99 mol% Yb and 1 mol% for $NaYbF_4$:Tm (Figure S5). ICP-MS analysis on digested samples confirmed these surface-based analyses reflect the bulk composition (Table S1).

We utilised our previously reported two-step approach to coat the ZnO shell on the UCNP cores.[11] As zeolitic imidazolate framework-8 (ZIF-8), can be induced to form rapidly around functionalized nanoparticles, we used cetyltrimethylammonium bromide (CTAB) coated UCNPs to seed ZIF-8 shell growth and converted this to ZnO by calcination (400 °C for 5 hours in the air). This was shown to have minimal effects on the hexagonal to cubic phase change of the UCNP host while completely converting the ZIF-8 shell to ZnO nanoparticles.[11] Pure ZnO nanoparticles have a low photocatalytic efficiency due to their wide band gap energy and a high recombination rate of charge carriers.[22] To overcome this, we doped Co^{2+} ion into the ZnO nanoparticle coating by introducing it during the ZIF-8 shell formation step. PXRD data showed the successful formation of $NaYF_4$:Yb/Tm@ZIF-8:Co and $NaYbF_4$:Tm@ZIF-8:Co (Figure 1c and S1) with retention of the hexagonal UCNP structure and addition of the ZIF-8 phase. Calcination in the air for five hours at 400 °C gave UCNPs@ZnO:Co (UCNPs = $NaYF_4$:Yb/Tm and $NaYbF_4$:Tm) samples, with PXRD

data (Figure 1c and S1) showing that the peaks for ZIF-8 have disappeared while new peaks corresponding to ZnO have appeared in the PXRD traces. The UCNP@ZnO:Co samples showed small traces of the cubic phases of α-$NaYF_4$ (# 06-0342) and α-$NaYbF_4$ (# 77-2043) (Figure 1c and S1), which were minimized by conducting the calcination at 400 °C. HRTEM and SEM imaging (Figures S2.b, S2.e, S4.b and S3.e), combined with elemental mapping (Figure 1F and 1J) of both composites, confirmed non-epitaxial cobalt-doped ZnO shell formation around UCNP cores, with the formation of small ZnO:Co nanoparticles on the surface of an unchanged UCNP core.

Finally, the aPDT composites were loaded with Ag nanoparticles to further enhance the photocatalytic activity of ZnO:Co shell. This was achieved by treating a suspension of the UCNP@ZnO:Co samples with an Ag salt and sodium borohydride ($NaBH_4$) solution at low temperatures. PXRD data for the UCNP@ZnO:Co/Ag ($NaYF_4$:Yb/Tm and $NaYbF_4$:Tm) samples (Figures 1c and S1) confirmed the formation of Ag nanoparticles (additional peaks at 38.1°, 44.3 and 64.5 corresponding with the (111), (200), and (220) planes of Ag (# 1100136)). Furthermore, HRTEM (Figure 1g and 1k) and HRSEM (Figure S2.c and f) images confirmed the formation of Ag NPs localised on the surface of both UCNP@ZnO:Co/Ag samples.

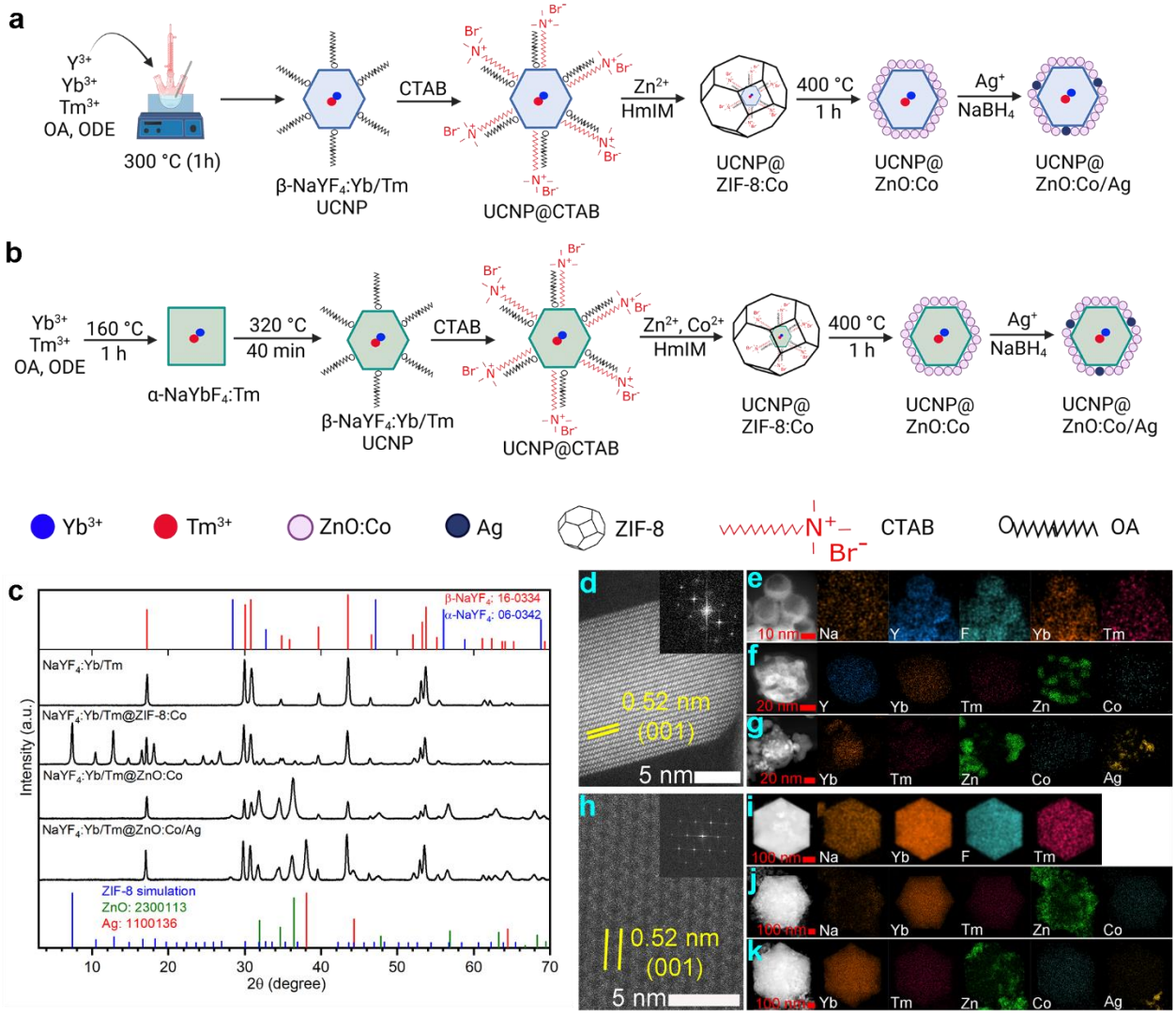

Figure 1. Details of the preparation of core/shell $NaYF_4$:Yb/Tm@ZnO:Co/Ag and $NaYbF_4$:Tm@ZnO:Co/Ag nanoparticles (a-b). PXRD data for all steps involved in the synthesis of $NaYF_4$:Yb/Tm@ZnO:Co/Ag (c). HR-TEM image of $NaYF_4$:Yb/Tm, selected area diffraction in the inset (d), and EDS element mapping for $NaYF_4$:Yb/Tm, $NaYF_4$:Yb/Tm@ZnO:Co, $NaYF_4$:Yb/Tm@ZnO:Co/Ag (e to g). HR-TEM image of $NaYbF_4$:Tm, selected area diffraction in the inset (h), and EDS element mapping for $NaYbF_4$:Tm, $NaYF_4$:Yb/Tm@ZnO:Co and $NaYbF_4$:Tm@ZnO:Co/Ag (i to k). Parts a and b were Created with BioRender.com.

3.3.2 Photoluminescence analysis

Since the ZnO shell in the UCNP@ZnO composites must be activated by UV or short wavelength visible light to produce ROS for antibacterial activity, we investigate photoluminescence by the core and composites. Specifically, solid-state photoluminescence (PL) spectroscopy was utilised to examine the impact of Yb^{3+} sensitizer concentration on UV emission by NaY(81%)F_4:Yb(18%)/Tm(1%) and NaYb(99%)F_4:Tm(1%) UCNPs (Figure 2a and b - pink lines). In these UCNPs, sequential energy transfers from Yb^{3+} to Tm^{3+} result in visible and UV emissions, which are generated from the $^1D_2$ level in four steps and from the $^2I_6$ level in five steps (Figure S6).

A typical Tm^{3+} ion emission spectrum for Yb/Tm UCNPs includes $^1I_6 \rightarrow {}^3F_4$ (345 nm), $^1D_2 \rightarrow {}^3H_4$ (360 nm), $^1D_2 \rightarrow {}^3F_4$ (455 nm), and $^1G_4 \rightarrow {}^3H_6$ (475 nm), as well as several additional visible light emissions (Figure S6). Compared to visible light emission, the UV emissions from the Tm^{3+} ions in Yb/Tm UCNPs are considerably less intense. In Yb/Tm UCNPs, UV emission is mediated by additional energy transfer between the sensitizer (Yb^{3+}) ions and the activator (Tm^{3+}) ions. To utilise the UCNP@ZnO composite for aPDT applications, it is necessary to tune the optical properties of the UCNP core to enhance the UV and short wavelength visible emission from the UCNP core. A saturation of the Tm^{3+} energy levels, which can be achieved by increasing the ratio of Yb^{3+} to Tm^{3+} in UCNPs, may result in a higher UV emission rate than a non-saturated model. We analysed $NaYF_4$:Yb(18%)/Tm and NaYb(99%)F_4:Tm UCNP samples to determine which sample emits more UV light. The NaYb(99%)F_4:Tm UCNP sample compared to the $NaYF_4$:Yb(18%)/Tm UCNP sample, exhibited slightly higher UV emission and a significantly higher emission at 450 nm peak (Figure 2a and b – pink lines). In each sample, peak intensities were extracted and the ratio of the combined peaks in the UV-A region (320 to 400 nm) to the

475 nm peak was calculated based on the area under the curve for each peak. The ratio between the combined UV-A emission and 475 nm peak emission in the NaYb(99%)F_4:Tm UCNP sample was 0.27, whereas it was slightly lower at 0.21 in the $NaYF_4$:Yb(18%)/Tm UCNP sample. Based on these two Yb/Tm UCNP samples, the results indicated that increasing sensitizer (Yb^{3+}) concentration can lead to slightly more UV light being generated during the upconversion process.

As noted, further enhancing the photocatalytic activity of the ZnO-coated UCNPs can be achieved by doping the ZnO NP shell with other elements. The UV-visible absorption spectrum for the ZnO doped with Co showed the absorption band could be extended into the visible region with absorption to approximately 470 nm (Figure 2c). This is consistent with previous studies.[23,24] Importantly, ZnO:Co red-shifted absorption overlaps with the visible emission from the UCNPs at approximately 450 nm validating the choice to use cobalt-doped ZnO. As expected, for both UCNP@ZnO:Co samples, the peak ratio of UV to 475 nm emission has been significantly reduced (Figure 2a and b - green lines), consistent with the ZnO:Co shell in $NaYF_4$:Yb(18%)/Tm@ZnO:Co and NaYb(99%)F_4:Tm@ZnO:Co absorbing this UCNP emission (Figure 2a and b – green lines). Due to the stronger emission at 450 nm, the NaYb(99%)F_4:Tm@ZnO:Co sample is expected to perform better in aPDT.

Although the Co doping of the ZnO shell has expanded the absorption band into the visible range, we explored the possibility of using an additional cocatalyst in the form of Ag NP, which was also expected to provide additional antibacterial activity.[25,26] Rapid recombination of photoinduced electron-hole pairs adversely affects the photocatalytic activity of ZnO NP, limiting practical application in aPDT.[27] Ag NP incorporation on the surface of ZnO NP is proposed to act as an electron trapping site, preventing recombination and consequently improving the photocatalytic activity of ZnO NP.[28] Furthermore, the LSPR effect of Ag NP decoration on ZnO NP has been reported to enhance light absorption in the visible region of the spectrum and funnel it toward ZnO NP.[29] Additionally, as plasmonic metals rarely affect the energy band structures of semiconductors, except at the metal/semiconductor interface where the conduction and valence bands generally bend, the major properties of the semiconductor component are expected to remain unaffected.[30] The effect of Ag NP decoration of the NP composites was examined by UV-visible absorption spectroscopy, with the spectrum for ZnO:Co/Ag showing a broad absorption band in the visible range similar to previous studies (Figures 2c).[31,32] The broad absorption is consistent with electronic coupling between the Ag NP and the ZnO:Co semiconductor, and LSPR. Combined, these enhancements – better UCNP emission, and higher and efficient absorption from the ZnO:Co/Ag shell – are expected to lead to more active materials for aPDT.

Although the Co doping of the ZnO shell has expanded the absorption band into the visible range, we explored the possibility of using an additional cocatalyst in the form of Ag NP, which was also expected to provide additional antibacterial activity.[25,26] Rapid recombination of photoinduced electron-hole pairs adversely affects the photocatalytic activity of ZnO NP, limiting practical application in aPDT.[27] Ag NP incorporation on the surface of ZnO NP is proposed to act as an

electron trapping site, preventing recombination and consequently improving the photocatalytic activity of ZnO NP.[28] Furthermore, the LSPR effect of Ag NP decoration on ZnO NP has been reported to enhance light absorption in the visible region of the spectrum and funnel it toward ZnO NP.[29] Additionally, as plasmonic metals rarely affect the energy band structures of semiconductors, except at the metal/semiconductor interface where the conduction and valence bands generally bend, the major properties of the semiconductor component are expected to remain unaffected.[30] The effect of Ag NP decoration of the NP composites was examined by UV-visible absorption spectroscopy, with the spectrum for ZnO:Co/Ag showing a broad absorption band in the visible range similar to previous studies (Figures 2c).[31,32] The broad absorption is consistent with electronic coupling between the Ag NP and the ZnO:Co semiconductor, and LSPR. Combined, these enhancements – better UCNP emission, and higher and efficient absorption from the ZnO:Co/Ag shell – are expected to lead to more active materials for aPDT.

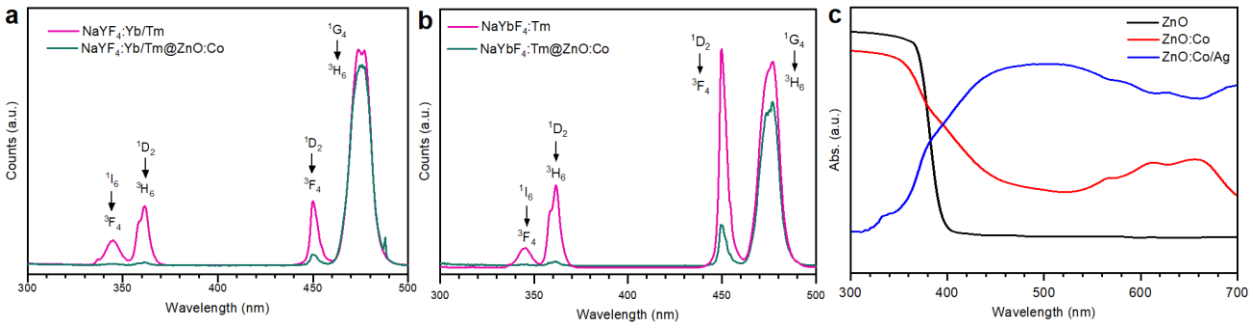

Figure 2. Photoluminescence spectra for $NaYF_4$:Yb/Tm and $NaYF_4$:Yb/Tm@ZnO:Co samples (a), and $NaYbF_4$:Tm and $NaYbF_4$:Tm@ZnO:Co samples (b), UV-Vis spectra for ZnO:Co and ZnO (c).

3.3.3 Antibacterial properties and mechanistic insights

To examine the effect of these chemical modifications, we evaluated the antibacterial activity of $NaYF_4$:Yb/Tm@ZnO, $NaYbF_4$:Tm@ZnO, $NaYF_4$:Yb/Tm@ZnO:Co, $NaYbF_4$:Tm@ZnO:Co, $NaYF_4$:Yb/Tm@ZnO:Co/Ag, and $NaYF_4$:Tm@ZnO:Co/Ag against S. *aureus* 6850 and its SCV

phenotype *S. aureus* JB1-SCV (Figure 3). *S. aureus* JB1-SCV is believed to be responsible for chronic and relapsing infections.[33,34] Experiments were conducted under both NIR illumination (using a CW laser with a power density of 1.75 W/cm^2) and dark conditions to probe both antibacterial activity and the mechanism of action for these new composites. $NaYF_4$:Yb/Tm@ZnO showed 0.29 and 0.10 log CFU reduction in cell viability in the NIR light-illuminated mode for *S. aureus* 6850 and JB1-SCV, respectively (Figure 3a and b, Table 1). $NaYbF_4$:Tm@ZnO exhibited a comparable antibacterial efficacy against *S. aureus* 6850 and JB1-SCV, respectively with a 0.27 and 0.12 log CFU reduction in cell viability, under NIR illumination. As expected, $NaYF_4$:Tm@ZnO and NaYbF4:Tm@ZnO samples both showed no reduction in CFUs under dark conditions against either bacteria strains. With the addition of Co dopant to UCNPs@ZnO samples, the $NaYF_4$:Yb/Tm@ZnO:Co showed 0.36 and 0.18 log CFU reductions in cell viability in the NIR light-illuminated mode for S. *aureus* 6850 and JB1-SCV, respectively (Figure 3a and b). Interestingly, $NaYbF_4$:Tm@ZnO:Co demonstrated much higher antibacterial efficacy against S. *aureus* 6850 with a 1.02 log CFU reduction in cell viability compared to *S. aureus* JB1-SCV (0.17 log CFU reduction), under NIR illumination (Figure 3a and b and Table 1). In contrast, $NaYbF_4$:Tm@ZnO:Co and $NaYbF_4$:Tm@ZnO:Co samples showed almost no reduction in CFUs under dark conditions against these bacteria strains (except a 0.04 log CFU reduction against S. *aureus* JB1-SCV for $NaYF_4$:Yb/Tm@ZnO:Co) (Figure 3a and b and Table 1).

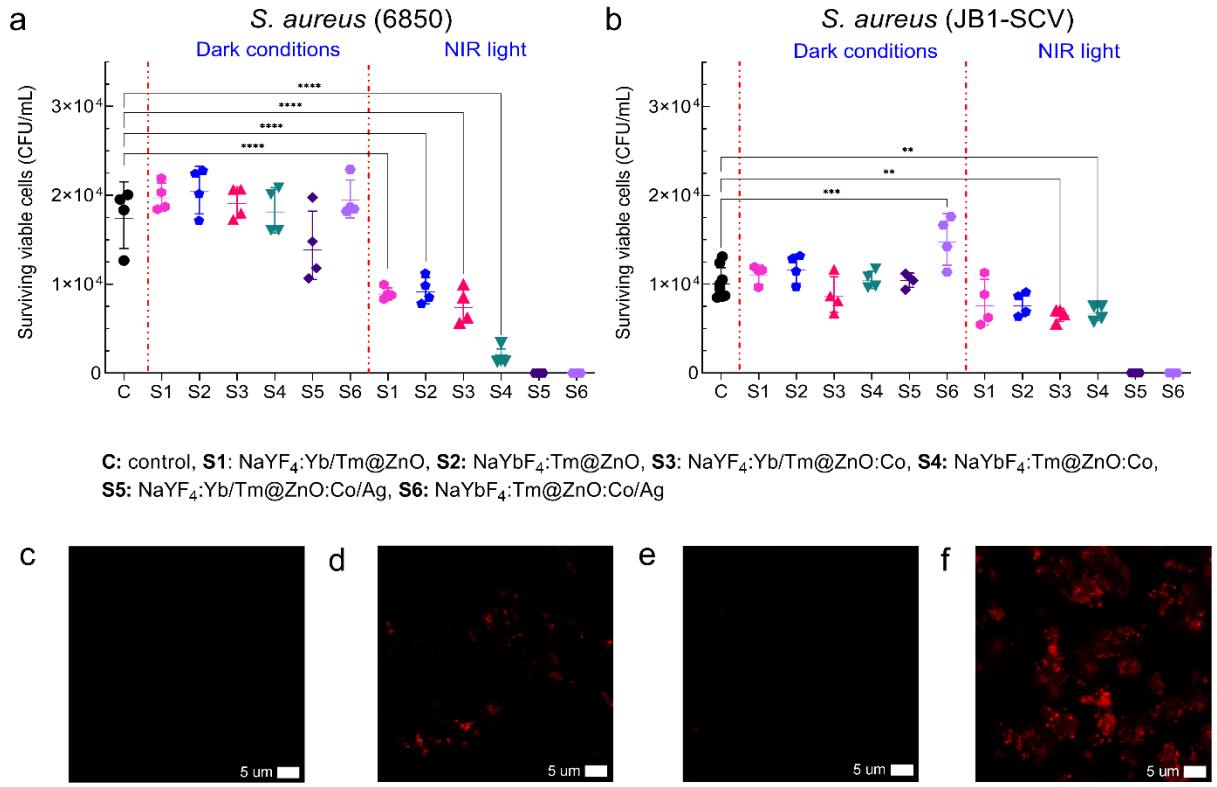

Figure 3. Antibacterial efficacy results for the $NaYF_4$:Yb/Tm@ZnO:Co, $NaYF_4$:Yb/Tm@ZnO:Co/Ag, $NaYbF_4$:Tm@ZnO:Co and $NaYbF_4$:Tm@ZnO:Co/Ag in the NIR light-activated and dark conditions modes against *S. aureus* 6850 (a), and against *S. aureus* JB1-SCV (b). Photo-generated ROS analysis evaluated by confocal laser scanning microscope and the CellROX® Deep Red reagent for $NaYF_4$:Yb/Tm@ZnO:Co/Ag NPs in NIR light-activated mode (c), $NaYF_4$:Yb/Tm@ZnO:Co/Ag NPs in dark conditions (d), $NaYbF_4$:Tm@ZnO:Co/Ag NPs in NIR light-activated mode (e), and $NaYbF_4$:Tm@ZnO:Co/Ag NPs in dark conditions (f).

Table 1. Summary of antibacterial efficacy data.

Nanoparticle samples		CFU log10 reduction (reduction ratio, %)			
		Dark conditions mode		NIR light illuminated mode	
		S. aureus (6850)	*S. aureus* (JB1-SCV)	*S. aureus* (6850)	*S. aureus* (JB1-SCV)
1	$NaYF_4$:Yb/Tm@ZnO	0.00 (0.0%)	0.00 (0.0%)	0.29 (48.7%)	0.10 (21.5%)
2	$NaYbF_4$:Tm@ZnO	0.00 (0.0%)	0.00 (0.0%)	0.27 (46.7%)	0.12 (23.6%)
3	$NaYF_4$:Yb/Tm@ZnO:Co	0.00 (0.0%)	0.04 (9.5%)	0.36 (56.4%)	0.18 (34.3%)
4	$NaYbF_4$:Tm@ZnO:Co	0.00 (0.0%)	0.00 (0.0%)	1.02 (90.4%)	0.17 (32.5%)
5	$NaYF_4$:Yb/Tm@ZnO:Co/Ag	0.08 (17.5%)	0.00 (0.0%)	4.24 (100.0%)	4.24 (100.0%)
6	$NaYbF_4$:Tm@ZnO:Co/Ag	0.00 (0.0%)	0.00 (0.0%)	4.24 (100.0%)	4.24 (100.0%)

In comparison, both $NaYbF_4$:Tm@ZnO:Co/Ag and $NaYbF_4$:Tm@ZnO:Co/Ag completely eliminated cells (4.24 log CFU reduction) for both *S. aureus* strains under NIR illumination (Figure 3a and b and Table 1). Satisfyingly, in the dark, again almost no reduction in CFUs was observed (except a minor 0.08 log CFU reduction for $NaYF_4$:Yb/Tm@ZnO:Co/Ag against *S. aureus* 6850) (Figure 3a and b and Table 1). Critically, these experiments demonstrated that the core/shell UCNPs were effective against both *S. aureus* strains under light-activated NIR conditions, and under dark conditions are not toxic to bacteria, even for the silver-incorporated NP samples. Finally, a control without ZnO-coated UCNPs showed no CFU reduction in the experiment, confirming the NIR light source used had a minimal contribution to eliminating bacteria.

Having established the composites have excellent antibacterial activity, we examined the mechanisms of action, in particular focussing on the Ag NP loaded samples. Like other ZnO-

coated UCNPs, the likely antibacterial activities of $NaYF_4$:Yb/Tm@ZnO:Co and $NaYbF_4$:Tm@ZnO:Co are primarily due to the ZnO:Co shell, as the core has low toxicity.[35] Generation of photo-induced ROS is the main antibacterial mechanism for ZnO NP, although other mechanisms have been reported, including the release of Zn^{2+} ions and mechanical damage to bacteria caused by direct interaction with NPs.[11] The photo-induced ROS mechanism is consistent with observations in our current study, which indicates limited antibacterial activity for $NaYbF_4$:Tm@ZnO:Co and $NaYbF_4$:Tm@ZnO:Co samples under dark conditions and only those samples used under NIR illumination had statistically significant reductions in log CFU.

As noted, the addition of Ag NP to ZnO-coated UCNPs could increase the effectiveness of ZnO NP in three ways: they may act as a co-catalyst to prevent electron-hole pairs recombining;[36] as a plasmonic sensitizer, which enhances the absorption of light by the ZnO;[18] and as a source of toxic Ag ions,[37] particularly where Ag ion release is coupled to irradiation. In NIR-illuminated mode, $NaYF_4$:Yb/Tm@ZnO:Co/Ag and $NaYbF_4$:Yb/Tm@ZnO:Co/Ag NP samples completely eradicated both bacterial strains. Pleasingly, under dark conditions, the antibacterial activity of these materials was negligible, and the small amount of Ag NP dopant did not lead to a reduction in the viability of cells. These results are desirable for an ideal antibacterial material, specifically preventing unwanted toxicity when the compound is not activated (e.g., under dark conditions).

To obtain insight into the mode of action of $NaYbF_4$:Tm@ZnO:Co/Ag and $NaYbF_4$:Tm@ZnO:Co/Ag (Figure 3c to f), we checked for photogenerated ROS by confocal microscopy with the CellROX Deep Red Reagent. The assay was performed in both NIR and dark conditions simultaneously, and compared to dark conditions, both $NaYF_4$:Yb/Tm@ZnO:Co/Ag and $NaYbF_4$:Tm@ZnO:Co/Ag generated a significant amount of ROS during NIR illumination. These observations are consistent with the PL results shown in Figure 2. As a further step, Ag

release from NaYF4:Yb/Tm@ZnO:Co/Ag and NaYbF4:Tm@ZnO:Co/Ag was quantified by ICP-MS in NIR light illumination and dark illumination. Based on the ICP-MS results, the Ag release from both $NaYF_4$:Yb/Tm@ZnO:Co/Ag and $NaYbF_4$:Tm@ZnO:Co/Ag was 1.3 mmol in the NIR light-illumination mode, while only 0.4 and 0.6 mmol was released in the dark conditions over the same timescale, respectively. The results confirm that NIR-light irradiation stimulates Ag ion release from these composites. While these data confirm that in NIR-light mode, an increase in ROS and Ag release from $NaYF_4$:Yb/Tm@ZnO:Co/Ag and $NaYbF_4$:Tm@ZnO:Co/Ag, the results; however, we are unable to determine which mechanism of antibacterial action is most dominant. The co-catalytic and LSPR effects of Ag NP may have enhanced the photocatalytic activity and thereby ROS generation by the ZnO shell but, in addition, this improved ROS generation in turn facilitates the oxidation of Ag NP which could release more Ag ions. Nonetheless, a combination of ROS and Ag^+ is responsible for the strong antibacterial activity of both Ag-doped materials against *S. aureus* and associated SCV bacteria. In spite of this excellent activity when NIR activated, UCNPs@ZnO:Co/Ag NPs are nontoxic in dark conditions, making them ideal as an antibacterial agent for a variety of applications. If we compare UCNPs@ZnO:Co/Ag materials with other antibacterial agents and photosensitisers used in aPDT, we see some potential advantages. Although Ag NPs have been reported to eliminate bacteria completely, the lack of activation mode (uncontrolled release), leading to potential local cell toxicity, remains an issue.[38] Among the most common photosensitisers used in aPDT are chlorine, chlorin-e6 (Ce6), pheophorbide, and porphyrin, along with their derivatives.[39] A number of studies have demonstrated the excellent performance of these photosensitisers against a variety of bacteria.[40,41] UCNP-based photosensitiser (such as the one employed here) has the advantage of utilising NIR light for activation, which only has limited absorption by cells.

3.4 Conclusions

The development of alternative antibacterial strategies, such as antibacterial photodynamic therapy (aPDT) using ZnO-coated UCNP, is critical for dealing with antibacterial-resistant bacteria, such as *S. aureus* small colony variants (SCV). In this study, different approaches were evaluated to improve the photocatalytic activity of ZnO-coated UCNP for use as an effective photosensitiser for aPDT, ultimately in topical applications. Firstly, increasing the amount of activator (Yb^{3+}) was used to enhance the emission of the UCNP core. Secondly, Co was first doped to the ZnO shell in order to narrow the band gap energy, followed by Ag loading onto UCNP@ZnO:Co in order to prevent electron-hole recombination.

In dark conditions, neither of the bacteria strains was affected by these new NP composites (with or without the incorporation of Ag). NIR-activated $NaYF_4$:Yb/Tm@ZnO:Co and $NaYbF_4$:Tm@ZnO:Co samples both exhibited significant antibacterial properties against *S. aureus* SCV and parental 6850 (cell viability decreased between 32 to 90%). For UCNPs@ZnO:Co NP samples, ROS arising from the ZnO:Co shell have been confirmed as the main mode of antibacterial activity. By incorporating Ag NP into these materials ($NaYF_4$:Yb/Tm@ZnO:Co/Ag and $NaYbF_4$:Tm@ZnO:Co/Ag), they are able to completely eliminate both *S. aureus SCV* and parental 6850 strains under NIR illumination. With the addition of Ag NP to the UCNPs@ZnO:Co materials, ROS generation by the shell is likely enhanced due to the combined effects of co-catalysis and improved LSPR. Furthermore, we show that irradiation stimulates the release of Ag^+, which is responsible for the improved antibacterial activity of UCNPs@ZnO:Co/Ag samples over the non-doped materials.

Overall, the materials show excellent antibacterial activity against chronic *S. aureus* and associated SCV bacteria. The findings from this study, improving the efficacy of UCNP-based compounds for aPDT, should pave the way for effective and safe antibacterial treatments based on UCNP. Future potential research could examine ZnO:Co/Ag coated UCNP with different UCNP host materials that utilise a longer NIR light wavelength. Furthermore, to target bacteria cells, targeting compounds may be added to the composite surface.

3.5 Experimental section

3.5.1 Raw materials

Oleic acid (Sigma-Aldrich, technical grade, 90%), 1-octadecene (Sigma–Aldrich, technical grade, 90%), chloroform (Chem–Supply, 99.8%), cyclohexane (Chem–Supply), methanol (Sigma-Aldrich, 100%), ethanol (Chem–Supply, 100%), yttrium (III) chloride hexahydrate (Sigma-Aldrich, 99.9%), ytterbium(III) chloride hexahydrate (Sigma–Aldrich, 99.9%), thulium (III) chloride (Sigma-Aldrich, 99.9%), sodium hydroxide (Sigma–Aldrich, 99.99%), zinc acetate dihydrate (Sigma-Aldrich, ≥98%), hexadecyltrimethylammonium bromide (Sigma-Aldrich, ≥98%), polyvinylpyrrolidone (Sigma-Aldrich), 2-methylimidazole (Sigma–Aldrich, 99%), 3′-p-(aminophenyl) fluorescein (APF) (Thermo Fisher (Invitrogen)), and ammonium fluoride (Chem–Supply, 98%) were obtained from commercial sources and used without further purification.

3.5.2 Synthesis of UCNP@ZnO:Co/Ag nanoparticles

UCNP@ZnO:Co/Ag NP was synthesised in a multistep process involving (a) synthesis of core $NaYF_4$:Yb/Tm and $NaYbF_4$:Tm UCNPs; (b) deposition of CTAB coating; (c) formation of ZIF-8:Co coatings followed by conversion to ZnO:Co through calcination; and (d) deposition of Ag NPs on the surface of UCNP@ZnO:Co.

Step (a): The synthesis of $NaYF_4$:Yb/Tm and $NaYbF_4$:Tm upconversion NPs was performed by a thermolysis method which included a few variations.[21] In a typical synthesis for $NaYF_4$:Yb/Tm NP (18% Yb and 1% Tm), $YCl_3 \cdot 6H_2O$ (0.81 mmol), $YbCl_3 \cdot 6H_2O$ (0.18 mmol) and $TmCl_3$ (0.01 mmol) were mixed with oleic acid (OA, 6 mL) and 1-octadecene (ODE, 15 mL) in a 150 mL 3-neck round bottom flask. A homogeneous solution was formed by heating the suspension under argon protection to 150 °C before cooling it to room temperature. A solution of NaOH (2.5 mmol) and NH_4F (4 mmol) in methanol (10 mL) was added to the reaction mixture and stirred at room temperature for 30 minutes. Under argon gas protection, the solution was heated to evaporate the methanol from it and then gradually increased to 300 °C. Once the solution had cooled to room temperature, ethanol (10 mL) was used to precipitate the NPs from the solution. Following precipitation, the NPs were centrifuged at 10,000 rpm for 10 minutes with an Eppendorf 5920 R, Fa-6x50, washed several times with cyclohexane, ethanol, and MilliQ water, and then dried at 70 °C overnight. The $NaYbF_4$:Tm UCNPs were synthesised with a similar method but were maintained at 160 °C for one hour, then were heated to 320 °C under argon gas for 40 minutes. The remaining steps of the synthesis, including product precipitation and washing/drying, were similar to those of $NaYF_4$:Yb/Tm UCNP.

Step (b): CTAB (0.82 mmol) was dissolved in Milli-Q water (10 mL) and then a suspension of UCNP (45 mg) from the previous section, dispersed in chloroform (10 mL), was added and the combined biphasic solution was stirred for 2 h. A clear solution of CTAB-coated UCNPs was obtained by heating the mixture to evaporate the chloroform.

Step (c): $Zn(NO_3)_2.6H_2O$ (4 mmol) and $Co(NO_3)_2.6H_2O$ (0.02 mmol) were dissolved in Milli-Q water (5 mL) then added the CTAB-coated UCNP solution from the previous section and vortexed to mix. 2-methylimidazole (16.84 mmol) was dissolved in ethanol (10 mL) and added to the

previous solution and stirred at 250 rpm overnight. The UCNPs@ZIF-8:Co NP product was precipitated from the solution by the addition of ethanol (5 mL), collected by centrifugation (9,000 rpm for 10 min), washed with ethanol several times, and dried at 70 °C overnight. The UCNPs@ZnO:Co NPs were synthesised by calcination of UCNPs@ZIF-8:Co NPs in the air at 400 °C for 5 h with a heating rate of 10 °C/ min.

Step (d): $AgNO_3$ (0.05 mmol) and UCNPs@ZnO:Co NPs (50 mg) were added to Milli-Q water (5 mL) in a flask. The mixture was stirred at 800 rpm for 5 min. A freshly made solution of $NaBH_4$ (2.64 mmol) in Milli-Q water (5 mL) was dropwise added to the previous mixture in the iced bath. The mixture was stirred for 1 h then the product was collected by centrifugation (9,000 rpm for 10 min), washed with ethanol and Milli-Q water several times, and dried at 70 °C overnight.

Using the above method, Co^{2+} doped ZnO NPs and ZnO without any dopant were also synthesised. In order to prepare Co(II) doped ZnO NP, $Zn(NO_3)_2.6H_2O$ (4 mmol) and $Co(NO_3)_2.6H_2O$ (0.02 mmol) were dissolved in Milli-Q water (10 mL). A solution of HmIM (16.84 mmol) in ethanol (10 mL) was prepared and added to the previous solution, which was stirred overnight at 250 rpm. The product was collected by addition of ethanol (5 mL) and centrifugation (9,000 rpm for 10 min), then washed with ethanol several times, and dried at 70 °C overnight. Finally, the ZnO:Co NP was synthesised by calcination of ZIF-8:Co NP in the air at 400 °C for 5 h with a heating rate of 10 °C/ min. The ZnO NP was also synthesised via a similar method but without any dopant precursor.

3.5.3 Characterisation of as-prepared NPs

Powder X-ray diffraction (PXRD) data collected on a MiniFlex 600 (Rigaku, Cu Kα, λ = 0.15418 nm) was used to confirm the structure of the synthesised NPs. Samples were mounted in

a flat plate holder and the data was collected with the instrument operating at 40 kV and 15 mA by scanning 2θ from 10° to 70° with a step size of 0.02°. The hexagonal structure β-$NaYbF_4$ (#27-1427), hexagonal β-$NaYF_4$ (#16-0334), ZnO (#2300113), Ag (1100136) and simulated PXRD pattern of ZIF-8 (from the cif) were used for comparison to the experimental data.

The particle size and morphology of the NPs were investigated by scanning electron microscopy (SEM) on a Quanta 450 and high-resolution SEM (HRSEM) Hitachi SU7000, and transmission electron microscopy (TEM) on an FEI Tecnai G2 Spirit TEM and high-resolution TEM (HRTEM) on an FEI Titan Themis 80-200 G TEM operated at an accelerating voltage of 120 and 200 kV, respectively. The NP samples were coated with platinum (3 nm) before SEM measurements. Samples for TEM were dispersed in absolute ethanol using a vortex shaker, a small droplet of each suspension was transferred to the TEM sample holder and the ethanol evaporated before being placed into the TEM.

Photoluminescence measurements were carried out under 980 nm excitation by a continuous wave (CW) laser. A fixed amount of powdered NP sample was used in the experiment for each sample. The samples were excited by MDL-III-980 diode laser at 980 nm. The emission spectra were collected using a spectrofluorometer (Edinburgh Instruments F980) with an air-cooled photomultiplier (Hamamatsu R928) for detection.

The optical property of the pure ZnO and Co, Cu and Ni doped ZnO NP samples was evaluated by a spectrophotometer UV-3600 Plus, Shimadzu with an integrated sphere and a Renishaw inVia Raman Microscope integrated with Photoluminescence at an excitation wavelength of 325 nm. The band gap energy then was calculated by the Tauc plot using the following equation: $(h\nu\alpha)1/n = A(h\nu - Eg)$, where h is Planck's constant, ν is the frequency of vibration, α is the absorption

coefficient, Eg is the band gap, A is a proportion constant and n is the nature of sample transition (n=2 for indirect allowed transition).[42]

3.5.4 Antibacterial assays

The *S. aureus* JB1-SCV along with parental *S. aureus* 6850 were used in the antibacterial efficacy studies. Both NIR light illumination and dark illumination were used to evaluate the efficacy of ZnO-coated UCNPs in antibacterial efficacy. UCNPs were activated with NIR light, while dark conditions were used as controls to compare the reduction in bacteria caused by NIR light. In addition, a bacterial assay without any NPs was used as a control in NIR light-illuminated experiments.

The antibacterial properties of the NPs were assessed against *S. aureus* 6850 and the associated JB1-SCV in tryptic soy broth (TSB) media. After growing the cells to the mid-logarithmic phase, they were diluted in PBS solution to approximately 10^5 colony-forming units per mL (CFU/mL). The experiment was conducted using 2.5 mL sterile glass vials. The NIR-activated mode utilised a CW NIR laser (MDL-III-980) with a central wavelength of 980 $\pm$ 10 nm and a power intensity of 700 mW (equivalent to an estimated power density of 1.75 W/cm^2). We used a 30 minute treatment time for both NIR-activated and dark conditions. We tested the laser power intensity for the duration of the treatment and found no reduction in viable cells.

The antibacterial experiment was conducted in the setup fabricated specifically for this purpose (Figure S8). A rotor with automated ON and OFF (approximately 10 s ON and 3 S OFF) was used to confirm the powder nanoparticles are in the pathway of the laser beam. The experiment under dark conditions was conducted simultaneously using the same treatment time of 30 min. Each assay included 1 mL of normalised bacteria and 5 mg of NP sample. The powder NPs were added

to each glass vial and sterilised by a UV light before use in the assay. After completion of the experiment, the assay samples were spread on LB agar (1.5%) plates for bacterial counting and evaluation. The experiments were repeated three times. The one-way ANOVA was performed using GraphPad Prism V9.0.0, with a statistical significance indicated by ns for $P>0.05$; * for $P<0.05$; ** for $P<0.01$; *** for $P<0.001$; and **** for $P<0.0001$, respectively.

A fluorescent indicator (CellROX® deep red reagent, Ex./Em. 640/660 nm, Thermo Fisher Scientific) was used to determine ROS generation from NP samples. The deep red reagent is non-fluorescent in a reduced state but exhibits a fluorogenic signal when oxidised by ROS such as hydrogen peroxide (H_2O_2), hydroxyl radical (•OH) and superoxide anion ($•O_2^-$). The NP sample (5 mg) was added to the glass vial containing Milli-Q water (1 mL). The CellROX reagent diluted in Milli-Q water was added at a final concentration of 5 µM. The treatment time of 30 min was used to illuminate the mixture in NIR-activated mode. The experiment under dark conditions was conducted using the same treatment time of 30 min. A FLUOVIEW FV3000 (Olympus) confocal laser scanning microscope was used to image the samples.

ICP−MS was conducted on an Agilent 8900x ICP-MS/MS instrument. A series of mixed-element standard solutions were used to determine the calibration curve needed to quantify Ag. Calibration standard solutions with concentrations of 0.004, 0.02, 0.1, 0.5, 1, 5, 10, 50, 100 and 200 ppb were prepared using ICP-MS-68A-B (High Purity Standard, 10 µg/mL in 2% HNO_3) solution. 5 mg of each $NaYbF_4$:Tm@ZnO:Co/Ag and $NaYbF_4$:Tm@ZnO:Co/Ag NP samples and 1 mL of Milli-Q water was used in each assay. The experiment was conducted in NIR-activated and dark conditions using the same setup for antibacterial, laser power and experiment time. Upon completion of assays, the samples were centrifuged and the supernatant was collected and filtered (0.2 µm syringe filter). Each sample was digested in HNO_3 (70% v/v) and then diluted in HNO_3 (2% v/v)

sequentially several times. Pure HNO_3 (2% v/v) was also used as the control (blank sample). The plasma conditions of RF power 1,550 W, sample depth 10 mm and Ar carrier gas flow rate of 0.95 L/min and makeup gas flow rate of 0.1 L/min with a Micro Mist nebuliser and Scott Type spray chamber were used for measurements. The collision cell was run in He mode (4 ml/min He gas flow) for the 107 Ag isotope. Online addition of Indium was used as the internal standard element.

3.6 Acknowledgements

The support from the Australian Government Research Training Program Scholarship, Alice Chu postgraduate scholarship in Chemical Engineering and The University of Adelaide is acknowledged. The authors acknowledge the instruments and scientific and technical assistance of Microscopy Australia at Adelaide Microscopy, The University of Adelaide, a facility that is funded by the university, and state and federal governments. Afshin Karami would particularly like to thank Dr Ashley Slattery from Adelaide Microscopy for valuable advice and feedback.

3.7 Supporting information

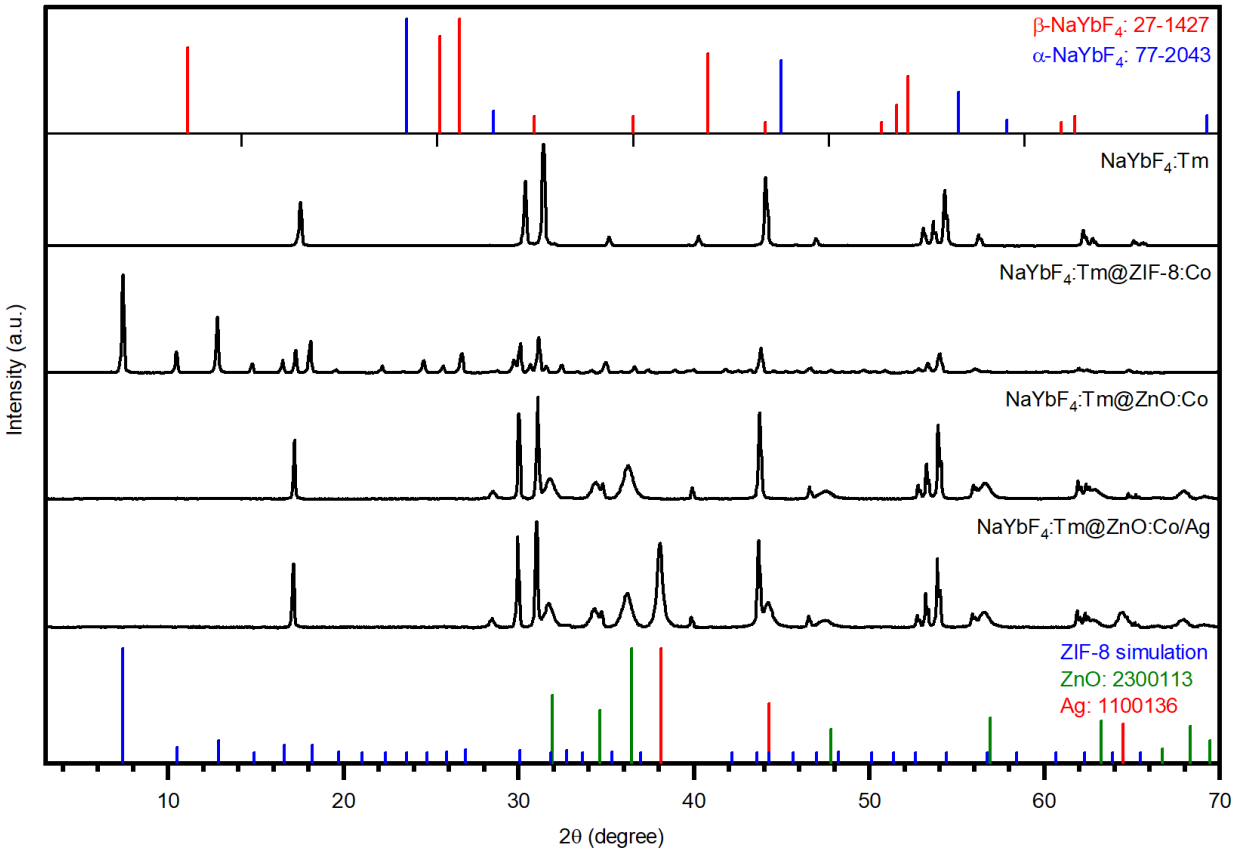

Figure S1. PXRD data for the as-synthesised $NaYbF_4$:Tm, $NaYbF_4$:Tm@ZIF-8:Co, $NaYbF_4$:Tm@ZnO:Co and $NaYbF_4$:Tm@ZnO:Co/Ag NP samples. The PDF cards for hexagonal β-$NaYbF_4$ (#27-1427), ZIF-8 simulation, ZnO (#2300113) and Ag (#1100136) are also presented.

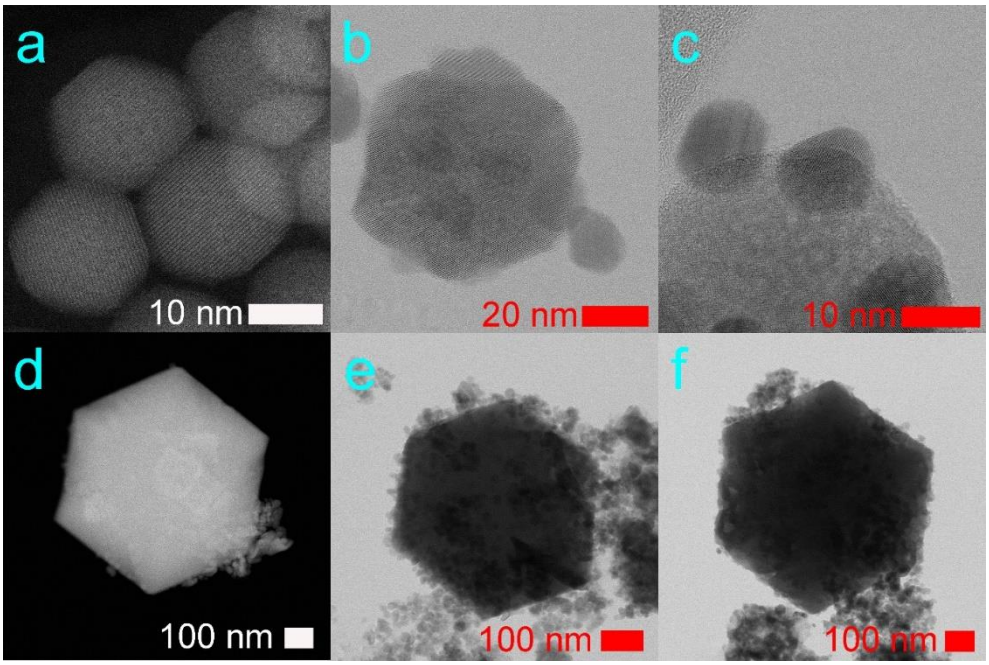

Figure S2. HRTEM image of $NaYF_4$:Yb/Tm (a), $NaYF_4$:Yb/Tm@ZnO:Co (b), $NaYF_4$:Yb/Tm@ZnO:Co/Ag (c), $NaYbF_4$:Tm (d), $NaYbF_4$:Tm@ZnO:Co (e), and $NaYbF_4$:Tm@ZnO:Co/Ag (f).

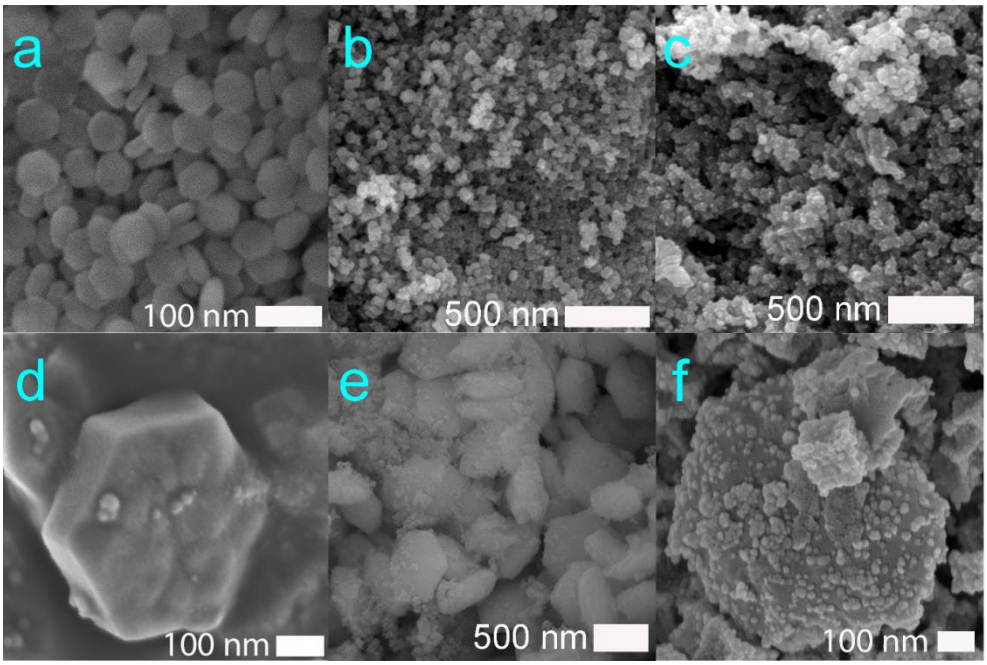

Figure S3. HRSEM image of $NaYF_4$:Yb/Tm (a), $NaYF_4$:Yb/Tm@ZnO:Co (b), $NaYF_4$:Yb/Tm@ZnO:Co/Ag (c), $NaYbF_4$:Tm (d), $NaYbF_4$:Tm@ZnO:Co (e), and $NaYbF_4$:Tm@ZnO:Co/Ag (f).

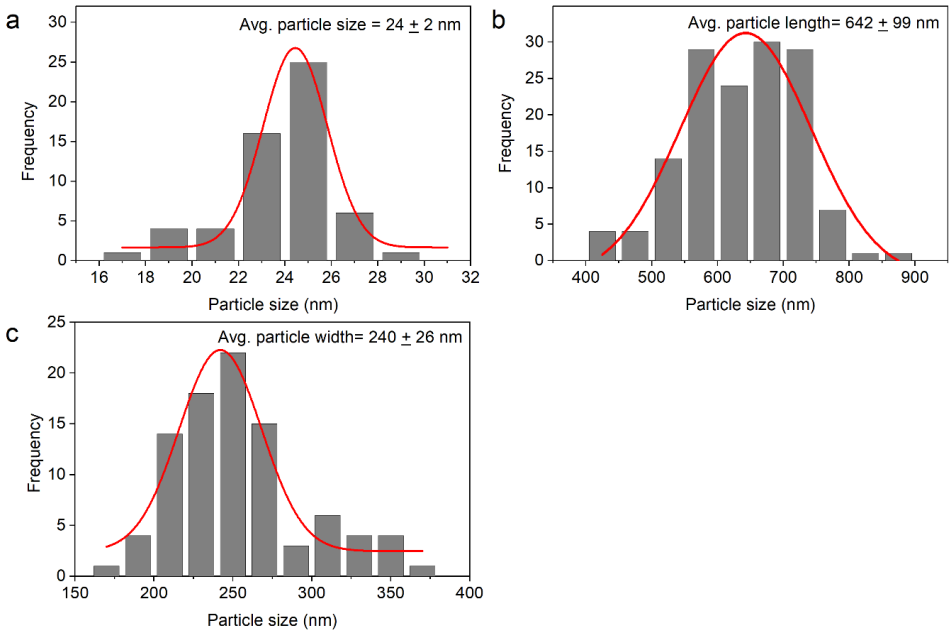

Figure S4. Particle sizes for $NaYF_4$:Yb/Tm (a), particle sizes for $NaYbF_4$:Tm (b, c).

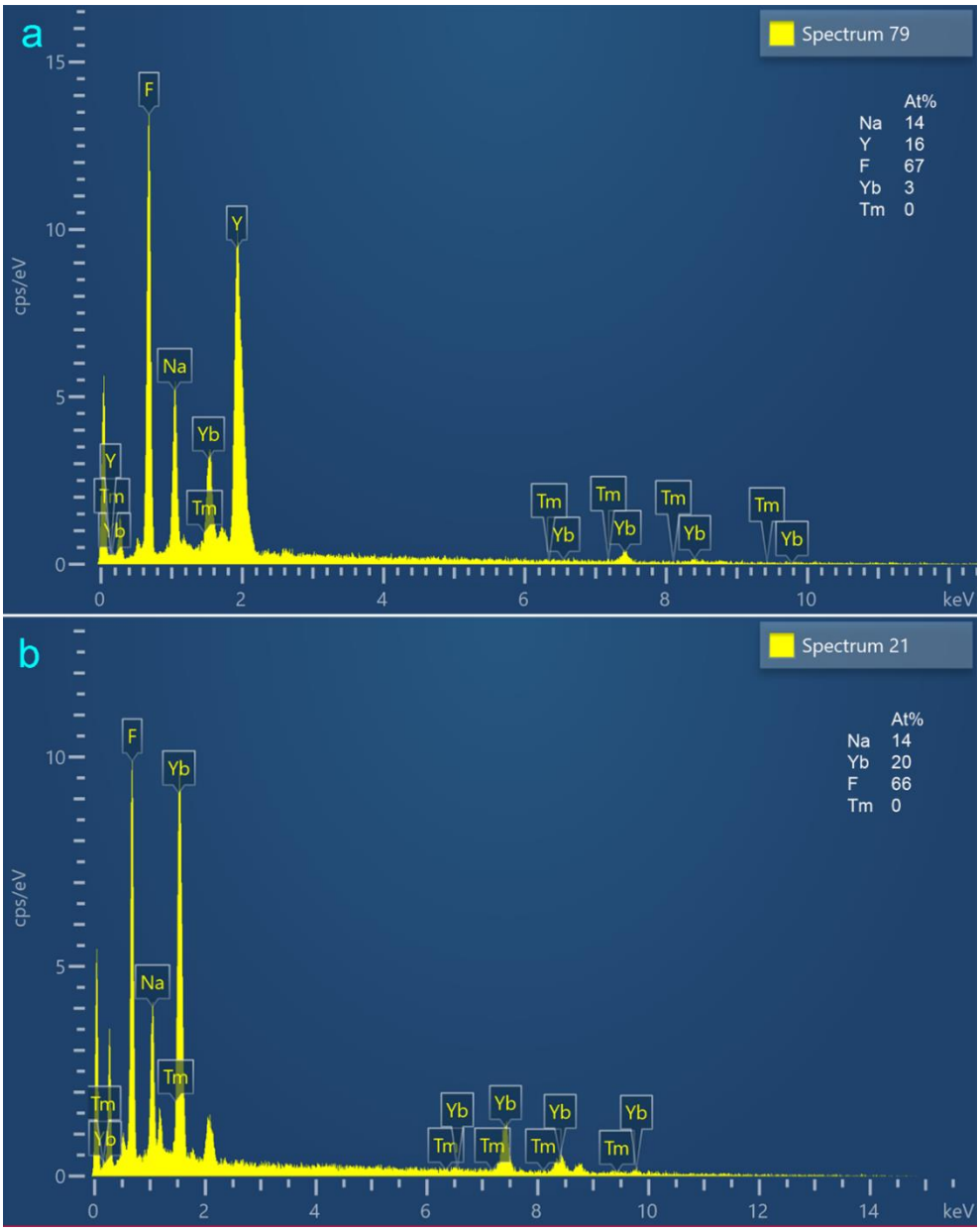

Figure S5. Example spectrum and elemental analysis determined from the SEM-EDS spectrum for $NaYF_4$:Yb/Tm (a), and $NaYbF_4$:Tm (b).

Table S1. Raw ICP-MS data for the concentration of Co, Zn, Y, Ag, Tm and Yb in the as-synthesised UCNP samples.

Samples	**Co**		**Zn**		**Y**		**Ag**		**Tm**		**Yb**	
	Conc. [ppb]	Conc. RSD[a]	Conc. [ppb]	Conc. RSD	Conc. [ppb]	Conc. RSD	Conc. [ppb]	Conc. RSD	Conc. [ppb]	Conc. RSD	Conc. [ppb]	Conc. RSD
$NaYbF_4$:Tm									1.75	0.25	197.21	0.98
$NaYbF_4$:Tm@ZnO:Co	0.64	1.58	586.14	0.70					0.57	3.33	65.18	0.42
$NaYbF_4$:Tm@ZnO:Co/Ag	0.56	5.91	553.30	0.31			58.64	0.25	0.50	5.67	55.01	0.93
$NaYF_4$:Yb/Tm					91.94	4.48			1.81	4.34	33.66	6.38
$NaYF_4$:Yb/Tm@ZnO:Co	0.78	5.26	345.08	1.05	30.97	0.60			0.57	5.85	11.78	5.58
$NaYF_4$:Yb/Tm@ZnO:Co/Ag	0.98	5.30	410.84	3.09	35.03	9.90	79.23	1.50	0.64	7.53	12.71	1.57

[a] RSD: relative standard deviation.

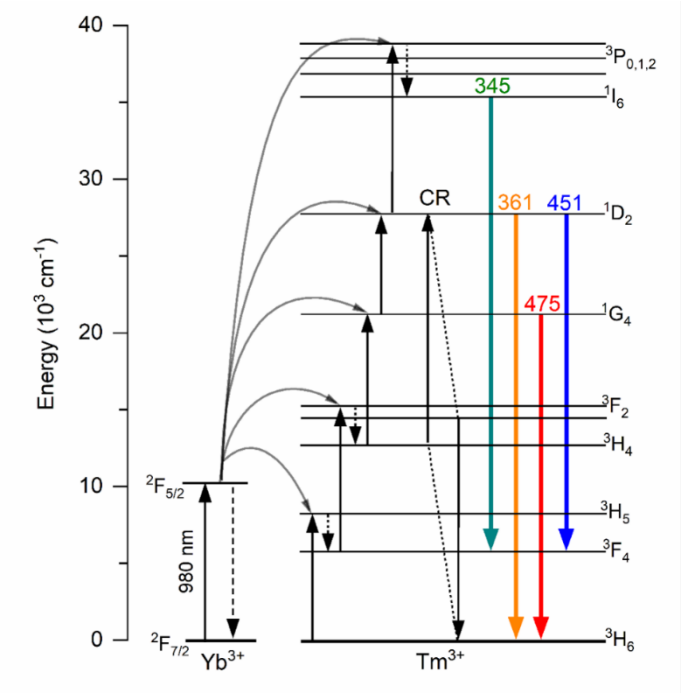

Figure S6. The schematic energy diagram for an ideal energy transfer process of Yb^{3+} to Tm^{3+}

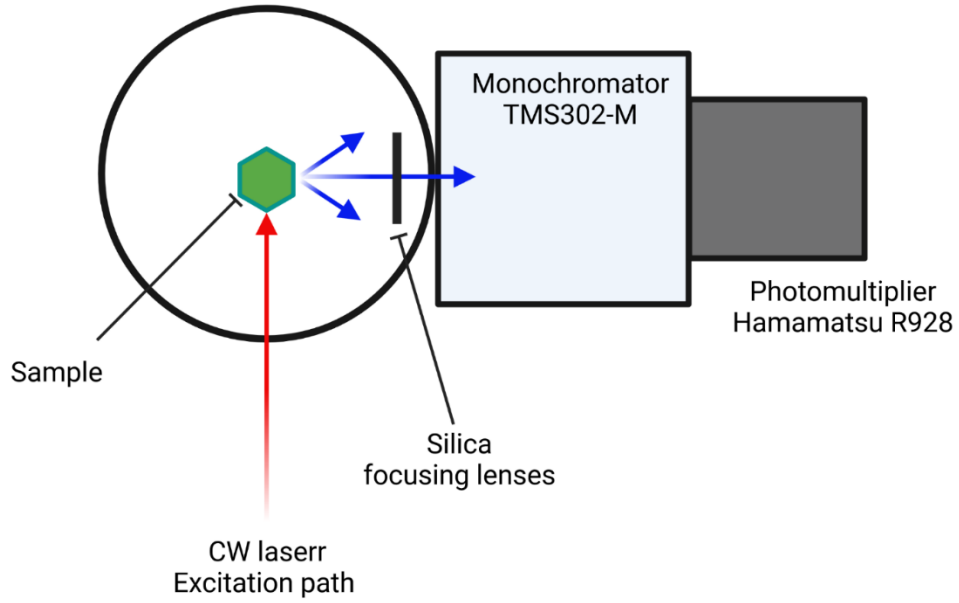

Figure S7. Schematic of the Edinburgh instruments spectrofluorimeter experimental configuration. Created with BioRender.com.

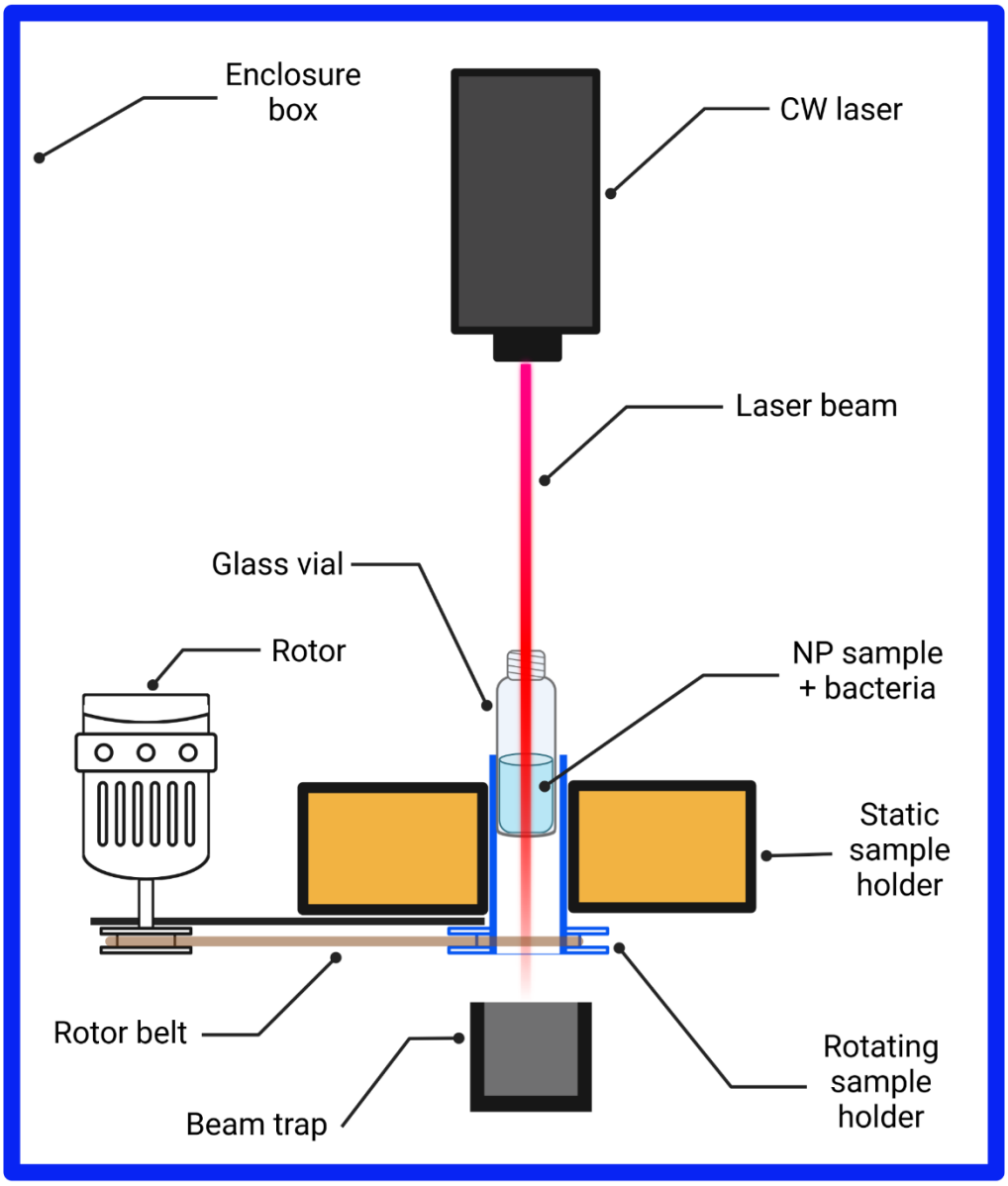

Figure S8. Schematic of the antibacterial experiment setup. Created with BioRender.com

3.8 References

(1) Wang, H.; Wang, M.; Xu, X.; Gao, P.; et al. Multi-target mode of action of silver against Staphylococcus aureus endows it with capability to combat antibiotic resistance. *Nature Communications* **2021**, *12* (1), 3331. DOI: 10.1038/s41467-021-23659-y.

(2) Zeiler, M. J.; Connors, G. M.; Durling, G. M.; Oliver, A. G.; et al. Synthesis, Stereochemical Confirmation, and Derivatization of 12(S),16ϵ-Dihydroxycleroda-3,13-dien-15,16-olide, a Clerodane Diterpene That Sensitizes Methicillin-Resistant Staphylococcus aureus to β-Lactam Antibiotics. *Angew. Chem. Int. Ed.* **2022**, *61* (17), e202117458. DOI: 10.1002/anie.202117458.

(3) Chambers, H. F.; DeLeo, F. R. Waves of resistance: Staphylococcus aureus in the antibiotic era. *Nature Reviews Microbiology* **2009**, *7* (9), 629-641. DOI: 10.1038/nrmicro2200.

(4) (ACSQHC), A. c. o. s. a. q. i. h. c. *AURA 2021: fourth Australian report on antimicrobial use and resistance in human health*; Australia, 2021.

(5) Ali, M. M.; Silva, R.; White, D.; Mohammadi, S.; Li, Y.; Capretta, A.; Brennan, J. D. A Lateral Flow Test for Staphylococcus aureus in Nasal Mucus Using a New DNAzyme as the Recognition Element. *Angew. Chem. Int. Ed.* **2022**, *61* (3), e202112346. DOI: 10.1002/anie.202112346.

(6) Tuchscherr, L.; Löffler, B.; Proctor, R. A. Persistence of Staphylococcus aureus: Multiple Metabolic Pathways Impact the Expression of Virulence Factors in Small-Colony Variants (SCVs). *Front. Microbiol.* **2020**, *11*. DOI: 10.3389/fmicb.2020.01028.

(7) Proctor, R. A.; von Eiff, C.; Kahl, B. C.; Becker, K.; McNamara, P.; Herrmann, M.; Peters, G. Small colony variants: a pathogenic form of bacteria that facilitates persistent and recurrent infections. *Nature Reviews Microbiology* **2006**, *4* (4), 295-305. DOI: 10.1038/nrmicro1384.

(8) Falanga, V.; Isseroff, R. R.; Soulika, A. M.; Romanelli, M.; et al. Chronic wounds. *Nature Reviews Disease Primers* **2022**, *8* (1), 50. DOI: 10.1038/s41572-022-00377-3.

(9) Zhang, Y.; Huang, P.; Wang, D.; Chen, J.; et al. Near-infrared-triggered antibacterial and antifungal photodynamic therapy based on lanthanide-doped upconversion nanoparticles. *Nanoscale* **2018**, *10* (33), 15485-15495. DOI: 10.1039/C8NR01967C.

(10) Chen, C.; Wang, F.; Wen, S.; Su, Q. P.; et al. Multi-photon near-infrared emission saturation nanoscopy using upconversion nanoparticles. *Nat. Commun.* **2018**, *9* (1), 3290. DOI: 10.1038/s41467-018-05842-w.

(11) Karami, A.; Farivar, F.; de Prinse, T. J.; Rabiee, H.; Kidd, S.; Sumby, C. J.; Bi, J. Facile Multistep Synthesis of ZnO-Coated β-NaYF4:Yb/Tm Upconversion Nanoparticles as an Antimicrobial Photodynamic Therapy for Persistent Staphylococcus aureus Small Colony Variants. *ACS Applied Bio Materials* **2021**, *4* (8), 6125-6136. DOI: 10.1021/acsabm.1c00473.

(12) Al-Momani, H.; Al Balawi, D. a.; Hamed, S.; Albiss, B. A.; et al. The impact of biosynthesized ZnO nanoparticles from Olea europaea (Common Olive) on Pseudomonas aeruginosa growth and biofilm formation. *Sci. Rep.* **2023**, *13* (1), 5096. DOI: 10.1038/s41598-023-32366-1.

(13) Karami, A.; de Prinse, T. J.; Spooner, N. A.; Kidd, S. P.; Sumby, C. J.; Bi, J. UV Emission from Lanthanide-Doped Upconversion Nanoparticles in Super-Resolution Microscopy: Potential for Cellular Damage. *ACS Applied Nano Materials* **2023**. DOI: 10.1021/acsanm.3c00775.

(14) Wang, L.; Tan, H.; Zhang, L.; Cheng, B.; Yu, J. In-situ growth of few-layer graphene on ZnO with intimate interfacial contact for enhanced photocatalytic CO2 reduction activity. *Chem. Eng. J.* **2021**, *411*, 128501. DOI: 10.1016/j.cej.2021.128501.

(15) Jiang, Z.; Cheng, B.; Zhang, Y.; Wageh, S.; Al-Ghamdi, A. A.; Yu, J.; Wang, L. S-scheme ZnO/WO3 heterojunction photocatalyst for efficient H2O2 production. *Journal of Materials Science & Technology* **2022**, *124*, 193-201. DOI: 10.1016/j.jmst.2022.01.029.

(16) Pradhan, N.; Das Adhikari, S.; Nag, A.; Sarma, D. D. Luminescence, Plasmonic, and Magnetic Properties of Doped Semiconductor Nanocrystals. *Angew. Chem. Int. Ed.* **2017**, *56* (25), 7038-7054. DOI: 10.1002/anie.201611526.

(17) Liu, C.; Qian, B.; Xiao, T.; Lv, C.; Luo, J.; Bao, J.; Pan, Y. Illustrating the Fate of Methyl Radical in Photocatalytic Methane Oxidation over Ag−ZnO by in situ Synchrotron Radiation Photoionization Mass Spectrometry. *Angew. Chem. Int. Ed.* **2023**, *62* (32), e202304352. DOI: 10.1002/anie.202304352.

(18) Huang, J.; Li, Q.; Lu, X.; Meng, J.; Li, Z. LSPR-Enhanced Pyro-Phototronic Effect for UV Detection with an Ag–ZnO Schottky Junction Device. *Advanced Materials Interfaces* **2022**, *9* (23), 2200327. DOI: 10.1002/admi.202200327.

(19) Shao, H.; Zhang, T.; Gong, Y.; He, Y. Silver-Containing Biomaterials for Biomedical Hard Tissue Implants. *Advanced Healthcare Materials* **2023**, *n/a* (n/a), 2300932. DOI: 10.1002/adhm.202300932.

(20) Fan, W.; Bu, W.; Shi, J. On The Latest Three-Stage Development of Nanomedicines based on Upconversion Nanoparticles. *Adv. Mater.* **2016**, *28* (21), 3987-4011, Review article. DOI: 10.1002/adma.201505678.

(21) Shi, R.; Ling, X.; Li, X.; Zhang, L.; et al. Tuning hexagonal $NaYbF_4$ nanocrystals down to sub-10 nm for enhanced photon upconversion. *Nanoscale* **2017**, *9* (36), 13739-13746. DOI: 10.1039/C7NR04877G.

(22) Zhu, Z.; Jin, L.; Yu, F.; Wang, F.; et al. ZnO/CPAN Modified Contact Lens with Antibacterial and Harmful Light Reduction Capabilities. *Advanced Healthcare Materials* **2021**, *10* (13), 2100259. DOI: 10.1002/adhm.202100259.

(23) Lü, Y.; Zhou, Q.; Chen, L.; Zhan, W.; Xie, Z.; Kuang, Q.; Zheng, L. Templated synthesis of diluted magnetic semiconductors using transition metal ion-doped metal–organic frameworks: the case of Co-doped ZnO. *CrystEngComm* **2016**, *18* (22), 4121-4126. DOI: 10.1039/C5CE02488A.

(24) Venieri, D.; Fraggedaki, A.; Kostadima, M.; Chatzisymeon, E.; et al. Solar light and metal-doped TiO2 to eliminate water-transmitted bacterial pathogens: Photocatalyst characterization and disinfection performance. *Applied Catalysis B: Environmental* **2014**, *154-155*, 93-101. DOI: 10.1016/j.apcatb.2014.02.007.

(25) Uroro, E. O.; Bright, R.; Dabare, P. R. L.; Bera, D.; Quek, J. Y.; Goswami, N.; Vasilev, K. Biocompatible Polycationic Silver Nanocluster-Impregnated PLGA Nanocomposites with Potent Antimicrobial Activity. *ChemNanoMat* **2022**, *8* (11), e202200349. DOI: 10.1002/cnma.202200349.

(26) Singh, P.; Pandit, S.; Jers, C.; Joshi, A. S.; Garnæs, J.; Mijakovic, I. Silver nanoparticles produced from Cedecea sp. exhibit antibiofilm activity and remarkable stability. *Sci. Rep.* **2021**, *11* (1), 12619. DOI: 10.1038/s41598-021-92006-4.

(27) Mehrjou, B.; Wu, Y.; Liu, P.; Wang, G.; Chu, P. K. Design and Properties of Antimicrobial Biomaterials Surfaces. *Advanced Healthcare Materials* **2023**, *12* (16), 2202073. DOI: 10.1002/adhm.202202073.

(28) Iqbal, S.; Bahadur, A.; Ali, S.; Ahmad, Z.; et al. Critical role of the heterojunction interface of silver decorated ZnO nanocomposite with sulfurized graphitic carbon nitride heterostructure materials for photocatalytic applications. *J. Alloys Compd.* **2021**, *858*, 158338. DOI: 10.1016/j.jallcom.2020.158338.

(29) Wenderich, K.; Mul, G. Methods, Mechanism, and Applications of Photodeposition in Photocatalysis: A Review. *Chem. Rev.* **2016**, *116* (23), 14587-14619. DOI: 10.1021/acs.chemrev.6b00327.

(30) Jiang, R.; Li, B.; Fang, C.; Wang, J. Metal/Semiconductor Hybrid Nanostructures for Plasmon-Enhanced Applications. *Adv. Mater.* **2014**, *26* (31), 5274-5309. DOI: 10.1002/adma.201400203.

(31) Liu, H. R.; Shao, G. X.; Zhao, J. F.; Zhang, Z. X.; et al. Worm-Like Ag/ZnO Core–Shell Heterostructural Composites: Fabrication, Characterization, and Photocatalysis. *The Journal of Physical Chemistry C* **2012**, *116* (30), 16182-16190. DOI: 10.1021/jp2115143.

(32) Buengkitcharoen, L.; Amnuaypanich, S.; Naknonhan, S.; Loiha, S.; Patdhanagul, N.; Makdee, A.; Amnuaypanich, S. Facile synthesis of robust Ag/ZnO composites by sol–gel autocombustion and ion-impregnation for the photocatalytic degradation of sucrose. *Sci. Rep.* **2023**, *13* (1), 12173. DOI: 10.1038/s41598-023-39479-7.

(33) Kriegeskorte, A.; Grubmüller, S.; Huber, C.; Kahl, B. C.; et al. Staphylococcus aureus small colony variants show common metabolic features in central metabolism irrespective of the underlying auxotrophism. *Front Cell Infect Microbiol* **2014**, *4*, 141. DOI: 10.3389/fcimb.2014.00141 From NLM.

(34) Schleimer, N.; Kaspar, U.; Knaack, D.; von Eiff, C.; et al. In Vitro Activity of the Bacteriophage Endolysin HY-133 against Staphylococcus aureus Small-Colony Variants and Their Corresponding Wild Types. *Int. J. Mol. Sci.* **2019**, *20* (3). DOI: 10.3390/ijms20030716.

(35) Gnach, A.; Lipinski, T.; Bednarkiewicz, A.; Rybka, J.; Capobianco, J. A. Upconverting nanoparticles: assessing the toxicity. *Chem. Soc. Rev.* **2015**, *44* (6), 1561-1584, Review article. DOI: 10.1039/C4CS00177J.

(36) Li, Y.; Li, S.; Huang, H. Metal-enhanced strategies for photocatalytic and photoelectrochemical CO2 reduction. *Chem. Eng. J.* **2023**, *457*, 141179. DOI: 10.1016/j.cej.2022.141179.

(37) Zhang, Y.; Wang, L.; Wang, Y.; Li, L.; et al. Degradable Antimicrobial Ureteral Stent Construction with Silver@graphdiyne Nanocomposite. *Advanced Healthcare Materials* **2023**, *n/a* (n/a), 2300885. DOI: 10.1002/adhm.202300885.

(38) Chen, Y.; Younis, M. R.; He, G.; Zheng, Z.; et al. Oxidative Stimuli-responsive "pollen-like" Exosomes from Silver Nanoflowers Remodeling Diabetic Wound Microenvironment for Accelerating wound Healing. *Advanced Healthcare Materials* **2023**, *n/a* (n/a), 2300456. DOI: 10.1002/adhm.202300456.

(39) Cieplik, F.; Deng, D.; Crielaard, W.; Buchalla, W.; Hellwig, E.; Al-Ahmad, A.; Maisch, T. Antimicrobial photodynamic therapy – what we know and what we don't. *Crit. Rev. Microbiol.* **2018**, *44* (5), 571-589. DOI: 10.1080/1040841X.2018.1467876.

(40) Sun, X.; Sun, J.; Sun, Y.; Li, C.; et al. Oxygen Self-Sufficient Nanoplatform for Enhanced and Selective Antibacterial Photodynamic Therapy against Anaerobe-Induced Periodontal Disease. *Adv. Funct. Mater.* **2021**, *31* (20), 2101040. DOI: 10.1002/adfm.202101040.

(41) Musolino, S. F.; Shatila, F.; Tieman, G. M. O.; Masarsky, A. C.; Thibodeau, M. C.; Wulff, J. E.; Buckley, H. L. Light-Induced Anti-Bacterial Effect Against Staphylococcus aureus of Porphyrin Covalently Bonded to a Polyethylene Terephthalate Surface. *ACS Omega* **2022**, *7* (33), 29517-29525. DOI: 10.1021/acsomega.2c04294.

(42) Karami, A.; Xie, Z.; Zhang, J.; Kabir, M. S.; Munroe, P.; Kidd, S.; Zhang, H. Insights into the antimicrobial mechanism of Ag and I incorporated ZnO nanoparticle derivatives under visible light. *Materials Science and Engineering: C* **2020**, *107*, 110220. DOI: 10.1016/j.msec.2019.110220.

Chapter 4: Publication 3

Publication title: UV Emission from Lanthanide-Doped Upconversion Nanoparticles in Super-resolution Microscopy: Potential for Cellular Damage

The manuscript was published in the journal of *ACS Applied Nano Materials.*

Statement of Authorship

Title of Paper	UV Emission from Lanthanide-Doped Upconversion Nanoparticles in Super-Resolution Microscopy: Potential for Cellular Damage
Publication Status	☑ Published ☐ Accepted for Publication ☐ Submitted for Publication ☐ Unpublished and Unsubmitted work written in manuscript style
Publication Details	Karami, A.; de Prinse, T. J.; Spooner, N. A.; Kidd, S. P.; Sumby, C. J.; Bi, J. UV Emission from Lanthanide-Doped Upconversion Nanoparticles in Super-Resolution Microscopy: Potential for Cellular Damage. ACS Applied Nano Materials 2023. DOI: 10.1021/acsanm.3c00775

Principal Author

Name of Principal Author (Candidate)	Afshin Karami		
Contribution to the Paper	Concept development, samples synthesis and characterization, spectral data acquisition, data processing, manuscript writing and review		
Overall percentage (%)	85%		
Certification:	This paper reports on original research I conducted during the period of my Higher Degree by Research candidature and is not subject to any obligations or contractual agreements with a third party that would constrain its inclusion in this thesis. I am the primary author of this paper.		
Signature		Date	01/06/2023

Co-Author Contributions

By signing the Statement of Authorship, each author certifies that:

i. the candidate's stated contribution to the publication is accurate (as detailed above);

ii. permission is granted for the candidate in include the publication in the thesis; and

iii. the sum of all co-author contributions is equal to 100% less the candidate's stated contribution.

Name of Co-Author	Thomas de Prinse		
Contribution to the Paper	Concept development, spectral data acquisition, data processing, manuscript writing and review		
Signature		Date	14/06/2023

Name of Co-Author	Prof. Nigel Spooner		
Contribution to the Paper	Manuscript writing and review, supervision of work		
Signature		Date	14/06/2023

Name of Co-Author	Dr. Stephen Kidd		
Contribution to the Paper	Manuscript writing and review, supervision of work		
Signature		Date	09/06/2023

Name of Co-Author	Prof. Christopher Sumby		
Contribution to the Paper	Concept development, manuscript writing and review, supervision of work		
Signature		Date	08/06/2023

Name of Co-Author	A/Prof Jingxiu Bi		
Contribution to the Paper	Manuscript writing and review, supervision of work		
Signature		Date	15/06/2023

4.1 Abstract

Upconversion nanoparticles (UCNPs) co-doped with lanthanide ions have recently attracted significant attention as fluorescent probes for super-resolution microscopy (SRM). This is due to the advantages of UCNPs over other fluorescence probes, such as fluorescent proteins, owing to their unique optical properties, limited photobleaching and sharp emissions. However, the concurrent emission of ultraviolet (UV) wavelength radiation by UCNPs and the potential for cell photodamage, which may limit useful live cell analysis, have been overlooked. Here, UCNPs synthesised with eight commonly used combinations of Yb/Tm and Yb/Tm/Gd dopants were excited by either pulsed or continuous wave (CW) lasers to evaluate their UV emission. The ratio of emitted UV-A and UV-B were measured relative to blue emission at 475 nm, which is traditionally used for imaging during SRM. We demonstrate that most UCNP samples emit UV light and that the dopant concentration has a key role in generating UV emissions. In addition, the use of pulsed or CW lasers for excitation could lead to a large variation in the amount of UV emitted. This work highlights the importance of considering upconversion dopant composition and concentration, as well as analysing the emission of synthesised UCNPs before their use to prevent unwanted cell photodamage during live cell imaging by SRM. Moreover, it established a need to improve the visible light emission of UCNPs with respect to UV emission for SRM applications.

4.2 Introduction

Fluorescence microscopy is a widespread tool used to enhance our understanding of biological interactions, especially spatial organization.[1] It visualises the physiological details and interactions of biological molecules with high sensitivity in real-time whilst being a low-invasive technique.[2] However, fluorescence microscopes are characterised by their spatial resolution limitation of

200 nm. This limitation is enforced by the light diffraction limit rationalised by Abbe's rule.[3] This weakness has limited the use of these microscopes as an effective tool in biological sciences for the study of nanosized bio-structures, such as neurons and cytoskeletons. The development of super-resolution microscopy (SRM) techniques has solved the resolution limitations of fluorescence microscopy.[4] The prime technique in SRM is stimulated emission depletion (STED), implemented by either pulsed or continuous wave (CW) lasers.[5-7] The SRM approaches rely upon fluorescence probes that are capable of emission upon excitation by light in an intensity range from W/cm^2 to GW/cm^2 (compared with fluorescence microscopy at mW/cm^2 to W/cm^2) and a specific wavelength, while being photostable.[8]

Recently, lanthanide ion-doped upconversion nanoparticle (UCNP) probes have gained attention for SRM over the traditionally used organic fluorophores.[9] The UCNP probes have advantages including sharp and tuneable light emission, long lifetimes, low background autofluorescence and limited photobleaching.[10] The most common co-doped UCNP ion pairs used as a probe in SRM are Yb^{3+} and Tm^{3+}.[11] Yb/Tm based UCNPs produce bright emissions in the blue region at 475 nm when excited by near-infrared (NIR) light at 980 nm. The NIR photon is absorbed by the Yb^{3+} ion (sensitiser) and transferred sequentially to the Tm^{3+} ion (activator), with consecutive energy transfer events exciting the Tm^{3+} ion into the emissive $^1D_2$ state. The $^1D_2$ state then emits blue fluorescence at 450 nm, undergoing a $^1D_2 \rightarrow {}^3F_4$ transition. Additionally, this excitation pathway promotes a $^1G_4 \rightarrow {}^3H_6$ transition that emits fluorescence at 475 nm. The blue emissions at 450 and 475 nm are imaged together through a NIR short pass blocking filter in a microscopy setting due to the similar wavelength of these emissions. Continual development of Yb/Tm doped UCNPs to achieve brighter blue emissions suitable for imaging in SRM has been pursued.[12] In that work, the focus has been on improving the efficiencies of photon transfer processes and the lifetimes of the

sequential Tm^{3+} excited states.[13,14] A high concentration of Yb^{3+} sensitiser improves the transfer of the photon to Tm^{3+} in Yb/Tm doped UCNPs, while the core/shell structure of Yb/Tm UCNPs reduces surface quenching effects, hence improving the upconversion efficiency.[15,16] These strategies have been implemented to produce brighter blue light emission from a given power density of 980 nm excitation light.[17] However, this improvement in the blue fluorescence yield has a drawback. The energy transfer process continues past the blue, generating fluorescence in the ultraviolet (UV) range (wavelengths 280 to 400 nm). Thus, Yb/Tm doped UCNPs imaged near or inside of cells will have the ability to emit UV light in this wavelength range too.

While some studies intentionally generate UV light from UCNPs to directly influence or kill cells[18-20], most imaging applications do not consider the emissions in this range. This raises questions as to whether some UCNPs have significant energetic UV emissions that are not being detected, commonly due to most spectral systems having difficulty readily characterising UV emissions. While UV emissions are rarely studied and do not contribute to standard imaging experiments, UV emission is potentially damaging to the cells under study at such close range.

The UV light spectral region is subdivided into three distinct regions UV-A (wavelengths between 320 to 400 nm), UV-B (wavelengths between 280 to 320 nm) and UV-C (wavelengths between 200 to 280 nm).[21] UV light causes cell phototoxicity by intracellular interactions or generating reactive oxygen species (ROS) that consequently cause oxidative damage to the cell. DNA strand breakage and thymidine dimerisations, UV response activation apoptosis and toxic reactive oxygen species (ROS) generation (endogenous and exogenous) have been identified as the main causes of cell damage by UV light (Scheme 1).[22]

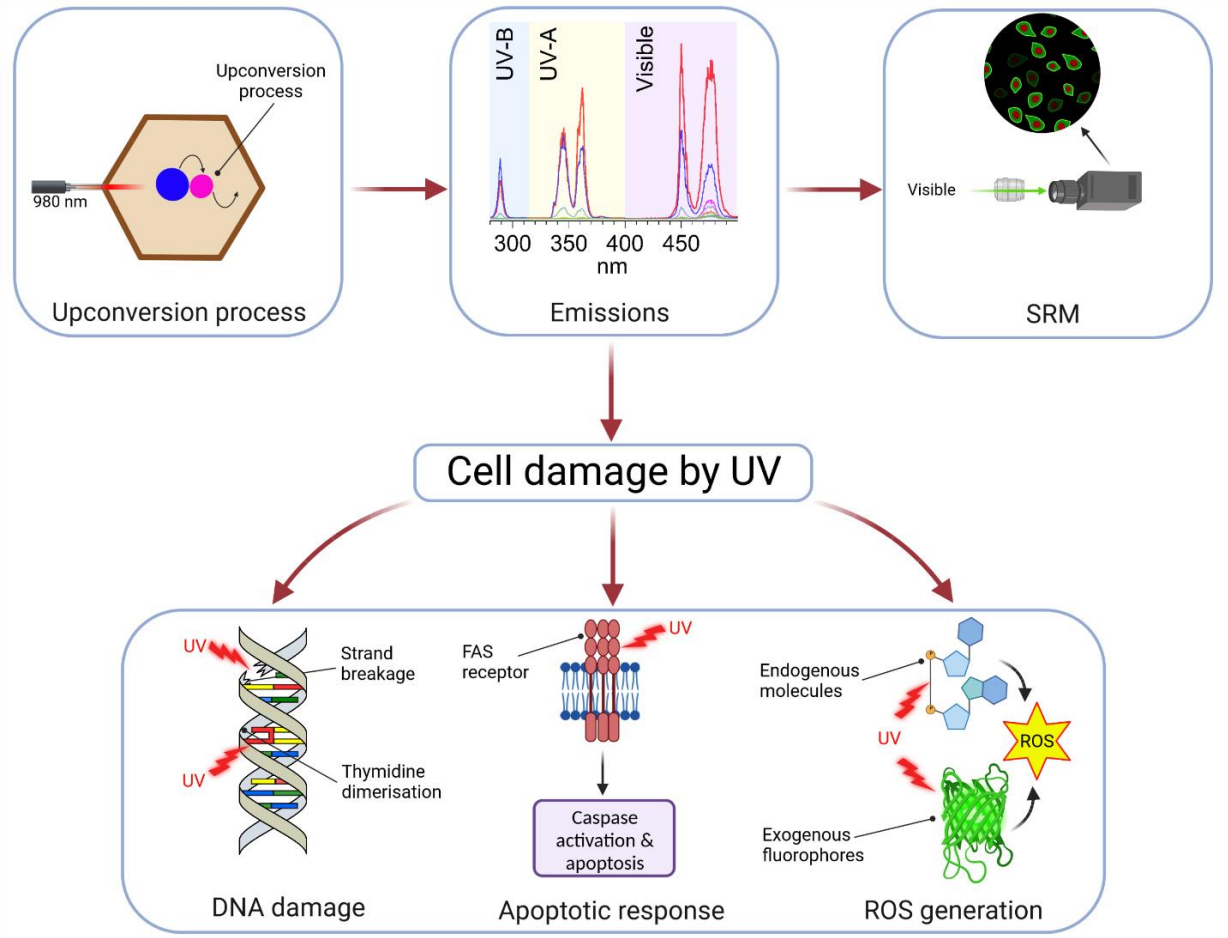

Scheme 1. Excitation of lanthanide-doped upconversion nanoparticles (UCNPs) with near-infrared (NIR) light and the associated upconversion emissions in the UV-A, B and visible regions. The Yb3+ is shown as blue and Tm3+ in pink in the UCNP in the scheme. The visible emissions at 450 and 475 nm are desired for super-resolution microscopy (SRM); however, certain lanthanide-doped materials, such as Tm/Yb doped UCNPs, also emit UV-A and UV-B light. The potential cell damage by the emitted UV light is presented when it causes damage to biological molecules, e.g. DNA strand breakage/base dimerization, initiates apoptotic pathways, or interacts with endogenous (e.g. NADH) or exogenous (e.g. GFP) molecules to generate reactive oxygen species. Components adapted with permission from Ref.[22]. Copyright 2020 IOP Publishing Ltd. Created with BioRender.com.

This paper reports the UV emission properties for several UCNPs designed for SRM applications. Eight UCNPs, based on $NaYF_4$:Yb/Tm, $NaYbF_4$:Tm and $NaYbF_4$:Tm/Gd structures, were

synthesised and characterised for this purpose. The presence and extent of UV emissions under continuous and pulsed excitation regimes were measured using UV sensitive detector systems, with the potential negative impact of high energy emissions from these UCNPs on a surrounding biological sample discussed. The findings from this work suggest that a correct measurement of emission across the UV range, in addition to the targeted visible emission measurements, should be strongly considered when developing UCNPs for SRM applications.

4.3 Results and discussion

4.3.1 Synthesis, composition, and morphology

Lanthanide-doped UCNPs, NaYb(100-x%)F_4:Tm(x%) (x = 1, 2.5, 5 and 10 mol%), NaY(100-x%)F_4:Yb(18%)/Tm(x%) (x = 1 and 5 mol%) and NaYb(100-x%)F_4:Tm(0.5%)/Gd(x%) (x = 5 and 20 mol%), were synthesised via the thermolysis method (Scheme 2).[23]

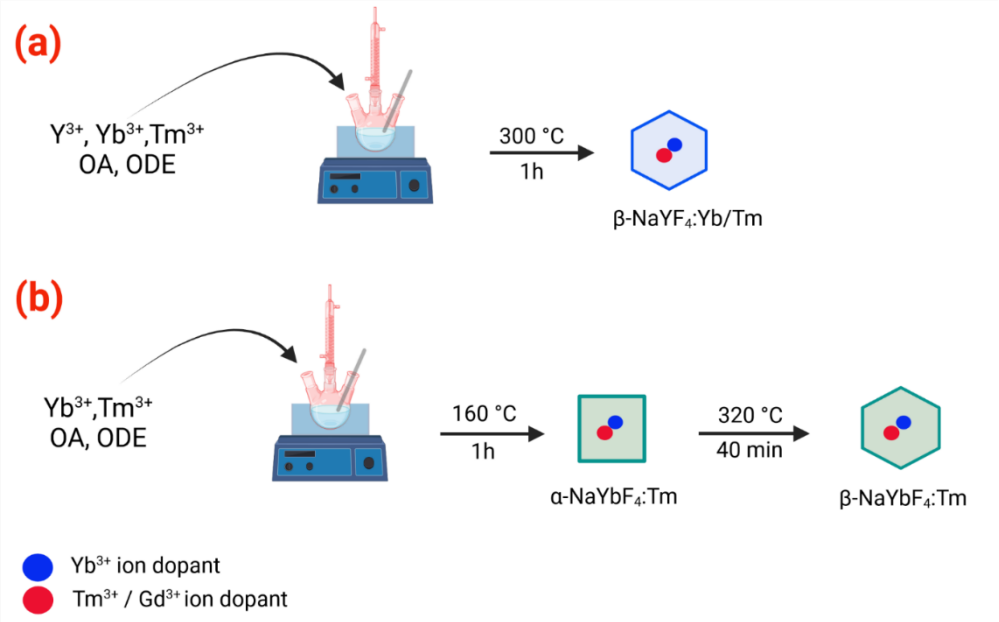

Scheme 2. Methods used to synthesise the lanthanide-doped upconversion nanoparticles. (a) Synthetic procedure for hexagonal β-$NaYF_4$:Yb/Tm materials and (b) for hexagonal β-$NaYbF_4$:Tm UCNPs. Created with BioRender.com.

Powder X-ray diffraction (PXRD) data for NaYb(100-x)F_4:Tm(x) and NaY(100-x%)F_4:Yb(18%)/Tm(x%) samples confirmed all materials are crystalline, with the diffraction peaks indexed to the hexagonal β-$NaYbF_4$ (# 27-1427) and hexagonal β-$NaYF_4$ (# 16-0334) structures (Figure 1a and Table S1). The only exception is nanoparticle sample NaYb(90%)F_4:Tm(10%) which shows a small trace of the cubic structure of α-$NaYbF_4$ (# 77-2043) (Figure 1a and Table S1). The 5% Gd loaded sample of NaYb(100-x)F_4:Tm(0.5%)/Gd(x) shows diffraction peaks that match a mixture of hexagonal β-$NaYbF_4$ (# 27-1427) and cubic α-$NaYbF_4$ (# 77-2043) structures (Figure 1a and Table S1). In comparison, the sample with 20% Gd loading shows a predominately hexagonal structure with a small trace of the cubic structure (Figure 1a and Table S1). In the presence of Gd^{3+}, the formation of a phase pure hexagonal β-$NaYbF_4$ host material by the thermolysis method was challenging despite using a well-established two-step synthesis procedure (160 °C for 1 hour to form the cubic α-phase, then 320 °C for 40 minutes to convert cubic α-phase to hexagonal β-phase). Potentially, this issue could be overcome by adjusting the synthesis protocol, including the ratio of OA to ODE, the synthesis time, the use of different precursor salts, etc. As altering the synthesis parameters may affect the surface chemistry of the NP samples, leading to different emissions, we avoided this approach.

Transmission electron microscopy (TEM) images revealed that the synthesised UCNPs are uniformly sized, as shown by the mean particle sizes for each NP sample (Figure 1b to i, Table S1 and Figure S9-11). The as-synthesised hexagonal $NaYbF_4$ based samples are larger, as expected, as increasing the Yb^{3+} concentration and the synthesis time will normally lead to an increase in particle size (Figure 1d to g, S9-11). While this could be overcome by increasing the oleic acid (OA) to 1-octadecene (ODE) ratio in the synthesis and altering the other synthesis parameters,[24] the same ratio of OA to ODE was used in the synthesis of all NPs for consistency. The composition

of the nanoparticles, primarily determined by the feed ratios of the components, was confirmed by Energy Dispersive Spectroscopy (EDS) as well as inductively-coupled plasma mass spectrometry (ICP-MS). EDS analysis showed that the Tm concentrations were approximately 1 and 5 mol%, as expected, in the NaY(100-x%)F_4:Yb(18%)/Tm(x%) (x= 1 and 5 mol%) NP samples, respectively (Table S1 & Figure S1 to S2). The Tm dopant concentration was measured to be 1, 2, 5 and 11% for the NaYb(100-x%)F_4:Tm(x%) (x=1, 2.5, 5 and 10 mol%) NP samples, respectively (Table S1 & Figure S3 to S6). Finally, the Gd concentration was also measured to be 5 and 28%, while the Tm concentrations were found to be negligible for NaYb(100-x%)F_4:Tm(0.5%)/Gd(x) (x=5 and 20 mol%) NP samples, respectively (Table S1 & Figure S7 to S8. Note that the figures in Figures S1 to S8 show SEM-EDS measurement results rounded to whole numbers). In the SEM-EDS, Tm and Gd elemental doses were calculated based on Yb values and Tm/Yb and Gd/Yb ratios. ICP-MS data for the UCNP samples supported these results, confirming Tm concentrations of 0.9% and 4.8% in NaY(100-x%)F_4:Yb(18%)/Tm(x%) (x= 1 and 5 mol%), respectively (Table S1 & S2). Similarly, the Tm dopant concentration was measured to be 1.0, 2.5, 5.0 and 10.1% for the NaYb(100-x%)F_4:Tm(x%) (x=1, 2.5, 5 and 10 mol%), respectively. Finally, the Gd concentrations were found 4.9 and 20.0% while the Tm concentrations were 0.4 and 0.3% for NaYb(100-x%)F_4:Tm(0.5%)/Gd(x) (x=5 and 20 mol%) NP samples, respectively. Overall, the combined EDS and ICP-MS results confirmed that the Tm and Gd dopant concentrations broadly matched those used in the synthesis, and moreover, that the distribution of dopants was relatively homogenous, e.g. surface-sensitive EDS data matched that for the bulk sample determined by ICP-MS.

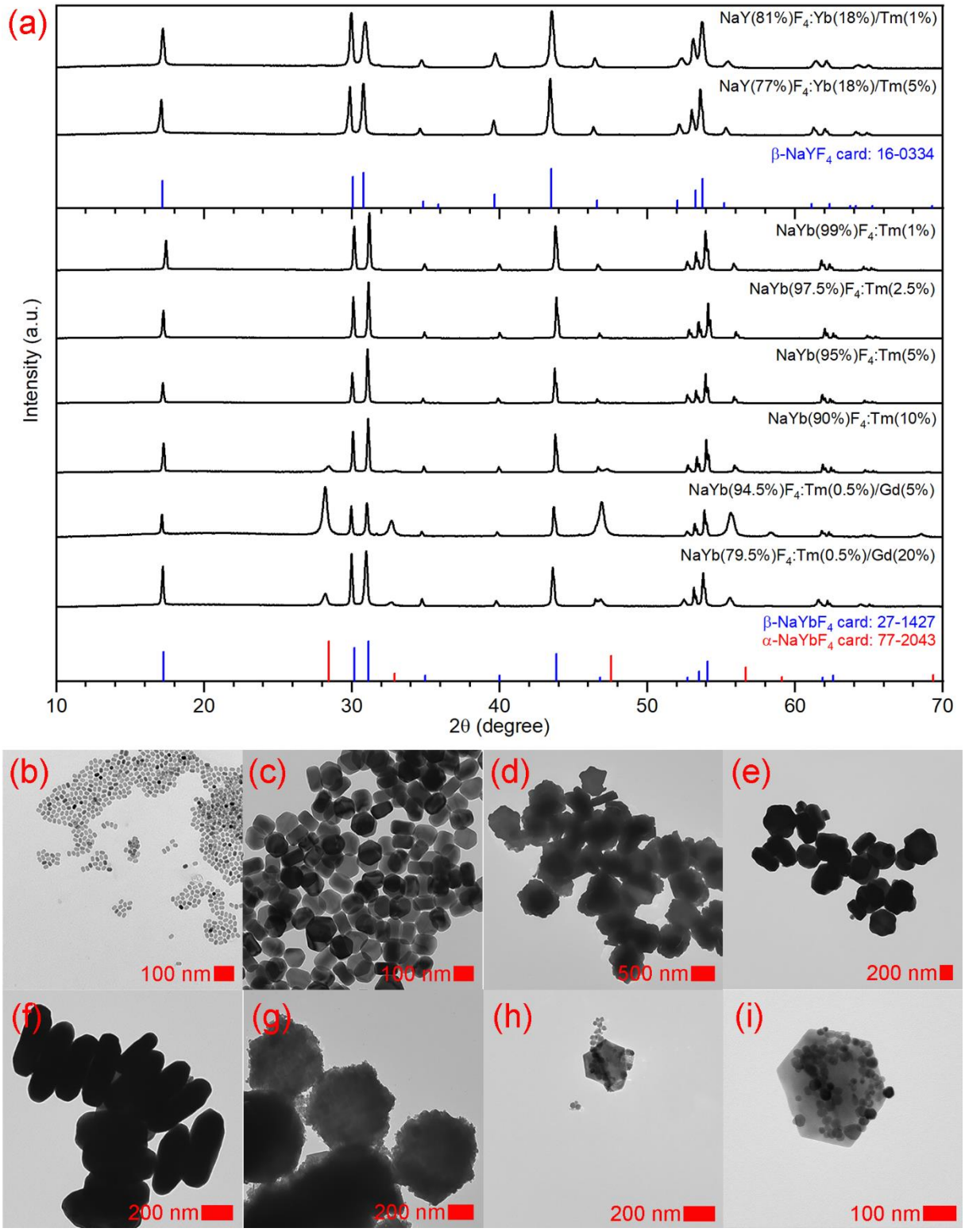

Figure 1. PXRD PXRD data and TEM images for the as-synthesised UCNP samples. (a) PXRD data for the NaYb(100-x)F_4:Tm(x) (x=1, 2.5, 5 and 10 mol%), NaY(100-x%)F_4:Yb(18%)/Tm(x%)(x=1 and 5 mol%) and NaYb(100-x)F_4:Tm(0.5%)/Gd(x) (x= 5, 16.5, and 20 mol%) UCNP samples. The PDF cards

for α-$NaYF_4$ # 06-0342, β-$NaYF_4$ # 16-0334, α-$NaYbF_4$ # 77-2043 and β-$NaYbF_4$ # 27-1427 are also presented. (b) TEM images for the as-synthesised hexagonal structure of β-$NaY(81\%)F_4$:Yb(18%)/Tm(1%), (c) hexagonal structure of β-$NaY(77\%)F_4$:Yb(18%)/Tm(5%), (d) hexagonal structure of β-$NaYb(99\%)F_4$:Tm(1%), (e) hexagonal structure of β-$NaYb(97.5\%)F_4$:Tm(2.5%), (f) hexagonal structure of β-$NaYb(95\%)F_4$:Tm(5%), (g) hexagonal structure of β-$NaYb(90\%)F_4$:Tm(10%). The β-$NaYb(90\%)F_4$:Tm(10%) UCNP sample shows a small trace of the cubic structure of α-$NaYbF_4$ while the majority of the sample is hexagonal structure β-$NaYbF_4$ as confirmed by the PXRD data, (h) $NaYb(94.5\%)F_4$:Tm(0.5%)/Gd(5%). The $NaYb(94.5\%)F_4$:Tm(0.5%)/Gd(5%) UCNP sample shows a mixture of hexagonal β-$NaYbF_4$ and cubic α-$NaYbF_4$ structures, (i) $NaYb(79.5\%)F_4$:Tm(0.5%)/Gd(20%) UCNP. The $NaYb(79.5\%)F_4$:Tm(0.5%)/Gd(20%) UCNP sample shows a small trace of the cubic structure α-$NaYbF_4$ while the majority of the sample is hexagonal β-$NaYbF_4$ as confirmed by the PXRD data.

4.3.2 Excitation power density used

UCNP samples can be excited by continuous laser sources, which offer high average power, or by pulsed lasers, which offer relatively low average power but can produce a large amount of light in a short period. Both pulsed and CW lasers are routinely used to excite UCNPs in microscopy; however, the behaviour of an upconversion material often changes depending on the power regime used (high average power or high peak power). To investigate this, different excitation lasers were used to excite the samples studied, with a CW diode laser allowing high average power and a pulsed optical parametric oscillator producing high peak excitation power. The CW measurements were conducted using a 980 nm solid-state diode laser with its power adjustable over 50 mW to 2 W. The emission spectra of the samples were collected at 75 mW spread over a beam spot size of 40 mm^2, exciting the samples at a power density of 0.185 W/cm^2. This laser was additionally used in the CW slope dependence measurements up to a maximum value of 4.5 W/cm^2. In comparison, the spectra for the samples under high peak power excitation were produced by a flashlamp pumped optical parametric oscillator (OPO) laser set at 980 nm which fired pulses 5 ns

in length at 20 Hz. The laser had an energy of 0.8 mJ per pulse and was focused down to a spot size of 2 mm, resulting in a peak power of 0.16 MW and a power density of 5.1 MW/cm^2. A second OPO laser was used for the high peak power slope dependence measurements due to its wider accessible range pulse of energies. This OPO fired pulses of 5 ns in length at 10 Hz with maximum energy at 980 nm of 7.5 mJ over a 5 mm diameter beam, giving a peak power density approaching 8 MW/cm^2.

While optical techniques can vary greatly between research groups, the excitation power densities used in this paper (hundreds of mW/cm^2 to several W/cm^2 for CW excitation and several MW/cm^2 for pulsed excitation) are representative of many examples of UCNP excitation and STED microscopy.[25-27]

4.3.3 Emission spectra

To examine the factors that govern the presence and extent of UV emission for UCNPs, including nanoparticle composition and excitation mode, the synthesised UCNPs were excited under continuous and pulsed excitation regimes and the emission was measured using a visible and UV sensitive detector system. The power density for the pulsed and CW lasers was kept unchanged for the excitation of all NP samples to allow comparison of the emissions. The NaYb(99%)F_4:Tm(1 mol%) and NaYb(97.5%)F_4:Tm(2.5 mol%) NP samples were the brightest of the eight samples with strong blue emissions at 450 and 475 nm. These also gave UV-A and B emissions at 289, 345 and 361 nm when excited by the pulsed laser (Figures 2a, b and c). Under non-saturated conditions, UV emission is considerably less likely than blue emission, due to the UV emission requiring additional transfers of energy from the sensitiser ion ($^1G_4 \rightarrow {}^3H_6 \propto I_{ex}{}^3$ (475 nm), $^1D_2 \rightarrow {}^3F_4$, $^1D_2 \rightarrow {}^3H_6 \propto I_{ex}{}^4$ (455, 362 nm), $^1I_6 \rightarrow {}^3F_4$, $^1I_6 \rightarrow {}^3H_6 \propto I_{ex}{}^5$ (345, 289 nm)).

If this model for excitation is used, any UV lines shorter than 362 nm would have low intensities relative to the blue emission lines. However, due to the high sensitiser (Yb^{3+}) to activator (Tm^{3+}) ion ratio, a saturation of the Tm energy levels results in much higher UV emission than a non-saturated model suggests. The $^1I_6 \rightarrow {}^3H_6$ peak has a significantly lower intensity than the other transitions and, as such, this emission line is difficult to observe for any other samples. Similar to the data with the pulsed laser, in a CW laser excitation experiment, the NaYb(99%)F_4:Tm(1%) and NaYb(97.5%)F_4:Tm(2.5 mol%) again showed among the strongest blue wavelength emissions (Figure 2d and e), although NaY(81%)F_4:Yb(18%)/Tm(1%) and NaYb(94.5%)F_4:Tm(0.5%):Gd(5%) samples had relatively brighter blue emission. CW excitation of the Gd doped samples showed a noticeable emission peak at 311 nm, compared with pulsed laser excitation, with a much lower excitation intensity.

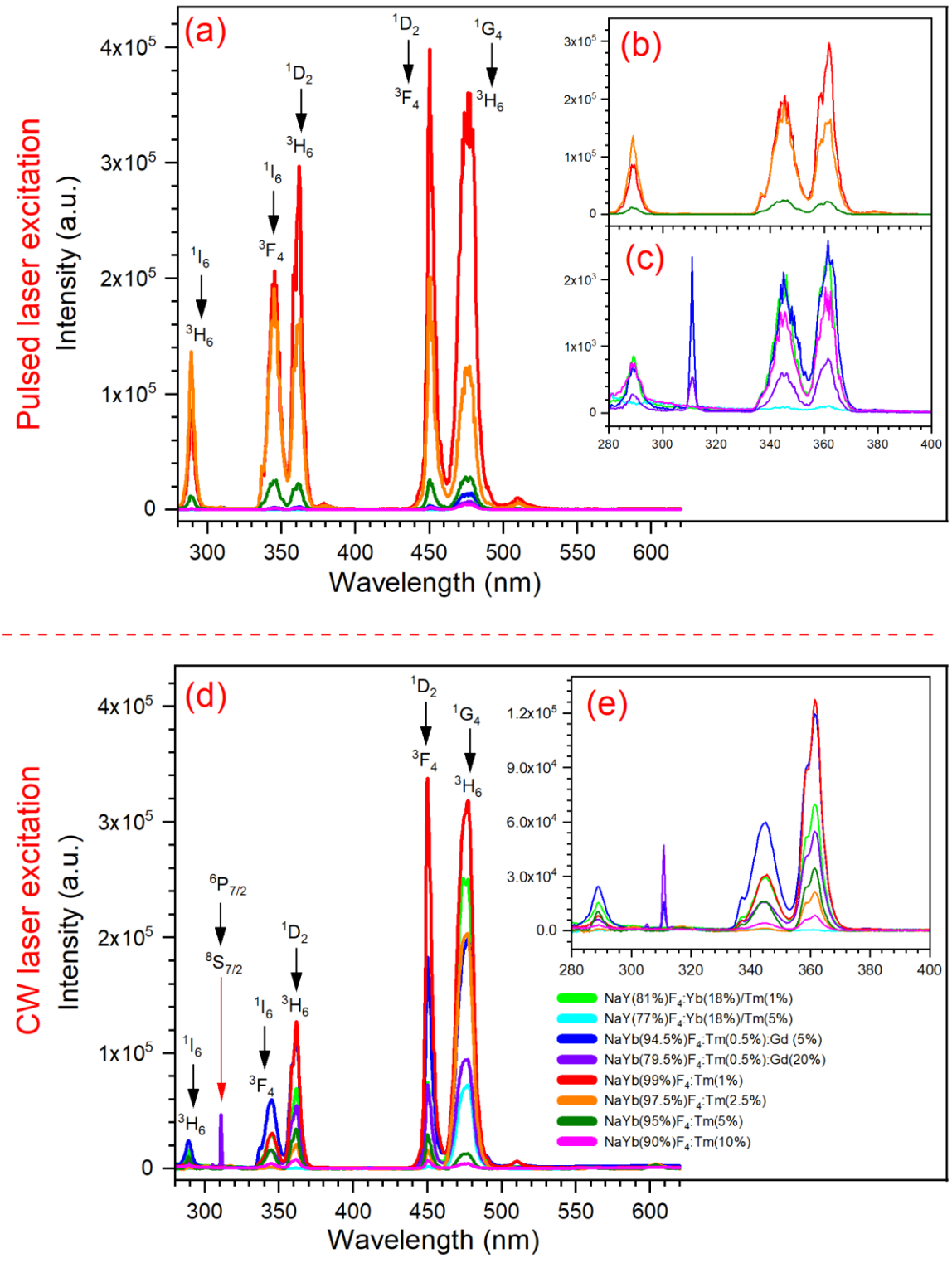

Figure 2. Emission spectra for UCNP samples excited by pulsed and CW lasers. (a) Emission spectra for pulsed laser excitation, and (b and c) enlargements of the emission spectra for the UV-A and B regions for

brightest and less bright NP samples excited by pulsed laser. (d) Emission spectra for CW laser excitation, and (e) enlargement of the emission spectra for the UV-A and B emissions excited by CW laser.

The emission peaks from UCNP samples were further analysed to assess the significance of the UV emission relative to the blue emission. For this purpose, first, the peak intensity for each sample was extracted and presented based on dopant concentration changes (Figures 3a and c, 4a and c, 5a and c). Then the ratio of combined peaks in the UV-A (320 to 400 nm) and UV-B (280-320 nm) ranges to the blue (475 nm) peak for each sample was calculated, based on the area under the curve for each peak (Figure 3b and d, 4b and d, 5b and d). For the NaY(100-x%)F_4:Yb(18%)/Tm(x%) (x = 1 and 5 mol%) samples, the 1% Tm doped sample showed higher peak intensity for the 289, 345 and 361 nm peaks, when excited by pulsed laser (Figure 3a). The UV-A ratio to 475 nm peak was also much higher than the UV-B ratio for the 1% Tm sample in the pulsed laser excitation mode (Figure 3b). This result reveals that in $NaYF_4$ UCNPs, a lower Tm composition may lead to a higher chance of generating UV emissions. This behaviour could be due to a reduced number of emitting ions and this appears to be suppressed by increasing the Tm doping. A similar observation occurs when the NP samples were excited by the CW laser (Figures 3c and d). The emission peak intensity for the 1% Tm sample again showed a higher value than the 5% Tm sample (Figure 3c). The 1% Tm sample showed a larger UV-A to 475 nm emission ratio (Figure 3d), while the ratio of UV-B to 475 nm is similar for both 1 and 5% Tm samples under CW laser excitation (Figure 3d), highlighting the importance of irradiation setup.

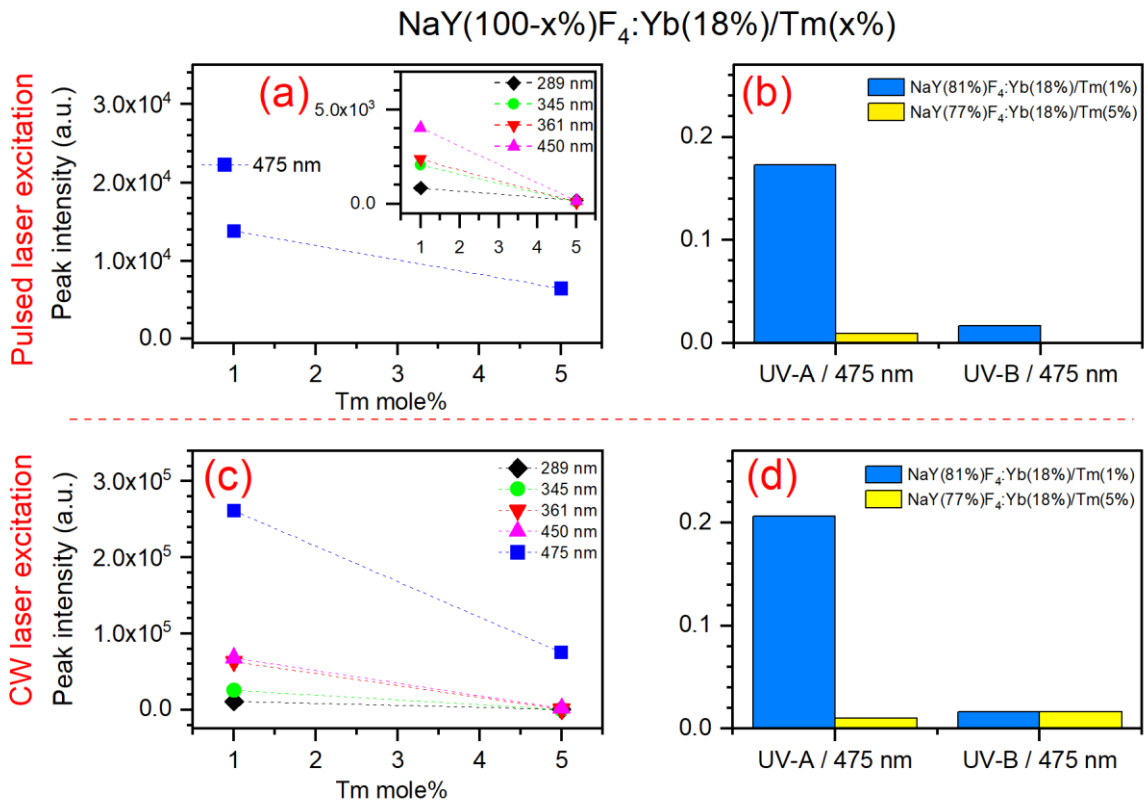

Figure 3. Emission peak intensities and ratios of UV-A and B to the 475 nm peak for NaY(100-x%)F_4:Yb(18%)/Tm(x%) (x = 1 and 5 mol%). (a) Emission peak intensity data excited by the pulsed laser, with the lower emission peaks are shown in the inset, (b) ratios of UV-A and B to the 475 nm peak excited by the pulsed laser, (c) emission peak intensity data excited by the CW laser, and (d) ratios of UV-A and B to the 475 nm peak excited by the CW laser.

For samples of composition NaYb(100-x%)F_4:Tm(x%) (x = 1, 2.5, 5 and 10 mole%) excited by the pulsed laser, the intensity of emission at 345, 361, 450 and 475 nm declines upon increasing the Tm loading from 1% to 10% (Figure 4a). This reduction in brightness can be explained by the combined effects from quenching caused by higher activator concentration (Tm^{3+}) and improved upconversion efficiency by increasing the sensitiser concentration (Yb^{3+}).[28,29] Interestingly, despite the 1% Tm loaded sample giving the most intense emission overall, the sample with 2.5% Tm loading showed the highest ratio of UV-A and B to 475 nm emission among all four samples

excited by pulsed laser (Figure 4b). This is due to the 475 nm peak in the 1% Tm loaded sample having a considerably higher emission intensity compared with the other samples. The ratio of UV-A and B to 475 nm emission decreased in the following order: 2.5 > 5 > 1 > 10% Tm doped samples, respectively (Figure 4b). This result demonstrates that although the sample with 1% Tm loading gives the most intense emission among these four samples (Figures 2a and 4a), the 2.5 and 5% Tm doped NP samples emit a larger proportion of UV radiation.

For excitation with the CW laser, again the sample with 1% Tm loading showed the most intense emissions at 345, 361, 450 and 475 nm among all these NP samples (Figure 4c), while the NP samples with 5 and 10% Tm loading showed the highest ratio of UV-A and B to 475 nm emission, respectively (Figure 4d). These results reveal that both the ratio of emissions at particular wavelengths and the emission intensities need to be considered to reduce the probability of phototoxicity in SRM applications. Of the four $NaYb(100-x\%)F_4:Tm(x\%)$ NP samples excited by the pulsed laser, both lower (1%) and higher (10%) doping leads to less pronounced UV emission relative to the desired 475 nm emission. However, the 475 nm emission is notably brighter for the 1% Tm sample (Figures 4a). In contrast, when these four samples are excited by the CW laser, the sample with 2.5% doping emits less UV emission relative to the 475 nm emission, while the 5% Tm doped sample emits the most intense UV emission relative to the 475 nm emission, definitively highlighting the importance of considering how the UCNPs are excited in an SRM application (Figure 4c and d).

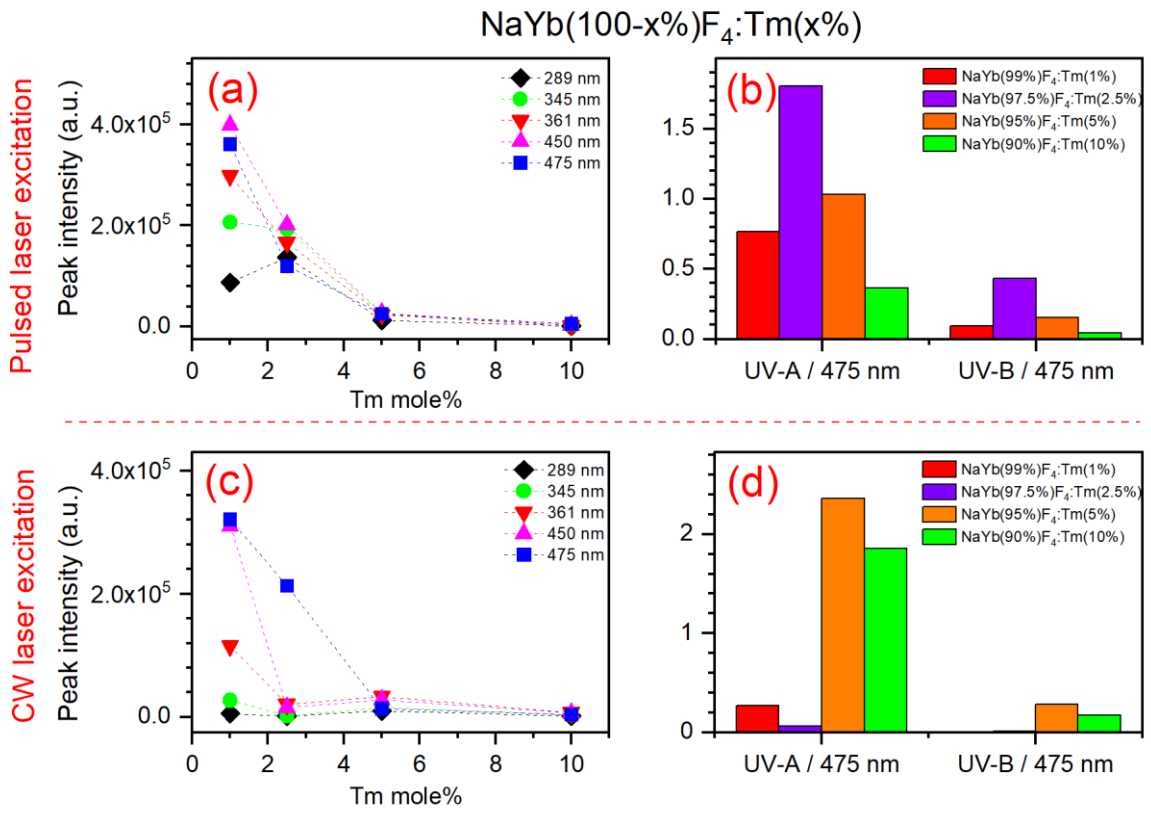

Figure 4. Emission peak intensities and ratios of UV-A and B to the 475 nm peak for NaYb(100-x%)F_4:Tm(x%) (x = 1, 2.5, 5 and 10 mol%). (a) Emission peak intensity data excited by the pulsed laser, (b) ratios of UV-A and B to the 475 nm peak excited by the pulsed laser, (c) emission peak intensity data excited by the CW laser, and (d) ratios of UV-A and B to the 475 nm peak excited by the CW laser.

Gd-doped UCNPs have attracted attention recently as a fluorescent probe for STED microscopy due to their ability to reduce depletion saturation intensity. Gd dopants create massive energy migration networks that move energy from the luminescent centre to surface quenchers. Consequently, STED microscopy using these nanoparticles benefits from a lower-intensity light source to deplete photons.[30] While, the Gd dopant in UCNP has addressed a fundamental problem with STED microscopy (high-intensity depletion), it also produces UV emission at 311 nm. With Yb/Tm co-doped UCNP exhibiting UV emission, we used $NaYbF_4$ host structure to investigate

Gd effects on UV generation. In these UCNP samples, the Tm^{3+} concentration was reduced from 1 mmole to 0.5 mmole to emphasise Gd^{3+} effects.

As the PXRD results (Figure 1a) demonstrated for the as-synthesised Gd-doped UCNP samples, a quantity of the α-$NaYbF_4$ host possessing a cubic crystal structure was formed in addition to the desired hexagonal β-$NaYbF_4$ crystal host phase. In the emission investigation conducted herein, the cubic α-$NaYbF_4$ crystal form is considered to be essentially silent and should not contribute to the emissions. Due to their structures, hexagonal β-$NaREF_4$ crystal structures (RE= rare earth, e.g. β-$NaYbF_4$ and β-$NaYF_4$) are generally regarded as more efficient than their cubic counterparts.[31-33] In both of these host UCNPs, emission from the cubic phase is extremely weak, due to a number of structural differences. In particular, the hexagonal β-$NaYF_4$ crystal structure has lanthanide sites in low-symmetry positions where distorted electron clouds are heavily coupled to the lattice. In comparison, the cubic crystal structure has random substitutions between the lanthanide cations and the Na^+ ions within the crystal lattice. This inevitably complicates their bonding, and thus the cubic phase suffers from a greater energy loss than the hexagonal phase.[34] Additionally, there is a smaller distance between adjacent lanthanide ions in the hexagonal structure, 3.548 Å compared to 3.868 Å in the cubic form.[31] For these reasons, typically the upconversion efficiency of lanthanide-doped $NaYF_4$ with a cubic structure is considerably lower than that of the hexagonal $NaYF_4$ forms.[34] For example, the hexagonal β-$NaYF_4$ crystal structure facilitates the emission of Er^{3+} lanthanide ions with a four times higher efficiency than the cubic α-$NaYF_4$ crystal structure.[33] Although potentially a Gd-doped UCNP with pure hexagonal $NaYbF_4$ host crystal could be synthesised by adjusting the synthesis procedure, for consistency and to prevent changing the surface chemistry of the as-synthesised UCNPs, the same synthesis protocol was used to synthesise

these NPs resulting in the analysis necessarily involving a small amount of the weakly emitting cubic phase.

For the NaY(100-x%)F_4:Yb(18%)/Tm(0.5%)/Gd(x%) (x = 5 and 20 mole%) samples excited by pulsed laser, the emission peaks at 289, 311, 345, 450 and 475 nm for the 5% Gd sample were of higher intensity compared with higher 20% Gd loaded sample (Figure 5a). The new peak observed at 311 nm is due to Gd emission in both samples. Interestingly, the peak intensities for these two samples were notably higher when excited by CW laser (Figure 5c). This in turn leads to a much higher ratio of UV-A and B to 475 nm emission in CW laser excitation mode compared with pulsed laser excitation mode (Figure 5b, d). The UV-A to 475 nm ratio of emission is higher for 5% Gd doped UCNPs, while the UV-B to 475 nm is higher at 20% Gd doped materials in both pulsed and CW laser mode (Figure 5b, d). These results indicate that Gd doping could play a key role in the UV light generation of these NP samples, possibly by the formation of crystal defects. It has been shown previously that crystal defects change the symmetry around the lanthanide emitter ions in the crystal structure, leading to better energy transfer and enhanced upconversion luminescence.[35] Hence, the phototoxicity of the NaYb(100-x%)F_4:Tm(0.5%)/Gd(x%) NP samples for SRM applications may directly be correlated with the Gd loading and concomitant changes in the crystal structure.

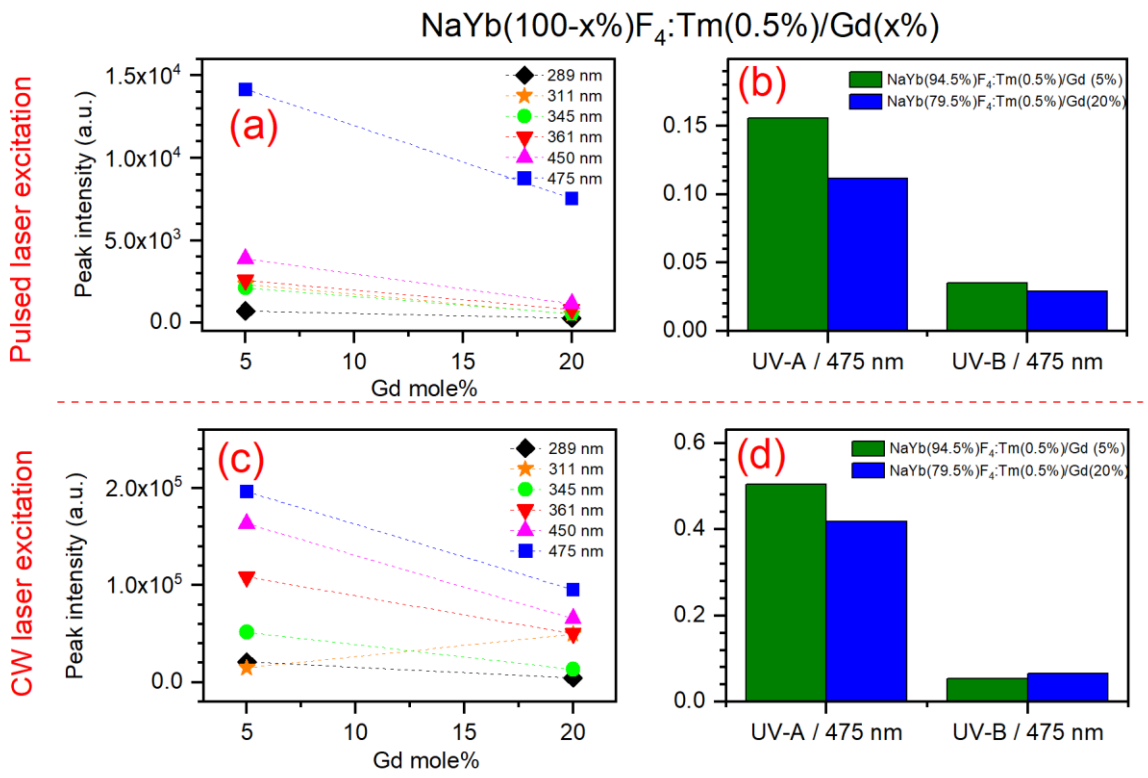

Figure 5. Emission peak intensities and ratios of UV-A and B to the 475 nm peak for NaYb(100-x%) F_4: Tm (0.5%)/Gd (x%) (x = 5 and 20 mol%). (a) Emission peak intensity data excited by the pulsed laser, (b) ratios of UV-A and B to the 475 nm peak excited by the pulsed laser, (c) emission peak intensity data excited by the CW laser, and (d) ratios of UV-A and B to the 475 nm peak excited by the CW laser.

The as-synthesised UCNP samples were all confirmed to generate UV emissions in the UV-A and B regions. The UV light generated from the same host crystal structure is directly correlated with the dopant concentration and whether a pulsed or CW laser is used for excitation. The amount of dopant concentration also affects the intensity of blue light emission, which is required for SRM. Therefore, adjusting the dopant concentration and conducting analysis of the emissions of any new UCNPs should provide a route to enhance the blue light emission, whilst reducing the UV emission, and thereby facilitate the development of more efficient and biologically benign fluorescence probes for SRM.

4.3.4 Excitation power dependency of visible and UV emission

In the UCNPs, visible and UV emission is generated from the Tm^{3+} ion by sequential energy transfer from the Yb^{3+} ion. This process involves four energy transfer steps to cause emission from the $^1D_2$ level in Tm^{3+}, and five steps to reach the $^1I_6$ level (Figure 6a). This process can be experimentally verified by adjusting the excitation intensity incident on the sample and measuring the change in intensity at each emission wavelength peak.[36] The change in emission compared to excitation intensity is directly proportional to the number of photons being used in the upconversion process,[37] and therefore, when the data is presented in a log-log plot, the power dependency is given by the slope of the excitation/emission curve. The excitation power dependency was measured for all the as-synthesised NP samples. The power dependency for the $NaYb(95\%)F_4$:$Tm(5\%)$ sample excited by pulsed laser is given in Figure 6b, while the slope values for all samples excited by both pulsed and CW lasers are presented in Tables S3 and S4, respectively. It should be noted that the experimentally determined slope values are less than the ideal values, as is often observed.[38,39] This is primarily due to Tm^{3+} - Tm^{3+} cross relaxation improving the photon efficiency of the system[40] (Figure 6a), especially in the CW case, as well as minor saturation effects at the high intensities used during both CW and pulsed excitation.

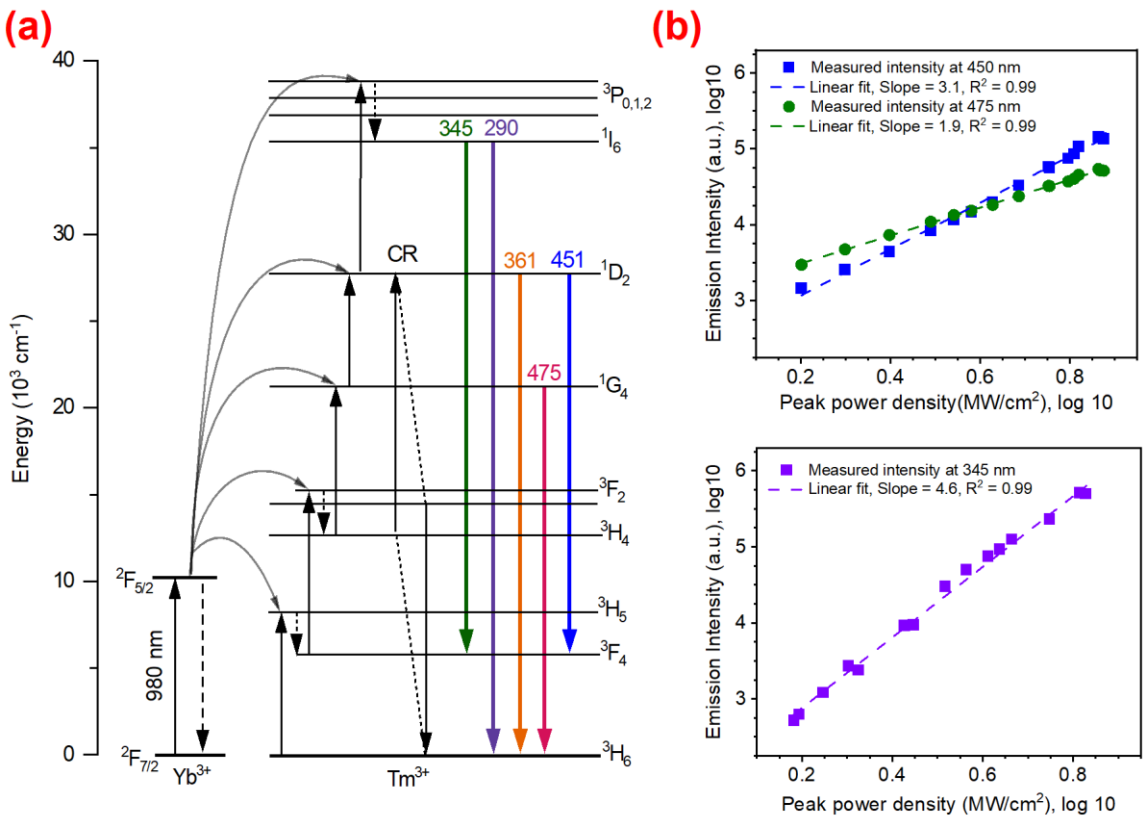

Figure 6. An energy diagram showing an ideal energy transfer process, and power dependence graphs for the UV and blue emissions from NaYb(95%)F_4:Tm(5%) excited by the pulsed laser. (a) The schematic shows energy transfer mechanism of Yb^{3+} to Tm^{3+}. (b) The observed slope values are less than the ideal values, but the UV energy dependence is clearly higher than either of the visible emissions and no saturation is observed.

These slope values are important as they show that the UV emissions are not uniquely saturated in comparison to the visible emission and that raising the excitation intensity incident on the samples will increase the UV emission more, relative to the visible emission. Considering the NaYb(95%)F_4:Tm(5%) case depicted in Figure 6b, if a microscopy experiment required the blue emission at 475 nm to be arbitrarily four times as bright, the excitation laser energy only needs to be increased two times the original intensity due to the 2-photon process occurring. This two-times increase in excitation power causes the other blue emission to amplify to approximately 8.5 times its original value, however, and the UV peak at 345 nm magnifies to over 25 times as intense.

Some reports of STED have utilised CW excitation power densities in excess of what is demonstrated in this report, reaching above the kW/cm^2 level.[12,41] Despite the upconversion pathways eventually saturating under these conditions, the UV light generation under this excitation power regime would be even higher than has been demonstrated in this work.

4.3.5 Difficulties in correct UV emission detection

It is of high importance for SRM applications of new fluorophores, like UCNPs, that measurement of the UV range be undertaken, as the difficulty of detecting this range can often lead to the erroneous assumption that a lack of detected UV emissions represents a true lack of emissions, with the true emission peaks simply being unobserved. Fluorescence emission can be difficult to detect and quantify in the UV range as a result of the intense absorption of UV light by many materials, including optical glass which is designed to have high transparency in the visible regime. This leads to an experimental bias where even strong UV light produced will not be measured and therefore not considered in its impact on the surrounding biological environment. To correctly analyse UV peaks without significant bias, the transparency of fibres, lenses, objectives, and filters should be assessed, as well as the ability of the spectrometer to detect the UV range.

Lenses and filters created using borosilicate, N-BK7 or sapphire glass have substantial absorption and will easily completely block the detection of UV light. This includes microscope slides or coverslips if they are placed in the light collection path. Often the specialised coating layer on interference filters will also have significant UV absorption that prevents meaningful measurements. If optical components are required for filtering or analysis, a common choice of material is calcium fluoride, due to its high UV/visible/NIR transmission as well as its robustness and affordability compared to other fluoride glasses. Fused silica or quartz glass components are

also popular but do exert some small deviations to the true UV intensity due to slightly increased absorption over the UV-B range. This is small enough to be compensated for if a response curve is known, such as is done for optical components in commercial spectrofluorometer systems.

Most visible/NIR detectors based on silicon imaging sensors do have some sensitivity below 350 nm, but this generally decreases to approximately a quarter of the visible light quantum efficiency by 300 nm.[42,43] Many fixed grating systems ignore this range however in favour of the optimised resolution and efficiency across the visible and NIR range through the choice of grating material and position that is often detrimental to UV detection.

To examine the ability of a given spectrometer and collection optics to detect UV emission, mercury calibration lamps are useful sources of bright, sharp peaks in the UV and visible region with well-defined emission wavelengths.[44,45] These can be found as small, low-powered and portable sources for easy calibration of bench-top spectrometer systems. Strong lines are present across the UV-A, UV-B and UV-C range and detection of these lines is positive confirmation that a spectrometer system is appropriately capable of UV light detection.

Water and most buffer systems offer acceptable UV transmission to allow for fluorescence peak detection; however, biological media often do not. This includes intracellular analysis, where the high transmission of an infrared excitation source and the emitted visible light are not matched by any UV emission, which is effectively absorbed by many parts of the cell including proteins[46] and DNA.[47] The consequence of this is that measurements to detect UV emission from doped nanoparticles cannot be undertaken while in a biological medium. The lack of detected UV emission could be falsely interpreted as a lack of UV light being produced, when the emission is

simply much more strongly absorbed relative to the visible light or NIR emission, and potentially influencing the environment in ways that are unaccounted for.

4.3.6 Potential impact of UV emission from UCNPs on the biological environment

Most studies on the biological impact of UV radiation have been focused on skin cancer caused by UV light from the sun.[48,49] UV-C has the highest energy level and causes the greatest biological damage, followed by UV-B and then UV-A.[50] Biological damage from exposure to UV light is mainly caused by the absorption of UV light by intracellular biomacromolecules or photosensitizing interactions via exogenous or endogenous reactions that generate ROS.[51,52] The main mechanism of cell damage by UV-A radiation is the interaction of UV-A with cellular chromophores (which act as photosensitisers) to generate ROS that damage DNA and the proteins that repair damaged DNA.[53] UV-A absorption by cellular chromophores generates a pair of radicals, including a photosensitiser anion and a target cation. The photosensitiser anion can generate superoxide, which can be converted into hydrogen peroxide and hydroxyl group via a series of reactions. Guanine (one of the building blocks of DNA and RNA), when excited by UV-A, reacts with water to form 8-hydroxy-7,8-dihydroguanyl radical which then oxidises to 8-oxo-7,8-dihydroguanine (8-oxoGua) by reaction with molecular oxygen.[54] UV-B directly damages cellular DNA by forming bulky adducts such as double-stranded breaks (DSBs) and cyclobutane pyrimidine dimers (CPDs), as well as generating ROS like UV-A.[55] The UV-B radiation specifically generates ROS following absorption by chromophores such as carotenoids, vitamin A, pyridoxamine, eumelanin and phaeomelanin, and heme groups.[56]

The wavelength and intensity of the light emitted, the exposure duration and the biological sample type are important factors influencing the potential for cell damage in microscopy analysis.[57] The

photosensitivity of U2OS, COS-7 and HeLa cells has been studied at 405, 488, 514 and 558 nm irradiation wavelengths for SRM,[58] and the study used both pulsed and CW lasers. While 100% of cells survived exposure to 514 nm wavelength light, the higher energy 405 nm wavelength light led to all cells being unviable. This was despite the 514 nm wavelength experiments being performed at an exposure duration of 4 times longer and with a laser power 10 times higher than used in the 405 nm wavelength case. While this is concerning for cell viability in SRM applications, it is worth noting that the UV emissions from the UCNPs shown in our study are related to the emission of light by UCNPs after near IR excitation. The UCNP UV emissions have lower fluxes in comparison to excitation laser used in the above study.

The as-synthesised UCNP samples emit three peaks in the UV region at 361 nm ($^1D_2 \rightarrow {}^3H_6$), 345 nm ($^1I_6 \rightarrow {}^3F_4$) and 290 nm ($^1I_6 \rightarrow {}^3H_6$), with the Gd doped UCNPs samples showing an additional peak at 311 nm ($^6P_{7/2} \rightarrow {}^8S_{7/2}$)[59]. The amount of UV- A and B generated by UCNP probes may not cause an immediate impact on the biological samples being examined by SRM; however, these UV emissions could cause phototoxicity in long dynamic imaging of live cells or more sensitive biological samples using SRM. Therefore, a consideration particularly needs to be given to the effects over a longer experiment or if the high excitation laser power is used in combination with particular UCNP fluorophores. In terms of the improvement of existing UCNP fluorophores or the development of new materials, there are opportunities to reduce the UV-A and B generation by modifying dopant types and ratios used.

4.4 Conclusions

UCNPs are in continuous development as fluorescence probes for the SRM due to their inherently favourable photoluminescence characteristics. This study evaluated the UV emissions generated

from UCNPs that have the potential to cause phototoxicity (cell damage). Eight combinations of Yb/Tm and Yb/Tm/Gd doped UCNPs were synthesised and the UCNPs were excited by pulsed or continuous wave (CW) lasers.

We found that a lower Tm activator loading, of 1 mol%, in a $NaYF_4$:Yb/Tm UCNP will lead to higher UV-A and B emissions relative to the desired emission at 475 nm when excited by a pulsed or CW laser. However, in UCNPs with a $NaYbF_4$:Tm structure, NPs with an intermediate Tm loading of 2.5 and 5 mol% showed higher UV emissions compared to 1 and 10 mol% doped materials when excited by both pulsed and CW lasers. Moreover, for $NaYF_4$:Yb/Tm/Gd nanoparticles, samples excited by the CW laser showed significantly higher UV emissions compared with a pulsed laser excitation methodology. Importantly, the work has shown that most samples emitted UV radiation but that the dopant concentration and the ratio of activator to sensitiser have a significant impact on the amount of UV generated relative to the desired visible emission at 475 nm. The use of pulsed or CW lasers for excitation of the UCNPs also leads to a large variation in the amount of UV light produced relative to the visible emission.

Overall, these combined results highlight the importance of carefully tailoring the upconversion dopant concentration, as well as undertaking detailed fluorescent analysis on synthesised UCNPs. These detailed spectroscopic studies need to consider the challenges of measuring emitted UV light and the experimental biases present in standard characterisation workflows and apparatus. These actions are deemed necessary to prevent potential unwanted cell photodamage during live cell imaging by SRM and to improve the performance of new UCNPs being developed for SRM applications.

4.5 Experimental section

4.5.1 Raw materials

Gadolinium (III) chloride hexahydrate (Sigma-Aldrich, 99%), thulium (III) chloride (Sigma-Aldrich, 99.9%), ytterbium(III) chloride hexahydrate (Sigma–Aldrich, 99.9%), yttrium (III) chloride hexahydrate (Sigma-Aldrich, 99.9%), ammonium fluoride (Chem–Supply, 98%), sodium hydroxide (Sigma–Aldrich, 99.99%), 1-octadecene (Sigma–Aldrich, technical grade, 90%), Oleic acid (Sigma-Aldrich, technical grade, 90%), methanol (Sigma–Aldrich, 99.9%), ethanol (Chem–Supply, 100%) and cyclohexane (Chem–Supply) were obtained from commercial sources and used without further purification.

4.5.2 Synthesis of nanoparticles

The $NaYb(100\text{-}x)F_4$:Tm(x) (x = 1, 2.5, 5 and 10 mol%) and $NaYb(100\text{-}x)F_4$:Tm(0.5%)/Gd(x) (x = 5 and 20 mol%) were synthesised via a similar method to that previously reported[18] with slight modifications. $NaYb(100\text{-}x)F_4$:Tm(x) (x = 1, 2.5, 5 and 10 mol%) and $NaYb(100\text{-}x)F_4$:Tm(0.5%)/Gd(x) (x = 5 and 20 mol%) were synthesised via the same method with the following modifications: after the addition of the $NaOH/NH_4F$ solution and evaporation of methanol, the suspension was heated to 160 °C for 1h then to 320 °C for 40 minutes.[24]

4.5.3 Characterisation

Powder X-ray diffraction (PXRD) data were collected on a MiniFlex 600 (Rigaku, Cu Kα, λ = 0.15418 nm). Samples were mounted in a flat plate holder and the data was collected with the instrument operating at 40 kV and 15 mA by scanning 2θ from 10° to 70° with a step size of 0.02°. The hexagonal structure β-$NaYbF_4$ (JCPDS # 27-1427), cubic structure α-$NaYbF_4$ (JCPDS

77-2043), hexagonal structure β-$NaYF_4$ (JCPDS # 16-0334) and cubic structure α-$NaYF_4$ (JCPDS # 06-0342) were used for comparison to the experimental data.

Scanning electron microscopy (SEM) was conducted on a Quanta 450, and transmission electron microscopy (TEM) on an FEI Tecnai G2 Spirit TEM operated at an accelerating voltage of 120 kV. The NP samples were coated with platinum (3 nm) before SEM measurements. Samples for TEM were dispersed in absolute ethanol using a vortex shaker, a small droplet of each suspension was transferred to the TEM sample holder, and the ethanol evaporated before placing into the TEM.

ICP−MS was conducted on an Agilent 8900x ICP-MS/MS instrument. A series of mixed element standard solutions were used to determine the calibration curve needed to quantify Y, Yb, Gd and Tm. Calibration standard solutions with concentrations of 10, 50, 100, 200 and 500 ppb were prepared using HPS-Q17617A (High Purity Standard, 10 mg/L in 2% HNO_3) solution. The NP samples were digested in HNO_3 (70% v/v) and then diluted in HNO_3 (2% v/v) to concentrations of 100 ppb for each NP sample. Pure HNO_3 (2% v/v) was also used as the control (blank sample). The plasma conditions of RF power 1,550 W, sample depth 10 mm and Ar carrier gas flow rate of 0.95 L/min and makeup gas flow rate of 0.1 L/min with a Micro Mist nebuliser and Scott Type spray chamber were used for measurements. The collision cell was run in He mode (4 ml/min He gas flow) for the following isotopes: 89Y, 173Yb, 157Gd, and 169Tm. Online addition of Indium was used as the internal standard element.

Photoluminescence measurements were carried out under 980 nm excitation using both a CW and pulsed laser. A fixed amount of powdered NP sample was used in the experiment for each sample. In the case of the pulsed laser, the samples were excited by pulses with a 5 ns duration and 20 Hz repetition rate from an Optical Parametric Oscillator (OPO) (Opotek LLC model "Opolette 355").

An 840 nm long-pass filter was placed before the sample to block visible wavelengths present in the OPO beam, and a silica lens was used to focus the spot size of the laser to approximately 2 mm. For the CW laser case, the samples were excited by MDL-III-980 diode laser at 980 nm. The emission spectra were collected using a spectrofluorometer (Edinburgh Instruments F980) with an air-cooled photomultiplier (Hamamatsu R928) for detection (Figure S12). The emission spectra were collected across the 280 to 630 nm detection range of the photomultiplier. CW laser power dependence scans were conducted using the 980 nm laser diode through a continuous neutral density filter with a SpectraPro SP-2300i spectrometer and PIXIS 100 CCD sensor for detection. Pulsed laser energy dependence data were conducted using a Radiant X30 OPO set at 980 nm (5 ns pulses at a repetition rate of 10 Hz), with variations in energy enabled by rotation of two Glan-laser calcite polarisers placed in the beam path. UV emission was collected through a 340 nm short pass absorptive filter while visible light was collected through a 770 nm short pass interference filter.

4.6 Acknowledgements

The support from the Australian Government Research Training Program Scholarship, Alice Chu postgraduate scholarship in Chemical Engineering, and The University of Adelaide is acknowledged. The upconversion facility was enabled by a LIEF grant (code LE140100042), and funding by CRC – Optimising Resource Extraction (ORE) project P1-005, and Commonwealth Government Department of Defence, Next Generation Technologies Fund, Grand Challenge-Counter Improvised Threats (CIED) grant CIT-186 is acknowledged.

The authors acknowledge the instruments and scientific and technical assistance of Microscopy Australia at Adelaide Microscopy, The University of Adelaide, a facility that is funded by the

university and state and federal governments. The table of contents (ToC) image was created with BioRender.com.

4.7 Supporting information

Table S1. Host crystal structure, average particle size and summary of the elemental analysis results for NaY(100-x%)F_4:Yb(18%)/Tm(x%)(x=1 and 5 mol%), NaYb(100-x%)F_4:Tm(x%) (x = 1, 2.5, 5 and 10 mol%), and NaYb(100-x%)F_4:Tm(0.5%)/Gd(x%) (x= 5 and 20 mol%) NP samples.

Samples	PXRD	TEM	SEM-EDS		ICP-MS	
	Host crystal structure	avg. size (nm)	Tm (%)	Gd (%)	Tm (%)	Gd (%)
NaY(81%)F_4:Yb(18%)/Tm(1%)	Hex. (# 06-0342)	Width= 18 ± 1 Length= 26 ± 2	1		0.9	
NaY(77%)F_4:Yb(18%)/Tm(5%)	Hex. (# 06-0342)	Width= 63 ± 5 Length= 114 ± 8	5		4.8	
NaYb(99%)F_4:Tm(1%)	Hex. (# 27-1427)	Width= 246 ± 29 Length= 647 ± 85	1		1.0	
NaYb(97.5%)F_4:Tm(2.5%)	Hex. (# 27-1427)	Width= 158 ± 18 Length= 410 ± 58	2		2.5	
NaYb(95%)F_4:Tm(5%)	Hex. (# 27-1427)	Width= 161 ± 13 Length= 465 ± 52	5		5.0	
NaYb(90%)F_4:Tm(10%)	Hex. (# 27-1427)*	Width= 256 ± 26 Length= 643 ± 84 Small= 27 ± 8	11		10.1	
NaYb(94.5%)F_4:Tm(0.5%):Gd(5%)	Hex. (# 27-1427), cub. (# 77-2043)	Small= 16 ± 4 Large= 268 ± 55	0	5	0.4	4.9
NaYb(79.5%)F_4:Tm(0.5%):Gd(20%)	Hex. (# 27-1427)*	Small= 33 ± 7 Large= 290 ± 11	0	28	0.3	20.0

* These NP samples also show a small trace of the cubic structure.

Table S2. Raw ICP-MS results to confirm the concentration of Y, Yb, Tm and Gd in the as-synthesised UCNP samples.

Sample name	Y		Yb		Tm		Gd	
	Conc. [ppb]	Conc. RSD*	Conc. [ppb]	Conc. RSD*	Conc. [ppb]	Conc. RSD*	Conc. [ppb]	Conc. RSD*
NaY(77%)F_4:Yb(18%)/Tm(5%)	21.74	2.26	8.56	1.48	2.23	0.79	0.11	11.55
NaY(81%)F_4:Yb(18%)/Tm(1%)	24.54	1.82	10.20	3.17	0.48	2.80	0.04	19.02
NaYb(99%)F_4:Tm(1%)	0.28	3.19	54.62	1.07	0.51	0.54	0.04	4.64
NaYb(97.5%)F_4:Tm(2.5%)	0.33	1.92	50.07	0.92	1.22	2.63	0.03	29.99
NaYb(95%)F_4:Tm(5%)	0.58	2.36	33.16	0.38	1.72	0.96	0.05	12.49
NaYb(90%)F_4:Tm(10%)	0.31	3.89	114.23	0.95	12.26	1.17	0.04	10.51
NaYb(94.5%)F_4:Tm(0.5%):Gd(5%)	0.28	1.26	47.57	1.07	0.18	1.67	2.20	2.35
NaYb(79.5%)F_4:Tm(0.5%):Gd(20%)	0.29	4.29	63.86	0.62	0.24	1.66	14.95	2.05

* RSD: relative standard deviation

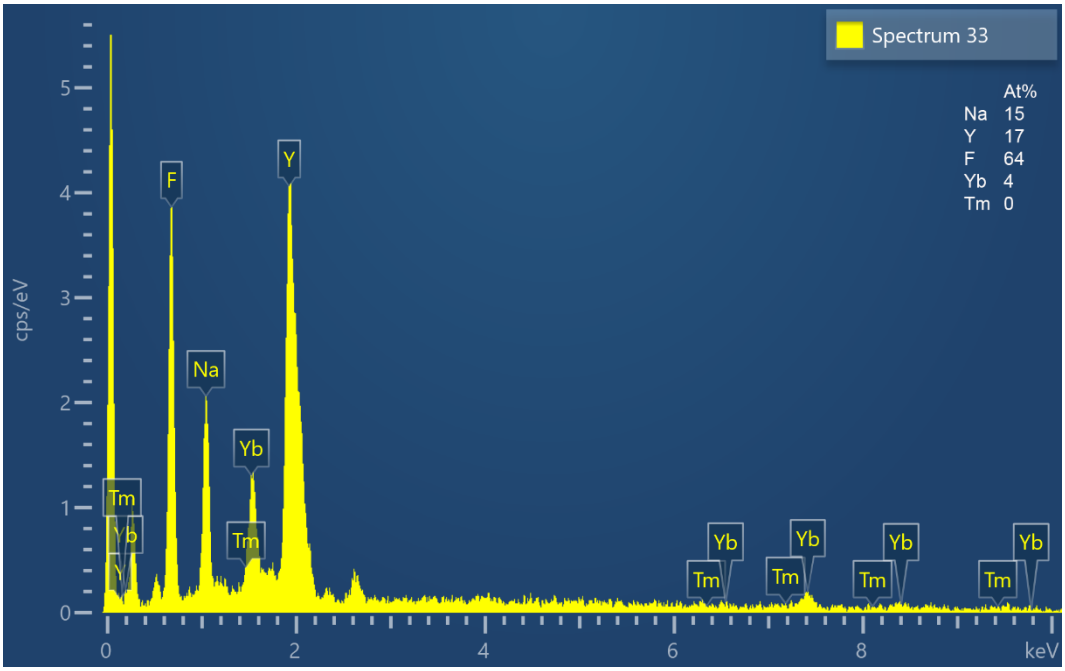

Figure S1. Example spectrum and elemental analysis for NaY(81%)F_4:Yb(18%)/Tm(1%) determined the Scanning Electron Microscopy Energy Dispersive X-ray (SEM-EDX) spectrum.

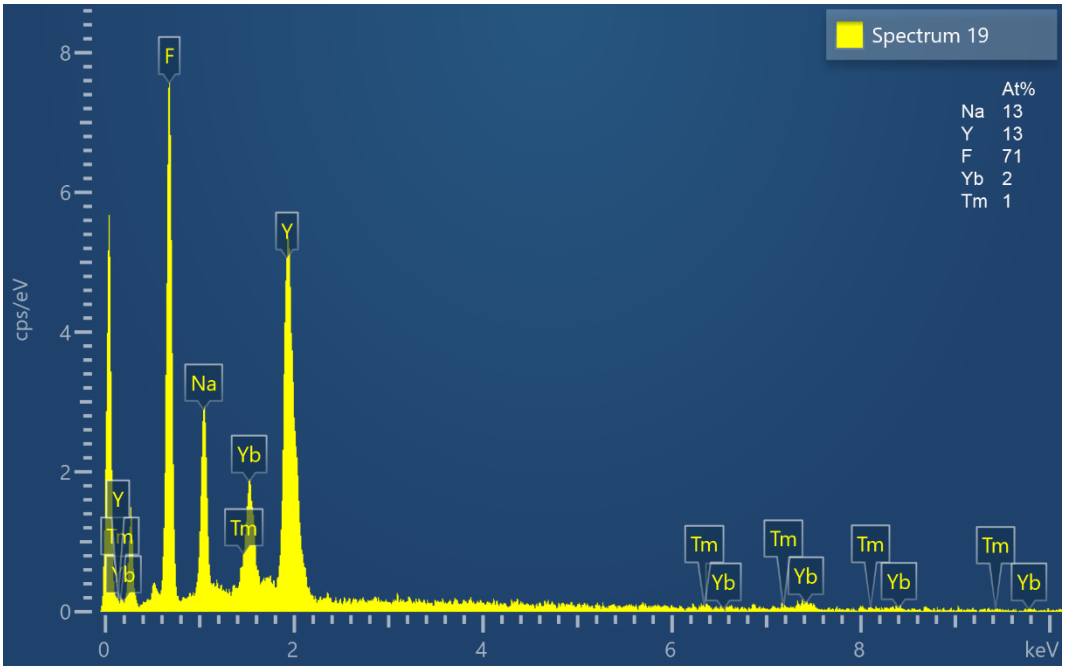

Figure S2. Example spectrum and elemental analysis for NaY(77%)F_4:Yb(18%)/Tm(5%) determined from the SEM-EDX spectrum.

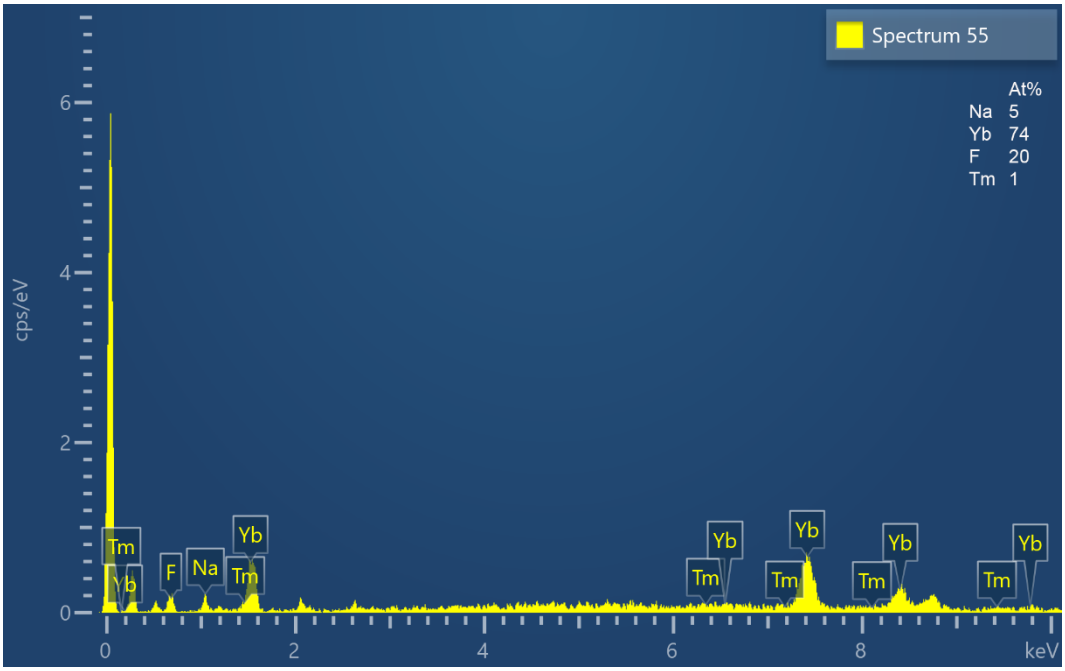

Figure S3. Example spectrum and elemental analysis for $NaYb(99\%)F_4$:Tm(1%) determined from the SEM-EDX spectrum.

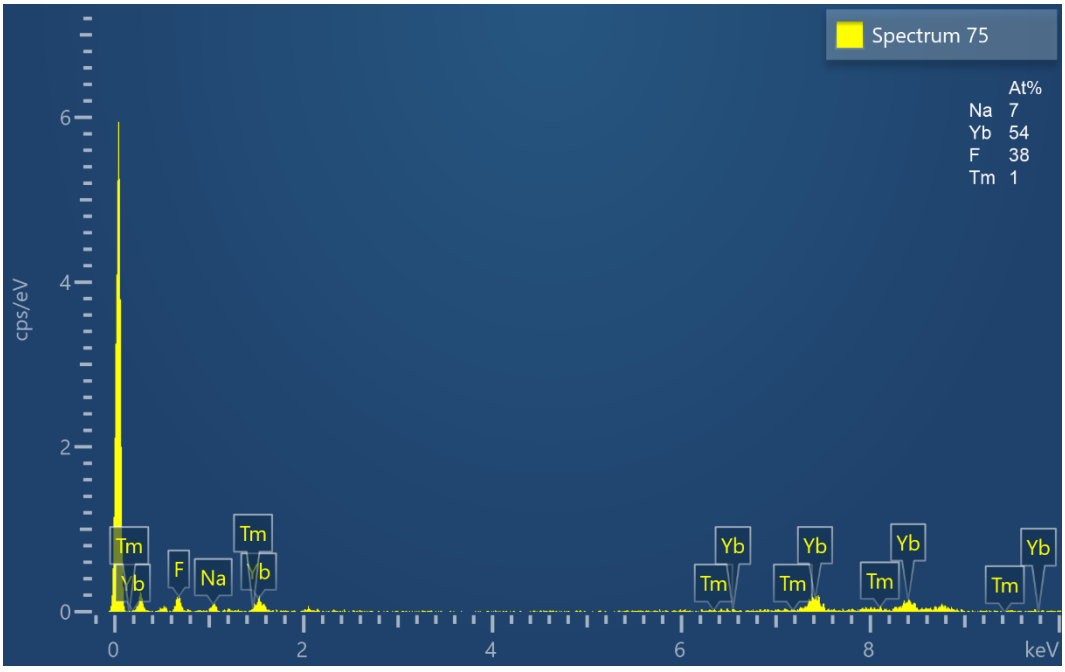

Figure S4. Example spectrum and elemental analysis for $NaYb(97.5\%)F_4$:Tm(2.5%) determined from the SEM-EDX spectrum.

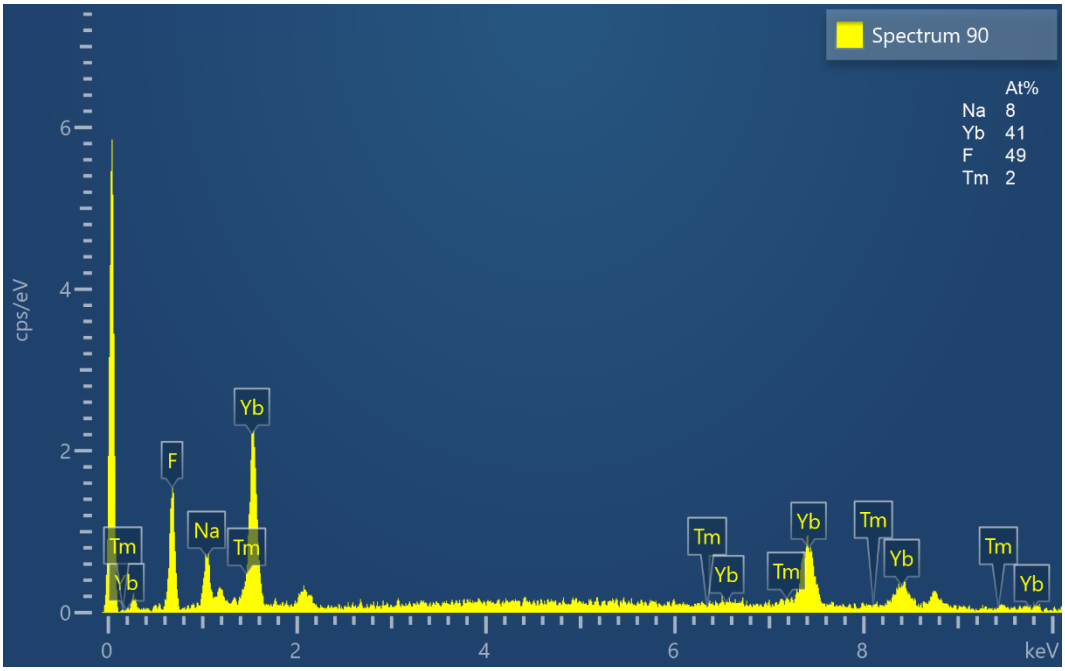

Figure S5. Example spectrum and elemental analysis for $NaYb(95\%)F_4$:Tm(5%) determined from the SEM-EDX spectrum.

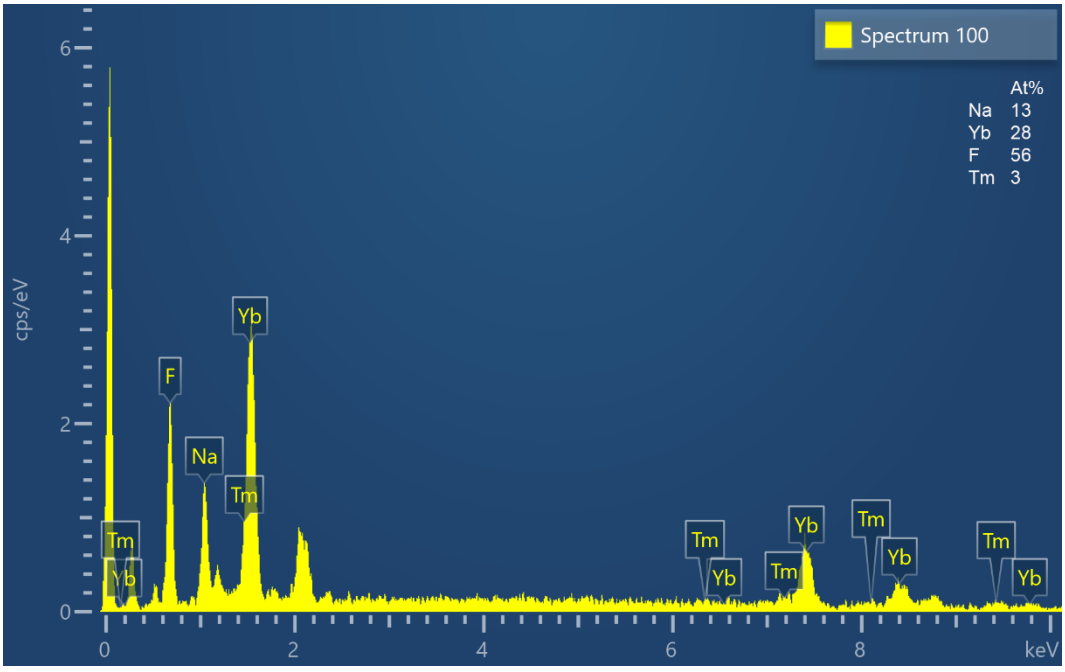

Figure S6. Example spectrum and elemental analysis for $NaYb(90\%)F_4$:Tm(10%) determined from the SEM-EDX spectrum.

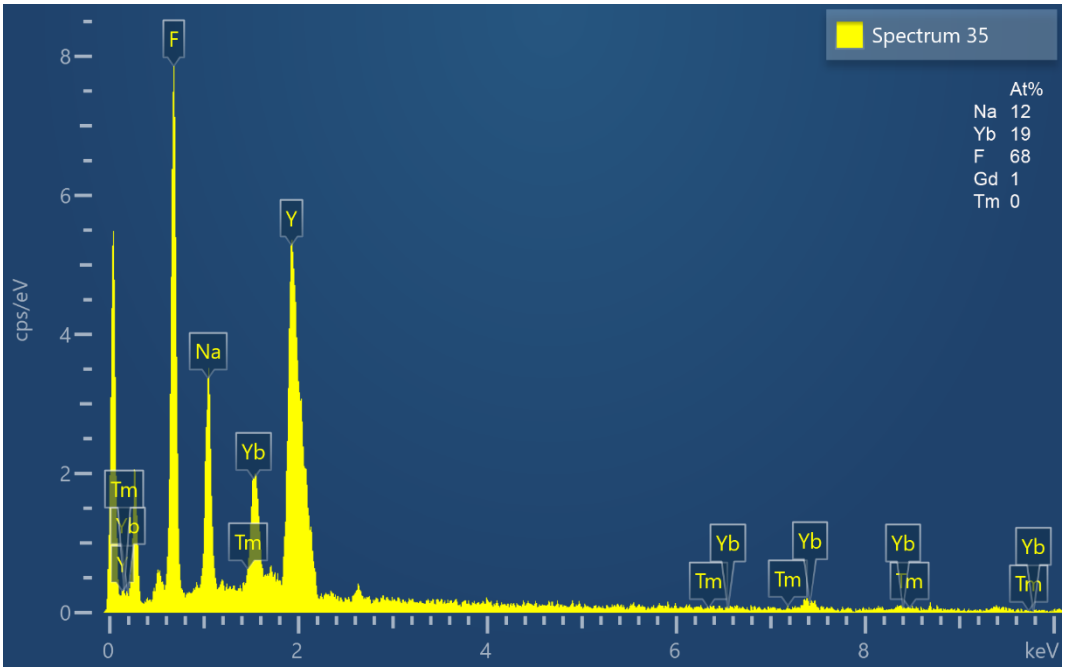

Figure S7. Example spectrum and elemental analysis for NaYb(94.5%)F_4:Tm(0.5%)/Gd(5%) determined from the SEM-EDX spectrum.

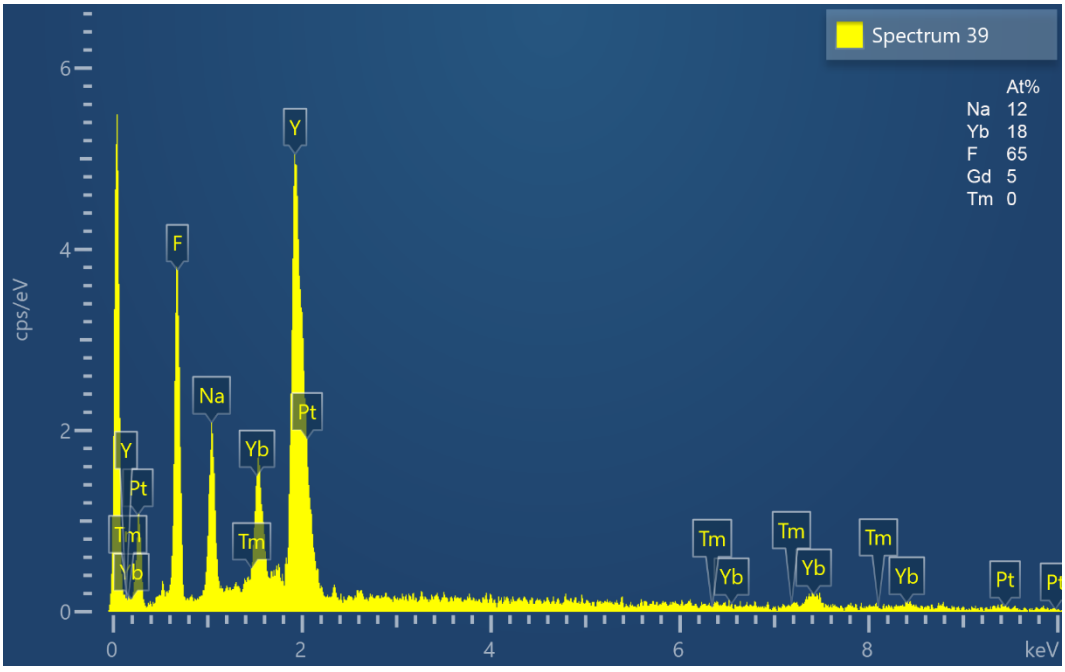

Figure S8. Example spectrum and elemental analysis for NaYb(79.5%)F_4:Tm(0.5%)/Gd(20%) determined from the SEM-EDX spectrum.

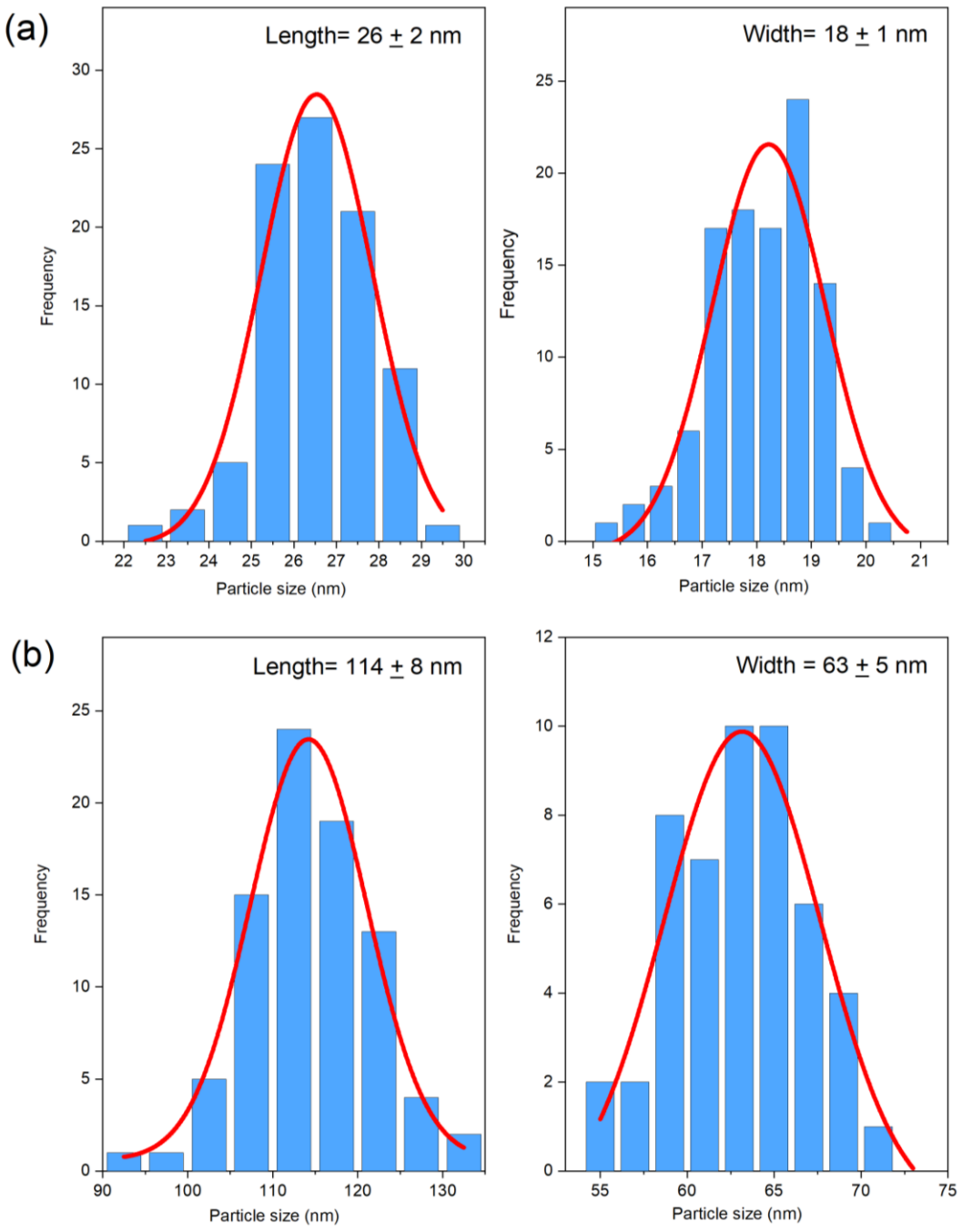

Figure S9. Particle size distribution plots for the length and width of the as-synthesised (a) NaY(81%)F_4:Yb(18%)/Tm(1%) UCNP and (b) NaY(81%)F_4:Yb(18%)/Tm(1%) UCNP.

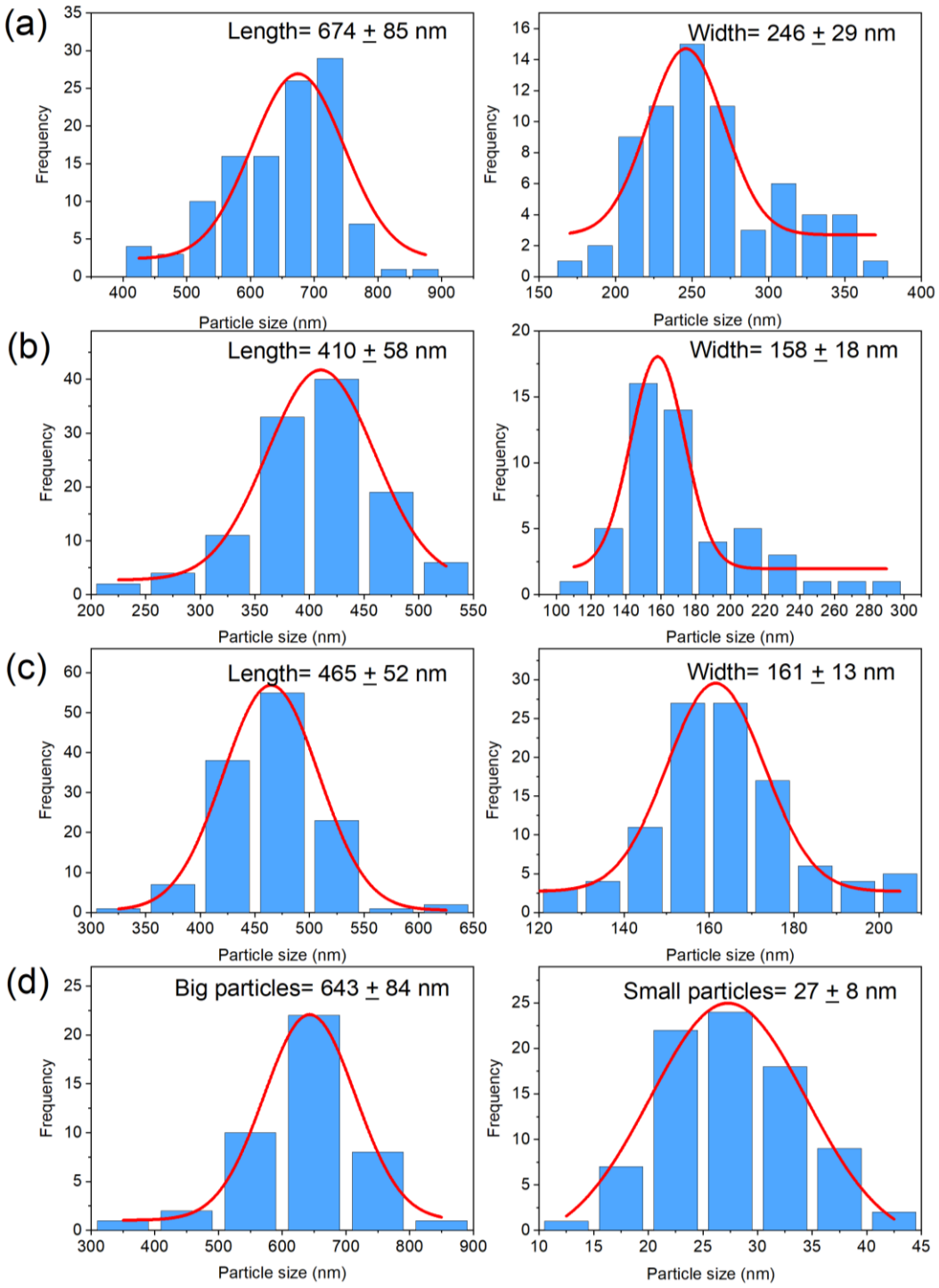

Figure S10. Particle size distribution plots for the length and width of the as-synthesised (a) NaYb(99%)F_4:Tm(1%) UCNP, (b) NaYb(97.5%)F_4:Tm(2.5%) UCNP, (c) NaYb(95%)F_4:Tm(5%) UCNP and (d) NaYb(90%)F_4:Tm(10%) UCNP.

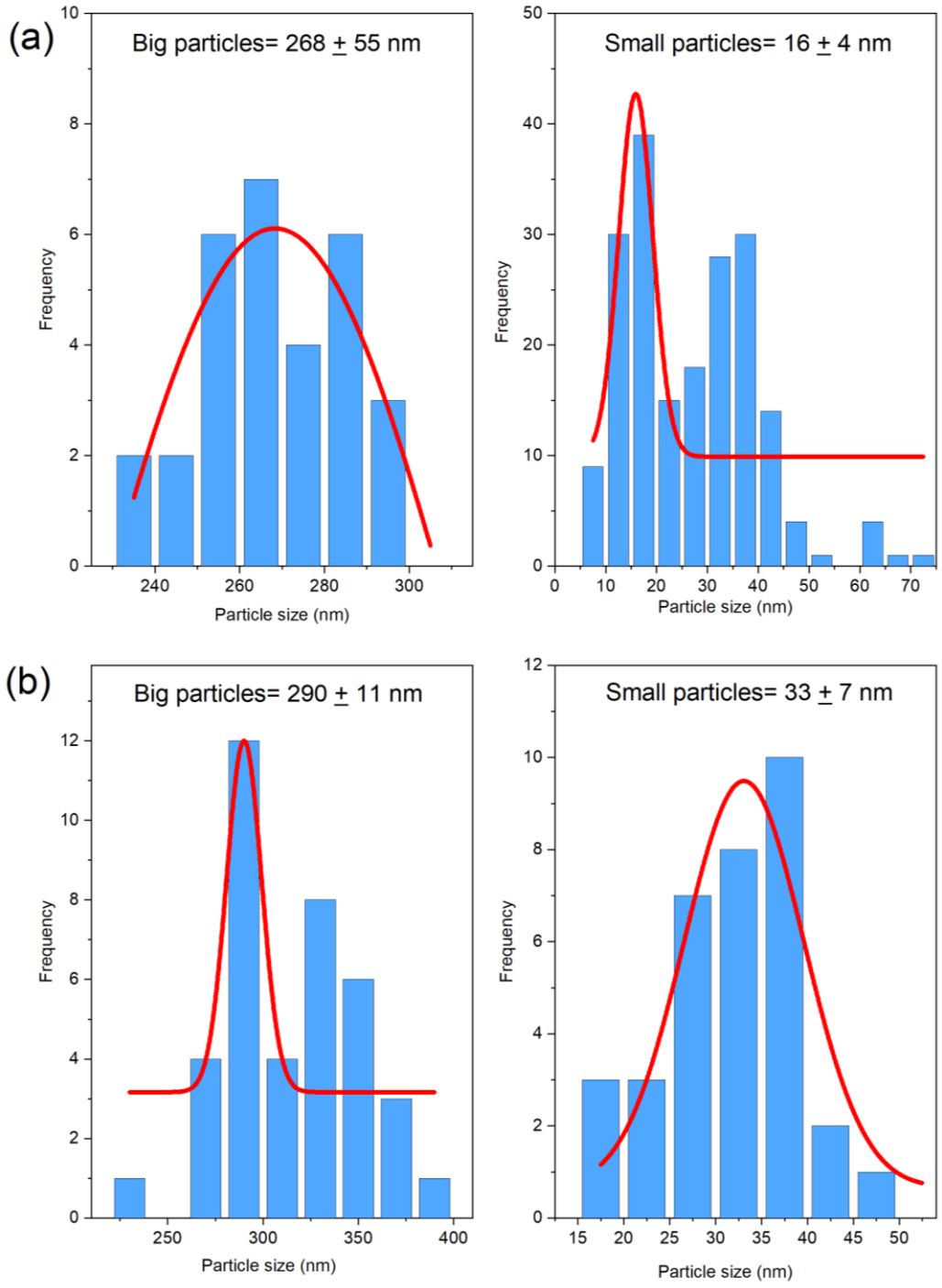

Figure S11. Particle size distribution plots for the length and width of the as-synthesised (a) NaYb(94.5%)F_4:Tm(0.5%)/Gd(5%) UCNP and (b) NaYb(79.5%)F_4:Tm(0.5%)/Gd(20%) UCNP.

Table S3. Experimentally determined power dependence slope values under pulsed excitation (5 ns pulses at 10 Hz) across a pulse energy range of 1 to 7.5 MW/cm2.

Samples	$^1G_4 \rightarrow {}^3H_6$	$^1D_2 \rightarrow {}^3F_4$	$^1I_6 \rightarrow {}^3F_4$
	475 nm	450 nm	345 nm
NaY(81%)F_4:Yb(18%)/Tm(1%)	2.7	2.8	3.5
NaY(77%)F_4:Yb(18%)/Tm(5%)	2.5	2.8	-*
NaYb(99%)F_4:Tm(1%)	2.2	2.7	3.3
NaYb(97.5%)F_4:Tm(2.5%)	2.0	3.0	3.9
NaYb(95%)F_4:Tm(5%)	1.9	3.1	4.7
NaYb(90%)F_4:Tm(10%)	2.1	2.6	4.1
NaYb(94.5%)F_4:Tm(0.5%):Gd(5%)	2.6	2.7	3.1
NaYb(79.5%)F_4:Tm(0.5%):Gd(20%)	2.6	2.6	3.4

* Emission intensity was too weak to permit accurate measurement of the slope value

Table S4. Experimentally determined power dependence slope values under CW excitation.

Samples	$^1G_4 \rightarrow {}^3H_6$	$^1D_2 \rightarrow {}^3F_4$	$^1I_6 \rightarrow {}^3F_4$
	475 nm	450 nm	345 nm
NaY(81%)F_4:Yb(18%)/Tm(1%)	1.8	2.0	2.0
NaY(77%)F_4:Yb(18%)/Tm(5%)	1.6	2.1	2.5
NaYb(99%)F_4:Tm(1%)	1.5	2.0	2.2
NaYb(97.5%)F_4:Tm(2.5%)	1.3	1.3	1.5
NaYb(95%)F_4:Tm(5%)	1.1	1.3	1.5
NaYb(90%)F_4:Tm(10%)	1.3	1.7	1.7
NaYb(94.5%)F_4:Tm(0.5%):Gd(5%)	1.6	2.1	2.1
NaYb(79.5%)F_4:Tm(0.5%):Gd(20%)	2.0	2.7	2.7

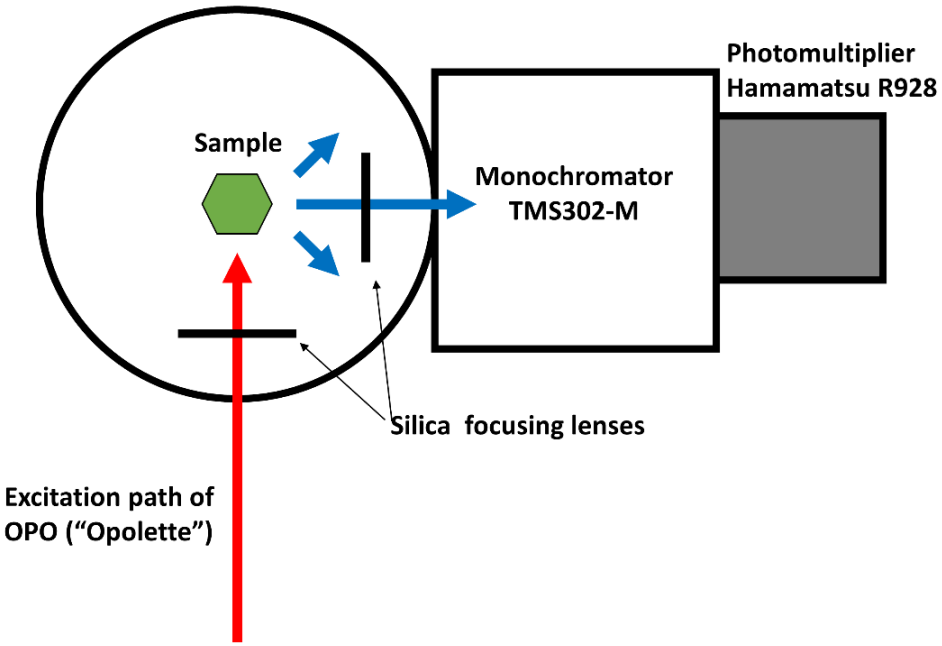

Figure S12. Schematic of the Edinburgh instruments spectrofluorimeter experimental configuration.

4.8 References

1) Zhang, H.; Zhao, M.; Ábrahám, I. M.; Zhang, F. Super-Resolution Imaging With Lanthanide Luminescent Nanocrystals: Progress and Prospect. *Front Bioeng Biotechnol* **2021**, *9*, 692075. DOI: 10.3389/fbioe.2021.692075.

(2) Dong, H.; Sun, L.-D.; Yan, C.-H. Lanthanide-Doped Upconversion Nanoparticles for Super-Resolution Microscopy. *Frontiers in Chemistry* **2021**, *8*. DOI: 10.3389/fchem.2020.619377.

(3) Valli, J.; Garcia-Burgos, A.; Rooney, L. M.; Vale de Melo e Oliveira, B.; Duncan, R. R.; Rickman, C. Seeing beyond the limit: A guide to choosing the right super-resolution microscopy technique. *J. Biol. Chem.* **2021**, *297* (1), 100791. DOI: 10.1016/j.jbc.2021.100791.

(4) Jing, Y.; Zhang, C.; Yu, B.; Lin, D.; Qu, J. Super-Resolution Microscopy: Shedding New Light on In Vivo Imaging. *Frontiers in chemistry* **2021**, *9*, 746900-746900. DOI: 10.3389/fchem.2021.746900.

(5) Sigal, Y. M.; Zhou, R.; Zhuang, X. Visualizing and discovering cellular structures with super-resolution microscopy. *Science* **2018**, *361* (6405), 880-887. DOI: 10.1126/science.aau1044.

(6) Yang, Z.; Samanta, S.; Yan, W.; Yu, B.; Qu, J. Super-resolution Microscopy for Biological Imaging. In *Adv Exp Med Biol*, Vol. 3233; 2021; pp 23-43.

(7) De Camillis, S.; Ren, P.; Cao, Y.; Plöschner, M.; et al. Controlling the non-linear emission of upconversion nanoparticles to enhance super-resolution imaging performance. *Nanoscale* **2020**, *12* (39), 20347-20355. DOI: 10.1039/D0NR04809G.

(8) Yadav, A.; Rao, C.; Nandi, C. K. Fluorescent Probes for Super-Resolution Microscopy of Lysosomes. *ACS Omega* **2020**, *5* (42), 26967-26977. DOI: 10.1021/acsomega.0c04018.

(9) Li, W.; Kaminski Schierle, G. S.; Lei, B.; Liu, Y.; Kaminski, C. F. Fluorescent Nanoparticles for Super-Resolution Imaging. *Chem. Rev.* **2022**, *122* (15), 12495-12543. DOI: 10.1021/acs.chemrev.2c00050.

(10) Cheng, L.; Wang, C.; Liu, Z. Upconversion nanoparticles and their composite nanostructures for biomedical imaging and cancer therapy. *Nanoscale* **2013**, *5* (1), 23-37. DOI: 10.1039/C2NR32311G.

(11) Chen, C.; Wang, F.; Wen, S.; Su, Q. P.; et al. Multi-photon near-infrared emission saturation nanoscopy using upconversion nanoparticles. *Nat. Commun.* **2018**, *9* (1), 3290. DOI: 10.1038/s41467-018-05842-w.

(12) Zhan, Q.; Liu, H.; Wang, B.; Wu, Q.; et al. Achieving high-efficiency emission depletion nanoscopy by employing cross relaxation in upconversion nanoparticles. *Nature Communications* **2017**, *8* (1), 1058. DOI: 10.1038/s41467-017-01141-y.

(13) Wen, S.; Zhou, J.; Zheng, K.; Bednarkiewicz, A.; Liu, X.; Jin, D. Advances in highly doped upconversion nanoparticles. *Nature Communications* **2018**, *9* (1), Review article. DOI: 10.1038/s41467-018-04813-5.

(14) Maurizio, S. L.; Tessitore, G.; Mandl, G. A.; Capobianco, J. A. Luminescence dynamics and enhancement of the UV and visible emissions of Tm^{3+} in $LiYF_4:Yb^{3+},Tm^{3+}$ upconverting nanoparticles. *Nanoscale Advances* **2019**, *1* (11), 4492-4500. DOI: 10.1039/C9NA00556K.

(15) Zheng, B.; Fan, J.; Chen, B.; Qin, X.; et al. Rare-Earth Doping in Nanostructured Inorganic Materials. *Chem. Rev.* **2022**, *122* (6), 5519-5603. DOI: 10.1021/acs.chemrev.1c00644.

(16) Wei, H.-L.; Zheng, W.; Zhang, X.; Suo, H.; Chen, B.; Wang, Y.; Wang, F. Tuning Near-Infrared-to-Ultraviolet Upconversion in Lanthanide-Doped Nanoparticles for Biomedical Applications. *Advanced Optical Materials* **2022**, *n/a* (n/a), 2201716. DOI: 10.1002/adom.202201716.

(17) Yu, T. h.; Xuan, Y.; Wang, X.; Yan, X. Infrared excitation induced upconversion fluorescence properties and photoelectric effect of $NaYbF_4$:Tm^{3+}@TiO_2 core–shell nanoparticles. *RSC Advances* **2014**, *4* (90), 49415-49420. DOI: 10.1039/C4RA06488G.

(18) Karami, A.; Farivar, F.; de Prinse, T. J.; Rabiee, H.; Kidd, S.; Sumby, C. J.; Bi, J. Facile Multistep Synthesis of ZnO-Coated β-NaYF4:Yb/Tm Upconversion Nanoparticles as an Antimicrobial Photodynamic Therapy for Persistent Staphylococcus aureus Small Colony Variants. *ACS Applied Bio Materials* **2021**, *4* (8), 6125-6136. DOI: 10.1021/acsabm.1c00473.

(19) Wei, J.; Zhao, H.; Zhang, L.; Chai, S.; Liu, H.; Wang, Y.; Xue, J. Vis-UV Upconverting bacteriostatic hydrophobic bacterial cellulose film for personal protective masks. *Carbohydr. Polym.* **2022**, *297*, 119967. DOI: 10.1016/j.carbpol.2022.119967.

(20) Shen, J.; Chen, G.; Ohulchanskyy, T. Y.; Kesseli, S. J.; et al. Tunable Near Infrared to Ultraviolet Upconversion Luminescence Enhancement in (α-$NaYF_4$:Yb,Tm)/CaF_2 Core/Shell Nanoparticles for In situ Real-time Recorded Biocompatible Photoactivation. *Small* **2013**, *9* (19), 3213-3217. DOI: 10.1002/smll.201300234.

(21) Sharma, V. K.; Demir, H. V. Bright Future of Deep-Ultraviolet Photonics: Emerging UVC Chip-Scale Light-Source Technology Platforms, Benchmarking, Challenges, and Outlook for UV Disinfection. *ACS Photonics* **2022**, *9* (5), 1513-1521. DOI: 10.1021/acsphotonics.2c00041.

(22) Tosheva, K. L.; Yuan, Y.; Matos Pereira, P.; Culley, S.; Henriques, R. Between life and death: strategies to reduce phototoxicity in super-resolution microscopy. *J. Phys. D: Appl. Phys.* **2020**, *53* (16), 163001. DOI: 10.1088/1361-6463/ab6b95.

(23) de Prinse, T. J.; Karami, A.; Moffatt, J. E.; Payten, T. B.; et al. Dual Laser Study of Non-Degenerate Two Wavelength Upconversion Demonstrated in Sensitizer-Free $NaYF_4$:Pr Nanoparticles. *Advanced Optical Materials* **2021**, *9* (7), 2001903. DOI: 10.1002/adom.202001903.

(24) Shi, R.; Ling, X.; Li, X.; Zhang, L.; et al. Tuning hexagonal $NaYbF_4$ nanocrystals down to sub-10 nm for enhanced photon upconversion. *Nanoscale* **2017**, *9* (36), 13739-13746. DOI: 10.1039/C7NR04877G.

(25) Xu, R.; Cao, H.; Lin, D.; Yu, B.; Qu, J. Lanthanide-doped upconversion nanoparticles for biological super-resolution fluorescence imaging. *Cell Reports Physical Science* **2022**, *3* (6), 100922. DOI: 10.1016/j.xcrp.2022.100922.

(26) Huang, B.; Wu, Q.; Peng, X.; Yao, L.; Peng, D.; Zhan, Q. One-scan fluorescence emission difference nanoscopy developed with excitation orthogonalized upconversion nanoparticles. *Nanoscale* **2018**, *10* (45), 21025-21030, 10.1039/C8NR07017B. DOI: 10.1039/C8NR07017B.

(27) Zhao, J.; Jin, D.; Schartner, E. P.; Lu, Y.; et al. Single-nanocrystal sensitivity achieved by enhanced upconversion luminescence. *Nature Nanotechnology* **2013**, *8* (10), 729-734. DOI: 10.1038/nnano.2013.171.

(28) Algar, W. R.; Massey, M.; Rees, K.; Higgins, R.; et al. Photoluminescent Nanoparticles for Chemical and Biological Analysis and Imaging. *Chem. Rev.* **2021**, *121* (15), 9243-9358. DOI: 10.1021/acs.chemrev.0c01176.

(29) Chen, G. Y.; Qiu, H. Q.; Prasad, P. N.; Chen, X. Y. Upconversion Nanoparticles: Design, Nanochemistry, and Applications in Theranostics. *Chem. Rev.* **2014**, *114*, 5161.

(30) Pu, R.; Zhan, Q.; Peng, X.; Liu, S.; et al. Super-resolution microscopy enabled by high-efficiency surface-migration emission depletion. *Nature Communications* **2022**, *13* (1), 6636. DOI: 10.1038/s41467-022-33726-7.

(31) Damasco, J. A.; Chen, G.; Shao, W.; Ågren, H.; et al. Size-Tunable and Monodisperse Tm^{3+}/Gd^{3+}-Doped Hexagonal $NaYbF_4$ Nanoparticles with Engineered Efficient Near Infrared-to-Near Infrared Upconversion for In Vivo Imaging. *ACS Applied Materials & Interfaces* **2014**, *6* (16), 13884-13893. DOI: 10.1021/am503288d.

(32) Dong, H.; Sun, L.-D.; Yan, C.-H. Energy transfer in lanthanide upconversion studies for extended optical applications. *Chem. Soc. Rev.* **2015**, *44* (6), 1608-1634, Review article. DOI: 10.1039/C4CS00188E.

(33) Wang, F.; Liu, X. G. Multicolor Tuning of Lanthanide-Doped Nanoparticles by Single Wavelength Excitation. *Acc. Chem. Res.* **2014**, *47*, 1378.

(34) Wang, L.; Li, X.; Li, Z.; Chu, W.; et al. A new cubic phase for a $NaYF_4$ host matrix offering high upconversion luminescence efficiency. *Adv. Mater.* **2015**, *27* (37), 5528-5533. DOI: 10.1002/adma.201502748.

(35) Vidyakina, A. A.; Kolesnikov, I. E.; Bogachev, N. A.; Skripkin, M. Y.; Tumkin, I. I.; Lähderanta, E.; Mereshchenko, A. S. Gd^{3+}-Doping Effect on Upconversion Emission of $NaYF_4$: Yb^{3+}, Er^{3+}/Tm^{3+} Microparticles. *Materials (Basel, Switzerland)* **2020**, *13* (15), 3397. DOI: 10.3390/ma13153397.

(36) Moffatt, J. E.; Tsiminis, G.; Klantsataya, E.; de Prinse, T. J.; Ottaway, D.; Spooner, N. A. A practical review of shorter than excitation wavelength light emission processes. *Applied Spectroscopy Reviews* **2020**, *55* (4), 327-349. DOI: 10.1080/05704928.2019.1672712.

(37) Pollnau, M.; Gamelin, D. R.; Lüthi, S. R.; Güdel, H. U.; Hehlen, M. P. Power dependence of upconversion luminescence in lanthanide and transition-metal-ion systems. *Physical Review B* **2000**, *61* (5), 3337-3346. DOI: 10.1103/PhysRevB.61.3337.

(38) Vidyakina, A. A.; Kolesnikov, I. E.; Bogachev, N. A.; Skripkin, M. Y.; Tumkin, I. I.; Lähderanta, E.; Mereshchenko, A. S. Gd^{3+}-Doping Effect on Upconversion Emission of NaYF4: Yb^{3+}, Er^{3+}/Tm^{3+} Microparticles. *Materials* **2020**, *13* (15), 3397. DOI: 10.3390/ma13153397.

(39) Quintanilla, M.; Cantarelli, I. X.; Pedroni, M.; Speghini, A.; Vetrone, F. Intense ultraviolet upconversion in water dispersible SrF2:Tm3+,Yb3+ nanoparticles: the effect of the environment on light emissions. *Journal of Materials Chemistry C* **2015**, *3* (13), 3108-3113, 10.1039/C4TC02791D. DOI: 10.1039/C4TC02791D.

(40) Shang, Y.; Zhou, J.; Cai, Y.; Wang, F.; et al. Low threshold lasing emissions from a single upconversion nanocrystal. *Nature Communications* **2020**, *11* (1), 6156. DOI: 10.1038/s41467-020-19797-4.

(41) Plöschner, M.; Denkova, D.; De Camillis, S.; Das, M.; et al. Simultaneous super-linear excitation-emission and emission depletion allows imaging of upconversion nanoparticles with higher sub-diffraction resolution. *Opt. Express* **2020**, *28* (16), 24308-24326. DOI: 10.1364/OE.400651.

(42) Greer, F.; Hamden, E.; Jacquot, B. C.; Hoenk, M. E.; et al. Atomically precise surface engineering of silicon CCDs for enhanced UV quantum efficiency. *Journal of Vacuum Science & Technology A* **2013**, *31* (1), 01A103.

(43) Yibin, B.; Jagmohan, B.; James, W. B.; Mark, C. F.; et al. Teledyne Imaging Sensors: silicon CMOS imaging technologies for x-ray, UV, visible, and near infrared. In *Proc.SPIE*, 2008; Vol. 7021, p 702102. DOI: 10.1117/12.792316.

(44) Zacharioudaki, D. E.; Fitilis, I.; Kotti, M. Review of Fluorescence Spectroscopy in Environmental Quality Applications. *Molecules* **2022**, *27* (15). DOI: 10.3390/molecules27154801 From NLM.

(45) Sansonetti, C. J.; Salit, M. L.; Reader, J. Wavelengths of spectral lines in mercury pencil lamps. *Appl. Opt.* **1996**, *35* (1), 74-77. DOI: 10.1364/AO.35.000074.

(46) Khoroshilova, E. V.; Repeyev, Y. A.; Nikogosyan, D. N. UV protolysis of aromatic amino acids and related dipeptides and tripeptides. *J. Photochem. Photobiol. B: Biol.* **1990**, *7* (2), 159-172. DOI: 10.1016/1011-1344(90)85153-N.

(47) Besaratinia, A.; Yoon, J. I.; Schroeder, C.; Bradforth, S. E.; Cockburn, M.; Pfeifer, G. P. Wavelength dependence of ultraviolet radiation-induced DNA damage as determined by laser irradiation suggests that cyclobutane pyrimidine dimers are the principal DNA lesions produced by terrestrial sunlight. *FASEB J.* **2011**, *25* (9), 3079-3091. DOI: 10.1096/fj.11-187336 From NLM.

(48) Tripp, M. K.; Watson, M.; Balk, S. J.; Swetter, S. M.; Gershenwald, J. E. State of the Science on Prevention and Screening to Reduce Melanoma Incidence and Mortality: The Time Is Now. *CA Cancer J. Clin.* **2016**, *66* (6), 460-480. DOI: 10.3322/caac.21352.

(49) Boo, Y. C. Emerging Strategies to Protect the Skin from Ultraviolet Rays Using Plant-Derived Materials. *Antioxidants* **2020**, *9* (7), 637.

(50) Lo, C.-W.; Matsuura, R.; Iimura, K.; Wada, S.; et al. UVC disinfects SARS-CoV-2 by induction of viral genome damage without apparent effects on viral morphology and proteins. *Sci. Rep.* **2021**, *11* (1), 13804. DOI: 10.1038/s41598-021-93231-7.

(51) Mullenders, L. H. F. Solar UV damage to cellular DNA: from mechanisms to biological effects. *Photochemical & Photobiological Sciences* **2018**, *17* (12), 1842-1852. DOI: 10.1039/c8pp00182k.

(52) Nawkar, G. M.; Maibam, P.; Park, J. H.; Sahi, V. P.; Lee, S. Y.; Kang, C. H. UV-Induced Cell Death in Plants. *Int. J. Mol. Sci.* **2013**, *14* (1), 1608-1628.

(53) Santos, A. L.; Oliveira, V.; Baptista, I.; Henriques, I.; et al. Wavelength dependence of biological damage induced by UV radiation on bacteria. *Arch. Microbiol.* **2013**, *195* (1), 63-74. DOI: 10.1007/s00203-012-0847-5.

(54) Brem, R.; Guven, M.; Karran, P. Oxidatively-generated damage to DNA and proteins mediated by photosensitized UVA. *Free Radical Biology and Medicine* **2017**, *107*, 101-109. DOI: 10.1016/j.freeradbiomed.2016.10.488.

(55) Kim, D. J.; Iwasaki, A.; Chien, A. L.; Kang, S. UVB-mediated DNA damage induces matrix metalloproteinases to promote photoaging in an AhR- and SP1-dependent manner. *JCI Insight* **2022**, *7* (9). DOI: 10.1172/jci.insight.156344.

(56) Pattison, D. I.; Davies, M. J. Actions of ultraviolet light on cellular structures. In *Cancer: Cell Structures, Carcinogens and Genomic Instability*, Birkhäuser Basel, 2006; pp 131-157.

(57) Laissue, P. P.; Alghamdi, R. A.; Tomancak, P.; Reynaud, E. G.; Shroff, H. Assessing phototoxicity in live fluorescence imaging. *Nat. Methods* **2017**, *14* (7), 657-661. DOI: 10.1038/nmeth.4344.

(58) Wäldchen, S.; Lehmann, J.; Klein, T.; van de Linde, S.; Sauer, M. Light-induced cell damage in live-cell super-resolution microscopy. *Sci. Rep.* **2015**, *5* (1), 15348. DOI: 10.1038/srep15348.

(59) Chen, X.; Jin, L.; Kong, W.; Sun, T.; et al. Confining energy migration in upconversion nanoparticles towards deep ultraviolet lasing. *Nature Communications* **2016**, *7* (1), 10304. DOI: 10.1038/ncomms10304.

Chapter 5: Conclusion and outlook

5.1 Conclusion

Alternative strategies are urgently required for dealing with persistent *Staphylococcus (S.) aureus* small colony variants (SCVs) and their antibacterial-resistant parental strains. SCVs are now known to be responsible for numerous chronic, persistent infections that do not respond to antibiotic treatment due to their slow growth rate and altered cellular features. Therefore, antibacterial photodynamic therapy (aPDT) utilizing ZnO-coated lanthanide-doped upconversion nanoparticle (UCNP) that is activated by NIR light was evaluated in this research work to treat antibacterial-resistant *S. aureus* and their SCVs.

The synthesis of ZnO-coated UCNPs has not been widely studied and preliminary results indicated the methods reported have limitations. As the first aim of this research work was focused on synthesising UCNPs@ZnO composites for aPDT applications against methicillin-resistant *S. aureus* SCVs and the parental strains, we considered the synthetic approaches in some detail before processing. The UCNP core was synthesised with solvo(hydro)thermal and thermolysis methods. The solvo(hydro)thermal methods did not yield quality spherical hexagonal UCNPs, and hence the thermolysis method was used throughout this work. We also concluded that the thermolysis method requires a setup with precise temperature control as elevated temperatures in different stages of the synthesis process influence the particle size. While not being the primary focus of the thesis we and others noted that a heating device (e.g. heating mantle) with automatic temperature control, a temperature sensor inside the reaction chamber and stirring capability must be used to produce small and uniform UCNPs. Additionally, we concluded that utilizing a vacuum to remove the volatiles and moisture from the reaction chamber affects the particle size and unwanted impurities.

For the ZnO coating, several synthesis methods were used and none of them provided an epitaxial ZnO shell around UCNPs. While it has limitations, the zeolitic imidazolate

framework 8 (ZIF-8) template method was selected as it potentially offered more flexibility and could accommodate modification of the ZnO shell, such as doping with transition metals to adjust the band gap. To achieve satisfactory ZnO coatings on the UCNPs, the synthesis parameters were evaluated to determine the optimal conditions for forming ZIF-8 around the UCNP and calcining ZIF-8 into the ZnO NP shell. Given the potential trade-off between increased ZnO formation and UCNP crystal structure change due to the calcination temperature, the calcination conditions were also investigated at different temperatures, showing that a 400 °C calcination step was the most advantageous (limited UCNP phase change and good ZnO formation), as discussed in chapter 2.

With the composites in hand, antibacterial activity was assessed. β-$NaYF_4$:Yb/Tm@ZnO composites activated with LEDs in NIR light for 3 hours showed efficacy against both *S. aureus* (SK2) and its associated SCV bacterial cell type. An LED illumination source was used in these antibacterial experiments as the laser and the antibacterial setup were under construction at the time of the experiment.

For the second objective of this research work, the UCNP@ZnO composites from the first part of the project were evaluated further in order to enhance their antibacterial activity. First, the effects of manipulating the lanthanide ions in the UCNP core were examined to increase the intensity of UV emissions. The photoluminescence efficiency of UCNPs can be enhanced by size or phase control, incorporation of impurities, modification of the host matrix, core/shell structures and increasing activator concentrations. Our goal here was to enhance the proportion of UV light emitted from the UCNP core which is crucial for the activation of UCNP@ZnO composite in aPDT. Based on the results of our experiments, we selected a higher sensitiser ratio of the Yb^{3+} ions as an approach to increase the UV emission of the core UCNP. To enhance the overall photocatalytic activity of the UCNP@ZnO composite, cobalt (Co) was first

doped into the ZnO shell to reduce the band gap energy, followed by the loading of silver (Ag) NPs on the β-$NaYF_4$:Yb/Tm@ZnO:Co composite to prevent electron-hole recombination. The improved β-$NaYF_4$:Yb/Tm@ZnO:Co/Ag composite showed promising antibacterial results using NIR continuous wave (CW) laser and a newly constructed antibacterial setup.

As part of the second objective of this research work, we investigated UV emissions from UCNP when used as fluorescent probes in super-resolution microscopy (SRM). In the previous objective, we had considered ways to enhance UV emission and this knowledge complemented this application of UCNPs in SRM. We assessed the UV emissions from eight UCNPs based on $NaYF_4$:Yb/Tm, $NaYbF_4$:Tm, and $NaYbF_4$:Tm/Gd structures. A UV-sensitive detector system and continuous and pulsed excitation regimes were used in the experiment. The experimental results demonstrate that most as-synthesised UCNPs can emit UV light and that the dopant concentration has a key role in generating UV emissions. In addition, it was observed that the use of pulsed or CW lasers for excitation could lead to a large variation in the amount of UV emitted. This work highlighted the important contribution of upconversion dopant composition and concentration, as well as analysing the emission of synthesised UCNPs before their use to prevent unwanted cell photodamage during in vivo imaging by SRM.

5.2 Outlook

Our first research project will investigate different synthesis approaches to achieve high-quality UCNPs. In the current synthesis method, thermolysis, composition, phase, and size can be precisely controlled. For the synthesis of UCNP by thermolysis, a heating mantle equipped with a temperature controller is required.[1] However, this synthesis device suffers from slow heating rates and underestimates the reaction times. The investigation of alternative devices, such as dielectric microwave heating (MW) may address this issue. The use of MW heating devices has shown promising results in reaching final reaction temperatures rapidly, reducing

reaction times and enabling small and uniform UCNP synthesis.[2] A MW heating device combined with optimised reaction conditions and solvent systems may enhance the efficiency and productivity of UCNP synthesis.

As a second potential research project, UCNPs will be fine-tuned to activate in different excitation wavelengths by adjusting their core composition. In particular, focusing on excitation wavelengths below 980 nm, such as around 800 nm, can minimise light absorption by biological tissues and make it possible to synthesise UCNPs with intense emissions in this range. Moreover, the NIR-II window (1000 to 1700 nm) has the potential for use in bioimaging and theranostic applications.[3] UCNPs can be optimised for excitation in these specific wavelength ranges in order to expand their applications in antibacterial/anticancer treatment and bioimaging.

An additional potential research area involves fine-tuning ZnO-coated UCNPs to enhance their antibacterial and anticancer properties. Although continuous ZnO coating of UCNP cores has been challenging, alternative approaches may be explored, including multi-step ZIF-8 or multi-step ZnO coatings. It is also possible to utilise the advantages of localised surface plasmon resonance (LSPR) by incorporating silver (Ag) or gold (Au) with UCNP,[4,5] potentially enhancing their photocatalytic efficiency. Utilizing molecular antennas to enhance the photocatalytic activity of UCNP cores is another area of potential improvement.[6] With the incorporation of these compounds, the photocatalytic efficiency of the UCNPs may be further improved, thereby expanding their potential as therapeutic agents. In addition, future research could explore the synthesis of UCNPs as fluorescent probes for SRMs. A major aim here would be to develop UCNPs that are brighter in the visible range, emit less UV light, and have increased selectivity for detecting particular cell types or features, e.g. cancer cells.

Through the application of the knowledge gained during the current study, the properties and applications of UCNPs can be further developed and expanded. It is anticipated that significant advances can be achieved by fine-tuning the structures and compositions of ZnO-coated UCNPs, exploring different excitation wavelengths, enhancing photocatalytic activity, and synthesising UCNPs for SRMs. These future endeavours, with their relevance to nanomedicine, will contribute to the growing body of knowledge in the field and pave the way for innovative approaches to combat bacteria, cancer, and improve diagnostics.

5.3 References

(1) Arafeh, K. M.; Asadirad, A. M.; Li, J. W.; Wilson, D.; Wu, T.; Branda, N. R. A 'Plug and Play' Method to Create Water-dispersible Nanoassemblies Containing an Amphiphilic Polymer, Organic Dyes and Upconverting Nanoparticles. *J Vis Exp* **2015**, (105). DOI: 10.3791/52987.

(2) Amouroux, B.; Roux, C.; Marty, J.-D.; Pasturel, M.; et al. Importance of the Mixing and High-Temperature Heating Steps in the Controlled Thermal Coprecipitation Synthesis of Sub-5-nm Na(Gd–Yb)F4:Tm. *Inorganic Chemistry* **2019**, *58* (8), 5082-5088. DOI: 10.1021/acs.inorgchem.9b00143.

(3) Zhu, S.; Hu, Z.; Tian, R.; Yung, B. C.; et al. Repurposing Cyanine NIR-I Dyes Accelerates Clinical Translation of Near-Infrared-II (NIR-II) Bioimaging. *Adv. Mater.* **2018**, *30* (34), 1802546. DOI: 10.1002/adma.201802546.

(4) Kataria, M.; Yadav, K.; Nain, A.; Lin, H.-I.; et al. Self-Sufficient and Highly Efficient Gold Sandwich Upconversion Nanocomposite Lasers for Stretchable and Bio-applications. *ACS Applied Materials & Interfaces* **2020**, *12* (17), 19840-19854. DOI: 10.1021/acsami.0c02602.

(5) Fang, G.; Ji, Y.; Xiao, Q.; Dong, X.; et al. Plasmonic Au@Ag-upconversion nanoparticle hybrids for NIR photodetection via an alternating self-assembly method. *Journal of Materials Chemistry C* **2022**, *10* (43), 16430-16438. DOI: 10.1039/D2TC02545K.

(6) Zhu, X.; Su, Q.; Feng, W.; Li, F. Anti-Stokes shift luminescent materials for bio-applications. *Chem. Soc. Rev.* **2017**, *46* (4), 1025-1039. DOI: 10.1039/c6cs00415f.

Chapter 6: Appendix

Statement of Authorship

Title of Paper	Dual Laser Study of Non-Degenerate Two Wavelength Upconversion Demonstrated in Sensitizer-Free $NaYF_4$:Pr Nanoparticles.
Publication Status	☑ Published ☐ Accepted for Publication ☐ Submitted for Publication ☐ Unpublished and Unsubmitted work written in manuscript style
Publication Details	de Prinse, T. J.; Karami, A.; Moffatt, J. E.; Payten, T. B.; Tsiminis, G.; Teixeira, L. D. S.; Bi, J.; Kee, T. W.; Klantsataya, E.; Sumby, C. J.; et al. Dual Laser Study of Non-Degenerate Two Wavelength Upconversion Demonstrated in Sensitizer-Free NaYF4:Pr Nanoparticles. Advanced Optical Materials 2021, 9 (7), 2001903. DOI: 10.1002/adom.202001903.

Principal Author

Name of Principal Author (Candidate)	Afshin Karami		
Contribution to the Paper	Synthesis of samples, material characterisation of samples (XRD, TEM, ICPMS), manuscript writing		
Overall percentage (%)	25%		
Certification:	This paper reports on original research I conducted during the period of my Higher Degree by Research candidature and is not subject to any obligations or contractual agreements with a third party that would constrain its inclusion in this thesis.		
Signature		Date	25/01/2023

Co-Author Contributions

By signing the Statement of Authorship, each author certifies that:

i. the candidate's stated contribution to the publication is accurate (as detailed above);
ii. permission is granted for the candidate in include the publication in the thesis; and

Name of Co-Author	Thomas de Prinse		
Contribution to the Paper	Spectral data acquisition, data processing, concept development, manuscript writing		
Signature		Date	27/01/2023

Name of Co-Author	Dr. Jillian Moffatt		
Contribution to the Paper	Initial pilot data, concept development, laboratory assistance and development of laser systems, data and manuscript review		
Signature		Date	27/01/2023

Name of Co-Author	Dr. Thomas Payten		
Contribution to the Paper	Assistance with lifetime experiments, assistance with manuscript drafting, data and manuscript review		
Signature		Date	27/01/2023

Name of Co-Author	Dr. Georgios Tsiminis		
Contribution to the Paper	Initial pilot data, concept development, laboratory assistance and development of laser systems, assistance with manuscript drafting		
Signature		Date	27/01/2023

Name of Co-Author	Lewis Teixeira		
Contribution to the Paper	Assistance with manuscript drafting		
Signature		Date	29/01/2023

Name of Co-Author	A/Prof Jingxiu Bi		
Contribution to the Paper	Manuscript review, proofing of manuscript, supervision of work		
Signature		Date	15/06/2023

Name of Co-Author	A/Prof. Tak Kee		
Contribution to the Paper	Manuscript review, proofing of manuscript, supervision of work		
Signature		Date	30/01/2023

Name of Co-Author	Dr. Elizaveta Klantsataya		
Contribution to the Paper	Concept development, laboratory assistance, manuscript review, supervision of work		
Signature		Date	30/01/2023

Name of Co-Author	Prof. Christopher Sumby		
Contribution to the Paper	Material characterisation analysis, manuscript review, proofing of manuscript, supervision of work		
Signature		Date	12/06/2023

Name of Co-Author	Prof. Nigel Spooner		
Contribution to the Paper	Concept development, manuscript review, proofing of manuscript, supervision of work		
Signature		Date	27/01/2023

ADVANCED OPTICAL MATERIALS
www.advopticalmat.de

Dual Laser Study of Non-Degenerate Two Wavelength Upconversion Demonstrated in Sensitizer-Free $NaYF_4$:Pr Nanoparticles

*Thomas J. de Prinse, Afshin Karami, Jillian E. Moffatt, Thomas B. Payten, Georgios Tsiminis, Lewis Da Silva Teixeira, Jingxiu Bi, Tak W. Kee, Elizaveta Klantsataya, Christopher J. Sumby, and Nigel A. Spooner**

Understanding the upconversion pathways of a rare-earth dopant is crucial to furthering the use of that material, either toward applications in imaging or elsewhere. This work outlines a new analysis approach that consists of using two synchronized widely-tunable laser sources to explore the properties of upconverting materials. By examining sensitizer-free rare-earth nanoparticles based on a matrix of hexagonal sodium yttrium tetrafluoride (β-$NaYF_4$) doped with praseodymium but no ytterbium sensitizer, a "non-degenerate" two-color upconversion fluorescence at a combined excitation of 1020–850 nm is shown. This insight demonstrates the ability of this technique to locate and interrogate novel upconversion pathways. The dopant level of the nanoparticles could be modified without altering other factors, such as the particle's shape or size, that would also change optical properties and this allows investigation of the dopant-level dependency of the optical properties. The approach also allows exploration of the time delay domain between the arrival times of the two non-degenerate excitation pulses, which allows modulation of the brightness from the visible light emissions. This work opens up the parameter space for the systematic synthesis and characterization of new materials with non-degenerate upconversion emission.

1. Introduction

Rare-earth doped materials can produce luminescence emission at wavelengths shorter than those used to excite them, a process known as upconversion.[1] For this to occur in ions, the energies of two or more photons are combined, either with sequential absorption of photons or by energy transfer processes between neighboring ions.[2] This collected energy is then released as one photon, which is blue shifted from the excitation wavelength. This effect has seen rare-earth dopants applied toward applications in sunlight harvesting,[3] high resolution imaging,[4] temperature sensing,[5] and biological markers,[6] among many others.[7]

In order to understand the optical properties of rare-earth ions within a matrix, a suitable host material must be doped with the ion. Ideally, this host is a low phonon material, allowing for long excited-state lifetimes and higher quantum efficiencies.[8] Also, importantly, the dopant level should be able to be systematically altered without changing the physical properties of the material in unexpected ways.[9] In this regard, hexagonal sodium yttrium tetrafluoride (β-$NaYF_4$) nanoparticles can be used as a host for a single rare-earth dopant species. This single dopant level can be modified easily during synthesis, with any changes to the optical properties resulting only from changes in the dopant ion interactions, as all other factors such as their morphology and crystal structure are shown to be controlled.[10]

Upconversion nanoparticles are usually designed to be excited by multiple photons of the same wavelength, such as

T. J. de Prinse, Dr. J. E. Moffatt, T. B. Payten, Dr. G. Tsiminis, L. Da Silva Teixeira, Dr. E. Klantsataya, Prof. N. A. Spooner
Institute for Photonics and Advanced Sensing (IPAS)
School of Physical Sciences
The University of Adelaide
Adelaide 5005, Australia
E-mail: nigel.spooner@adelaide.edu.au

A. Karami, Prof. J. Bi
School of Chemical Engineering
University of Adelaide
Adelaide 5005, Australia

The ORCID identification number(s) for the author(s) of this article can be found under https://doi.org/10.1002/adom.202001903.

DOI: 10.1002/adom.202001903

Dr. J. E. Moffatt, T. B. Payten, Dr. G. Tsiminis, L. Da Silva Teixeira, Prof. N. A. Spooner
CRC for Optimising Resource Extraction
Kenmore 4069, Australia

Dr. G. Tsiminis
ARC Centre of Excellence for Nanoscale BioPhotonics
The University of Adelaide
Adelaide 5005, Australia

Prof. T. W. Kee, Prof. C. J. Sumby
Department of Chemistry
The University of Adelaide
Adelaide 5005, Australia

Prof. N. A. Spooner
Defence Science and Technology Group
Edinburgh 5111, Australia

excitation by one laser line in the near-infrared (NIR). This simplifies their use in many applications. An alternative approach is to utilize two sources of differing wavelength to excite a material, referred to here as "dual non-degenerate" excitation. Dual non-degenerate excitation of nanoparticles has been demonstrated before, either to enhance a luminescence pathway[11] or to deplete an emission pathway.[4a,12] Additionally, display technologies based on rare-earth dopants have been proposed that utilize two different NIR wavelengths for excitation, with visible light emitted most prominently at the overlap of the two beams.[13] These materials most commonly have a single pathway toward upconversion luminescence, often due to their dependence on a co-doped sensitizer ion such as ytterbium that gives rise to a specific energy transfer process between ions, in addition to absorption and energy transfer between the individual doped ion's intrinsic energy levels.

These more complex excitation and energy transfer pathways can only partially be explored with established upconversion characterization techniques. To fully characterize the optical properties of rare-earth nanoparticles, two tunable sources are required. In this work, a dual tunable wavelength system has been built, capable of obtaining detailed excitation/emission profile maps over the visible and NIR range. Utilizing the single ion-doped β-$NaYF_4$ matrix as a platform, in combination with the novel dual tunable wavelength system, the properties of the praseodymium(III) ion are studied at differing dopant levels, which elucidated a strong dual non-degenerate upconversion pathway.[14]

2. Results and Discussion

$NaYF_4$:Pr nanoparticles (NP) with 1%, 2%, and 5% doping of praseodymium were synthesized by the established thermal decomposition method.[15] To examine their morphology the materials were investigated by high-resolution transmission electron microscopy (HRTEM) imaging. HRTEM images for $NaYF_4$:Pr (1% Pr) are presented in **Figure 1** while the data for $NaYF_4$:Pr (2% and 5% Pr) are presented in Figures S2 and S3, Supporting Information, respectively. The HRTEM images confirm that particles with a hexagonal morphology are formed, consistent with the β-$NaYF_4$ structure for all three samples. The HRTEM images also reveal that synthesized NPs are uniformly-sized with mean particle sizes for $NaYF_4$:Pr (1% Pr) of 30 ± 3 nm (based on 80 NPs, Figure 1c). $NaYF_4$:Pr (2% Pr) and $NaYF_4$:Pr (5% Pr) were also uniformly-sized with mean particle sizes of 40 ± 6 nm and mean particle sizes of 27 ± 4 nm respectively (see Supporting Information). In all cases the interplanar distance of the synthesized NPs was measured to be ≈0.52 nm (Figure 1a and Supporting Information), which corresponds to the interplanar distance of the (100) lattice plane for the hexagonal $NaYF_4$ structure (0.515 nm, JCPDS #16-0334). The selected area electron diffraction (SAED) of synthesized $NaYF_4$:Pr NPs presented in Figure 1b and Supporting Information also confirms a hexagonal structure for the $NaYF_4$:Pr NPs that is in good agreement with PXRD patterns shown in Figure S1, Supporting Information.

Element mapping was conducted to provide insight into the distribution of Pr^{3+} within the samples. While the Pr loading is low and thus the values not quantitative, the elemental mapping of the as-synthesized NP samples, along with EDX line scan analysis across a single NP sample (Figure 1d and Supporting Information), confirms that Pr is uniformly distributed

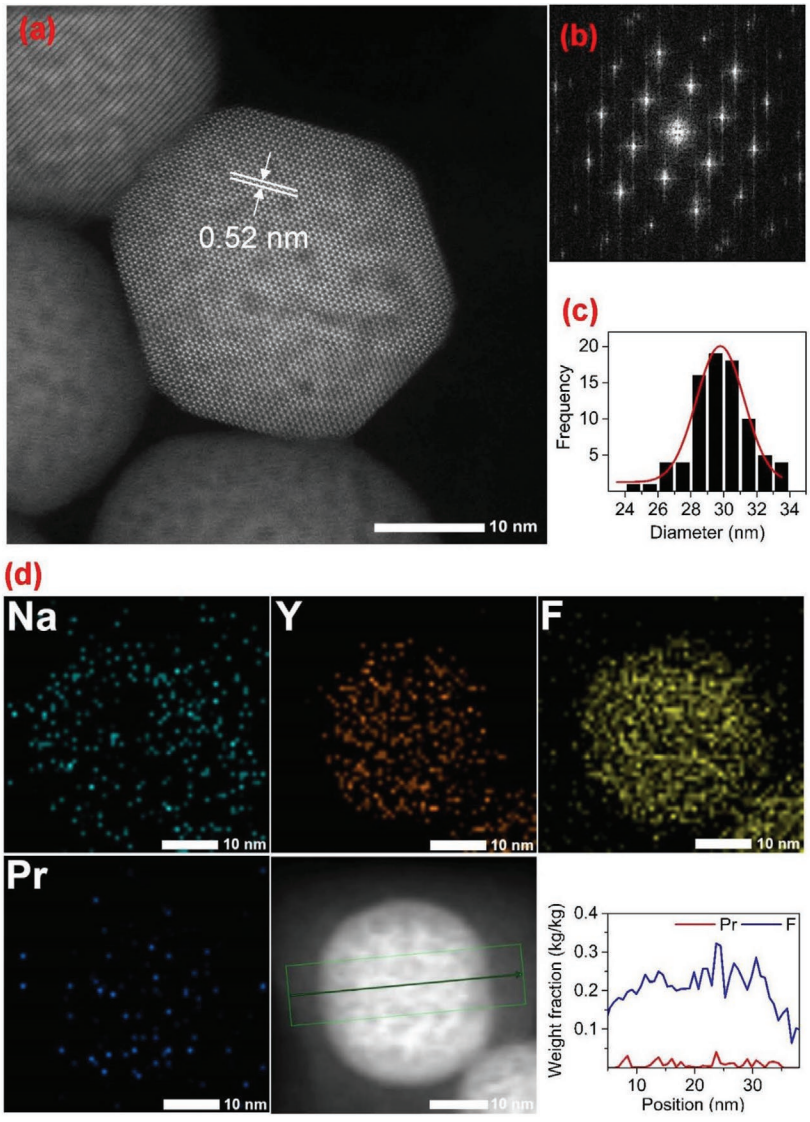

Figure 1. HRTEM image of the $NaYF_4$:Pr (1% Pr) NP sample. a) HRTEM image with interplanar distance of the synthesized NPs. b) SAED of synthesized NPs, c) size distribution and d) EDX line scan across the NP sample.

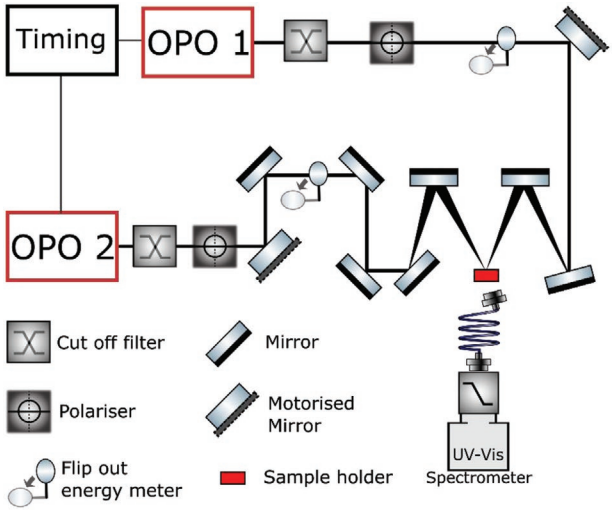

Figure 2. The dual laser setup used for the optical analysis of the rare-earth nanoparticles.

across the $NaYF_4$:Pr NP samples with minimal aggregation. The consistent PXRD patterns, particle size, particle morphology, and inter-planar distances confirm that the samples have the same structure and physical characteristics across the different dopant levels.

To explore the excitation parameter space and identify new upconverting pathways, the $NaYF_4$:Pr nanoparticles were excited by scanning in both the NIR and the visible using the dual excitation system (**Figure 2**). The system is driven by two tunable optical parametric oscillators (OPOs) with a pulse width of 5 ns, and repetition rate of 10 Hz. The pulse energy was between 0.5–15 mJ depending on wavelength, see Figures S4 and S5, Supporting Information. The flashlamps were synchronized by an external pulse controller such that the delay time between the laser pulses from OPO 1 and OPO 2 arriving at the sample could be independently controlled. Interference filters and beam splitting polarizer cubes were used to clean up each beam line, as shown in Figure 2. These were needed to remove parasitic pump lines from the lasers, as well as to selectively allow the OPO idler for NIR excitation, and signal for visible excitation (see Experimental Section). Emission spectra were collected with a fiber coupled spectrometer at the sample.

During the excitation maps, the delay between the pulse arrival times was tightly controlled and set to 10 ns peak to peak. This ensured that the pulses were not temporally overlapping at any point. This short delay time allows for the identification of sequential absorption features because as rare-earths such as praseodymium have excited state lifetimes much longer than the nanosecond regime delay time and pulse width.[16] Although kept constant, changes to the length of the excitation pulses will not result in changes to the emission spectra or upconversion pathway so long as they are considerably shorter than the lifetimes of the excited states of the ion. Under these conditions each instance of absorption is effectively instantaneous.

The visible wavelength excitation map for $NaYF_4$:Pr (2% Pr) in **Figure 3**a shows that upconversion emission was produced when either OPO excitation wavelength was in the range 585–590 nm. This corresponds with a Pr^{3+} absorption band promoting the $^3H_4 \rightarrow {}^1D_2$ transition. This is followed by a cooperative energy transfer process involving two Pr^{3+} ions corresponding to $^1D_2 + {}^1D_2 \rightarrow {}^3P_2 + {}^1G_4$, from which the $^3P_2$ state rapidly decays to the $^3P_{0,1}$ excited states.[17] These states emit fluorescence across the visible spectrum,[17c,18] for which the observed blue emission is anti-Stokes shifted relative to the initial excitation.

The 585–590 nm excitation could be observed through the use of only one laser source; however, the NIR excitation maps in Figure 3b,c show a prominent non-degenerate excitation feature, requiring both lasers to be observed. Excitation at 1020 nm followed by 850 nm leads to fluorescence at several visible wavelength bands, most prominently in the blue (490 nm) and the yellow (608 nm), which can all be assigned to emission from the $^3P_0$ and $^3P_1$ states.[19] This feature in the NIR corresponds to a upconversion excitation mechanism of ground state absorption/excited state absorption (GSA/ESA) corresponding to $^3H_4 \rightarrow {}^1G_4$, $^1G_4 \rightarrow {}^3P_{0,1}$, depicted in **Figure 4**a.

Rare-earth upconversion that heavily relies on energy transfer mechanisms usually shows dramatic changes in emission intensity with changes in dopant concentration.[2,14] To demonstrate that $NaYF_4$:Pr emission is not reliant on an ion–ion energy transfer mechanism, we additionally studied the $NaYF_4$:Pr (1% Pr) and $NaYF_4$:Pr (5% Pr) samples. The excitation maps and emission spectra were very similar for each of the Pr^{3+} doping levels synthesized (Figure 4b) supporting the proposed assignment of a GSA/ESA mechanism. Interestingly, minor differences were observed in the ratio of emission peaks at 490 and 610 nm across the differing dopant concentrations. The 5% Pr sample showed the least intense emission which may be a result of concentration quenching, as is often seen in highly doped Pr^{3+} samples.[20]

Changes in the excitation power did not change the profile of the emission spectrum for either pathway as the measured fluorescence is all being emitted from the $^3P_{0,1}$ excited states, and the fluorescence branching ratio at a given temperature is independent of the state's population.[21]

To further explore the dynamics of the non-degenerate upconversion fluorescence and associated energy levels, we performed excitation experiments for the combination of pump wavelengths that maximize emission from the nanoparticles where the two pulses were delayed in regards to one another. As the luminescence is due to a GSA/ESA process, no emission of light from the $NaYF_4$:Pr NP sample is seen if the 850 nm pulse arrives first; Pr^{3+} does not have a suitable energy level that allows it to absorb this wavelength from the ground state. Furthermore, upon excitation at 1020 nm no energy transfer interactions occur between ions in the $^1G_4$ state to produce light in the visible region, emphasizing the necessity of the sequential absorption of the 1020 nm then 850 nm pulses.

An artifact that can be observed in the NIR excitation maps in Figure 3 is an "echo" of the 1020 and 850 nm combination, showing up at the 850 and 1020 nm combination where the 850 nm pulse arrives first. As stated, no emission is expected at this point as the 1020 nm pulse must arrive first in order to attain the $^1G_4$ state and for the second pulse to be absorbed. However, the system operates at 10 Hz, so while there is a delay of 10 ns between the two pulses, there is only ≈100 ms before the next pair of pulses arrive. The $^1G_4$ state is long lived enough to allow interference between the first pair of pulses

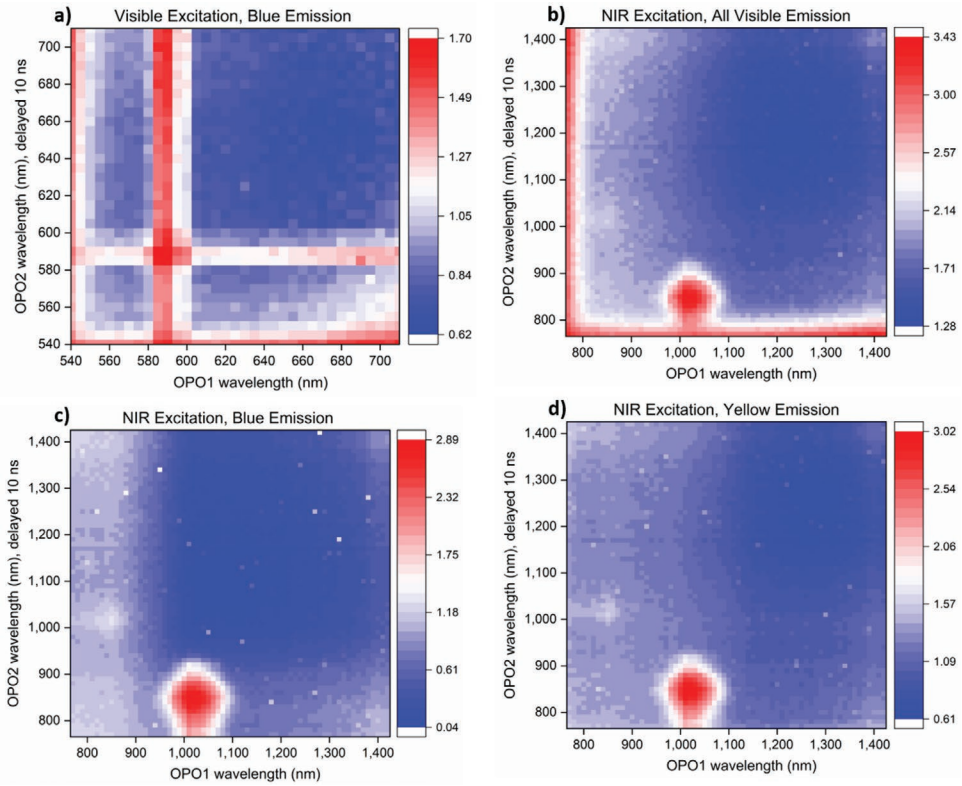

Figure 3. Excitation maps of the $NaYF_4$:Pr (2% Pr) sample. Color intensity indicates the log of emission intensity, summed over the notated range. a) Visible Excitation scan, emission intensity summed over 450–495 nm, b) NIR Excitation scan, emission intensity summed over 400–720 nm, c) NIR Excitation scan, emission intensity summed over 450–500 nm (blue) and d) NIR Excitation scan, emission intensity summed over 600–650 nm (yellow). We note that the bright lines at the edges of the excitation maps are due to scattered light, as the OPO source light approaches the edge of the filter's blocking range.

and the second pair; although, many ions have decayed over this interval so only a small signal is seen.

The time resolved emission intensity depletion during the dual non-degenerate excitation at 1020 and 850 nm is not constant for variations in dopant concentration, despite the total luminescence being very similar. **Figure 5** shows that at higher doping concentrations, the fluorescence intensity of the material at each emission peak decays more rapidly as the delay time between the two pulses is increased. An upconversion pathway based on GSA/ESA implies that the reduction in emission

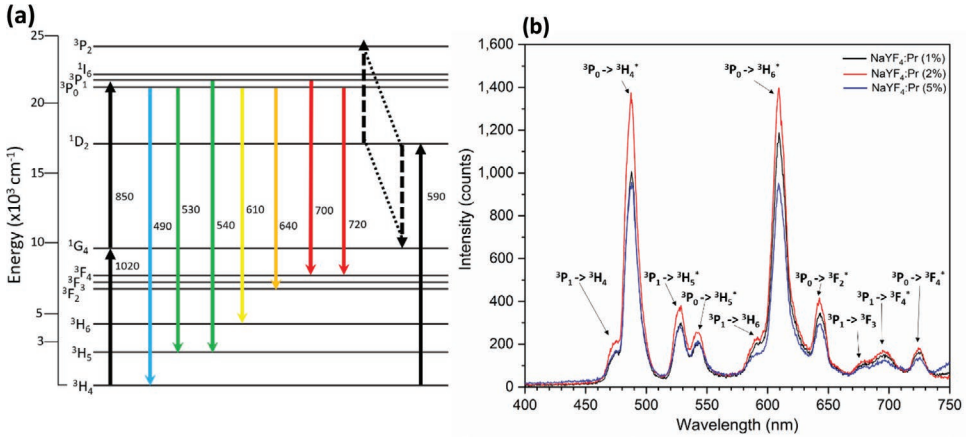

Figure 4. a) The energy levels present in the Pr^{3+} ion. The two upconversion pathways of 1020 + 850 nm and 590 nm seen in the excitation maps are shown, with dashed lines representing energy transfer between neighboring ions. Also shown are the seven most prominently observed emission bands, with approximate labels in nanometers. b) Emission spectra from a constant mass and volume of $NaYF_4$:Pr NP samples, after excitation with pulses of 1020 nm light followed by 850 nm light 10 ns after. Each dopant concentration responded to the excitation in a very similar way. The state transitions are labeled on the corresponding fluorescence peak, with (*) indicating the transitions depicted in Figure 3b.

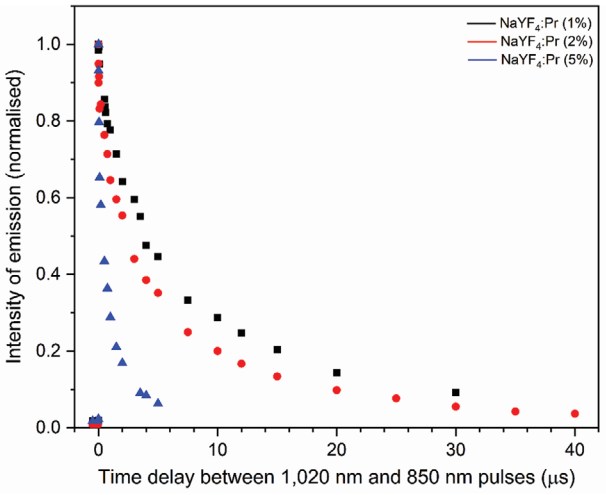

Figure 5. Decreasing luminescence intensity from the material is seen with an increase in the delay time between the GSA and ESA pulse, where a delay equaling zero indicates the 5 ns pulses arrive simultaneously. No emission is seen from any sample if the 850 nm pulse arrives first (before zero on the *x*-axis). Each sample's brightest emission is normalized to 1.

intensity as the delay between the pulses is increased depends only on the depletion of the intermediate $^1G_4$ state. Changes in the pulse delay response between dopant concentration levels therefore indicate a decrease in the observed $^1G_4$ state lifetime with increasing concentration, a trend that is seen in similar fluoride matrices, collated in **Table 1**. Due to cross relaxation energy transfer effects however the decay from this state is non-exponential at these high dopant concentrations, as has been previously observed.[22]

The dual-pump delay data does however allow for estimations of the $^1G_4$ state lifetime to be made, despite no time-resolved detection measurements being taken. The lifetime of this state is an important parameter in understanding how the material acts under dual excitation, and why the luminescence properties of the material is altered with changes in dopant concentration.

Despite the dual-pump delay data not conforming to a simple exponential model due to the aforementioned cross-relaxation effects, the data can be fit to a bi-exponential model corresponding to Equation (1):

$$\text{Intensity} = a_1 e^{-t/\tau_1} + a_2 e^{-t/\tau_2} \quad (1)$$

in which t is the time delay between pulses, a_1 and a_2 ($a_1 + a_2 = 1$) are the amplitudes of the exponentials. The dominant factor τ_1 is the lifetime of the $^1G_4$ state and is reported in Table 1, along with the standard deviation in each fitting parameter. τ_2 is a minor influence to the trend, assigned to the rate at which energy is lost to different states through cross-relaxation. As the two lasers are synchronized to external timing this means that only the total intensity is required to be measured by the spectrometer, with changes in emission intensity related back to the differing pulse arrival time of the lasers.

As the material emits light in the visible region after being excited sequentially by both pulses, the emission brightness is tunable by modifying the delay between the two pulses. Of note is that if a delay greater than 50 ms is implemented, visible emission drops to negligible amounts. The delay can be modulated to increase or decrease the emission brightness, with maximum brightness achieved with the 850 nm pulse arriving 10 ns or less after the 1020 nm pulse. Importantly, a chosen brightness can be selected and reproduced, without requiring changes in excitation power. For materials that produce upconversion emission from one wavelength of light, this type of control is not possible. Even if a similar two pulse system is used, there will always be some response from the material to the first laser pulse. This is often seen in systems based on the luminescence of the 980 nm transition of the erbium ion.[23] Modulating the emission brightness of a material sensitive to a one wavelength excitation source can be achieved through changing the power density of the excitation laser.[24] However, due to the non-linear nature of upconversion, achieving, and controlling both very low emission intensities as well as high brightness requires a large dynamic range in the excitation densities achievable with the laser, which is not often practical.

Praseodymium doped materials have been proposed for the application of dual laser excitation 3D displays, known as two-step, two frequency upconversion displays.[25] To be effective in such devices, the lifetime of the intermediate excited state (in this case the $^1G_4$ state) should be selected to match the raster rate of the excitation lasers across the display. As Figure 5 demonstrates, selection of a suitable lifetime could be done through careful choice of the dopant concentration. Moreover, modulating the brightness using the delay in dual pumping, while using constant excitation, has the added advantage of preserving the spectral emission profile. This is not the case when alterating excitation power density in materials with multiple doping ions and multiple excitation pathways.[26] Fixing the pulsed laser intensity and altering delay time in the single ion doped material allows for the emission color profile to be preserved over large changes in emission brightness.

Table 1. $^1G_4$ lifetime data for Pr^{3+} ions in various matrices.

Matrix	Pr^{3+} concentration [%]	$^1G_4$ lifetime [μs]	Ref.
ZBLAN[a)]	0.050	45	[22b]
ZBLAN[a)]	0.050	110	[22b]
ZBLANP[b)]	0.056	100	[14]
YBF[c)]	0.1	38	[22a]
YLF[d)]	0.24	17	[22a]
$NaYF_4$	1	13.2 ± 1.2	This work
$NaYF_4$	2	11.9 ± 1.6	This work
$NaYF_4$	5	1.7 ± 0.2	This work

[a)]ZrF_4-BaF_2-LaF_3-AlF_3-NaF glass; [b)]ZrF_4-BaF_2-LaF_3-AlF_3-NaF-PbF_2 glass; [c)]barium yttrium fluoride; [d)]yttrium lithium fluoride.

3. Conclusion

$NaYF_4$:Pr nanoparticles doped with 1%, 2%, and 5% praseodymium ions have been synthesized and their emission/excitation

properties have been mapped over a large parameter space of dual wavelength excitation combinations. This required the development of a new protocol using a custom system built around two highly tunable OPO lasers. Doping of low amounts of rare-earths into a $NaYF_4$ matrix, without co-doping of ytterbium, is an efficient way to study their native luminescence properties. In this work nanoparticles were synthesized with consistent size, shape, and controlled dopant concentration, with uniform dispersion of the Pr^{3+} observed in the particles. This allows factors such as dopant aggregation, morphology changes and surface effects to be obviated whilst altering only doping levels, an integral component of studying the fundamental optical properties of rare-earth ions. After doping of nanoparticles in this way, dual wavelength excitation maps of Pr^{3+} were produced and a non-degenerate two wavelength upconversion excitation pathway of 1020 and 850 nm leading to visible light emission was investigated.

Such non-degenerate two wavelength upconversion nanoparticles have interesting properties with many potential applications, such as tunable emission brightness through changes in the dual-pump delay times. Furthermore, changes in the synthesized $NaYF_4$:Pr doping level altered how the emission brightness was depleted in response to the pulse delay, with high doping levels more rapidly reducing in emission intensity with extended delays between the dual pulses. Further work utilizing this new technique is expected to enable a better understanding of energy transfer processes in upconversion nanoparticles and the development of novel, more efficient materials for applications relying on upconversion.

4. Experimental Section

Synthesis of $NaYF_4$:Pr Nanoparticles: $NaYF_4$:Pr nanoparticles (NPs) with 1%, 2%, and 5% Pr doping were prepared by thermal decomposition.[27] Specifically, 1-octadecene was used as a solvent due to its high boiling point (315 °C), while oleic acid was used as both a solvent and surfactant to control nanoparticle growth and to prevent the aggregation of nanoparticles.[28] A full method was provided in the supporting information. This provided nanoparticle samples designated $NaYF_4$:Pr (X% Pr) based on the feed ratio of $PrCl_3$ in the reaction.

Characterization of the NPs: The as-prepared nanoparticles were characterized by powder X-ray diffraction (PXRD, structure), TEM (particle size and morphology) and inductively-coupled plasma mass spectrometry (ICP-MS, composition). The crystal structure of the synthesized NPs was confirmed by PXRD. PXRD data for the synthesized $NaYF_4$:Pr NPs confirm all samples were crystalline. The PXRD patterns for the synthesized NP samples were presented in Figure S1, Supporting Information and show the diffraction peaks for the NPs were clearly indexed to β-$NaYF_4$ (JCPDS #16-034). The diffraction peaks located at 17.2°, 30.1°, 30.8°, 43.5°, and 53.7° (strong diffraction peaks) correspond to the $NaYF_4$ hexagonal structure indexed with (100), (110), (101), (201), and (211), respectively (JCPDS #16-034).

To determine if the feed ratios of Pr and Y salts used to prepare the NPs gave the expected dopant ratios, ICP-MS was used to evaluate the elemental compositions. The ICP-MS results confirmed that the molar ratio of Pr to Y in the synthesized $NaYF_4$:Pr NP samples were ≈1.1, ≈2.5, and ≈5.8 mol%, close to the expected values based on reactant feed ratios. The full ICP-MS results were included in Table S1, Supporting Information.

Optical Setup of Dual Excitation System: Excitation of the material was achieved through two OPOTEK Radiant HE 355 LD pulsed OPO lasers. Spectral information was obtained at each wavelength combination through a fiber coupled Princeton Instruments Acton SpectraPro Sp-2300 Spectrometer with a PIXIS 100 CCD.

The light from each OPO laser was filtered through two OD9 715 nm long pass filters for the NIR excitation range, and two OD9 715 nm short pass filters for the visible light excitation range. Each laser line was additionally cleaned through a polarizing beam splitting cube, before being directed by silver mirrors onto the sample. A computer-controlled motorized mirror was used in each beam line to adjust for small drifts in the beam position as the OPO laser scanned through the excitation wavelengths, allowing for the beam spot to stay on the sample.

The visible light excitation utilized a 498 nm short pass filter on the collection lens to allow for the blue emission band to be observed with the spectrometer. The NIR excitation scans utilized a 745 nm short pass filter to allow for the visible light region to be studied.

Flip out energy meters were present in each beam line, which measured the pulse energy of each laser at every excitation wavelength during the mapping procedure, averaged over 10 pulses. This allowed for the spectral data to be adjusted and normalized for changes in excitation intensity as each laser was tuned to different wavelengths.

Supporting Information

Supporting Information is available from the Wiley Online Library or from the author.

Acknowledgements

This research was funded by the Commonwealth Government Department of Defence, Next Generation Technologies Fund, Grand Challenge—Counter Improvised Threats (CIED) and CRC Optimising Resource Extraction (ORE) grants. The authors received funding from an Australian Government Research Training Program (RTP) scholarship, Alice Chu Postgraduate Scholarship in Chemical Engineering and the Australasian Institute of Mining and Metallurgy Education Endowment Fund (EEF) Postgraduate Research Scholarship 2020. The authors acknowledge the instruments and scientific and technical assistance of Microscopy Australia at Adelaide Microscopy, The University of Adelaide, a facility that is funded by the University, and State and Federal Governments. The authors thank Spectragryph[29] for the Academic license to their software, used during routine analysis.

Conflict of Interest

The authors declare no conflict of interest.

Data Availability Statement

Research data are not shared.

Keywords

dual excitation upconversion, non-degenerate upconversion, optical parametric oscillator laser, praseodymium, upconversion nanoparticles

Received: November 3, 2020
Revised: December 24, 2020
Published online: February 1, 2021

[1] F. Auzel, *Chem. Rev.* **2004**, *104*, 139.
[2] J. E. Moffatt, G. Tsiminis, E. Klantsataya, T. J. de Prinse, D. Ottaway, N. A. Spooner, *Appl. Spectrosc. Rev.* **2020**, *55*, 327.

[3] a) D. Ma, Y. Shen, T. Su, J. Zhao, N. U. Rahman, Z. Xie, F. Shi, S. Zheng, Y. Zhang, Z. Chi, *Mater. Chem. Front.* **2019**, *3*, 2058; b) A. Shalav, B. S. Richards, T. Trupke, K. W. Krämer, H. U. Güdel, *App. Phys. Lett.* **2004**, *86*, 013505; c) M. He, X. Pang, X. Liu, B. Jiang, Y. He, H. Snaith, Z. Lin, *Angew. Chem., Int. Ed.* **2016**, *55*, 4280.

[4] a) Q. Zhan, H. Liu, B. Wang, Q. Wu, R. Pu, C. Zhou, B. Huang, X. Peng, H. Ågren, S. He, *Nat. Commun.* **2017**, *8*, 1058; b) Y. Zhong, Z. Ma, F. Wang, X. Wang, Y. Yang, Y. Liu, X. Zhao, J. Li, H. Du, M. Zhang, Q. Cui, S. Zhu, Q. Sun, H. Wan, Y. Tian, Q. Liu, W. Wang, K. C. Garcia, H. Dai, *Nat. Biotechnol.* **2019**, *37*, 1322; c) P. Reineck, B. C. Gibson, *Adv. Opt. Mater.* **2017**, *5*, 1600446; d) Y. Liu, Y. Lu, X. Yang, X. Zheng, S. Wen, F. Wang, X. Vidal, J. Zhao, D. Liu, Z. Zhou, C. Ma, J. Zhou, J. A. Piper, P. Xi, D. Jin, *Nature* **2017**, *543*, 229.

[5] a) M. Runowski, P. Woźny, I. R. Martín, V. Lavín, S. Lis, *J. Lumin.* **2019**, *214*, 116571; b) C. D. S. Brites, K. Fiaczyk, J. F. C. B. Ramalho, M. Sójka, L. D. Carlos, E. Zych, *Adv. Opt. Mater.* **2018**, *6*, 1701318; c) T. P. van Swieten, D. Yu, T. Yu, S. J. W. Vonk, M. Suta, Q. Zhang, A. Meijerink, F. T. Rabouw, *Adv. Opt. Mater.* **2020**, *9*, 2001518.

[6] a) F. Wang, S. Wen, H. He, B. Wang, Z. Zhou, O. Shimoni, D. Jin, *Light Sci. Appl.* **2018**, *7*, 18007; b) J. Zhou, Z. Liu, F. Li, *Chem. Soc. Rev.* **2012**, *41*, 1323; c) Z. Yi, W. Lu, Y. Xu, J. Yang, L. Deng, C. Qian, T. Zeng, H. Wang, L. Rao, H. Liu, S. Zeng, *Biomaterials* **2014**, *35*, 9689.

[7] a) X. Zhu, J. Zhang, J. Liu, Y. Zhang, *Adv. Sci.* **2019**, *6*, 1901358; b) D. M. Samhadaneh, G. A. Mandl, Z. Han, M. Mahjoob, S. C. Weber, M. Tuznik, D. A. Rudko, J. A. Capobianco, U. Stochaj, *ACS Appl. Bio Mater.* **2020**, *3*, 4358; c) S. Wen, J. Zhou, K. Zheng, A. Bednarkiewicz, X. Liu, D. Jin, *Nat. Commun.* **2018**, *9*, 2415.

[8] a) A. Nadort, J. Zhao, E. M. Goldys, *Nanoscale* **2016**, *8*, 13099; b) R. Reisfeld, M. Eyal, *J. Phys. Colloquiums* **1985**, *46*, 349.

[9] C. Wang, X. Cheng, *J. Alloys Compd.* **2015**, *649*, 196.

[10] a) K. L. Reddy, M. Rai, N. Prabhakar, R. Arppe, S. B. Rai, S. K. Singh, J. M. Rosenholm, V. Krishnan, *RSC Adv.* **2016**, *6*, 53698; b) M. Liu, Y. Ye, C. Yao, W. Zhao, X. Huang, *J. Mater. Chem. B* **2014**, *2*, 6626.

[11] a) M. S. Shariatdoust, A. L. Frencken, A. Khademi, A. Alizadehkhaledi, F. C. J. M. van Veggel, R. Gordon, *ACS Photonics* **2018**, *5*, 3507; b) A. M. Kotulska, K. Prorok, A. Bednarkiewicz, *Methods Appl. Fluoresc.* **2019**, *7*, 034001; c) S. Krause, M. Koerstz, R. Arppe-Tabbara, T. Soukka, T. Vosch, *Methods Appl. Fluoresc.* **2018**, *6*, 044001; d) P. Chen, M. Xu, L. Li, B. Peng, *J. Alloys Compd.* **2017**, *727*, 1083.

[12] a) H. Zhang, T. Jia, L. Chen, Y. Zhang, S. Zhang, D. Feng, Z. Sun, J. Qiu, *Phys. Chem. Chem. Phys.* **2017**, *19*, 17756; b) M. Ploschner, D. Denkova, S. De Camillis, M. Das, L. M. Parker, X. Zheng, Y. Lu, S. Ojosnegros, J. A. Piper, *Opt. Express* **2020**, *28*, 24308; c) Z. Li, S. Xiao, X. Yang, J. W. Ding, G. Y. Tan, X. H. Yan, *Phys. B* **2012**, *407*, 2584.

[13] J. Cao, U. Parasuraman, J. Liu, T. Sun, in *Cockpit and Future Displays for Defense and Security*, Proc. SPIE, Vol. *5801* (Eds: D. G. Hopper, E. W. Forsythe, D. C. Morton, C. E. Bradford, H. J. Girolamo), SPIE, Bellingham, WA **2005**, p. 278.

[14] R. G. Smart, D. C. Hanna, A. C. Tropper, S. T. Davey, S. F. Carter, D. Szebesta, *Electron. Lett.* **1991**, *27*, 1307.

[15] D. Liu, X. Xu, Y. Du, X. Qin, Y. Zhang, C. Ma, S. Wen, W. Ren, E. M. Goldys, J. A. Piper, S. Dou, X. Liu, D. Jin, *Nat. Commun.* **2016**, *7*, 10254.

[16] A. Vogler, H. Kunkely, *Inorg. Chim. Acta* **2006**, *359*, 4130.

[17] a) R. Buisson, J.-C. Vial, *J. Phys. Lett.* **1981**, *42*, 115; b) M. Kaczkan, D. A. Pawlak, S. Turczynski, M. Malinowski, *J. Alloys Compd.* **2017**, *728*, 1009; c) L. E. E. de Araújo, A. S. L. Gomes, C. B. de Araújo, Y. Messaddeq, A. Florez, M. A. Aegerter, *Phys. Rev. B* **1994**, *50*, 16219.

[18] a) R. Piramidowicz, R. Mahiou, P. Boutinaud, M. Malinowski, *Appl. Phys. B* **2011**, *104*, 873; b) D. J. Rátiva, C. B. de Araújo, Y. Messaddeq, *J. Appl. Phys.* **2006**, *99*, 083505.

[19] a) Y. Fujimoto, J. Nakanishi, T. Yamada, O. Ishii, M. Yamazaki, *Prog. Quantum Electron.* **2013**, *37*, 185; b) H. Okamoto, K. Kasuga, I. Hara, Y. Kubota, *Opt. Express* **2009**, *17*, 20227.

[20] a) J. Hölsä, T. Laamanen, T. Laihinen, M. Lastusaari, L. Pihlgren, L. C. V. Rodrigues, *Opt. Mater.* **2014**, *36*, 1627; b) T. Wei, W. Bo, C. Yan, C. Yeqing, L. Jun, Z. Qingguang, *Opt. Mater. Express* **2019**, *9*, 223.

[21] B. Walsh, N. Barnes, B. Di Bartolo, *J. Appl. Phys.* **1998**, *83*, 2772.

[22] a) C. Garapon, M. Malinowski, M. F. Joubert, A. A. Kaminskii, B. Jacquier, *J. Phys. IV* **1994**, *4*, 349; b) Y. Ohishi, T. Kanamori, T. Nishi, S. Takahashi, *Int. Photonics Technol. Lett.* **1991**, *3*, 715; c) B. Jacquier, A. Remillieux, M. F. Joubert, P. Christensen, H. Poignant, *J. Non-Cryst. Solids* **1993**, *161*, 241.

[23] T. Honda, T. Doumuki, A. Akella, L. Galambos, L. Hesselink, *Opt. Lett.* **1998**, *23*, 1108.

[24] L. X. Sun, H. Gong, B. J. Chen, H. Lin, E. Y. B. Pun, *J. Appl. Phys.* **2009**, *105*, 106109.

[25] a) E. Downing, L. Hesselink, J. Ralston, R. Macfarlane, *Science* **1996**, *273*, 1185; b) J.-H. Cho, M. Bass, H. P. Jenssen, *J. Soc. Inf. Disp.* **2007**, *15*, 1029.

[26] a) C. Zhang, L. Yang, J. Zhao, B. Liu, M.-Y. Han, Z. Zhang, *Angew. Chem., Int. Ed.* **2015**, *54*, 11531; *Angew. Chem.* **2015**, *127*, 11693; b) M. Hu, D. Ma, C. Liu, J. Wang, Z. Zhang, L. Meng, *J. Mater. Chem. C* **2016**, *4*, 6975; c) Q. Shao, G. Zhang, L. Ouyang, Y. Hu, Y. Dong, J. Jiang, *Nanoscale* **2017**, *9*, 12132.

[27] X. Guo, W. Song, C. Chen, W. Di, W. Qin, *Phys. Chem. Chem. Phys.* **2013**, *15*, 14681.

[28] X. Chen, D. Peng, Q. Ju, F. Wang, *Chem. Soc. Rev.* **2015**, *44*, 1318.

[29] F. Menges, Spectragryph—Optical Spectroscopy Software Version 1.2.14, http://www.effemm2.de/spectragryph/ (accessed: September 2020).

ADVANCED OPTICAL MATERIALS

Supporting Information

for *Adv. Optical Mater.*, DOI: 10.1002/adom.202001903

Dual Laser Study of Non-Degenerate Two Wavelength Upconversion Demonstrated in Sensitizer-Free $NaYF_4$:Pr Nanoparticles

Thomas J. de Prinse, Afshin Karami, Jillian E. Moffatt, Thomas B. Payten, Georgios Tsiminis, Lewis Da Silva Teixeira, Jingxiu Bi, Tak W. Kee, Elizaveta Klantsataya, Christopher J. Sumby, and Nigel A. Spooner*

Supporting Information

1. Synthesis and Characterisation

1.1.1 Raw material

Sodium hydroxide (Sigma–Aldrich, 99.99%), oleic acid (Sigma-Aldrich, technical grade, 90%), 1-octadecene (Sigma–Aldrich, technical grade, 90%), yttrium (III) chloride hexahydrate (Sigma-Aldrich, 99.9%), praseodymium (III) chloride anhydrous (Sigma–Aldrich, 99.99%), cyclohexane (Chem–Supply), methanol (Chem–Supply), ethanol (Chem–Supply), and ammonium fluoride (Chem–Supply, 98%) were obtained from commercial sources and used without further purification.

1.1.2 Synthesis of $NaYF_4$:Pr nanoparticles (1, 2 and 5% Pr)

The nanoparticles (NPs) were synthesized via a thermal decomposition method [1]. In a typical synthesis for $NaYF_4$:Pr NPs (1% Pr), $YCl_3.6H_2O$ (242.7 mg, 0.8 mmol) and $PrCl_3$ (2.5 mg, 0.01 mmol) were mixed with oleic acid (OA, 6 mL) and 1-octadecene (ODE, 15 ml) in a 150 ml 3-neck round bottom flask.. The suspension was then heated to approximately 150 °C to form a homogeneous solution before being cooled to room temperature. A solution of NaOH (100 mg, 2.5 mmol) and NH_4F (148.1 mg, 4 mmol) in methanol (10 ml) was added to the reaction mixture, which was stirred at room temperature for 20 min. The solution was heated to approximately 70 °C to evaporate the methanol from solution, increased gradually to 110 °C and maintained for approximately 10 min while argon gas flow was used to degas the solution, and finally heated to approximately 300 °C and maintained for 1 h under argon

gas flow. The solution was then cooled to room temperature and the NPs were precipitated from the solution by addition of ethanol (30 ml). The precipitated NPs were then collected by centrifugation (10,000 rpm for 5 min, Eppendorf 5920 R, Fa-6x50), washed with cyclohexane and ethanol several times and finally dried at 70 °C overnight. $NaYF_4$:Pr NPs with Pr dopant percentages of 2 and 5% were also synthesized using the above method.

1.2.1 Characterization of as-prepared NPs

The structure of the synthesized NP samples was confirmed by powder X-ray diffraction (PXRD) on MiniFlex 600 (Rigaku, Cu Kα, λ = 0.15418 nm). The instrument was operated at 40 kV and 15 mA and data were collected by scanning 2θ from 10° to 70° with a step size of 0.02°. JCPDS cards # 16-034 (hexagonal $NaYF_4$) and 06-0342 (cubical $NaYF_4$) were used to determine the crystal structure of as-synthesized NPs.

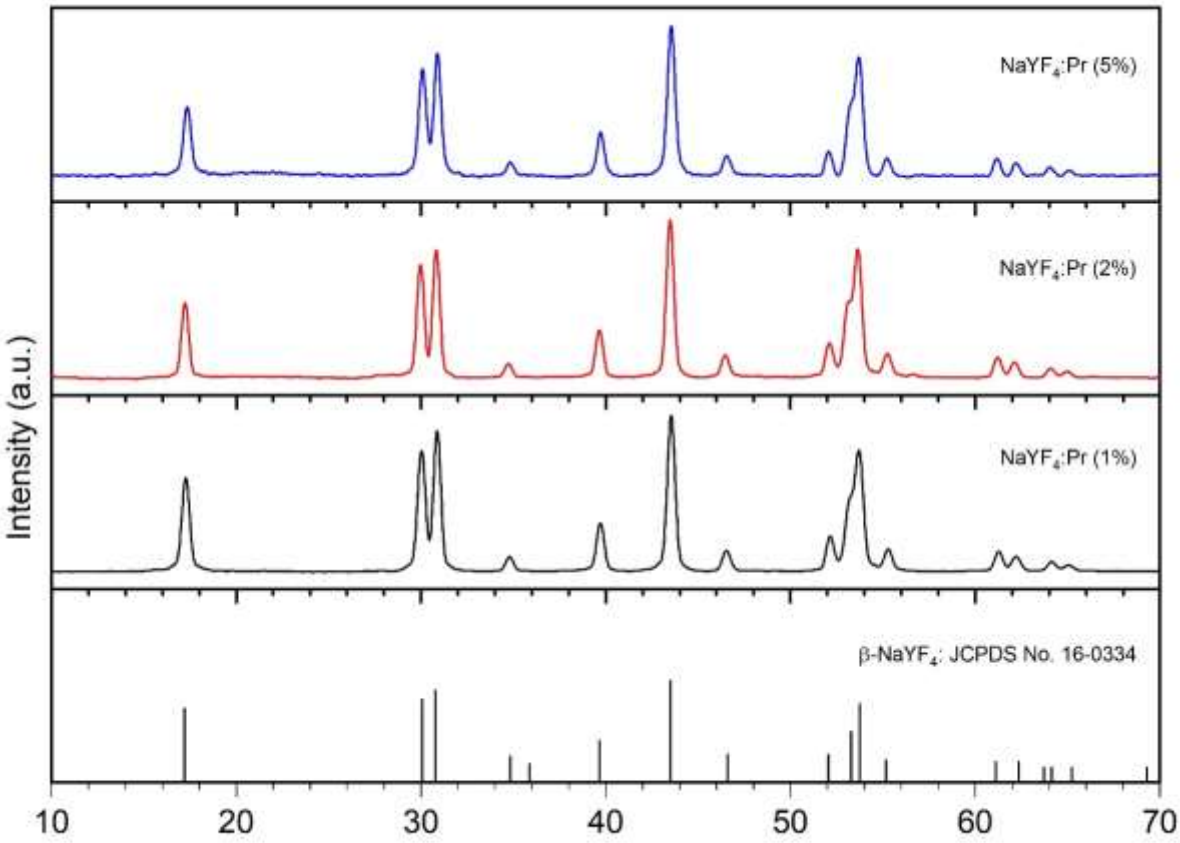

Figure 1S- PXRD patterns of $NaYF_4$:Pr NP samples with 1, 2 and 5% Pr dopant percentages.

The particle size and morphology of synthesized NPs were investigated by a transmission electron microscopy (TEM) on an FEI Titan Themis 80-200 G TEM operated at 200 kV accelerating voltage. The NP samples were dispersed in absolute ethanol using vortex shaker then small droplet of each suspension was transferred to a TEM sample holder and ethanol evaporated before placing into the TEM.

The composition of the nanoparticles was studied with an inductively coupled plasma mass spectrometer (ICP−MS, Agilent 8900x ICP-MS/MS) to confirm the Pr dopant concentration in the crystalline NPs. A series of mixed element standard solutions were used to determine the calibration curve needed to quantify Na, Y and Pr in the synthesized NP samples. The calibration standard solutions with concentrations of 10, 20, 50, 100, 200, 500 and 1,000 ppb were prepared using the HPS-Q17617A (10 mg/L in 2% HNO_3) standard solution. The NP samples with concentrations of 100 and 500 ppb for each of $NaYF_4$:Pr (1, 2 and 5%) NP samples were prepared by dissolving a measured amount of each NP sample in HNO_3 (2% v/v). Pure HNO_3 (2% v/v) was also used as the control (blank sample). The plasma conditions of RF power 1,550 W, sample depth 10 mm and Ar carrier gas flow rate 0.95 l/min and makeup gas flow rate of 0.1 l/min with a Micro Mist nebuliser and Scott Type spray chamber were used for measurements. The collision cell was run in He mode (4 ml/min He gas flow) for the following isotopes: 23Na, 89Y and 141Pr. On-line addition of Indium was used as the internal standard element.

1.2.2 ICP−MS Results

2. Table S1. The ICP-MS results for the $NaYF_4$:Pr (1, 2 and 5%) NP samples.

Sample		Pr (ppb)	Y (ppb)	Pr (%)
$NaYF_4$:Pr (1% Pr)	100 ppb	0.57 ± 0.002	31.45 ± 0.13	1.19%
	500 ppb	2.75 ± 0.02	165.75 ± 0.70	1.10%
$NaYF_4$:Pr (2% Pr)	100 ppb	1.54 ± 0.004	39.88 ± 0.04	2.56%
	500 ppb	7.63 ± 0.02	202.71 ± 0.32	2.49%
$NaYF_4$:Pr (5% Pr)	100 ppb	3.21 ± 0.003	35.64 ± 0.06	5.96%
	500 ppb	15.31 ± 0.04	178.71 ± 0.05	5.66%

1.3.1 Additional HRTEM and Elemental Mapping Images

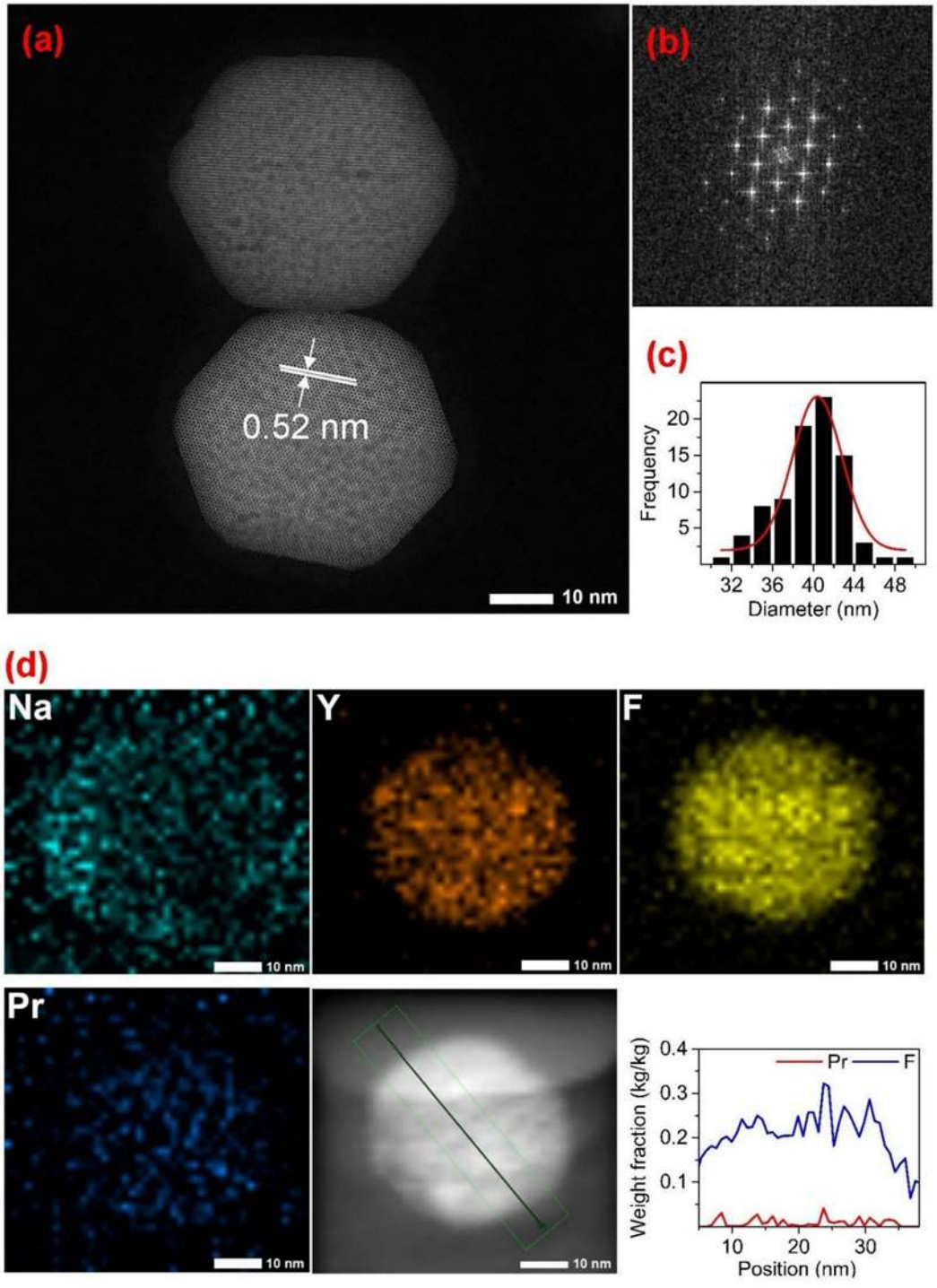

Figure 2S. HRTEM images of synthesised $NaYF_4$:Pr (2% Pr) NP samples. (a) HRTEM image with inter-planar distance of the synthesized NPs (b) SAED of synthesized NPs (c) size distribution and (d) EDX line scan across the NP sample.

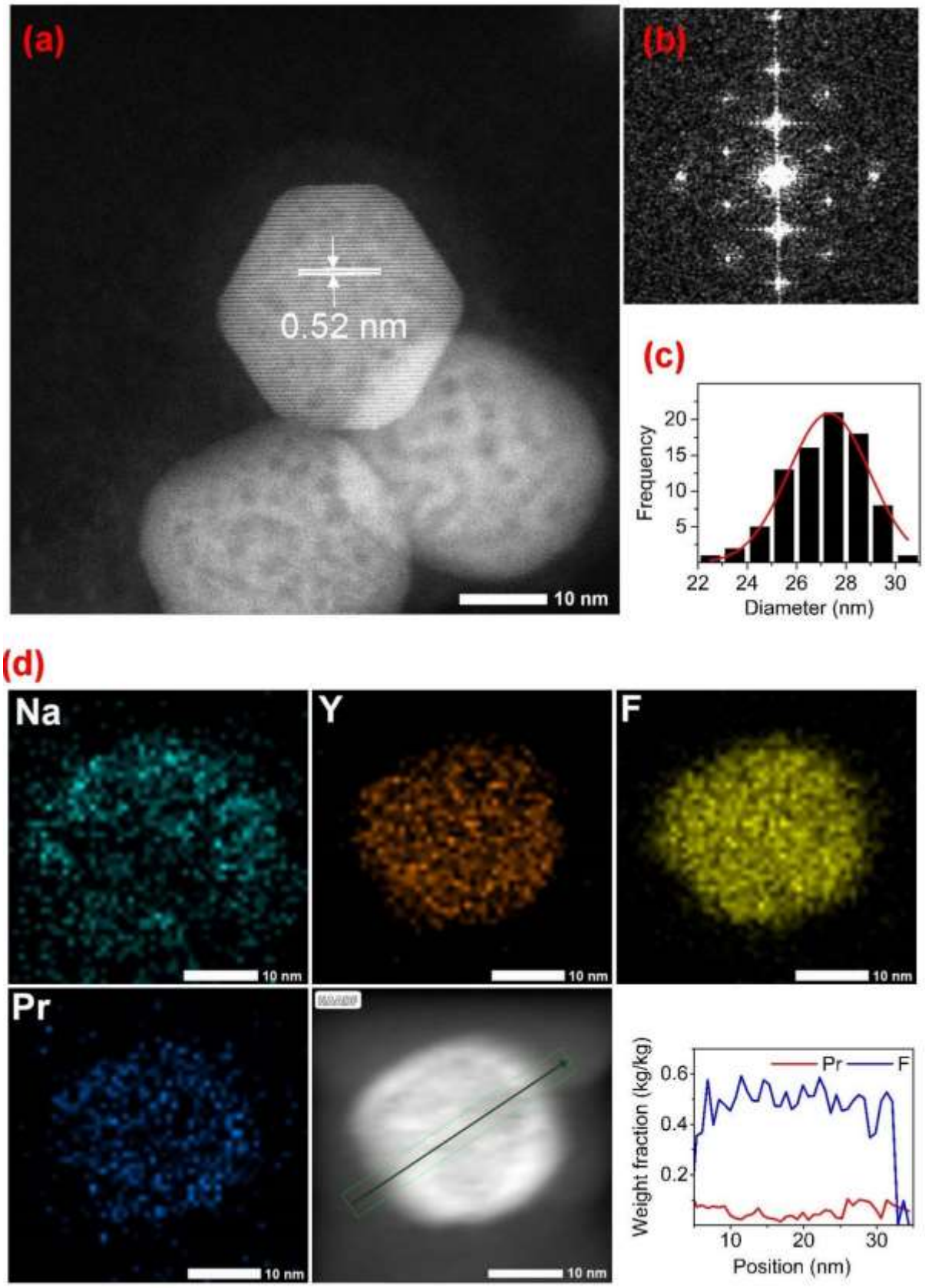

Figure 3S. HRTEM images of synthesised $NaYF_4$:Pr (5% Pr) NP samples. (a) HRTEM image with inter-planar distance of the synthesized NPs (b) SAED of synthesized NPs (c) size distribution and (d) EDX line scan across the NP sample.

2. Optical Analysis

2.1 Spectral comparison of samples

3.1 mg of the 1, 2 and 5% $NaYF_4$:Pr NP samples were weighed out into indentical aluminium sample holders, approximately 3 mm in diameter. The sample volumes completely covered the bottom of each holder. Each sample holder was placed into the center of the beams, which have a laser spot size of approximately 10 mm, completely illuminating the exposed surface of the NP sample. An imaging EMCCD capturing the visible fluorescence light was utalised to ensure that the surface of each sample was the same and each sample was evenly illuminated.

Excitation energy and collection efficiency was held constant during the measurements which allows the direct comparison of spectral brightness of each sample. The energy used on both lasers for this measurement was 0.5 mJ per pulse.

2.2 Energy Measurements of OPO lasers during experiment

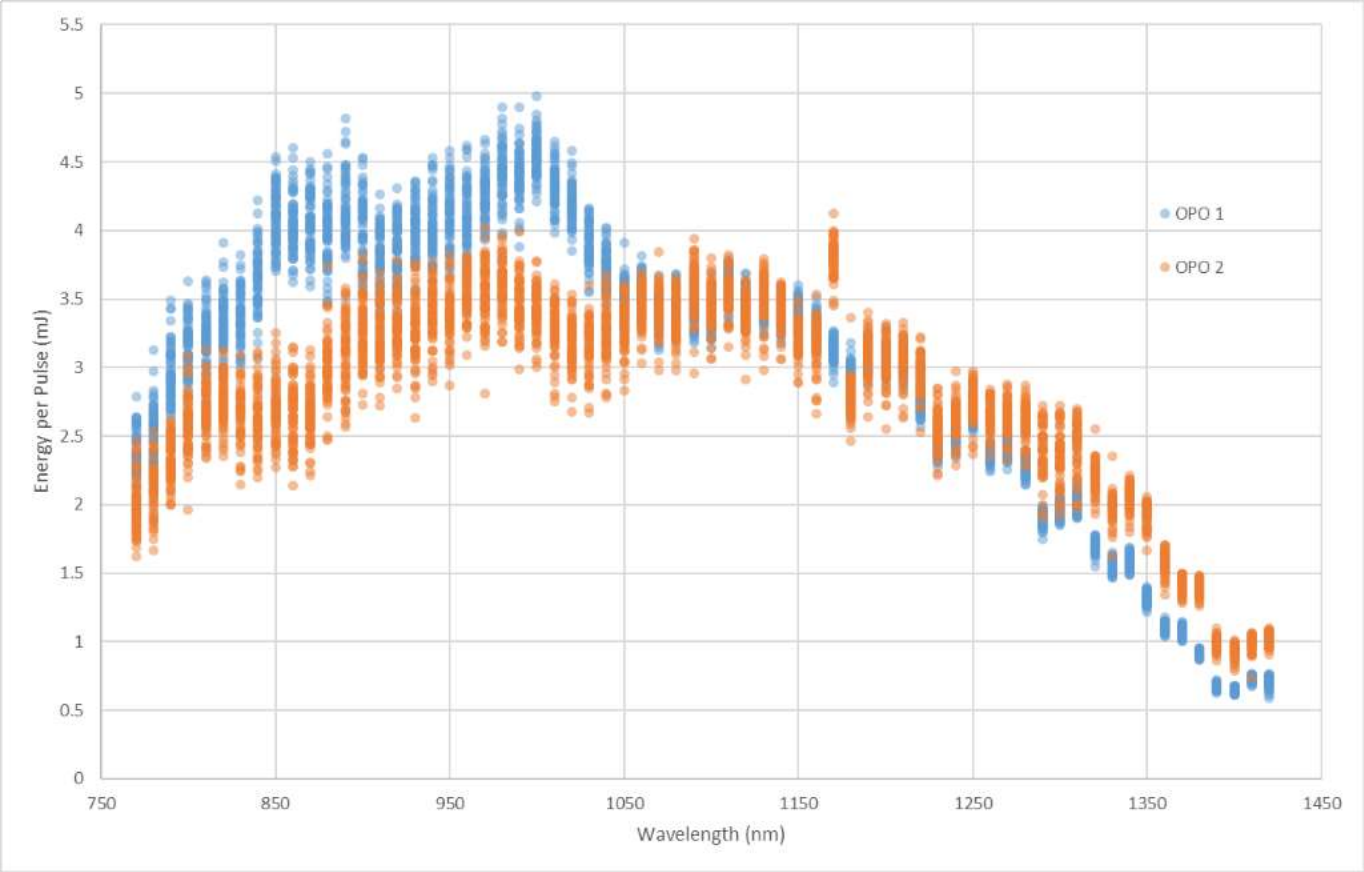

Figure 4S. Energy of both OPO lasers at differing wavelengths during the near-infrared excitation scan.

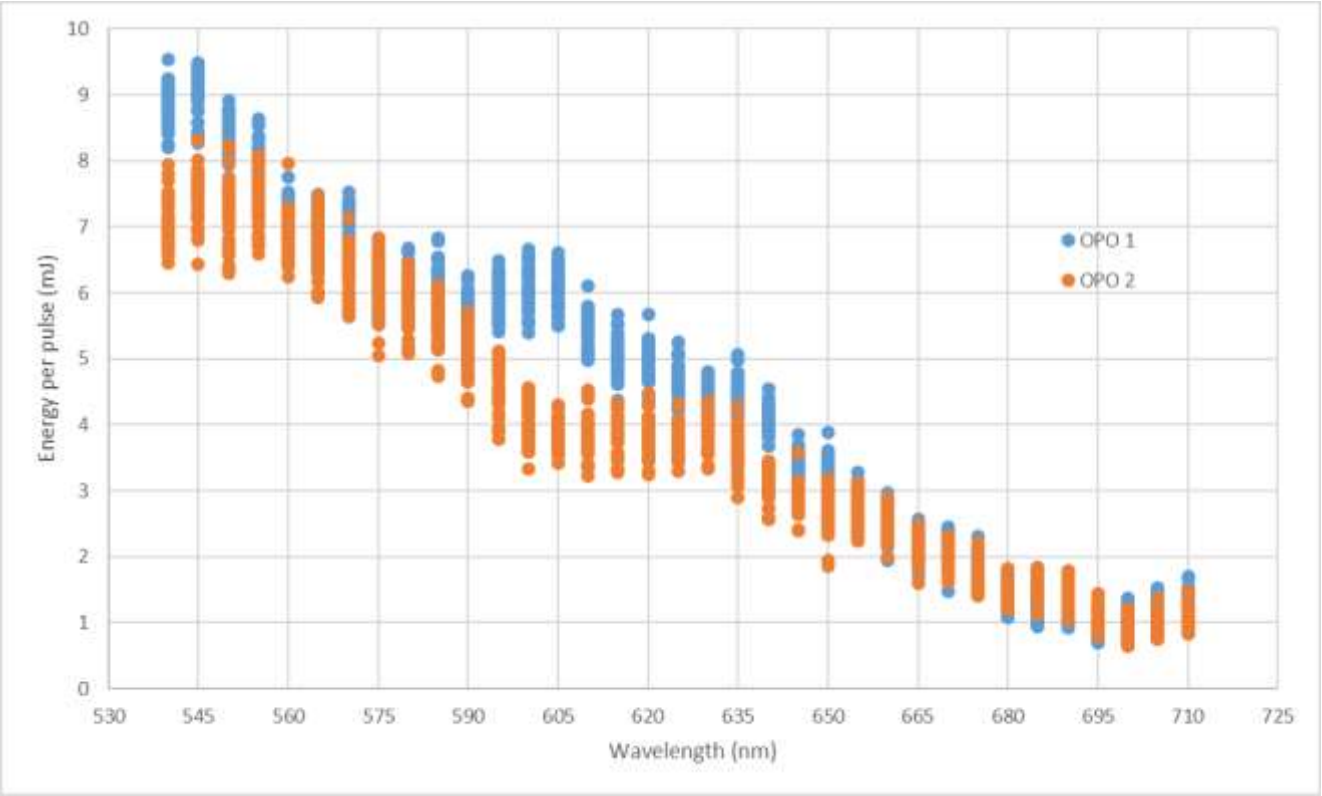

Figure 5S. Energy of both OPO lasers at differing wavelengths during the near-infrared excitation scan.

References

1 X. Guo, W. Song, C. Chen, W. Di, W. Qin, *Phys. Chem. Chem. Phys.* **2013**, 15, 14681.